

Design and Optimization of Adhesively Bonded Joints Mating Novel 3D-Fiber
Metal Laminates Subjected to Static and Dynamic In-plane and Out-of-plane Loadings

by

Fatemeh (Elnaz) Mottaghian

Submitted in partial fulfillment of the requirements
for the degree of Doctor of Philosophy

at

Dalhousie University

Halifax, Nova Scotia

April 2023

© Copyright by Fatemeh (Elnaz) Mottaghian, 2023

To, all the brave women of my beloved country, Iran. The true heroes who've been fighting for their life, freedom, and rights for the last 44 years.

and

To my mother, the strongest woman I've ever known, who taught me how to keep tight to my dreams, fight for them, and always keep my chin up.

Table of Contents

Table of Contents	iii
List of Tables	viii
List of Figures	x
Abstract	xviii
List of Abbreviations and Symbols Used	xix
Acknowledgments	xxvi
Chapter 1: Introduction	1
1.1. Context of the Present Research	1
1.2. Adhesively Bonded Joints	5
1.2.1. Introduction.....	5
1.2.2. Fabrication of ABJs	6
1.2.3. Loading and Failure Modes in ABJs	7
1.2.4. Configurations of ABJs.....	10
1.2.5. Applications of ABJs	12
1.3. Thesis Motivations.....	16
1.4. Thesis Objectives.....	17
1.5. Thesis Layout.....	18
Chapter 2: Literature Review	22
2.1. Sandwich Structures	22
2.2. General Introduction to FML.....	24
2.3. Adhesively Bonded Joints (ABJs).....	27
2.3.1. Joint Strength Enhancement	28
2.3.1.1. Surface Modification Procedures.....	28
2.3.1.2. Joint Configuration Advancement	29
2.3.1.3. Adhesive Properties Advancement	31
2.3.2. Lap-shear and Fatigue Response of ABJs	33
2.3.3. Flexural and Axial Compressive Responses of ABJs.....	35
2.3.4. Impact Response of ABJs	36
2.3.5. Numerical Analysis of ABJs.....	37
2.3.5.1. Cohesive Zone Model (CZM) Overview	40
2.3.6. Artificial Intelligence	45

Chapter 3: Numerical and Experimental Investigations Into Post-Buckling Responses of Stainless Steel- and Magnesium-Based 3D-Fiber Metal Laminates Reinforced by Basalt and Glass Fabrics	48
3.1. Abstract.....	48
3.2. Introduction.....	49
3.3. Experimental Procedures	50
3.3.1. Materials	50
3.3.2. Specimen Fabrication.....	50
3.3.3. Buckling Experiments.....	52
3.4. FE simulation Procedure.....	53
3.5. Results and Discussion	57
3.5.1. Experimental Results	57
3.5.2. Comparison of the Experimental and Numerical Results.....	60
3.5.3. Parametric Studies	67
3.5.3.1. Effect of Fiber Orientation.....	67
3.5.3.2. Effect of Glass and Basalt Fiber Hybridization.....	68
3.6. Summary and Conclusion.....	69
Chapter 4: Strength and Failure Mechanism of Single-Lap Magnesium-Basalt Fiber Metal Laminate Adhesively Bonded Joints: Experimental and Numerical Assessments	71
4.1. Abstract.....	71
4.2. Introduction.....	72
4.3. Experimental Investigation	74
4.3.1. Materials	74
4.3.2. Fabrication Procedure and Configuration of the Joints	74
4.3.2.1. MB-FML Fabrication.....	74
4.3.2.2. SLJs Fabrication.....	75
4.3.2.3. Surface Treatment.....	76
4.3.3. Test Setup.....	77
4.4. Results and Discussion	78
4.4.1. Experimental Results	78
4.4.1.1. Effects of Surface Treatment on the Bond Strength of SLJs.....	78
4.4.1.2. The Failure Mechanism of SLJs	80
4.4.2. Numerical Investigation and Results	81

4.4.2.1. Optimized Overlap Length	85
4.4.2.2. Stress Distribution in the Adhesive.....	86
4.4.2.3. Effects of Adhesive Thickness on the Bond Strength of SLJs	88
4.5. Summary and Conclusion.....	90
Chapter 5: On the Flexural Response of Nanoparticle-Reinforced Adhesively Bonded Joints Mating 3D-Fiber Metal Laminates – A Coupled Numerical and Experimental Investigation	93
5.1. Abstract.....	93
5.2. Introduction.....	94
5.3. Experimental Procedure.....	96
5.3.1. Selection of Materials	96
5.3.2. Fabrication Methodology	97
5.3.2.1. FML Fabrication	97
5.3.2.2. SLJs Fabrication.....	99
5.3.3. Characterization	101
5.4. Numerical Procedure	102
5.4.1. Cohesive Zone Modelling (CZM) Details	105
5.5. Results and Discussion	107
5.5.1. Experimental Results	107
5.5.1.1. Lap-shear Performance	107
5.5.1.2. Flexural Performance.....	111
5.5.1.3. Bond Failure Mechanism and Morphological Analysis	115
5.5.2. Numerical Results.....	118
5.6. Summary and Conclusion.....	120
Chapter 6: Performance of a Unique Fiber-Reinforced Foam-Cored Metal Sandwich System Joined with Adhesively Bonded CFRP Straps Under Compressive and Tensile Loadings.....	122
6.1. Abstract.....	122
6.2. Introduction.....	122
6.3. Material and Methods	123
6.3.1. Materials	123
6.3.2. Materials Characterization	124
6.3.3. Metal Sandwich Panels Fabrication Process.....	125
6.3.4. Fabrication of Double-Strap Joints	126

6.3.5. Surface Preparation Techniques.....	127
6.4. Results and Discussions.....	129
6.4.1. Microscopic Analysis.....	129
6.4.2. Effects of Surface Treatments on Joint Capacity.....	133
6.4.3. Effects of Surface Treatment on Failure Mode.....	135
6.4.4. Effects of CFRP Strap Geometry on Buckling and Tensile Capacities.....	137
6.4.4.1. Tensile Loading	137
6.4.4.2. Compressive Loading	139
6.5. Conclusion	144
Chapter 7: Assessment of Failure Mechanism of Double-Strap 3D-FML Adhesively Bonded Joints under Tensile and Compressive Loadings Using Cohesive Zone Modelling Approach	146
7.1. Abstract.....	146
7.2. Introduction.....	147
7.3. Summary of the Experimental Study.....	148
7.4. Numerical Study	149
7.4.1. Geometry Modelling.....	149
7.4.2. Material Modelling	151
7.4.2.1. CZM Formulation	153
7.4.2.2. FE Modeling of the Bonded Region	157
7.5. Results and Discussions.....	159
7.5.1. Refinement of the Interface Model	159
7.5.1.1. Damage Evolution in the Adhesive	159
7.5.2. CFRP Straps Length and Thickness Optimization	163
7.5.3. Stress Distribution in the Bond Regions.....	166
7.5.4. Failure Simulation in Buckling Analysis.....	172
7.6. Conclusion	175
Chapter 8: Machine Learning/Finite Element Analysis - A Collaborative Approach for Predicting the Axial Impact Response of Adhesively Bonded Joints with Unique Sandwich Composite Adherends	177
8.1. Abstract.....	177
8.2. Introduction.....	178
8.3. Experimental Framework	179
8.3.1. Materials	179

8.3.2. Specimen Fabrication.....	180
8.3.3. Impact Testing Procedure	181
8.4. Numerical Framework	182
8.5. Machine Learning Framework.....	186
8.5.1. Data Collection	186
8.5.2. Data Pre-processing	187
8.5.3. Deep Neural Networks.....	188
8.5.4. Evolutionary Models.....	190
8.5.4.1. Genetic Programming	190
8.5.4.2. Genetic Algorithm	193
8.6. Results and Discussions.....	194
8.6.1. Experimental and Numerical Validation.....	194
8.6.2. Machine Learning Results	197
8.6.3. Design Variable Importance and Selection.....	201
8.6.4. Optimization	206
8.7. Conclusions.....	206
Chapter 9: Conclusion.....	209
9.1. Summary and Conclusion.....	209
9.2. Recommendations for Future Works.....	216
References.....	219
Appendix A: Fabrication Manual of 3DFGF (Parabeam, 2022).....	238
Appendix B: Basalt-Epoxy Fabrication with Vacuum-Assisted Resin Infusion Procedure.....	239
Appendix C: Copyright Permissions.....	241
Copyright Permission for Chapter 3	241
Copyright Permission for Chapter 4	242
Copyright Permission for Chapter 5	243
Copyright Permission for Chapter 6	244

List of Tables

Table 3-1. Material properties used in the finite element simulations.....	56
Table 3-2. LS-DYNA material-related keywords used in the analyses.....	56
Table 3-3. Influence of initial imperfection on the buckling capacity of Mg-3DFGF-Mg calculated numerically and the error margin with respect to the average experimental results.....	62
Table 3-4. Comparison of the buckling capacity results (kN) obtained numerically and experimentally.	65
Table 4-1. Categories of the fabricated single-lap MB-FML ABJ specimens.	81
Table 4-2. Mechanical properties of the materials used in the FE model (Mohamed, 2020; Mottaghian et al., 2020; Yaghoobi et al., 2021a).	83
Table 4-3. LS-DYNA Material models utilized in constructing the FE model.	84
Table 4-4. Comparison of the experimental and numerical failure loads of single-lap MB-FML ABJs.....	86
Table 4-5. Effects of adhesive thickness on the failure load and shear strength of single-lap MB-FML ABJs with 35 mm overlap.....	90
Table 5-1. Groupings of the fabricated single-lap FML ABJ specimens and their flexural modulus.	100
Table 5-2. Material models utilized in LS-DYNA.	102
Table 5-3. Mechanical properties of the materials used in the FE model (Mottaghian et al., 2020).	104
Table 5-4. CZM parameter for neat and GNP-reinforced adhesive (Mohamed & Taheri, 2017).....	107
Table 5-5. Comparison of the experimental and numerical failure loads of single-lap 3D-FML ABJs.	118
Table 6-1. Mechanical properties of the materials (Mottaghian & Taheri, 2022b; Mottaghian et al., 2020).....	124
Table 6-2. Configurations of the fabricated adhesively bonded joints.	127
Table 6-3. Classifications of the surface treatments.	128
Table 6-4. Joint capacities, shear strength, and average surface roughness parameter values for C5-L25 configuration.	132

Table 6-5. The average dimension of C5-L25 configuration adhesively bonded joints.	134
Table 6-6. Average values of the capacity, energy absorption, and strength of each group of double-strap ABJ systems.	138
Table 7-1. Configurations of fabricated double-strap adhesive joints.	149
Table 7-2. LS-DYNA Material models utilized the numerical models.	151
Table 7-3. Mechanical properties of the materials used in the FE model (Mottaghian et al., 2020).	152
Table 7-4. CZM parameter for structural adhesive (Mohamed & Taheri, 2017).	156
Table 7-5. Specifications of the developed FE configurations.	158
Table 7-6. Comparison of numerical and experimental results.	165
Table 8-1. Mechanical properties of 3DFRP (Yaghoobi et al., 2021b).	183
Table 8-2. CZM parameter of adhesive in the bonded area.	184
Table 8-3. Mechanical properties of the strap and face sheets.	185
Table 8-4. Defined design parameters in double-strap sandwich structure bonded joints.	186
Table 8-5. Configurations of the designed DNNs model.	189
Table 8-6. Specific parameters used in the designed GP model.	192
Table 8-7. Specific parameters used in the designed GA model.	193
Table 8-8. Specifications of the configurations selected for parametric study and optimization.	202

List of Figures

Figure 1-1. The trend in the use of composites by weight in Airbus aircraft (Xu et al., 2018).	2
Figure 1-2. Typical configuration of a conventional FML.	2
Figure 1-3. 3DFGF: (a) knitted pillars to plies (Parabeam, 2022), (b) front-view, and (c) side-view (Mottaghian & Taheri, 2022).	3
Figure 1-4. 3D-FML (a) exploded view, indicating the different components, and (b) the final product (De Cicco, 2019).	4
Figure 1-5. Application of Glass-reinforced aluminum laminates (GLARE) in Airbus A380 (Yang, 2008).	5
Figure 1-6. Mechanical interlocking facilitates the flow of the adhesive into the morphological irregularities of an adherend's surface.	6
Figure 1-7. Typical load stress of ABJs (a) compression, (b) tensile, (c) shear, (d) cleavage, (e) peel, and (f) torsion (Mata, 2013).	7
Figure 1-8. (a) interfacial, (b) cohesion, (c) interfacial-cohesion combination, and (d) adherend failure modes in ABJs.	9
Figure 1-9. Delamination failure in composite adherends (Banea & da Silva, 2009).	9
Figure 1-10. Configurations of the commonly used ABJs, (a) butt, (b) single-lap, (c) double-lap, (d) stepped, (e) scarf, (f) single-strap, (g) double-strap, (h)T, and (i) L.	10
Figure 1-11. Schematic of SLJ bending due to eccentricity of the load path (Redmann et al., 2021).	11
Figure 1-12. Application of ABJs in the aviation industry, (a) Cirrus SR20, (b) PZL I-23 Manager, (c) a section of the fuselage, and (d) Generic-bonded wing spar (Dobrzański & Oleksiak, 2021).	13
Figure 1-13. Application of ABJs in the automotive industry (Kolnerová et al., 2010).	14
Figure 1-14. Cross-section of Sandia National Laboratories' National Rotor Testbed 13-m blade, showing the ABJ parts (Murray et al., 2019).	15
Figure 1-15. ABJs in (a) bonding composite to steel hull (Anyfantis, 2012), (b) different types of joints in bulkhead (Delzendehrooy et al., 2022).	15
Figure 2-1. Schematic of the sandwich structure geometry (Zheng et al., 2022).	23

Figure 2-2. Different plausible failure modes in sandwich structures (Zenkert, 1997)....	23
Figure 2-3. Fiber bridging attribute to limit crack growth in FMLs (Malingam et al., 2020).	24
Figure 2-4. Summary of various FML configurations.....	25
Figure 2-5. The interlocking mechanism generated by an effective surface treatment procedure.	29
Figure 2-6. (a) Effects of scarf angle on the ABJs strength, (b) damage repair with bonded joints (Srinivasan et al., 2022). Note that the repair signature refers to the area that has been repaired.....	31
Figure 2-7. Schematic of strengthening and toughening mechanisms generated by MWCNTs in ABJs (Kumar et al., 2018).	32
Figure 2-8. Crack tip singularity in LEFM (Ameh, 2020).....	38
Figure 2-9. Crack simulation (a) FEM, (b) XFEM (Swati et al., 2019).	39
Figure 2-10. Failure modes (Hadei et al., 2020).....	40
Figure 2-11. Fracture tests (a) DCB, (b) ENF, and (c) SLB (Burlayenko & Sadowski, 2008).	40
Figure 2-12. Graphic depictions of (a) cohesive fracture area, and (b) void deformation at the crack tip (Zan et al., 2017).	41
Figure 2-13. Traction-separation curves (Alfano, 2006).	42
Figure 2-14. Graphical sketch of parameters of the bilinear cohesive model.	44
Figure 3-1. Fabrication process sequence of the base 3D-FMLs.....	52
Figure 3-2. Various 3D-FMLs configurations considered in this study: (a) SS-3DFGF-SS, (b) SS-G-3DFGF-G-SS, (c) SS-B-3DFGF-B-SS, (d) Mg-3DFGF-Mg, (e) Mg-G-3DFGF-G-Mg and (f) Mg-B-3DFGF-B-Mg.....	53
Figure 3-3. Buckling test setup.	54
Figure 3-4. Finite element model of the 3D-FML.	55
Figure 3-5. Buckling capacities of 3D-FML configurations.	58
Figure 3-6. Comparison of the normalized buckling capacities (with respect to weight) of 3D-FML configurations.	59

Figure 3-7. Comparison of the normalized buckling capacities (with respect to cost) of 3D-FML configurations.....	59
Figure 3-8. Comparison of the normalized buckling capacities (with respect to stiffness) of 3D-FML configurations.....	60
Figure 3-9. Buckling failure modes (a) SS-3DFGF-SS, (b) SS-G-3DFGF-G-SS, (c) SS-B-3DFGF-B-SS, (d) Mg-3DFGF-Mg, (e) Mg-G-3DFGF-G-Mg and (f) Mg-B-3DFGF-B-Mg.....	61
Figure 3-10. Mesh convergence analysis of FE model for Mg-3DFGF-Mg configuration.....	62
Figure 3-11. Comparison of the numerical and experimental load-axial shortening curves of the SS-3DFGF-SS (black line) and Mg-3DFGF-Mg (blue line) configurations tested under compressive loading.....	63
Figure 3-12. Comparison of the numerical and experimental load-axial shortening curves of the SS-G-3DFGF-G-SS (black line) and Mg-G-3DFGF-G-Mg (blue line) configurations tested under compressive loading.	64
Figure 3-13. Comparison of the numerical and experimental load-axial shortening curves of the SS-B-3DFGF-B-SS (black line) and Mg-B-3DFGF-B-Mg (blue line) configurations tested under compressive loading.	64
Figure 3-14. Deformed shapes and core failure of SS-B-3DFGF-B-SS (a) Experiment and (b) FE simulation.	66
Figure 3-15. Comparison of load-axial shortening curves based on modelling of metal/FRP interface resin with elastic and plastic material models (a) Mg-3DFGF-Mg and (b) SS-3DFGF-SS.....	66
Figure 3-16. Effects of fiber orientation on the buckling behaviour of (a) SS-G-3DFGF-G-SS and (b) SS-B-3DFGF-B-SS.....	67
Figure 3-17. Effects of fiber hybridization on the buckling behaviour of (a) Mg-G-3DFGF-G-Mg and (b) SS-G-3DFGF-G-SS.	68
Figure 4-1. Schematic of the fabrication scheme used to produce the single-lap MB-FML ABJs.	75
Figure 4-2. Schematic and dimensions of single-lap MB-FML ABJs.....	76
Figure 4-3. (a) lap-shear test setup, (b) MB-FML SLJ specimens.	76
Figure 4-4. Load-displacement responses of the single-lap MB-FML ABJs.	77

Figure 4-5. Experimentally obtained average failure load and shear strength of MB-FML-S-25 and MB-FML-H-25 group of specimens.....	78
Figure 4-6. The fracture surfaces of the single-lap MB-FML ABJs (a) adhesion, and (b) cohesion failure modes.....	80
Figure 4-7. Details of the FE model of the single-lap MB-FML ABJ and the boundary conditions.....	82
Figure 4-8. Stress-strain responses of (a) Mg alloy, and (b) adhesive utilized in the FE model.	83
Figure 4-9. Details of the FE model of the single-lap MB-FML ABJ and the boundary conditions.....	84
Figure 4-10. Effects of overlap length on the failure load of single-lap MB-FML ABJs.	85
Figure 4-11. Comparison of the numerical and experimental load-displacement responses of MB-FML-H-35 group of specimens.....	86
Figure 4-12. Effects of overlap length on the distribution of (a) shear and (b) peel stresses.	89
Figure 4-13. Stress distributions (a) along the length, (b) across the width of the overlap in the MB-FML-H-35 group of specimens.....	90
Figure 5-1. The sequence 3D-FML Fabrications.....	98
Figure 5-2. Schematic of (a) specially designed fabrication jig, (b) dimension of single-lap 3D-FML ABJs.	99
Figure 5-3. Fabrication process sequence of the GNP-reinforced 3D-FML SLJs.....	101
Figure 5-4. (a) Single-lap quasi-static flexural test setup, (b) details of the FE models of the single-lap 3D-FML ABJs.	103
Figure 5-5. The trapezoidal mixed-mode CZM.....	107
Figure 5-6. Joint capacities of single-lap FML ABJs subjected to quasi-static lap-shear load.	108
Figure 5-7. Load-displacement responses of single-lap FML ABJs subjected to quasi-static lap-shear load.	109
Figure 5-8. Energy absorption capacities and shear strengths of single-lap FML ABJs subjected to quasi-static lap-shear load.	110

Figure 5-9. Load-displacement response of single-lap 3D-FML-3 ABJ subjected to quasi-static lap-shear load.....	111
Figure 5-10. Joint capacities of 3D-FML SLJs subjected to quasi-static flexural load..	112
Figure 5-11. Delamination failure of Mg/3D-FGF interface of 3D-FML-3 SLJ with 0.5 wt% GNP reinforced-adhesive subjected to quasi-static flexural load.	113
Figure 5-12. Load-displacement curves of 3D-FML SLJs subjected to quasi-static flexural load.	114
Figure 5-13. The ultimate flexural strengths and strains of 3D-FML SLJs subjected to quasi-static flexural load.....	115
Figure 5-14. Failure surface morphologies of GNP-reinforced 3D-FML SLJs.....	116
Figure 5-15. FESEM micrographs of the fracture surfaces of 3D-FML SLJs (a–d) GNPs pull-out, (e–f) agglomerated GNPs in adhesive, (g) EDX of a typical GNPs-impregnated adhesive.	117
Figure 5-16. Damage propagation in 3D-FML SLJs (a-b) crack growth in bonding area, (c-d) delamination growth in Mg/3DFGF interface.....	119
Figure 6-1. (a) Tensile (lap-shear) test setup, (b) confocal laser scanning microscope, (c) compression/buckling test set-up.	125
Figure 6-2. Components of the metal sandwich panel (a) 3DFGF-epoxy, (b) 3DFGF cavities infilled with foam, and (c) fiber-reinforced foam-cored metal sandwich system.	126
Figure 6-3. Schematics and dimensions of the double-strap bonded metal sandwich panels.	127
Figure 6-4. The surafce topographies of (a) UT, (b) GS, (c) GS+PC, (d) GS+AN, (e) AS, (f) AS+AE, and (g) UT CFRP, and (h) AP surface treatments.	131
Figure 6-5. Schematic of surface roughness parameters (a) Sa, (b) Ra, (c) Rz, (d) Rsm, and (e) Rku (Mikroskop-Lösungen)	132
Figure 6-6. The failure modes in the bond regions of adhesively bonded joints prepared by different surface treatment methods: (a) GS, (b) GS+PC, (c) GS+AN, (d) AS, (e) AS+AE.	137
Figure 6-7. The typical load-displacement response of different double-strap ABJ configurations subjected to tensile and compressive loadings.	140
Figure 6-8. Buckling responses of (a) C3-L25, (b) C5-L25, (c) closer view of C5-L25, (d) C5-L35 configurations.	142

Figure 7-1. A typical double-strap adhesive joint (a) dimensions of the quarter symmetry model (used for tensile loading) and the full model (used for compressive loading) and the associated boundary conditions, (b) FE mesh of the cross-section of the 3D-FML and the actual 3D-FML.	148
Figure 7-2. The schematics of trapezoidal mixed-mode CZM.	154
Figure 7-3. SSchematics of different FE configurations for the adhesive layers	158
Figure 7-4. Comparison of the numerically predicted load-displacement responses of the FE models of the C5-L25 configuration subjected to tensile loading and the experimental results.	160
Figure 7-5. Top view (x-z plane) showing the sequence of cohesive crack growth in the bonded region of configuration VII (a) first layer, (b) second layer, (c) third layer, (d) fourth layer, and (e) fifth layer at different time steps,(f) mixed interfacial-cohesion failure mode in the actual C5-L25 configuration.	162
Figure 7-6. Magnitudes of the shear and peel stress at a different layer of the model for C5-L25 configuration under a tensile load.	163
Figure 7-7. Effects of strap length and thickness (number of CFRP layers) on joint capacity.	164
Figure 7-8. Comparison of the experimental and numerical responses of various configurations of the double-strap adhesive joints under tensile loading....	165
Figure 7-9. Deformation of the quarter symmetry model of the double-strap adhesive joints subjected to tensile loading.	166
Figure 7-10. Variation in the distributions of the longitudinal stress (σ_x) within the thickness of the strap (path ab is identified in Figure 7-1), at its midspan. .	167
Figure 7-11. Distribution of the shear (a) and peel (b) stresses on each CFRP layer of the straps in C5-L35 configuration.	168
Figure 7-12. Shear stress distribution on each CFRP layer of the straps in the C5-L35 configuration without any midspan gap.	169
Figure 7-13. Influence of strap thickness on the distribution of (a) shear and (b) peel stresses on the adhesive layer.	170
Figure 7-14. Influence of strap length on the distribution of (a) shear and (b) peel stresses on the adhesive layer.	171

Figure 7-15. Comparison of the experimental and numerical responses of various configurations of the double-strap adhesive joints under compressive loading.	173
Figure 7-16. Comparison of the experimental and numerically predicted global failure modes in (a) C3-L25, (b) C5-L25, and (c) C5-L35 joint configurations subjected to compressive loading.	174
Figure 8-1. Schematic of the research conducted in this study.....	179
Figure 8-2. (a) Dimensions of the double strap bonded sandwich joints, impact-buckling set up (b) overall view of the test setup, (c) close-up side- and top view of the specimen holding fixture.	181
Figure 8-3. The FE model (a) overall model, (b) FE mesh of the cross-section of the adherends and actual sandwich composite, and (c) FE mesh of the bonded area including three layers of zero-thickness cohesive elements combined with continuum solid elements.	183
Figure 8-4. Schematic of 3-fold cross-validation technique.	187
Figure 8-5. Schematic of (a) biological and mimicked artificial neural network (Gerstner et al., 2014), (b) architecture of the deep neural network designed to predict the impact-buckling ultimate capacity of the bonded joints.	188
Figure 8-6. Evolutionary schematic of (a) biological DNA mutation, (b) tree structure of GP cross-over representing $2 - 4(3 - z)/8 + y$ and $6 + 5x$ equations.	191
Figure 8-7. Representation of single point cross-over evolution in a GA population. ...	192
Figure 8-8. Flowcharts of GP and GA processes.....	194
Figure 8-9. Comparison of experimental and numerical load and axial shortening history of double-strap sandwich composite bonded joints subjected to different impact energies.	195
Figure 8-10. Qualitative comparison between the experimental and numerically predicted deformed shapes at different time instances during the impact event, indicating the second mode of buckling followed by shear crimping.	196
Figure 8-11. Ultimate impact-buckling capacities calculated through 410 FE-CZ analyses by considering 13 different design parameters.	197
Figure 8-12. The correlation between FEM and DNNs for the train and test datasets in (a) cluster 1, (b) cluster 2, and (c) cluster 3.	198

Figure 8-13. The correlation between FEM and GP for the train and test datasets in (a) cluster 1, (b) cluster 2, and (c) cluster 3.	200
Figure 8-14. Sensitivity analysis on the design variables defined for double-strap sandwich structure bonded joints subjected to impact-buckling loading.	202
Figure 8-15. 3D surface plot indicating the effects of (a) straps and metal stiffness, (b) specimen length, and impact energy, (c) strap length and face sheet thickness, and (d) 3DFRP thickness and perturbation on the ultimate impact-buckling capacity of bonded joints based on DNNs model.	204
Figure 8-16. 3D surface plot indicating the effects of (a) straps and metal stiffness, (b) specimen length, and impact energy, (c) strap length and face sheet thickness, and (d) 3DFRP thickness and perturbation on the ultimate impact-buckling capacity of bonded joints based on GP model.....	205
Figure D-1. VARI setup (a) front-view schematic, (b) top-view, and (c) the fabricated basalt-epoxy laminates.....	240

Abstract

The automotive and aerospace industries are rapidly growing sectors of the global economy. The global commercial vehicle market is projected to grow from \$955 billion in 2020 to \$1.7 trillion in 2029. According to Boeing's Commercial Market Outlook 2019-2038, the air travel market is projected to be 2.5 times larger in 20 years. As a consequence, energy conservation in the transportation industry has become a worldwide priority due to growing fuel consumption, as well as increased emphasis on reducing carbon dioxide (CO₂) emissions to combat global warming.

Over the last few decades, many researchers have been working on developing lightweight materials such as composites and Fiber Metal Laminates (FMLs) to address the aforementioned issues. Large industrial structural systems consist of components and sub-components; therefore, special attention must be paid to ensure proper assembly. Adhesively bonded joints (ABJs) have emerged as a promising alternative to traditional joining methods due to several advantages they offer, including a higher strength-to-weight ratio and lower magnitude of stress concentration in multi-material joining systems. Most of the studies conducted on ABJs investigated their performance under tensile and fatigue loadings. However, over their life cycle, ABJs may also become subjected to flexural, compressive, and various impact-loading scenarios. The bonded structural system must be able to ensure such loading states while performing the expected functions.

Therefore, the main objective of the research presented in this dissertation is the design and optimization of suitable adhesively bonded systems for mating 3D-FMLs subjected to both static and dynamic in-plane and out-of-plane loadings. A series of systematic experimental, numerical investigations, and computational data analyses are conducted to accomplish the objectives. New renditions of 3D-FMLs are developed by incorporating various metallic alloys and synthetic and biodegradable materials. Several finite element (FE) models are developed, using the LS-DYNA platform, to investigate the influence of different geometrical and material design parameters on the developed ABJs systems under different loading scenarios. The models are capable of accurately predicting each joint's capacity and performance, including the initiation and evolution of local (i.e., cohesion and interfacial failure), and global (i.e., delamination and shear failure) damage mechanisms. The performance of the 3D-FMLs bonded joints is compared against their 2D counterparts, and the optimal configuration with respect to strap length and thickness is established.

The feasibility of strengthening the system's bonded interfaces by incorporation of inexpensive Graphene Nanoplatelets (GNP) and implementation of several surface treatment procedures are explored. Finally, the FE models are used to examine the influence of 13 parameters on the joint capacity, generating an extensive database. The database is then fed into three designed Machine Learning (ML) algorithms. The ML models are trained to predict the response of various ABJs accurately. The models are also capable of examining the simultaneous effects of different geometrical-, material- and performance-based design parameters on the joint capacity with high precision. The ML models are used to establish a simple yet effective semi-empirical equation, which would enable practicing engineers to quickly evaluate the ultimate load-bearing capacity.

List of Abbreviations and Symbols Used

2D-FML	Two-dimensional fiber-metal laminate
3DFGF	Three-dimensional fiberglass fabric
ABJ	Adhesively bonded joint
A&D	Aerospace and defence
AE	Acoustic emission
AI	Artificial intelligence
Al	Aluminum
Al-FML	Aluminum fiber metal laminate
ANNs	Artificial neural networks
AP	Surface treatment with abrasive paper
AS	Grit blasting by alumina grit surface treatment procedure
AS+AE	AS followed by acid etching surface treatment procedure
ARRAL	Aramid-reinforced aluminum laminates
CARALL	Carbon-reinforced aluminum laminates
CFRP	Carbon fiber-reinforced plastic
CLSM	Confocal laser scanning microscope
Cn	Continuum elements
CNF	Carbon nanofibers
CNT	Carbon nanotubes
CO ₂	Carbon dioxide
COD	Crack opening displacement
CPU	Central processing unit
CZ	Cohesive zone

CZM	Cohesive zone model(ling)
DCB	Double cantilever beam
DIC	Digital image correlation
DLVDT	Dynamic linear variable displacement transducer
DNNs	Deep neural networks
DOF	Degrees of freedom
DSJ	Double-strap joint
ELFORM	Element formulation
ENF	End notched flexural
EUASA	European Union Aviation Safety Agency
FE	Finite element
FEM	Finite element method
ERT	Extremely randomized tree
FESEM	Field emission scanning electron microscopy
FE-CZ	Finite element-cohesive zone
ELFORM	Element formulation
FML	Fiber-metal laminate
FRP	Fiber-reinforced plastic
GA	Genetic algorithms
GFRP	Glass fiber-reinforced plastic
GLARE	Glass-reinforced aluminum laminates
GNPs	Graphene nanoplatelets
G-NH ₂	Amino-functionalized GNP
G-Si	Silane-modified GNPs
GS	Grit blasting with glass grits surface treatment procedure

GP	Genetic programming
GS+AN	GS followed by an annealing surface treatment procedure
GS+PC	GS followed by the peel-ply surface treatment procedure
H	Hybrid sandblasting with resin coating surface treatment
HAZ	Heat-affected zone
LVI	Low-velocity impact
Mg	Magnesium
MB-FML	Magnesium-basalt fiber metal laminate
MB-FML-H	MB-FML surface modified with the hybrid method
MB-FML-S	MB-FML surface modified with sandblasting
Mg-3DFGF-Mg	Magnesium-3DFGF- magnesium
Mg-B-3DFGF-B-Mg	Magnesium -basalt-3DFGF-basalt- magnesium
Mg-G-3DFGF-G-Mg	Magnesium -glass-3DFGF-glass- magnesium
Mg-to-Mg	Magnesium to magnesium
ML	Machine learning
MWCNT	Multi-walled carbon nanotubes
NzCs	Non-zero-thickness cohesive elements
OFAT	One-factor-at-a-time
OSLJ	One-step lap joint
PAA	Phosphoric acid anodizing
PEEK	Poly-ether-ether-ketone
PC	Personal computer
Ra	Profile arithmetical mean height
Rku	The maximum Kurtosis
RMS	Root mean square

Rsm	Arithmetic mean width of profile elements
Rz	Maximum height of the profile
S	Sandblasting surface treatment procedure
Sa	Surface arithmetical mean height
SAA	Sulfuric acid anodizing
SiC	Silicon carbide
SLB	Single-leg bending
SLJ	Single-lap joint
SS	Stainless steel
SS-3DFGF-SS	Stainless steel-3DFGF- stainless steel
SS-B-3DFGF-B-SS	Stainless steel-basalt-3DFGF-basalt-stainless steel
SS-G-3DFGF-G-SS	Stainless steel-glass-3DFGF-glass-stainless steel
SSJ	Single-strap joints
TGML	Theory-guided machine learning
Ti	Titanium
TSLJ	Three-step lap joint
UT	Untreated surface
VARI	Vacuum-assisted resin infusion
ZCs	Zero-thickness cohesive elements
A	Sampling area in surface roughness measurement
D	Damage variable
E, E_{11}, E_{22}	Young's Modulus
E_f	Flexural modulus
$E_n (E_t)$	Normal (and tangential) initial stiffness
F	Failure load

G	Strain energy release rate
$G_I (G_{II}, G_{III}),$	Strain energy release rate in mode I (II, III)
G_{12}, G_{13}, G_{23}	Shear Moduli
lr	Sampling length in surface roughness measurement
K	Stiffness matrix of the interface material
L	Overlap (bond) length
L_s	Specimen's span length
M	Bending moment
m	Slope of the linear region of the load-displacement curve
R^2	Coefficient of multiple determination
S_C	In-plane shear strength
T	Tensile load
T_g	Glass-transition temperature
t_0	Thickness of cohesive element
u_y	Transverse displacement
u_x	Longitudinal displacement
w	Joint (specimen) width
x	Lateral position
X_C	Longitudinal compressive strengths
X_T	Longitudinal tensile strengths
Y_C	Transverse compressive strengths
Y_T	Transverse tensile strengths
y	Transverse position
Z	Sampling height in surface roughness measurement
β	Cohesive mixed-mode ratio

δ	Relative displacement
δ^0	Displacement at the damage onset
δ^f	Displacement at the evaluated damage
δ_m	Mid-span deflection
δ_n	Separation in the normal (out-of-plane) direction
δ_s	Separation in the first in-plane shear direction
δ_t	Separation in the second in-plane shear direction
δ_{mf}	Ultimate relative displacement
δ_{mi}	Equivalent mixed-mode displacement
$\delta_{ni}(\delta_{ti})$	Relative separation pure mode I (II)
$\Delta_n(\Delta_t)$	Current displacement in the peel (shear) direction
ε_n^{max}	Maximum strain in the normal (out-of-plane) direction
ε_s^{max}	Maximum normal (out-of-plane) strain
ε_t^{max}	Maximum strain in the second in-plane shear direction
ε_{max}	Maximum strain
ε_f	Flexural strain
κ	Axial-shortening coefficient
η	Power-Law exponent
$\nu, \nu_{12}, \nu_{13}, \nu_{23}$	Poisson's ratio in different planes
ρ	Density
σ	Cohesive stress
σ	Stress
σ_n	Traction stresses in the normal (out-of-plane) direction
σ_s	Traction stresses in the first in-plane shear direction
σ_t	Traction stresses in the second in-plane shear direction

σ_n^{max}	Maximum normal (out-of-plane) stresses
σ_s^{max}	Maximum stresses in the first in-plane shear direction
σ_t^{max}	Maximum stresses in the second in-plane shear direction
σ_{yield}	Yield stress
σ_y	Peel stress
σ_V	von Mises stress
σ_f	Flexural strength
$\sigma_n(\sigma_t)$	Local stresses in each pure mode, I (II)
σ_{un}	Local strength in each pure mode I (“n” or peel)
σ_{ut}	Local strength in each pure mode II (“t” or shear)
σ_{max}	Maximum principal stress
τ	Average shear strength
τ_{xy}, τ_{zy}	In-plane and out-of-plane shear stresses

Acknowledgments

First and foremost, I wish to express my deepest gratitude to my supervisor, Dr. Farid Taheri. This Ph.D. adventure would not have been possible without his continued support, encouragement, and professional attitude. I am grateful for all his invaluable advice, guidance, technical discussion, and patience which greatly helped me to overcome all the obstacles and challenges and also broaden my vision.

I would like to acknowledge my Guiding Committee members Dr. Noubar Yemenidjian, Dr. Darrel Doman, Dr. Dmitry Garagash, and the external examiner, Dr. Jeremy Laliberté for reviewing this research work and providing suggestions and technical feedback.

My gratitude also extends to the skillful technicians at the Faculty of Engineering, especially to Mr. Brian Kennedy, Albert Murphy, Jesse Keane, Peter Jones, and Ms. Patricia Scallion. I would like to thank Dr. Andrew Corkum for providing a useful piece of equipment for the research.

I also wish to extend my appreciation to the Natural Sciences and Engineering Research Council of Canada for providing funding for this research, and the Government of Nova Scotia for the Nova Scotia Research and Innovation Graduate Scholarship. I would also like to gratefully acknowledge my colleagues, Drs. Hessameddin Yaghoobi and Davide De Cicco for helping me during the initial stages of my research and also Ke Wang for his technical discussions and great bits of help.

Last but not least, I would like to express my heartfelt gratitude to my love, Mladen, for being my anchor and strength through rough times. For having deep faith in me every single second and providing sincere emotional support. To my parents who greatly sacrificed their lives to raise me in love and brighten my life. Who always encouraged me and taught me to be strong, independent, brave, and embrace challenges. To my dearest friends Zohreh, Masoud, and Ehsani for always being supportive for more than a decade, particularly on the darkest nights of my life during the COVID pandemic and on the hardest years of my student life.

Chapter 1: Introduction

1.1. Context of the Present Research

The growing fuel consumption, the depletion of fossil fuel resources, and the urgent need for the reduction of carbon dioxide (CO₂) emissions into the atmosphere have made energy conservation a major global priority over the last few decades. Nowadays, stringent fuel consumption regulations have been established by many countries around the world. One of the most promising approaches to meet these regulations is the greater usage of lightweight and low-cost materials for developing industrial components. Additionally, according to the Canadian Association of Chiefs of Police, approximately 2,000 people are killed and 165,000 are injured (10,000 seriously) each year in Canada while using the road transportation system, at a cost of \$37 billion to society (i.e., 2.2% of Canadian Gross Domestic Product). The reported statistics indicate that vehicle collisions occur frequently, thus, a significant amount of effort is required to improve the safety of vehicles and minimize the number of fatalities and injuries, and the loss of billions of dollars. This, indeed, has created additional constraints on the weight-reduction approaches

In response to this issue, many engineers have conducted extensive research to overcome the challenges in industrial and structural designs over the past decades. The research has examined the strategic utilization of various metals (e.g., steel, aluminum, magnesium, and titanium), and fiber-reinforced plastics (FRPs) composites.

FRPs can be lightweight if designed properly to take full advantage of their positive attributes. Additionally, they are durable and resistant to corrosion, with comparable, or better specific strength and stiffness compared to metals. The applications of lightweight materials have become commonplace in the design of weight-sensitive structural components across multiple engineering sectors, especially in the aerospace/defence and automotive industries. The significance and the exponential increase in the application of FRPs in the aviation industry can be seen in Figure 1-1. Also, based on a recent report published by Lucintel, the market of composites is expected to reach an estimated \$59.8

billion by 2027 with a compounding annual growth rate of 5.8% from 2021 to 2027 (Lucintel, 2021).

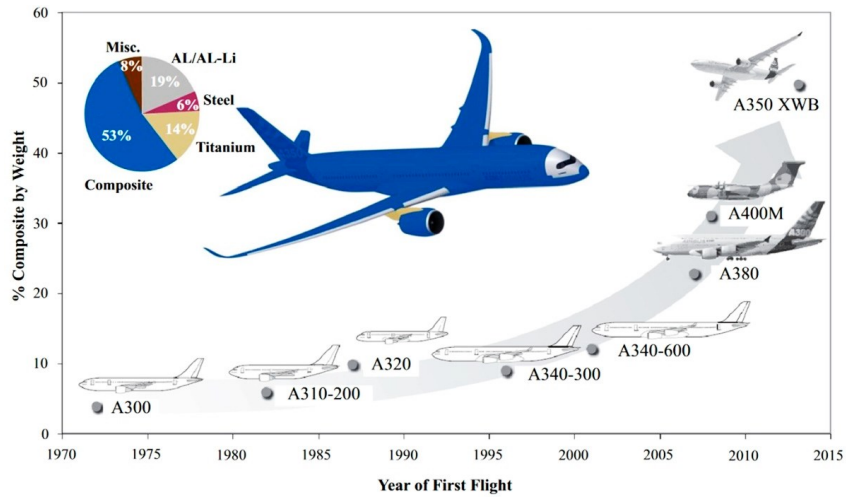


Figure 1-1. The trend in the use of composites by weight in Airbus aircraft (Xu et al., 2018).

One of the innovations in the field of composites is the development of a novel material known as fiber-metal laminates (FMLs), fabricated by a synergistic marriage of metals and FRPs, which has managed to achieve optimal results with minimal limitations. FMLs consist of thin layers of metal sheets interleaved with layers of FRPs as shown in Figure 1-2. They combine the stiffness, strength, superior impact properties, and fatigue resistance of FRPs with the durability, ductility, and toughness of metals. The first FML was originally developed by researchers at the Delft University of Technology in the Netherlands in the 1970s and has thereafter been the subject of continuous improvement by researchers across the world.

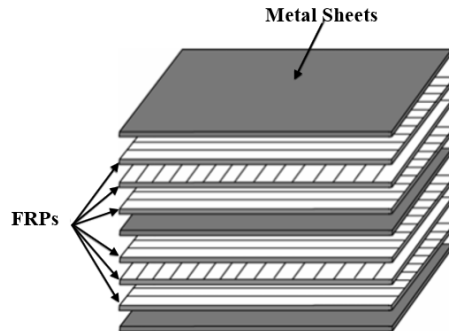


Figure 1-2. Typical configuration of a conventional FML.

Other developments included sandwich structures consisting of stiff metallic or FRP skins, interleaved together with a lightweight core. Some of the superior characteristics of these composite structures include high mechanical strength and stiffness, high energy absorption capability, and relatively low cost. Despite the aforementioned benefits, the connection between the face sheet and the core is one of the main concerns in the performance of sandwich structures, which can cause delamination failure. Later development observed the introduction of 3D-fiberglass fabric (3DFGF), an integrated sandwich composite comprising two bi-directional woven fabric surfaces, knitted together by vertical braided E-glass fiber pillars. The E-glass pillars have an intricate figure-8 type orientation (see Figure 1-3), with a 30° inclination with respect to the through-thickness direction as seen in Figure 1-3(c).

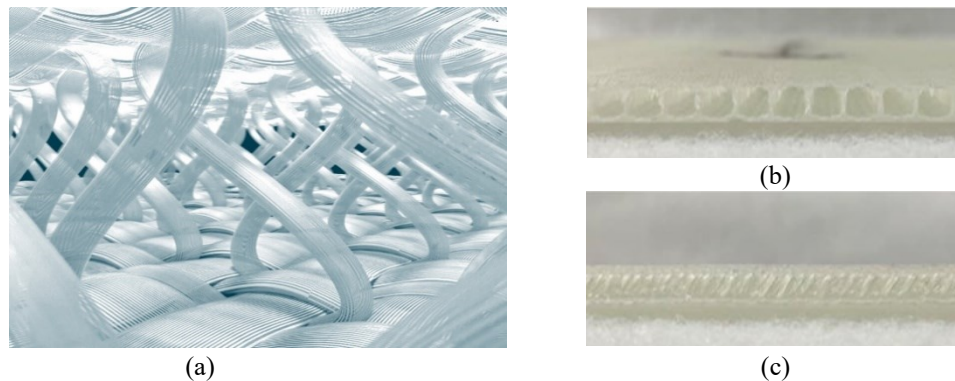


Figure 1-3. 3DFGF: (a) knitted pillars to plies (Parabeam, 2022), (b) front-view, and (c) side-view (Mottaghian & Taheri, 2022)

These novel 3D sandwich structures are lightweight, providing greater bending stiffness and impact resistance compared to traditional sandwich structures. They are also cost-effective, as they are made in one process and from one material. Due to their unique structure, the delamination between the core and face sheets is completely suppressed in this material (Vaidya et al., 2000). As mentioned previously, the incorporation of thin sheets of metals along with sheet(s) of composite materials to form FMLs is one of the most effective means to improve the performance of composite materials, especially their ductility, impact, and fatigue responses. Following this path, our research group developed a novel 3D-FML by combining 3DFGFs and epoxy resin skeleton infilled with polyurethane foam, sandwiched in between two thin sheets of metals, as per Figure 1-4. In comparison to 2D-FML and 3DFGF, 3D-FMLs offer several significant advantages,

including remarkable specific stiffness and strength, superior impact response, and excellent damage tolerance properties (especially through-thickness resiliency, which is the Achilles heel of most laminated polymer composites). These characteristics make it an economically viable alternative lightweight material for the generation of weight-sensitive structural components and thereby reducing energy consumption. As demonstrated in recent studies (De Cicco, 2019; Soltannia et al., 2020), this class of 3D-FMLs also offers excellent vibration and damping characteristics, which should make them particularly attractive for use in the automotive and aerospace industries.

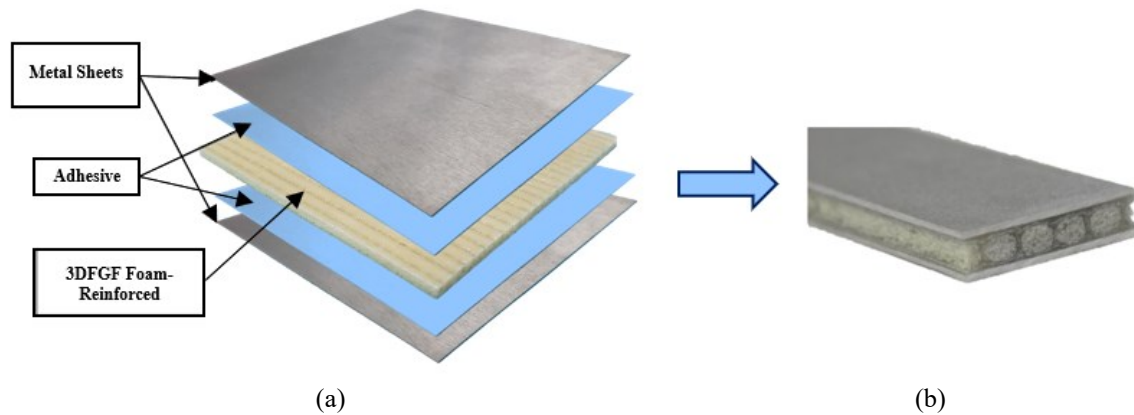


Figure 1-4. 3D-FML (a) exploded view, indicating the different components, and (b) the final product (De Cicco, 2019).

Since their inception, FMLs have seen increased applications in the aerospace sector, and the number of scholarly articles reporting research on FMLs has also increased exponentially. For instance, in each A380, there is a total of 440 m² of FMLs present in the fuselage panels as well as in the leading edges of the horizontal and vertical stabilizers. This amount is roughly the same as the surface area of the pressurized fuselage in an A320 (Ucan et al., 2019). FMLs are also used in rear pressure bulkheads, Wing panels, and Landing gear doors. The applications of FMLs as fuselage panels are shown in Figure 1-5.

Consequently, developing effective methods of joining FRPs and FMLs is of paramount importance and had consumed a significant volume of research to date. However, there are still challenges involved in assembling large-scale FRP and FML structural systems effectively. Non-optimized designs of interconnections in structures often lead to an increase in the overall structural weight. Various joining techniques for

mating composite components have been developed by researchers in recent decades. These include welded (e.g., ultrasonic welding in thermoplastic composites), bolted, riveted, adhesively bonded, and hybrid bolted-bonded techniques. However, the performance of such joints under various loading conditions, especially under impact loading states, and more specifically, under compressive impact loading, have not yet been fully examined.

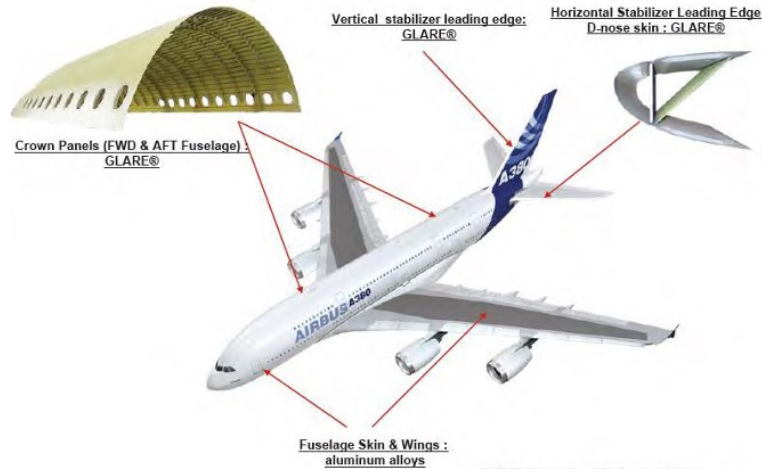


Figure 1-5. Application of Glass-reinforced aluminum laminates (GLARE) in Airbus A380 (Yang, 2008)

1.2. Adhesively Bonded Joints

1.2.1. Introduction

The applications of adhesively bonded joints (ABJs) as an effective method for joining various materials have increased significantly in recent years in various sectors, such as the automotive, aeronautics, defence, and marine industries. ABJs offer several notable advantages compared to conventional joining techniques such as welded and mechanically fastened joints using rivets or bolts. Compared to their counterparts, they also offer a relatively simple and low-cost fabrication process, reduced stress concentration and more uniform stress distribution, and are non-corrosive. ABJs can be used to join metallic, ceramic, composite, and other types of dissimilar materials, which outclass their effectiveness compared to most of the conventional bonding techniques. In addition, ABJs do not damage the mating materials compared to mechanically fastened (bolted and rivet)

joints' perforations or the Heat-Affected Zone (HAZ) developed by welding (Baldan 2012). ABJs are also comparatively lighter, thus helping reduce energy consumption and greenhouse gas emissions as well as facilitating better structural efficiency (Ye et al., 2018). Ironically, however, approximately 1.5 million rivets are used to assemble the components of a typical aircraft, which means 1.5 million perforations or weakened areas (de Freitas, 2015). Compared to conventional metallic systems assembled by rivets, riveting adversely affects composite materials significantly since composites have relatively lower shear and bearing capacities.

1.2.2. Fabrication of ABJs

The fabrication of ABJs is a straightforward procedure; however, it must be followed carefully. The quality of a bonded joint is a critical parameter that governs the structural integrity and long-term performance of the joint. The fabrication process includes surface treatment, application of the adhesive, assembly, and curing time.

The use of appropriate surface preparation is arguably the most important parameter in the fabrication of ABJs, which governs the life cycle of ABJs. An effective surface treatment eliminates oil and chemical residues, dust, and other contaminations, and creates the required microcavities, which in turn facilitate strong interlocking of the surface to adhesive. Strong interlocking leads to improved joint strength. The mechanical interlocking theory proposes that the adhesive must flow into any pores, furrows, and morphological irregularities on the adherend's surface before curing as depicted in Figure 1-6.



Figure 1-6. Mechanical interlocking facilitates the flow of the adhesive into the morphological irregularities of an adherend's surface.

Roughening the surfaces of adherends could be achieved by various methods including chemical, mechanical, thermomechanical, electrical (laser) processes, or a combination

thereof. Among all available methods, chemical and mechanical surface treatment are the most common ones. Generally, chemical surface modifications involve acid etching, anodizing, and pickling. Moreover, grit-blasting, sand-blasting, and wire-drawing are among the most common techniques that are used individually or in combination with a chemical process. Grit blasting is considered a simple, cost-effective, and yet very effective procedure as it generates chemical changes on the surfaces of the adherends and thus enhances the bond strength and structural integrity (Harris & Beevers, 1999). Nonetheless, there is an optimum degree for surface roughness, which not only enhances the strength of the adhesive-adherend interface but also has a profound and significant influence on the distribution of the stresses in the interfaces (de Morais et al., 2007).

Also, primers and conversion coatings are essential materials used in adhesive bonding and painting applications in various industries. They create a strong foundation for subsequent layers of coating or adhesive, improving adhesion, durability and resistance against corrosion. Primers are applied to create a smooth and consistent surface, while conversion coatings are used to convert metal surfaces into a chemically inert and corrosion-resistant layer. Proper selection of primers and conversion coatings is crucial to achieve the desired results in any bonding or painting process (Marques et al., 2020).

1.2.3. Loading and Failure Modes in ABJs

Apart from materials mating in a joint, an in-depth understanding of the type of loading and the resulting developed stresses involved in the ABJs is essential in successfully designing a bonded joint. Generally, there are six basic and common types of loading scenarios in different configurations of ABJs as shown in Figure 1-7; they are compression, tensile, shear, cleavage, peel, and torsion.

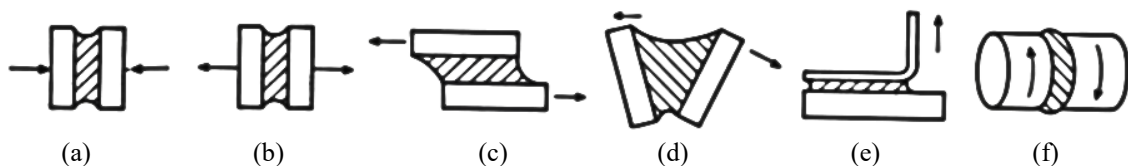


Figure 1-7. Typical load stress of ABJs (a) compression, (b) tensile, (c) shear, (d) cleavage, (e) peel, and (f) torsion (Mata, 2013).

Compressive stresses that develop due to perpendicular loading to the plane of the joint would result in a reduction in the thickness of the adhesive. In the case of aligned perpendicular loads, pure compressive stress would be generated within the adhesive. As the adhesives have relatively high compressive strengths, they hardly ever fail in compression, however, they may experience crack initiation on some weaker parts due to uneven stress distribution or the presence of voids. On the other hand, tensile stresses generated by load acting perpendicular to the plane of the joint will be distributed over the entire bond region. In this case, the entire adhesive contributes to the strength of the joint; consequently, the ABJs would perform well with tensile loading. However, loads are seldom purely axial, and generally, cleavage or peel stresses would be generated due to the eccentricity of the loading. These two types of loadings are undesirable and could cause catastrophic and detrimental joint failure. Therefore, specific constraints should be designed to avoid the development of such stresses in a tension-loading mode. Adhesives are reasonably strong in enduring shear stress, where the entire bonded area contributes to the strength of the joint. Shear stresses develop once the force acts in the plane of adhesive and leads to the separation of adherends. Design and manufacturing the bonded joints where the adhesive would be in shear mode are relatively easier and more common.

Cleavage stress occurs when pulling loads are concentrated at one end of a bonded assembly, causing the adherends to separate. Theoretically, the opposite edge of the joint experiences zero stress. However, peel stress develops when pulling loads are applied along a thin line at one or both edges of the bond where the adherends are flexible. This thin line is where the adhesive separates as the surface peels away from its mating surface. In this case, the rest of the bonded area does not contribute to the joint's strength. Bonded joints subjected to peel and cleavage stress have a weaker performance compared to those subjected to shear stress as the stress is concentrated in a small, localized area. Peel stress is mainly caused by eccentric loads, while cleavage stress is caused by bending moments or offset tensile loads.

When an ABJ is subjected to a stress field caused by tensile, compression, shear, peel, or cleavage loadings, the load is transferred from one adherend to the other through the adhesive layer. The ABJ will fail at its weakest point, which is usually the adhesive. In

many cases, the crack will grow by splitting the bulk adhesive and travelling from one interface to the other. Failure mechanisms in ABJs are usually categorized into four modes (as shown in Figure 1-8).

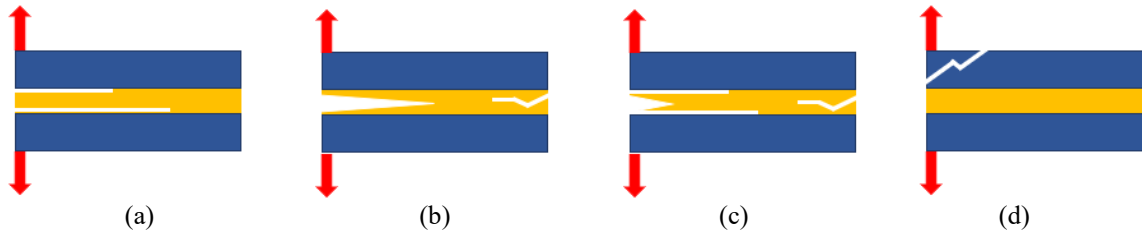


Figure 1-8. (a) interfacial, (b) cohesion, (c) interfacial-cohesion combination, and (d) adherend failure modes in ABJs.

The first mode is an interfacial failure, in which the failure occurs at the mating surface of the adhesive and adherend(s). This mode is common when the adherend surface is contaminated or has an inadequate interlocking mechanism due to poor surface treatment. This is the worst failure mode, indicating a defective manufacturing process or a wrong choice of surface treatment. The second mode is cohesion failure, in which the failure occurs within the bulk adhesive. This is the most desirable failure mode in the bonded area as it indicates an appropriate surface treatment and the generation of an adequate interlocking mechanism between the adherends and adhesive. The third mode is the interfacial-cohesion hybrid mode, which is a mixture of interfacial and cohesion failure. The fourth mode is adherend failure, in which the failure occurs in the adherend or strap(s). This is the most desirable failure mode outside the bonded area as it indicates that a strong interlocking mechanism exists in the bonded area and that the adherend has fulfilled its structural performance. In this case, changes need to be made to analyze and redesign the adherend's structural integrity.

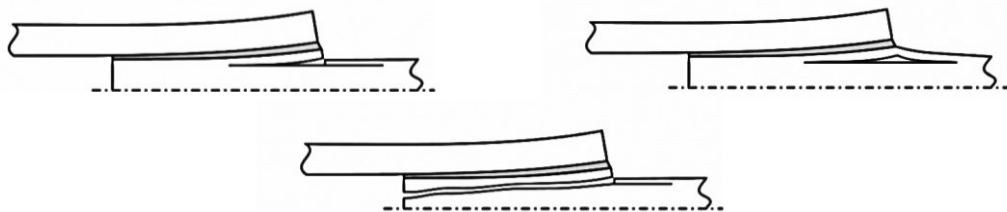


Figure 1-9. Delamination failure in composite adherends (Banea & da Silva, 2009).

In the case of FRPs or FMLs, the adherends failure mode is referred to as delamination, as shown in Figure 1-9. In composite adherends, high peel, and cleavage stresses developed through the thickness at the overlap ends are a major concern due to the relatively low through-thickness strength of most composites. To address this issue, the joint design must minimize stress concentrations and enhance the bonding between different composite layers. Decreasing peel and cleavage stress and increasing shear and compression/tension stress are also potential solutions.

1.2.4. Configurations of ABJs

ABJs must be designed carefully to withstand harsh environmental and loading conditions. In bonded joints, the mating materials are commonly referred to as substrates or adherends, and the strength of the interface (bonding region) is known as the joint strength. ABJs can be fabricated in various configurations, as shown in Figure 1-10. The configuration of ABJs should be chosen based on their intended application and the type of loads they will be subjected to. The main differences between each configuration include the distribution of stress concentrations and ease of fabrication. ABJs can be used to bond structural components or repair structural defects such as cracks or ballistic damage in system components.

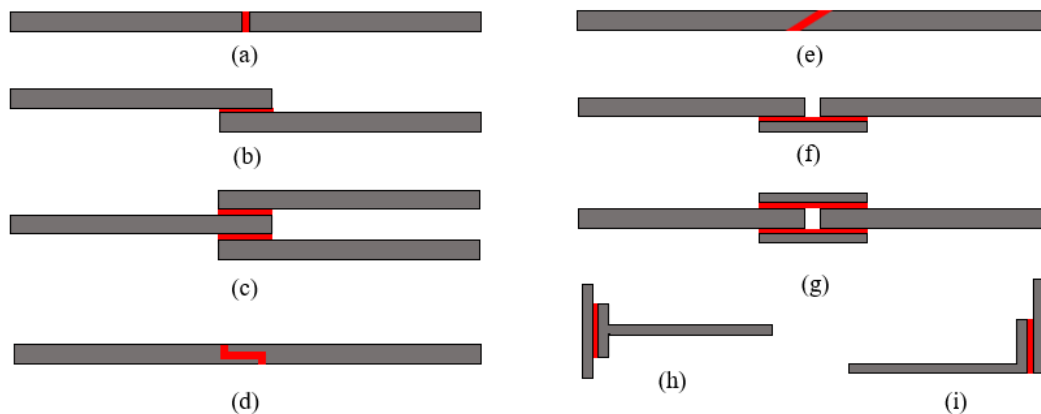


Figure 1-10. Configurations of the commonly used ABJs, (a) butt, (b) single-lap, (c) double-lap, (d) stepped, (e) scarf, (f) single-strap, (g) double-strap, (h)T, and (i) L.

The simplest ABJ configuration is the butt joint. However, this design is not effective in resisting bending forces as cleavage stress can readily be developed in the adhesive.

Aligning the adherends during the fabrication of butt joints can also be challenging, making it not recommended for bonding composite-to-metal or thin composite-to-composite joints.

Single-lap joint (SLJ) is the most commonly used configuration due to its standardization and ease of fabrication. However, a SLJ is susceptible to bending moments, especially when subjected to nonconcentric forces, as shown in Figure 1-11. The bending could also occur due to the relative flexibility of the overlap region in such slender systems when tabs are used to minimize the load (Jairaja & Naik, 2019). The bending causes rotation of the overlap region, leading to the development of additional peel and shear stresses, hence, larger stress concentrations near the ends of the overlap, which could cause failure of the joint. The rotation is a function of the adherends and adhesive thickness, the distance between the alignment adherends and overlap region (Guo et al., 2006).

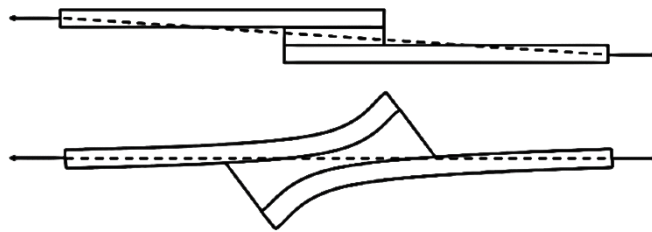


Figure 1-11. Schematic of SLJ bending due to eccentricity of the load path (Redmann et al., 2021).

Double-lap configuration is considered an improvement over the single-lap joint as it eliminates load path eccentricity and has twice the overlap surface area. However, significant magnitudes of both shear and peel stresses can still be generated at the joint ends.

The other ABJ configurations that have been thoroughly investigated include the scarf, stepped, single-strap, and double-strap joints. Scarf and stepped joints are considered effective configurations for joining similar and dissimilar materials, as they keep the axis of loading aligned with the joint, resulting in uniform stress distribution along the bond length and better post-repair strength. This is an improvement over the butt joint configuration, which is prone to large cleavage stress when the joint is subjected to out-of-plane loading. However, the efficiency of a scarf joint is highly dependent on the scarf angle. At a low scarf angle, the scarf joint may have higher strength compared to single-

strap joints, but at higher scarf angles, single-strap joints may provide similar or higher capacity. The precise machining required for preparing effective scarf angles is a costly task.

Single-strap and double-strap Joints were developed to align the loads and are typically used when overlap joints are impractical due to the thickness of the adherends. Adding a second strap to the bottom side of the single-strap ABJ provides symmetry and increases bond strength, overcoming the susceptibility to premature failure from cleavage and peel stresses in single-strap joints. This type of joint is desirable if a significant load-bearing capacity is required.

T- and L-joints are other joint configurations that are typically used as stiffeners. They have been widely used in industries such as automotive, marine, and aerospace. An example of their use in aviation structures would be at bulkhead-to-skin, rib-to-skin, and spar-to-skin interfaces (Masoudi Nejad et al., 2022). These configurations will be discussed further in the following section.

1.2.5. Applications of ABJs

Since the late 1930s, ABJs have been successfully used in the aerospace and defence industries. Early examples are the application of ABJs in the bonding of plywood laminates in the British Mosquito, in the Meltbond bombers during World War II, and the Vultee B-36 bombers developed by Narmco in the United States. Since then, ABJs have been used to join similar or dissimilar structural materials in various aircraft. The Cirrus SR20 demonstrated in Figure 1-12(a) is one of the first nearly all-composite aircraft in which ABJs are widely utilized. The aircraft was manufactured by Cirrus Aircraft and certified by the Federal Aviation Administration (FAA) in 1998 (Kim & Kedward, 2001). The application of ABJs in modern aviation systems can be found in the construction of the McDonnell Douglas F-18 Hornet and Northrop Grumman F-20 Tigershark fighter aircraft, where the wing skins and control surfaces are formed by adhesively bonded composite. In addition, the first nearly all-composite aircraft with extensive use of ABJs was the Polish PZL I-23 Manager, shown in Figure 1-12(b). This aircraft was certified by the Polish Civil Aviation Authority and the European Union Aviation Safety Agency (EUASA) in 2001

and 2006, respectively (Dobrzański & Oleksiak, 2021). The Airbus A380, Boeing 787, and the Airbus A350 are among the commercial aircraft that benefit from more than 45% bonded composite structural systems, leading to appreciable weight reductions (Anyfantis, 2012). The close-view examples of ABJs applications in aerospace industries are presented in Figure 1-13(c-d).

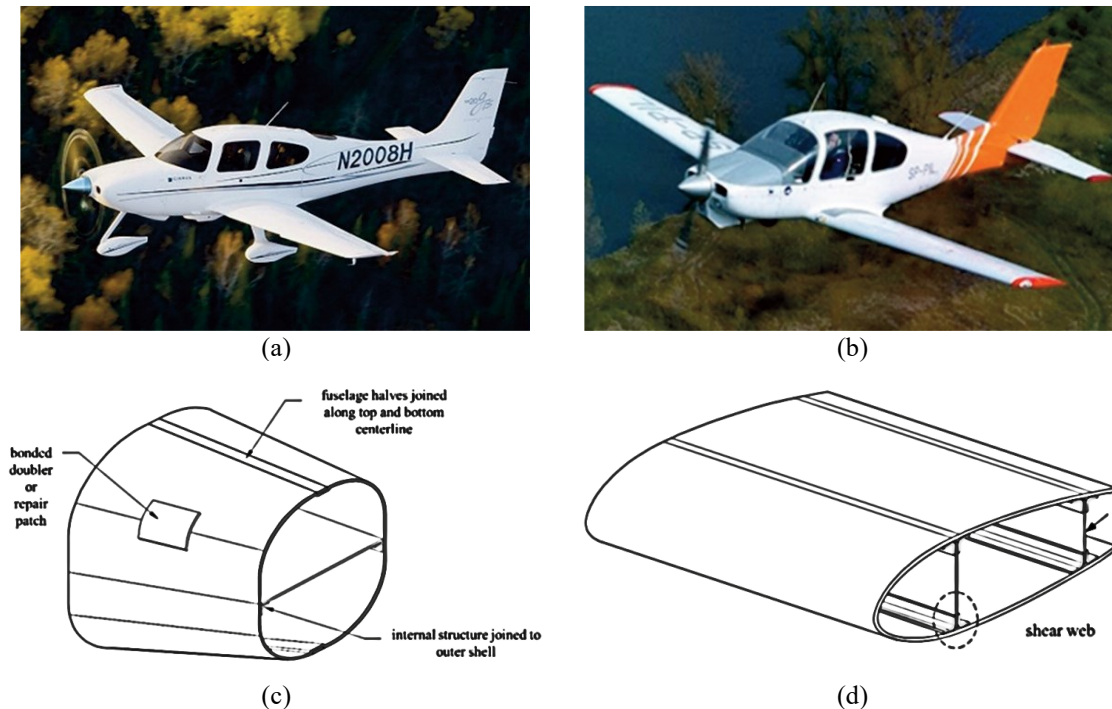


Figure 1-12. Application of ABJs in the aviation industry, (a) Cirrus SR20, (b) PZL I-23 Manager, (c) a section of the fuselage, and (d) Generic-bonded wing spar (Dobrzański & Oleksiak, 2021).

The selection of lighter materials in the automotive industry has been recognized as a key element to reduce vehicle weight, thereby improving fuel consumption. Since a few decades ago, steel has been replaced with lightweight metals (e.g., magnesium, aluminum) and FRPs. However, welding these materials could be challenging, and the use of mechanical fastening could cause permanent perforations and added weight to the vehicle structures. Consequently, ABJs have experienced exponential growth since the 1960s by joining a variety of automotive components, including closures and structural modules. Examples of the application of ABJs could be found in the construction of the BMW i8 (Dirschmid, 2014); the new S-Class Coupé (with more than 100 m of structural bonds), and the BMW 7 series. In addition, ABJs have been used in the production of Ford's AIV, Jaguar's XJ220, Rover's ECV3, Honda's NSX, Audi's A2 and A8, BMW's Z8 and the

Lotus Elise (Borsellino et al., 2009). The space frame of the 2002 Aston Martin’s V12 Vanquish is also made of extruded aluminum that is adhesively bonded and joined to the rest of the vehicle (Silva, 2019). In general, ABJs are employed for anti-flutter bonding or structural bonding in the automotive industry (Hill, 2003). Anti-flutter adhesives are used to compensate for tolerances (e.g., in large gaps in windshield installation), and to absorb vibration, while structural adhesives are used to join panels, hem, and stiffen the joined panels (Omar, 2011). Some of the applications of ABJs in car design are presented in Figure 1-13.

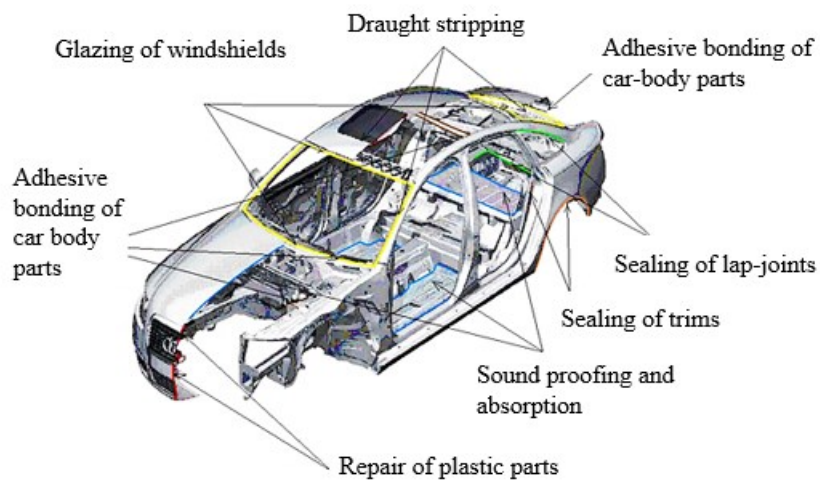


Figure 1-13. Application of ABJs in the automotive industry (Kolnerová et al., 2010).

Based on the successful performances of ABJs in the above-mentioned applications, they are being also adopted in other industrial applications, including wind turbines, the marine industry, piping, and civil engineering. A considerable volume of research has been conducted on the design and analysis of ABJs in wind turbine blades, which are constructed mostly from monolithic sandwich FRPs in a box-section type. Figure 1-14 shows a cross-section view of Sandia National Laboratories’ National Rotor Testbed 13-m blade, consisting of shear webs that are adhesively bonded to the upper and lower shells of the blade.



Figure 1-14. Cross-section of Sandia National Laboratories' National Rotor Testbed 13-m blade, showing the ABJ parts (Murray et al., 2019).

ABJs were also adopted in the marine industry in the 1980s, and since then their design and analysis have been an area of research for many researchers. Ship components such as bulkheads, superstructures, masts, or even the entire deck can be bonded to metals or composites. Figure 1-15 shows the application of ABJs in bonding a composite ship deck to a steel hull, as well as various applications of ABJs for assembling composite bulkheads.

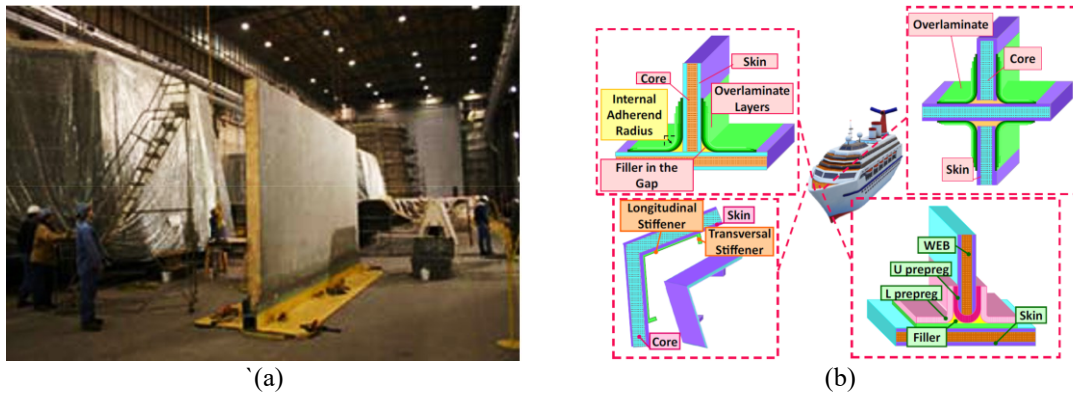


Figure 1-15. ABJs in (a) bonding composite to steel hull (Anyfantis, 2012), (b) different types of joints in bulkhead (Delzendehrooy et al., 2022).

More recently, ABJs motivated a significant volume of research intending to optimize techniques used for repairing defective structures. The optimal design of ABJs can compensate for the loss of strength and/or stiffness of the defective parts. Bonded repairs have gained popularity in various industries due to their advantages over traditional welding and mechanical fastening techniques. They can be performed on complex surface geometries that are not accessible or reachable by other methods, which makes them a practical solution in many applications. In addition, bonded repairs are less expensive and

lighter than traditional methods, making them a potentially attractive alternative for reducing repair and maintenance costs and improving overall efficiency. However, there are still challenges regarding the lower strength, safety, and certification of ABJs compared to traditional bonding methods (e.g., mechanically fastened or welded joints) that need to be addressed.

1.3. Thesis Motivations

As previously mentioned, the use and potential applications of FMLs are continually expanding. In recent years they have been widely utilized as effective alternatives to metallic alloys in different industries. As also stated, 3D-FMLs offer several advantages over traditional 2D-FMLs including higher specific stiffness and strength, enhanced impact response, and superior damage tolerance properties. The thickness of 3D-FML can be varied between 3 mm to 21 mm, depending on the choice of thickness for the core and face sheet components. The out-of-plane and in-plane low-velocity impact responses of the novel class of 3D-FML developed in our research group have been systematically investigated by two former Ph.D. students of our group.

In practice, bonding would be the preferred method for joining 3D-FML panels, since mechanical fasteners will induce through-the-thickness crushing issues to this FML. Nonetheless, there is a clear lack of research on the performance of ABJs that mate 2D-FMLs and especially 3D-FMLs. This is a crucial area that needs attention and further investigation. With the increasing use of lightweight materials, the understanding of the performance of ABJs under various loading scenarios such as flexural, axial compressive, and impact loading, becomes even more important. This will help to improve the design and reliability of these joints and increase their applications in various industries. It should be noted that the Achilles' heel of all laminated composites is their relatively weaker interlaminar strength compared to their bending and axial strengths. FMLs are also susceptible to initiation of delamination of their FRP/metal constituents. Therefore, investigation of the performance of joints mating such complex hybrid materials configuration and their interfaces are critical in promoting their applications in various industries.

Moreover, the effective evaluation of the performance of modern lightweight hybrid materials necessitates effective, efficient, and affordable methodologies and approaches. Numerical methods have become indispensable and effective alternatives to physical experimentation as they significantly shorten the required development times for analyzing new materials and products. Nevertheless, one of the disadvantages of the numerical method in most practical cases is its lengthy simulation time required for analyzing complex nonlinear problems. Indeed, the balance between the accuracy of the results, the effort put into modelling, and computational cost are among the main challenges in the implementation of numerical studies. Despite the extensive research and the advancement in computational mechanics in the past few decades, accurate prediction of damage initiation and growth in ABJs is still a challenging task.

1.4. Thesis Objectives

The main objectives of the research presented in this thesis are as follows: (i) to provide a deep insight into the characterization of different configurations of ABJs mating 2D- and 3D-FMLs under in-plane and out-of-plane loadings (i.e., lap-shear, bending, compressive) with various strain rates (i.e., quasi-static, dynamic); (ii) to optimize the surface treatment procedure, adhesive bonding length, and thickness to enhance the capacity of the bonded joints mating 3D-FML; and (iii) to develop empirical equations and practical design guidelines to facilitate the design of bonded joints mating such intricate materials and thereby accelerate their application. These goals are met by executing a systematic series of experimental assessments, coupled with a series of numerical analyses (i.e., Finite Element Method (FEM)), concluded by the development of effective and accurate Artificial Intelligence (AI) based models.

The contributions made to the scientific arena through the research work conducted and presented in this dissertation are summarized as follows:

- Development of a new rendition of 3D-FMLs by incorporation of different metallic alloys, basalt, and glass fabrics and characterization of their performance under compressive loadings.
- Optimization of 3D-FMLs in terms of weight, mechanical performance, and cost.

- Design, characterization, and optimization of an SLJ mating 2D Mg-based FMLs and 3D-FMLs.
- Identification of the most optimal surface treatment process.
- Cost-effective enhancement of single-lap joints mating 3DFMLs by nanoparticles.
- Developing an accurate and robust cohesive zone-based numerical modelling framework for predicting the initiation and propagation of failure in the bonded joints.
- Development and characterization of the most optimal double-strap joining system for mating 3D-FMLs and establishment of the performances of the joint under various loadings including axial compressive and impact loading
- Establishment of the impact-buckling performances of adhesively bonded sandwich composite and FMLs made of various constituents using neural network, genetic programming, and genetic algorithm methodologies.
- Development of an empirical equation for the design of double strap bonded joints mating various sandwich composites subject to axial compressive impact loading taking into consideration 13 different design parameters.

1.5. Thesis Layout

The research conducted within the framework of this doctoral dissertation is presented herein according to the following layout.

Chapter 1 provides a general introduction to the various topics examined in this thesis. The subsequent chapter (chapter 2) presents a literature review of the research related to the specific subject of the thesis. The review covers the experimental and numerical works conducted on the characterization of the response of adhesively bonded joints under static and dynamic loading scenarios. Specifically, emphasis has been put on the works that have considered flexural, axial compression, and impact loadings on joints mating composite adherends. The notable studies covering surface treatment techniques and other joint strength enhancement methods are also summarized.

It should be noted that this thesis follows the “collection of published papers” format option sanctioned by the Faculty of Graduate Studies of Dalhousie University. Therefore,

although each paper (published, in-press, or submitted) has its literature review section, some parts of the introduction sections of the papers enclosed in chapters 3 to 8 have been removed in this thesis to avoid redundancy, as they are included in chapter two of the thesis. Moreover, the reference section of all papers has been combined into one reference section.

Chapter 3 presents the development of different renditions of 3D-FMLs fabricated with stainless steel (SS) and magnesium (Mg) face sheets and by incorporating additional layers of basalt or glass fabrics. Subsequently, the detail of an accurate and robust numerical framework developed for simulating the buckling and post-buckling responses of the rendered 3D-FMLs is presented. The performance of six different configurations of 3D-FMLs is compared and ranked based on their weight, cost, and material efficiency.

In Chapter 4, a simplified numerical analysis is developed for conducting a parametric study to establish lap-shear joint capacities and the optimal configuration of single-lap joints mating 2D-FMLs adherends accurately and efficiently. The effects of two types of surface treatments, namely, “sandblasting” and “sandblasting with resin coating” on the bond strength and failure mechanism of the ABJs are studied. The distributions of the shear and peel stress in the bonded region for different overlap lengths as well as the effects of adhesive thickness on the performance of the joints are systematically examined.

Chapter 5 is dedicated to the experimental and numerical assessment of single-lap ABJs mating 3D-FMLs under flexural and tensile loading scenarios. The performance of 3D-FML bonded joints is examined against their 2D-FML counterparts. The influences of the inclusion of different GNP contents on the axial and flexural responses of single-lap 3D-FML ABJs are considered. The field emission scanning electron microscopy (FESEM) technique is employed to evaluate the distribution and agglomeration of GNPs in the adhesive. A Finite Element-Cohesive Zone (FE-CZ) model is also developed which accurately simulates the performances of ABJs and the damage initiation/growth, including 3DFGF/Metal delamination in the bonded region.

Chapter 6 highlights the effects of five different combinations of chemical, thermochemical, and mechanical surface treatment procedures on the joint capacity and failure mode of double-strap 3D-FML ABJs. The resulting surface morphologies and

surface roughness parameters are probed by a confocal laser scanning microscope (CLSM) and the optimal surface treatment in terms of ease of processing and the resultant joint capacity is established. Subsequently, the effects of the length and thickness of the carbon fiber-reinforced plastic (CFRP) straps on the responses of the joints subjected to tensile and compressive loadings are thoroughly studied.

Chapter 7 presents details of a robust mixed-mode tri-linear CZM-based FE framework developed in LS-DYNA FE software. A total of seven models are constructed and their capabilities are systematically examined. The influence of CZM element thickness (i.e., zero and non-zero thicknesses) and the number of layers (i.e., one to five) on the progressive damage failure is evaluated. The most accurate and effective model is selected by the assessment of the sequence of failure along the bond region followed by the examination of the local failure modes (i.e., interfacial, cohesion, or thereof). This model is also capable of capturing the global failure modes (i.e., FRP/metal delamination, CFRP debonding, shear-crimping). Subsequently, an extensive series of parametric studies are performed to investigate the effects of CFRP straps' length and thicknesses on the lap-shear and buckling capacities of the joints, thereby establishing the optimal 3D-FML ABJs configurations.

Chapter 8 is dedicated to the experimental, numerical, and analytical assessment of the in-plane impact performances of double-strap 3D-FMLs ABJs. Extensive series of FE models are developed followed by a parametric study to develop an extensive database required for the next phase of the study. Subsequently, three machine learning (ML) models are developed to analyze the data generated by FE models, leading to the establishment of guidelines and empirical equations for evaluating the capacity of joints subjected to impact loading. The thesis is concluded with a chapter that includes the summary and conclusions of the works presented herein, and recommendations for future studies.

The list of published or under-review manuscripts included in this thesis is as follows:

- Mottaghian, F., Yaghoobi, H., & Taheri, F. (2020). Numerical and experimental investigations into post-buckling responses of stainless steel- and magnesium-based

- 3D-fiber metal laminates reinforced by basalt and glass fabrics. *Composites Part B: Engineering*, 200, 108300.
- Mottaghian, F., & Taheri, F. (2022). Strength and failure mechanism of single-lap magnesium-basalt fiber metal laminate adhesively bonded joints: Experimental and numerical assessments. *Journal of Composite Materials*, 56(12), 1941-1955.
 - Mottaghian, F., & Taheri, F. (2023). Mottaghian, F., & Taheri, F. (2023). On the flexural response of nanoparticle-reinforced adhesively bonded joints mating 3D-Fiber Metal Laminates—A coupled numerical and experimental investigation. *International Journal of Adhesion and Adhesives*, 120, 103278.
 - Mottaghian, F., & Taheri, F. (2023). Performance of a unique fiber-reinforced foam-cored metal sandwich system joined with adhesively bonded CFRP straps under compressive and tensile loadings. *Applied Composite Materials*. 30, 339–359.
 - Mottaghian, F., & Taheri, F. Assessment of failure mechanism of double-strap 3d-fml adhesively-bonded joints under tensile and compressive loadings using cohesive zone modelling approach. *Under Review, Journal of Composite Structures*.
 - Mottaghian, F., & Taheri, F. Machine learning/finite element analysis - a collaborative approach for predicting the axial impact response of adhesively bonded joints with unique sandwich composite adherends. *Under review, the Journal of Composites Science and Technology*.

Chapter 2: Literature Review

This literature review is a summary of the works closely related to ABJs mating 3D-FMLs subjected to static and dynamic loadings. It covers the general background of sandwich structures and fiber metal laminates (FMLs) and responses of bonded systems subject to lap-shear, flexural, compressive, and low-velocity impact loading states and the effective numerical modelling techniques used to simulate the response. In addition, the surface treatment procedures used to develop effective ABJs are also reviewed. The literature regarding these topics is relatively vast and therefore, some of the notable studies are summarized and presented in this chapter. To date and to the best of the author's knowledge, other than the studies conducted by former Ph.D. students in our research group (Asaee et al., 2017; De Cicco, 2019), no other public domain literature could be found concerning the performances of 3D-FMLs presented in this thesis.

2.1. Sandwich Structures

Sandwich structures have been widely adopted in several applications across the aerospace, defence, renewable energy, automotive and marine industries (Vinson, 2001). Sandwich structures consist of a lightweight internal core sandwiched in between a pair of thin and stiff external skins, as shown in Figure 2-1. The relatively thick lightweight core could lead to a significant enhancement in the bending rigidity of the component with a negligible increase in the structure's weight. However, the increased thickness could be a downside where the thickness is a design criterion. Steel, aluminum, and FRPs are the most commonly used materials to serve as skins on a structural sandwich system (Birman & Kardomateas, 2018). They are used to provide high stiffness and strength, good resistance to abrasion, impact, and chemicals; and, for some specific applications, resistance to UV rays and radiation. For the core, however, materials with light weight and relatively high shear stiffness are preferred. Consequently, balsa wood, honeycomb core, and a variety of thermoplastics, thermosets, and metallic foams are among the most common core materials.

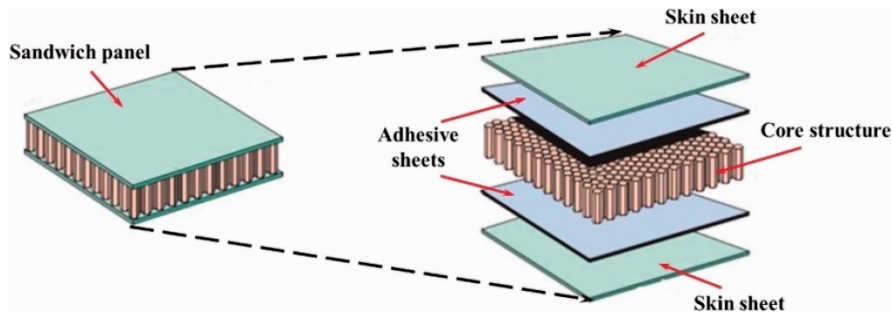


Figure 2-1. Schematic of the sandwich structure geometry (Zheng et al., 2022).

A sandwich structure may experience different modes of failure depending on the loading scenario and geometry, which are depicted in Figure 2-2. In case (a), the structure undergoes pure bending and the failure occurs due to fracture or yielding of the skins. In case (b), the applied shear load to the panel could potentially cause the characteristic diagonal shape shear failure of the core. In cases (c) and (d), the applied bending and/or axial compression could develop a localized buckling of the core that may cause delamination of the skin from the core. In case (e), when relatively slender sandwich panels are subjected to axial compressive load, they may experience global buckling. If the core stiffness of a sandwich structure is relatively low, the structure may experience a shear crimping failure. The face wrinkling failure mode observed in case (g) usually occurs in sandwich systems consisting of a honeycomb. Such a response is influenced by the core compressive strength and the face sheet's stiffness. This failure is often seen under impact buckling load or in sandwich structures typically with honeycomb cores and thin layers (shim). Last, the failure in case (h) occurs due to a concentrated transverse load applied to a sandwich system face (Xu & Rosakis, 2002; Zenkert, 1997).

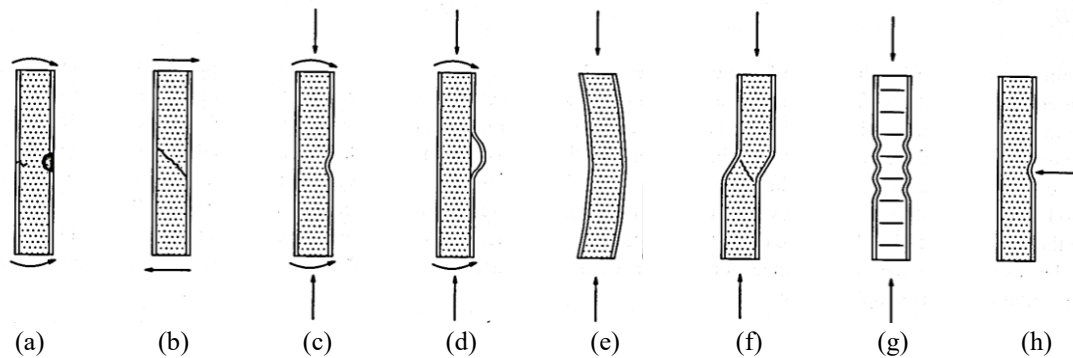


Figure 2-2. Different plausible failure modes in sandwich structures (Zenkert, 1997).

2.2. General Introduction to FML

In recent years, several efforts have been made to meet the demands of various industries for materials that are lightweight, cost-effective, and have superior static and fatigue properties. One of the most successful attempts led to the development of 2D-FMLs (Carrillo et al., 2019; Majerski et al., 2018). FMLs were developed in the 90s as lightweight hybrid composite materials to take advantage of the ductility offered by metals and the positive attributes offered by FRPs (Vlot, 2001; Vlot & Gunnink, 2011). FMLs are therefore desirable alternatives to FRPs in that they compensate for the inherent brittle response of thermoset resin FRPs, yet still offer lightweight, resilient, and cost-effective properties (Chai & Manikandan, 2014; Lawcock et al., 1997). The key parameter in the excellent performance of FMLs is the so-called “crack-bridging” mechanism as depicted graphically in Figure 2-3. The crack opening in the metal layers is restricted by the fibers. The fibers do not experience failure during the crack opening, as the shear stresses at the interface result in a gradual and controlled delamination growth. The resulting delamination causes the bridging fibers to elongate over a longer length when the crack opens, and consequently hinders the strain and inhibits fiber failure (Alderliesten, 2017).

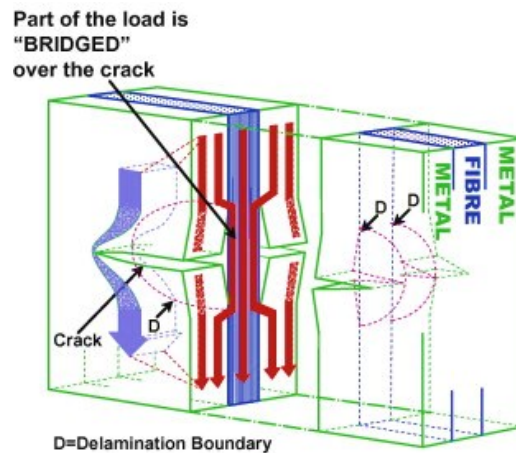


Figure 2-3. Fiber bridging attribute to limit crack growth in FMLs (Malingam et al., 2020).

The most commonly used FML configurations have been the aluminum (Al)-based FMLs, such as aramid-reinforced Al laminates (ARRAL), glass-reinforced Al laminates (GLARE), and carbon-reinforced Al laminates (CARALL). Nonetheless, there have been several attempts to enhance the performance of FMLs by using various material

combinations, such as steel-based FMLs (Lee et al., 2018; Yaghoobi et al., 2021a), Mg-based FMLs (Alderliesten et al., 2008; De Cicco & Taheri, 2019b), titanium (Ti)-based FMLs (Kazemi et al., 2020; Nassir et al., 2020), basalt fiber reinforced FMLs (Medjahed et al., 2019), and 3D-FMLs (De Cicco, 2019). The main motivations for choosing different metals have been motivated by several important factors such as higher specific static and fatigue strengths, higher stiffness, corrosion resistance, low density, less onerous surface preparation, and their usability at higher temperatures (Alderliesten, 2017). A summary of the various FML configurations is provided in Figure 2-4.

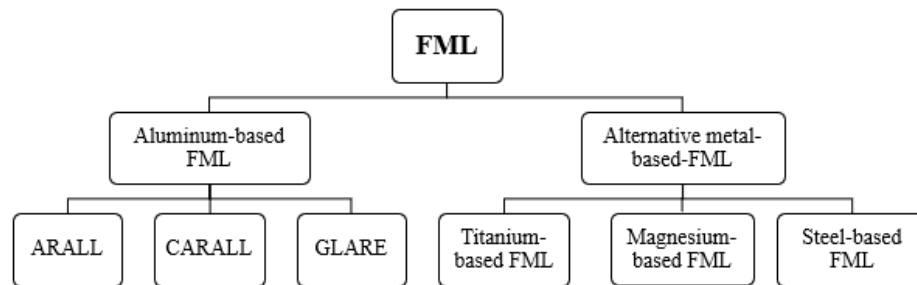


Figure 2-4. Summary of various FML configurations.

Extensive research has been conducted on Al-based FML. Therefore several studies have been performed on alternative metal-based FMLs. Lee et al. (2018) analyzed the mechanical behaviour of steel-based FMLs by performing tensile, compressive, in-plane shear, and low-velocity impact tests. The FMLs were fabricated from carbon and glass prepregs and high-stiffness steel using autoclave moulding. They concluded that the fabricated FMLs have higher strength and stiffness than conventional FMLs; therefore, their investigation accelerated the design of high-stiffness and lightweight FMLs for automotive parts. Pärnänen et al. (2015) investigated debonding and impact damage mechanisms developed before metal fracture in steel-based FMLs containing alternately laid carbon and glass fiber-reinforced epoxy plies. Their results showed that debonding proceeded either at the metal and adhesive film interface, or cohesively inside the adhesive film, and the steel's surface condition had a negligible effect on impact response. In another analysis, Singh & Angra (2018) examined the hygrothermal degradation of the compressive and tensile strengths of steel-based FMLs constructed with glass-epoxy. The results revealed that the tensile and compressive strengths of the FMLs decreased by 23.4%

and 32.6%, respectively after the FMLs had been immersed in 70°C distilled water for three months.

Cortés & Cantwell (2005) investigated fatigue and low-velocity impact (LVI) of Mg-based FMLs fabricated by two types of FRP layers, including a woven and a unidirectional glass fiber-reinforced plastic (GFRP). The FML showed higher specific energy absorption capacities compared to a similar Al-based FML and outperformed fiberglass-epoxy/Al-based FML. Later, Alderliesten et al. (2008) assessed the application of Mg-based FMLs for aircraft structural applications and provided a comparison between the standard GLARE and Mg-based FMLs. They concluded the static and fatigue properties of Mg-based FMLs were lower as compared to the current FML variants (i.e., GLARE, ARRAL) utilized in structural application.

Ali et al. (2016) studied the mechanical properties, fracture mechanisms, and corrosion response of Ti-based FMLs with CFRPs for marine applications after hygrothermal conditioning in 70°C seawater. The results indicated that the conditioned specimens exhibited 19.3%, 12.1%, 13.1%, and 31.9% decline in the longitudinal, transverse tensile, flexural, and interlaminar shear strengths, respectively. Cortés & Cantwell (2006) investigated the tensile properties of a lightweight FML constructed from Ti alloys and CFRP poly-ether-ether-ketone (PEEK) under quasi-static rates of strain. The results indicated that failure in laminates whose fibers were oriented at angles between 0° and 15° occurred because of fracture of the individual CFRPs. In the specimen with offset angles greater than 15°, the initial failure occurred as a localized debonding at the fiber/matrix interface.

Numerous researchers have used the finite element method (FEM) as an effective and efficient tool to analyze and establish the performances of hybrid material systems. For instance, Ahmad et al. (2015) developed a nonlinear numerical model by incorporating the Belytschko-Tsay quadrilateral shell element of LS-DYNA FE software to characterize the crushing and energy absorption capacity of thin-walled FML tubes under an impact loading scenario. Based on their developed model, they concluded that thin-walled FML tubes demonstrated profound responses and desirable energy absorption capacity compared to

purely Al and GFRP tubes. In another study, the ballistic impact behaviour of GLARE FML was analyzed by Yaghoubi & Liaw (2014) by developing an FE model in LS-DYNA, in which all components of their FML were modelled by solid elements to simulate the progressive damage due to a high-velocity impact loading. Their numerical model results were in good agreement with the experimental results and could simulate the damage mechanism. Buckling, post-buckling, and failure analyses of FML profile/column and thin-walled structure were investigated by FEM using solid and shell elements in ANSYS software (Banat & Mania, 2017, 2018). The numerical results matched well with their experiments and analytical solutions, and the model accurately represented certain fracture areas of the laminate during buckling and post-buckling.

More recently, a new class of FML was developed in our research group by incorporating a novel 3D glass fabric (3DFGF) in conjunction with a lightweight magnesium alloy and stainless steel, hereafter referred to as 3D-FML. The static and out-of-plane and in-plane impact responses of the various renditions/combinations of the 3D-FML were systematically investigated (Asaee, 2017; De Cicco, 2019). The authors carried out extensive experimental and numerical investigations to study the behaviour of the 3D-FMLs. Although the 3D-FMLs have been demonstrated to be promising material systems, further research is needed to fully understand and improve their response under different loading conditions, and to determine their potential for industrial use. Moreover, the joining of 3D-FML panels is a challenging issue that must be addressed before this complex material can be commercialized; therefore, this is the focus of the present thesis.

2.3. Adhesively Bonded Joints (ABJs)

Lightweight materials have been extensively used in various industries to reduce fuel consumption. However, as the use of lightweight materials increases, their joining and assemblage, and maintenance of their safety represent challenges that have hindered their widespread industrial use (AC 20-107B, 2009). As mentioned earlier, ABJs offer a simple and cost-effective fabrication process. They distribute stresses more uniformly and reduce stress concentration compared to other types of joints. These qualities, along with their non-corrosive nature, have led to their widespread adoption in various industries (Cavezza

et al., 2020). ABJs can be utilized to join metallic, ceramic, composite, and other types of dissimilar materials, which outclass their effectiveness compared to conventional bonding techniques. In addition, ABJs do not cause damage to the mating materials compared to bolted joints' perforations or the heat-affected zones generated by welding (Bowditch, 2006).

2.3.1. Joint Strength Enhancement

Although ABJs offer many advantages, their widespread use may be limited due to their lower strength, safety, and certification compared to traditional joining methods. Therefore, a great volume of research in the field of bonded joints has been dedicated to the development of efficient methods that could augment the mechanical performance of ABJs. For instance, bond strength can be improved by the selection of proper and adequate bond surface modification methods (e.g., mechanical, chemical, laser, and plasma surface treatment techniques). Bond strength can be increased by changing geometric parameters such as overlap length, adhesive thickness, and spew fillet geometry. Configurational means, such as stepped, scarf, or curved overlaps, can also improve bond strength. In addition, enhancing the properties of the adhesive and adherends materials can contribute to stronger bonds.

2.3.1.1. Surface Modification Procedures

As stated, an effective surface preparation technique is one of the means that could substantially affect the adhesion strength and longevity of a given ABJ. An effective surface preparation improves the mechanical interlocking (see Figure 2-5). Extensive research has been performed to advance the interface and boost the bond strength of ABJs, some of which will be discussed herein. Each adherend type requires a specific surface treatment method and a suitable adhesive. Guo et al. (2021) studied the effects of different surface treatments, including milling, sulfuric acid anodizing (SAA), phosphoric acid anodizing (PAA), and sandblasting with SAA, on the bond strength of SLJ formed with light-weight Al alloy subjected to tensile tests. They assessed the strength enhancement of SLJs as a function of their surface treatment and ranked them in order of effectiveness as PAA > Milling > SB + SAA > SAA. In another study, Park et al. (2020) studies the impact

of various surface treatments (e.g., manual sanding, grit blasting, and peel-ply plus grit blasting) on the behaviour of SLJs joining CFRP laminates under fatigue and tensile loads. The static strength retention at one million cycles was evaluated at 55.4% for the sanding treatment, 47.5% for grit blasting, and 50.3% for peel-ply plus grit blasting.

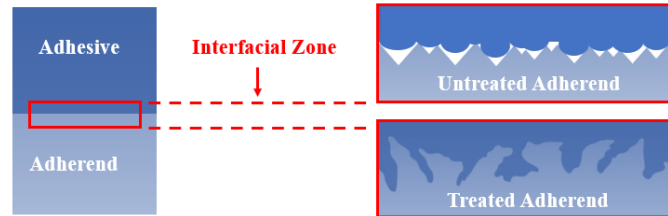


Figure 2-5. The interlocking mechanism generated by an effective surface treatment procedure.

Xie et al. (2020) employed a two-step laser surface modification to boost the SLJ shear-lap performance of CFRP-laminates, in which a 40.8% improvement in the shear strength of the specimens compared with untreated ones was evaluated. De Cicco & Taheri, (2019) used resin-applied peel-ply as a surface treatment to increase the interface bond strength of Mg sheets to FRPs under an LVI loading scenario. The treatment also resulted in increased mode I fracture toughness and delamination resistance. In addition, Russian et al. (2022) assessed the effect of surface preparation on the effectiveness of shape-memory alloy-CFRP double-strap joints. They studied the fatigue performance of repaired specimens treated with grit blasting and power-tool-abrasion, in terms of failure modes, fatigue lives, crack growth curves, and strain contours. The results indicated that grit-blasted surface-treated specimens exhibited an approximately three times improvement in fatigue life compared to the power-tool-abrasion technique.

A concise review of the surface preparation techniques, including the application of atmospheric plasma surface treatment and their influence on the bond strength of ABJs can be found in the following reference (Taheri, 2020).

2.3.1.2. Joint Configuration Advancement

As stated, the joint configuration can significantly affect the bond strength capacity of ABJ. The most commonly used ABJ configuration is the single-lap joint (SLJ), which involves a relatively simple procedure for joining adherends (Xi et al., 2020). Nevertheless,

the bending moment generated in the overlap region as a result of the applied tensile or compressive loadings could subject this joint configuration to a critical state (Duncan, 2010).

The other ABJ configurations that have been studied include the scarf, stepped, single- and double-strap ABJs. Scarf joints are also believed to be an effective configuration for joining composite materials due to the resulting uniform stress distribution across the bond length, and their better post-repair strength capacities (Moreira et al., 2020). Sonat & Özerinç (2021) assessed the effects of different scarf angles (i.e., 1.9°, 2.8°, and 5.7°) on the bond strength of CFRP scarf ABJs. The results of this study revealed that the tensile strength of their joints reduced as the scarf angle was increased. They also reported three types of failure, depending on the scarf angle; the failure types were predominantly cohesive for the 5.7° joints, fiber failure for the 1.9° joints, and a mixture of these for the 2.8° joints.

The efficiency of a scarf joint is extremely dependent on the scarf angle. At a low scarf angle, the scarf joint could provide higher strength compared to the strength generated by SLJs; however, at relatively higher scarf angles, the SLJs could support a similar or even higher joint capacity compared to the scarf joints, as depicted in Figure 2-6. In general, the accurate machining required for the preparation of effective scarf angles is an arduous task and therefore costly (Srinivasan et al., 2022). The lap-shear behaviour of 8.6° angle scarf joints in comparison to SLJs by considering 0.5 mm and 1.1 mm thick CFRP straps and 0.5 mm thin Ti-6Al-4V straps (with and without pins) was thoroughly investigated by Srinivasan et al. (2022). The results revealed that the failure load of the scarf and Ti-6Al-4V strap joints were similar and the higher scarf angle designs could be replaced with Ti-6Al-4V straps for greater repair effectiveness. They also concluded that delamination due to peel stresses was the crucial failure mode in the fabricated single-strap joints (SSJ).

Jiang et al. (2019) studied the bond strength, stress distribution, and failure of the adhesive in SSJ made of CFRPs under tensile loading scenarios. They found that increasing the adhesive thickness initially reduced and then improved the bond strength. They also concluded that using an adhesive interface with 0° stacking significantly enhanced the

tensile strength and reduced composite matrix damage. Adding a second strap on the bottom side of the single-strap ABJ could also boost the bond strength due to the symmetry in the design. Saleh et al. (2020) studied the response of double-strap joints (DSJs) made of steel-to-CFRP adherends under tensile loading using Digital Image Correlation (DIC) and Acoustic Emission (AE) techniques, as well as analytical and numerical analyses. They used DIC to capture strain/displacement maps and assess the damage locations and their effects on displacement contour maps, strain distribution, and load transfer between different parts of the joint. Their results showed good agreement between the results obtained by DIC, analytical, and numerical analyses. Razavi et al. (2018) used a strain-based failure criterion to evaluate the failure load of DSJs formed by CFRP and steel plates. Based on their approach, the adhesive joint was deemed failed when the normal strain along the adhesive mid-plane at a critical distance from the bonding edges attained a critical value. They also demonstrated the robustness of their model, which could predict failure loads effectively.

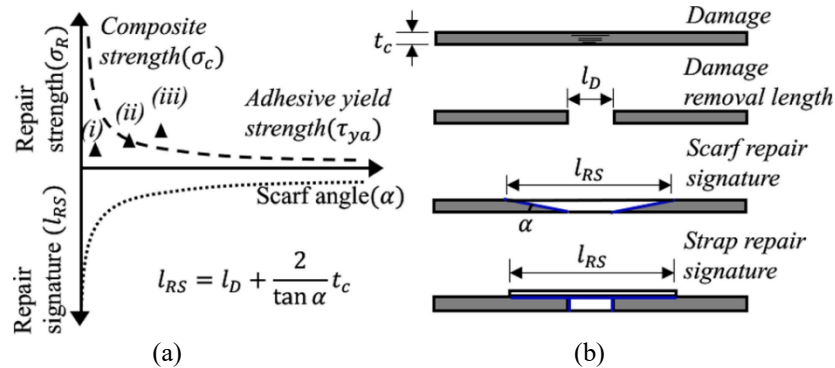


Figure 2-6. (a) Effects of scarf angle on the ABJs strength, (b) damage repair with bonded joints (Srinivasan et al., 2022). Note that the repair signature refers to the area that has been repaired.

2.3.1.3. Adhesive Properties Advancement

The relatively recent development of nanotechnology has prompted the development of several nano-reinforced adhesives, thus, expanding the applications of ABJs in various industries. Nano-reinforced adhesives are adhesives that consist of a polymeric matrix that hosts at least one type of nano-sized particle (Mariano et al., 2014). Hanumantharaya et al. (2020) investigated the inclusion of different contents of silicon carbide (SiC) nanoparticles to reinforce a structural acrylic adhesive used in single-lap GFRP joints configuration

subjected to the lap-shear test. The results demonstrated the shear strength and load-bearing capacity of SLJs with 0.75 wt.% SiC enhanced by 38% compared to neat-adhesive SLJs. The application of carbon nanotubes (CNTs) for enhancing the bond strength of ABJs has also received much attention in recent years (Han et al., 2019). For instance, Kumar et al. (2018) experimentally investigated the performance of SLJs mating mild steel adherends with multi-walled carbon nanotubes (MWCNT)-reinforced adhesive. The results demonstrated that the inclusion of 0.75 wt.% of MWCN improved the lap-shear strength by 37% and transferred the failure mode from interfacial to the preferred cohesion mode. The strengthening mechanism produced by MWCNT in the adhesive is depicted in Figure 2-7.

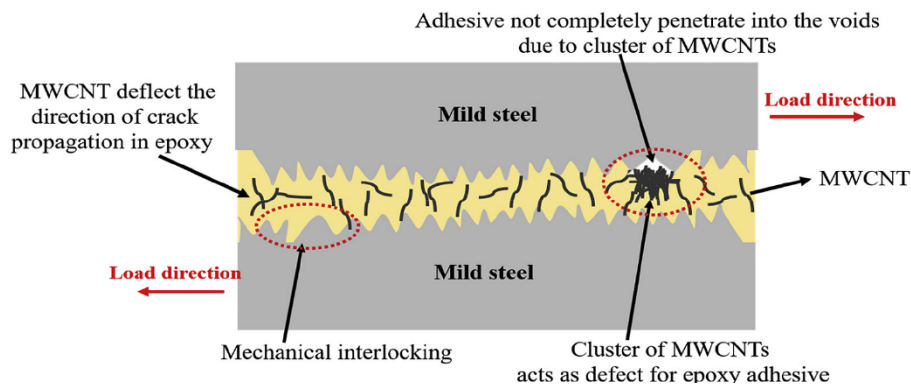


Figure 2-7. Schematic of strengthening and toughening mechanisms generated by MWCNTs in ABJs (Kumar et al., 2018).

Graphene nanoplatelets (GNPs) have also been proven to enhance the mechanical performance of adhesives due to their remarkably high strength and stiffness. Gültekin et al. (2016) investigated the effects of the inclusion of different contents of GNPs in structural epoxy adhesive via SLJs mating Al adherends subjected to the lap-shear loading condition. They also examined four different methods of dispersion of GNPs in the adhesive. Their results indicated that the failure load of the reinforced SLJs was enhanced compared to that of SLJs fabricated with neat adhesive. The optimal ratio of GNP was established as 1 wt.%; further increase in the GNP ratios reduced the failure joint capacity. Soltannia & Taheri (2015) examined the influence of loading rate (1.5, 3, and 2.04E+5 mm/min) on the performance of SLJ formed with GFRP and CFRP adherends and epoxy resin reinforced with carbon nanofibers (CNF), CNT and GNP nanoparticles and Q-cell (all at 0.5 wt.%). The results indicated that while Q-cell increased the workability of the

adhesive, it could not improve the mechanical response of the SLJs. In contrast, the addition of all nano-reinforcements led to an increase in the average ultimate shear strength of scarf adhesive lap joints (SLJs), with the greatest improvement of 32% seen with the addition of GNPs under the highest loading rate, and an improvement of 26% under quasi-static loading rate. It should also be noted that the synergy of combined nanoparticles can also augment the joint strength of bonded joints. For instance, Rao et al. (2020) established that the inclusion of 0.75 wt.% of hybrid MWCNTs/GNPs in the ABJ resulted in the highest gain in shear strength and elongation of 36.6% and 33.2% in SLJs mating CFRPs, respectively. In a notable study, Ahmadi-Moghadam et al. (2015) compared the gains in the mechanical properties of an epoxy resin reinforced with GNPs. The GNPs were processed by various means including silane-modified GNPs (G-Si) and amino-functionalized GNP (G-NH₂). The inclusion of 0.5 wt% neat GNPs increased the ultimate strength of the host resin by 38% on average, while the effect of functionalized GNPs produced strength values greater than this average. In addition, the ductility of the host epoxy resin was increased by the functionalized GNPs. They rated the contributions of G-Si and G-NH₂ as more significant than that of non-processed GNPs.

2.3.2. Lap-shear and Fatigue Response of ABJs

As mentioned previously, the performance of ABJs subjected to tensile and fatigue loading scenarios is supported by a large database. For instance, Anyfantis & Tsouvalis, (2013) performed a parametric study of seven different CFRP-steel SLJ geometries subjected to lap-shear tests. They indicated that the effects of the adhesive thickness and stiffness ratio were insignificant on the responses of their joints compared to the effect of the overlap length. Zou et al. (2004) developed an elegant analytical model for analyzing the performance of SLJs mating FRPs. The model was further extended by Taheri & Zou, (2004) to assess the performance of unsymmetric ABJs constructed by composite sandwich panels-to-flange joints.

Durmuş & Akpınar (2020) conducted numerical and experimental investigations on the performances of SLJ one-step lap joint (OSLJ) and three-step lap joint (TSLJ) with five different step lap lengths subjected to tensile loading. Based on the results, they concluded

that TSLJ carried the highest load among the considered types of joints, and the change in the step length in the TSLJ type resulted in a substantial effect on the failure load of the joints. Jairaja et al. (2019) investigated the performances of CFRP-Al SLJs bonded by using a single and a mixture of two adhesives (brittle and ductile). In this study, the Araldite-2015 ductile adhesive and the AV138 brittle adhesives were utilized at the ends and in the middle of the bonded region, respectively. The study demonstrated that the use of dual adhesives improved bond strength.

Masoudi Nejad et al. (2022) evaluated the static strength and fatigue life of two T-joint configurations of flat and grooved types under four loading rates of 1, 10, 50, and 100 mm/min. The average static failure load of grooved specimens was found to be 37.3%, 26.5%, 14.4%, and 9.3% higher than that of the flat type T-joints tested under 1, 10, 50, and 100 mm/min loading rates, respectively. The results also indicated that fatigue life cycles of grooved T-joints were 40.2%, 25.3%, and 11.6% longer than that of the flat bonded specimens under 40%, 60%, and 80% maximum fatigue loads, respectively. Gastens et al. (2022) developed a new approach to detect crack initiation in bonded joints subjected to constant and variable amplitude fatigue loading. They implemented the backface strain method, in which a strain gauge was placed at a highly sensitive location in the overlap area of the bonded joints to monitor the damage. The results indicated that the developed method could capture the striking converging-diverging trend in strain amplitude curves in the joints undergoing constant amplitude loading. The results were also in good agreement with the crack initiation observed with video microscopy. In another study, Khoshmanesh et al. (2022) studied the changes in the stiffness and damping of a thick adhesive joint specimen utilized in the shear webs of wind turbines during a fatigue test. Three distinct phases of damage were obtained in their fatigue tests. In the first phase, transverse cracks and delamination initiated and propagated with negligible change in the stiffness while damping increased; in the second phase, the number of transverse cracks increased and stiffness; in the final phase, the crack density remained constant, while de-bonding of the joint initiated and propagated until final failure.

2.3.3. Flexural and Axial Compressive Responses of ABJs

ABJs can experience different loading states during their service life, including axial loading, bending, and shear. When subjected to bending loads, ABJs are more likely to experience peel and cleavage stresses that can critically lower their strength. Therefore, it is crucial to investigate and enhance the mechanical responses of ABJs under bending and other complex loading scenarios to ensure their reliability and effectiveness in industrial applications. There is a distinct lack of information and data regarding the flexural and compressive performances of ABJs, especially when the adherends are made of composites. When such joints become subjected to flexural and compressive loading states, the inherent relatively weak interlaminar strength of laminated composite makes them susceptible to delamination.

A detailed series of experimental and FE analyses were performed by Grant et al., (2009) on SLJs constructed with toughened epoxy and mild steel adherends. The SLJ specimens were tested under tensile loading (i.e., subjecting the adhesive to a shear loading state), three-point loading (shear and bending) as well as four-point loading (pure bending) scenarios. The authors evaluated the effects of several parameters (e.g., overlap length, bond-line thickness, and spew fillet) on the strength of bonded joints. They observed that three-point bending and tension loadings were very similar in the way in which they affect the adhesive, whereas the four-point bending test did not cause failure, as the steel yielded prior to the joint failure. Abdelfattah et al. (2022) performed numerical and experimental studies on CFRP SLJs subjected to three-point bending to establish the effects of strap size on the flexural response of their bonded specimens. They indicated that increasing the strap size resulted in a considerable advancement in the joints' flexural stiffness and ultimate strength.

Zamani et al., (2021) studies the influence of GNPs and nano-silica-reinforced Araldite adhesive on the fatigue life of Al-to-composite SLJs subjected to four-point bending. They reported that a combination of 0.5 wt.% of each GNP and nano-silica (1 wt.% in total) lead to the enhancement of fatigue life of their SLJs compared to SLJs constructed by 1 wt.% content of the individual particle type. Çakır et al., (2021) experimentally investigated the lap-shear and flexural behaviours of SLJs made of GFRP

bonded with GNP-reinforced epoxy adhesive. They concluded that the inclusion of 0.3 wt.% of GNPs to the adhesive resulted in 145% augmentation in the lap-shear strength whereas a 100% improvement of the flexural strength was obtained by incorporation of the 0.2 wt.% of the GNPs in the adhesive.

Campilho et al., (2010) reported experimental and FE parametric studies on single- and double-strap ABJs formed by CFRP adherends under laterally unrestrained compressive loading. They investigated the effects of the overlap length and patch thickness on the failure modes, elastic stiffness, and strength of the joints and established the optimal configuration in each class of bonded joints. Their results indicated that their developed FEM was able to predict the load capacities and simulate the failure modes. In another study, Kadioglu (2021) conducted research on quasi-static buckling conditions of SLJs made of different types of adherends and film adhesive. They also developed a non-linear FE model to predict the failure loads and modes, which were found to be in good correlation with experimental results. They observed two different failure modes of the joints; a complete failure in the adhesive layer, and large plastic deformation of adherends which was considered a good source for crashworthiness situations in aerospace applications.

2.3.4. Impact Response of ABJs

In-plane and out-of-plane impact loadings are other common types of loading conditions that bonded joints could experience in their service life. Under such loading states, in particular, bonded joints must be capable of absorbing high levels of energy to guarantee design safety. Nonetheless, only a few researchers have investigated the response of ABJs under impact loading.

Li et al., (2020) performed an experimental–numerical comparative analysis of SLJ constructed of 2024-T3 Al adherends and FM 94K epoxy adhesive subjected to out-of-plane LVI. They systematically investigated the effects of four different temperatures and four different transverse impact energies on the adhesive failure, energy absorption and residual capacities of SLJs. Their results revealed that both the energy absorption and the residual capacities changed negligibly when temperature increased except at 80°C, which

was near the glass-transition temperature (T_g). In another study, Park & Kim (2010) investigated the out-of-plane high-velocity impact response of composite SLJ impacted by hailstones. They implemented ultrasonic scanning and optical microscopy to measure the damaged area and the exact location of the damage, respectively. They also developed an FE model, which indicated the highest peel and shear stresses where the plies were delaminated.

Galliot et al. (2012) assessed the dynamic response of SLJs made of CFRP adherends and compared the results to their base quasi-static test results. For that, they designed drop-weight equipment to subject their specimens to a tensile impact load applied at 4 m/s velocity. They observed an increase in the failure load energy absorption capacity as a function of increasing the loading rate. They also concluded that the joints behaved qualitatively similarly under quasi-static and subsequent impact loading states. Kemiklioğlu & Baba (2019) studies the influence of vibration cycles and axial impact energy level on the responses of GFRP SLJs. Their results indicated that the increase in impact energy applied on all specimens subjected to vibration resulted in a decline in the strength of the joints. However, the tensile strength of the joints was relatively enhanced when the specimens were subjected to 10 J impact energy.

2.3.5. Numerical Analysis of ABJs

As stated earlier, several parameters affect the performance of ABJs. Therefore, performing a systematic series of experiments to establish the optimal configuration of ABJ could be time-consuming and thus costly. Alternately, two main mathematical approaches, namely closed-form solutions (e.g., analytical methods) and numerical methods (e.g., FEM) could be utilized to evaluate the performance of ABJs (Silva & Campilho, 2012). The first analytical model was developed by Volkersen (1938), in which, an SLJ was modelled by one-dimensional bars joined by an infinite number of rivets, with the rivets representing a continuum analogous to an adhesive layer. In this model, the adherends were allowed to have only axial deformation, and the adhesive layers were modelled by a series of shear springs. Since then, extensive studies were conducted to establish and improve analytical solutions for ABJs (Silva et al., 2009; Sauer, 2016). Most of the available closed-

form solutions, which are relatively easy to use, apply to basic common configurations; those that apply to more realistic ABJs with complex geometries are generally intricate and complex, requiring several properties and coefficients that should be obtained experimentally. In such cases, certain assumptions are necessitated, which may restrict the applicability of a given model (Budhe et al., 2017). On the other hand, the numerical approach is capable of considering complex geometries, material and other types of nonlinearities, and different loading conditions. The conventional numerical methods available for predicting the strengths and failure mechanisms of ABJs are based on four main methodologies; continuum mechanics, fracture mechanics, eXtended-FEM (XFEM), and progressive damage mechanics (Silva & Campilho, 2012).

In the continuum mechanics approach, the maximum values of strain (Adams et al., 1986), stress (Harris & Adams, 1984), or plastic strain energy density (Adams & Harris, 1987) are utilized to estimate the failure load. Nevertheless, this approach assumes that the structure and its material are continuous; thus, in several cases, these criteria would become somewhat impractical due to the inherent singularities that develop at the edges of bonded joints (Bogy, 1968). On the other hand, in the fracture mechanism approach, the evaluation of fracture toughness or stress intensity factors is used to establish the strength of the ABJs (Xu et al., 1999). In contrast to the continuum model, the singularity at crack tips, depicted in Figure 2-8, is considered in this method. However, the commonly used fracture mechanics approaches are based on linear elasticity, and consequently, their applications are restricted to the cases where the adherends of a given ABJ would not experience plastic deformations.

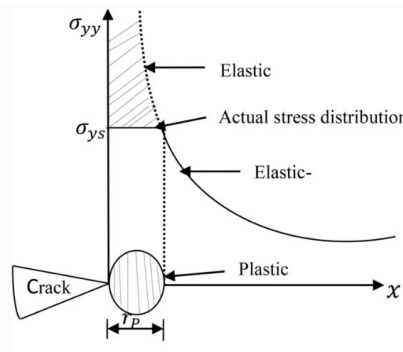


Figure 2-8. Crack tip singularity in LEFM (Ameh, 2020).

The eXtended Finite Element Method (XFEM) is an extension of the FEM, in which the crack length and tips are simulated by enrichment of displacement fields with discontinuous functions (i.e., the Heaviside function) and stress intensity/singularity functions, respectively. This robust method provides accurate results without pre-defining the crack growth path. Interestingly, once a crack propagates, there is no need for remeshing, as the crack travels virtually within the elements (see Figure 2-9), not on their edges (Mottaghian et al., 2018). However, the enrichment functions are only activated with a pre-existing crack which indeed turns the estimation of crack initiation into a challenging task. Campilho et al. (2011) considered the maximum principal stress criterion for crack initiation and observed that their developed XFEM failed to model the crack onset in the adhesive layer in single- and double-lap joints. In contrast, Xará & Campilho (2018) thoroughly studied the effects of different XFEM damage initiation criteria on the strength prediction of hybrid single-L bonded joints and proved that their model's predictions were quite accurate when incorporating the quadratic nominal stress or maximum nominal stress initiation criteria.

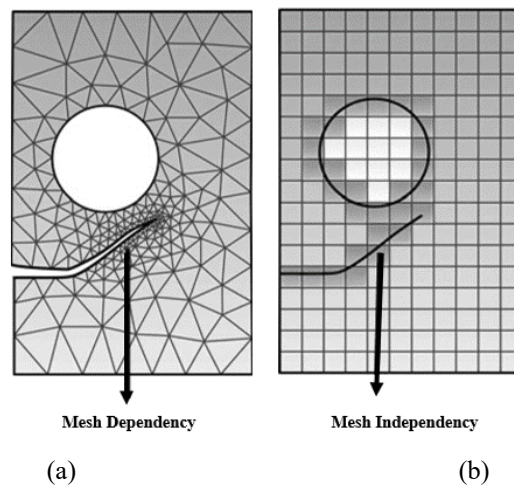


Figure 2-9. Crack simulation (a) FEM, (b) XFEM (Swati et al., 2019).

There are six different stress and strain-based criteria to assess the crack initiation in ABAQUS commercial FE software (Völkerink et al. 2019); however, LS-DYNA software does not support the implementation of XFEM without the existence of a pre-crack. Consequently, the progressive damage mechanism would be another prospective approach to evaluate the performance of ABJs.

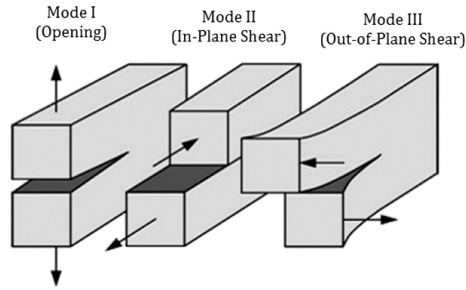


Figure 2-10. Failure modes (Hadei et al., 2020)

2.3.5.1. Cohesive Zone Model (CZM) Overview

Evaluation of the interlaminar fracture toughness in terms of strain energy release rate (G) could be a challenging task. Failure in materials could be initiated and propagated in pure single modes (see Figure 2-10), or through mixed mode. To characterize delamination and failure parameters, several methodologies have been suggested by researchers. Among all, the Double Cantilever Beam (DCB), End Notched Flexural (ENF), and Single Leg Bending (SLB) test methods are commonly used to evaluate fracture toughness in mode I (G_I), II (G_{II}), and III (G_{III}), respectively (see Figure 2-11). The values are used as input to numerical models.

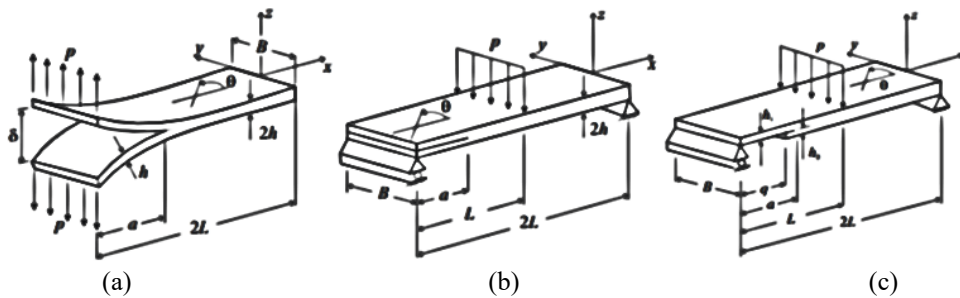


Figure 2-11. Fracture tests (a) DCB, (b) ENF, and (c) SLB (Burlayenko & Sadowski, 2008).

The CZM is a progressive damage and failure modelling approach that accounts for the onset and growth of damage without the prerequisite for the existence of an initial flaw; however, a pre-defined crack path must be defined. Within this approach, the complete response of a given system, up to the final stage of failure, could be simulated in a single analysis, and no post-processing analysis is needed (Banea & da Silva, 2009).

The CZ concept was originally developed to define the damage at the cohesive process zone ahead of an apparent crack tip, in which micro-voids form and subsequently grow

with the load increment and create thin fibrils until a crack appears (Anyfantis, 2012). The relation of cohesive stress (σ) and crack opening displacement (COD) characterizes the traction-separation law as shown in Figure 2-12(a). This law indicates the fracture process, including crack initiation, growth, and coalescence of voids which results in the deformation and decohesion of any materials in the immediate vicinity of the crack tip, as depicted in Figure 2-12(b) (Zan et al., 2017).

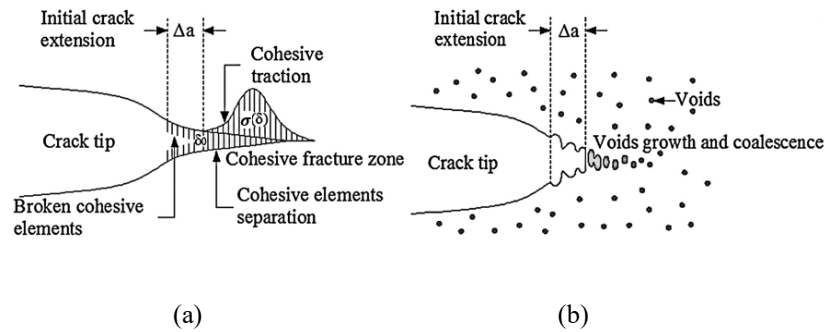


Figure 2-12. Graphic depictions of (a) cohesive fracture area, and (b) void deformation at the crack tip (Zan et al., 2017).

Based on the available literature, the most commonly utilized traction-separation laws are the bilinear, linear-parabolic, trapezoidal, and exponential as presented in Figure 2-13. Alfano (2006) studied the influence of different traction-separation laws on the assessment of debonding by CZM in pure modes I and II. The results indicated that the exponential model produced the most precise results, while the bilinear model was found to generate the most optimal solution in terms of the balance of the central processing unit (CPU) time and accuracy. The selection of traction-separation law in CZ depends on the way the material and interface traction would cause attractions under different modes. Selecting the appropriate traction-separation would facilitate CZM to assess the crack propagation (Campilho et al., 2013a). In the following, the linear elastic/linear softening model, commonly referred to as the bilinear cohesive model, is used to further explain the concept of CZM in detail.

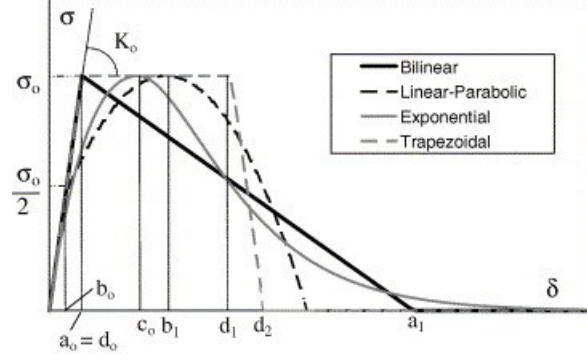


Figure 2-13. Traction-separation curves (Alfano, 2006).

In the bilinear cohesive model, the stress advances linearly as a function of increasing displacement up to the onset of damage (i.e., at the onset of separation of the cohesive surfaces which is the critical traction), followed by linear reduction of the stress to a zero traction decaying damage evolution regime. The elastic linear response is characterized by an elastic constitutive matrix, represented by the following mathematical equation, which relates the nominal stresses to the nominal strains along the interface:

$$\boldsymbol{\sigma} = \begin{Bmatrix} \sigma_n \\ \sigma_s \\ \sigma_t \end{Bmatrix} = \begin{bmatrix} K_{nn} & K_{ns} & K_{nt} \\ K_{ns} & K_{ss} & K_{st} \\ K_{nt} & K_{st} & K_{tt} \end{bmatrix} \begin{Bmatrix} \varepsilon_n \\ \varepsilon_s \\ \varepsilon_t \end{Bmatrix} = K \boldsymbol{\varepsilon} \quad (2-1)$$

$$K = \frac{E}{t_0}, \varepsilon_n = \frac{\delta_n}{t_0}, \varepsilon_s = \frac{\delta_s}{t_0}, \varepsilon_t = \frac{\delta_t}{t_0}$$

where σ_n , σ_s and σ_t represent the traction stresses in the normal (out-of-plane), and the first and second in-plane shear directions, respectively. δ_n , δ_s , δ_t , t_0 , E and K (generally refer to K_{nn} , K_{ns} , ..etc.,) represent the corresponding separation counterparts in different directions, the thickness of the cohesive element, and the elastic modulus and stiffness matrix of the interface material, respectively. Once the failure criterion is satisfied, the analysis is followed by the adoption of the evolution failure criterion. The equation representing the damage evolution is characterized as

$$\boldsymbol{\sigma} = K(1 - D)\boldsymbol{\delta} \quad (2-2)$$

where D corresponds to the damage variable. This variable, which is representative of the rate of material stiffness degradation, is initially zero, and it enhances by increasing the

loading and consequent damage initiation. When the value of D reaches unity, the failure of the material has occurred.

The selection of a CZM traction-separation curve (see Figure 2-13) would be based on various factors such as the interfacial behavior of the adhesive and adherends' materials, the level of accuracy required, and the ease of use and availability of CZM within a given finite element code. The area under the traction-separation curve represents the energy release rate. It is important to note that accurately establishing the parameters representing the traction-separation curve is crucial because the curve governs the progressive damage failure and establishment of incremental crack growth of the material. Therefore, appropriate failure criteria must be utilized to establish the required parameters for a given CZM model.

The damage will initiate when the stresses and/or strains reach their maximum values (end of the elastic region). A large number of damage initiation and evolution failure criteria have been developed by various researchers. The most common damage initiation criteria are provided below. Each criterion postulates that the process of material degradation would be initiated when the criterion meets the following mathematical equality.

(i) Maximum nominal stress (strain) criterion

$$\text{Max} \left\{ \frac{\sigma_n(\varepsilon_n)}{\sigma_n^{\text{max}}(\varepsilon_n^{\text{max}})}, \frac{\sigma_s(\varepsilon_s)}{\sigma_s^{\text{max}}(\varepsilon_s^{\text{max}})}, \frac{\sigma_t(\varepsilon_t)}{\sigma_t^{\text{max}}(\varepsilon_t^{\text{max}})} \right\} = 1 \quad (2-3)$$

(ii) Quadratic nominal stress (strain) criterion

$$\left\{ \frac{\sigma_n(\varepsilon_n)}{\sigma_n^{\text{max}}(\varepsilon_n^{\text{max}})} \right\}^2 + \left\{ \frac{\sigma_s(\varepsilon_s)}{\sigma_s^{\text{max}}(\varepsilon_s^{\text{max}})} \right\}^2 + \left\{ \frac{\sigma_t(\varepsilon_t)}{\sigma_t^{\text{max}}(\varepsilon_t^{\text{max}})} \right\}^2 = 1 \quad (2-4)$$

Moreover, one of the following damage evolution criteria can be implemented to establish the evolution of damage and its final failure of the material.

(i) Power Law

$$\left(\frac{G_I}{G_{IC}}\right)^\alpha + \left(\frac{G_{II}}{G_{IIC}}\right)^\alpha + \left(\frac{G_{III}}{G_{IIIC}}\right)^\alpha = 1 \quad (2-5)$$

(ii) BK (Benzeggagh & Kenane, 1996)

$$G_{IC} + (G_{IIC} - G_{IC}) \left(\frac{G_{II} + G_{III}}{G_T}\right)^2 = G_{TC} \quad (2-6)$$

where

$$G_T = G_I + G_{II} + G_{III} \quad (2-7)$$

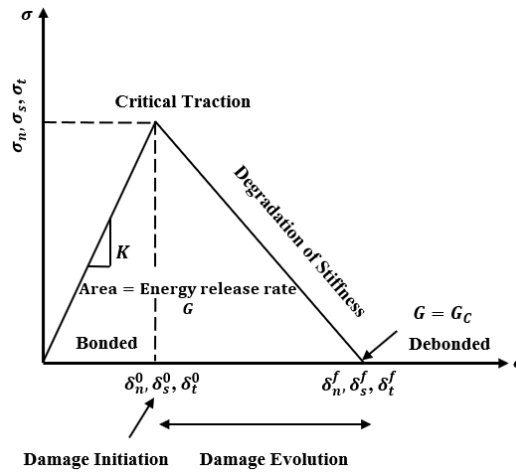


Figure 2-14. Graphical sketch of parameters of the bilinear cohesive model.

Upon damage initiation, the material properties would be degraded based on the selected damage evolution law. Generally, three crucial parameters (i.e., the stiffness, strength, and fracture energy) would control the damage initiation and evolution of the cohesive elements (see Figure 2-14).

The CZM is relatively easy to apply, yet accurate and computationally efficient; thus is rendered as a very practical and effective approach for damage assessment in ABJs. Marami et al. (2016) utilized a one-layer CZM to model the behaviour of reinforced Al single-lap bonded joint reinforced by reduced graphite oxide. The authors implemented a bilinear-cohesive law to account for material degradation in the adhesive layer. In another study, Barbosa et al. (2018) applied the same technique to simulate the lap-shear performances of SLJs, double-lap joints, stepped-lap joints, and scarf joints mating Al

alloys adherends. Campilho et al. (2009) developed a one-layer tri-linear mixed-mode cohesive element to assess the behaviour of single and double-strap bonded repairs on CFRP adherends subjected to tensile loadings. All of the results revealed that the CZM model predicted the failure load of ABJs within an acceptable margin of error. However, it was concluded that it would not be feasible to model the exact mode of local failure of the bonded region (i.e., interfacial or cohesive) by implementing one layer of cohesive elements.

Heshmati et al. (2018) developed one layer of mixed-mode CZ elements surrounded by two layers of continuum elements to simulate failure in the bonded region of CFRP-steel double-strap ABJs. In another study, Anyfantis & Tsouvalis, (2013) implemented an FE model for simulating the response of SLJs mating steel adherends, in which the damage was modelled by an embedded process zone CZM-based model. The failure loads in these studies were precisely predicted by the FE models; nevertheless, no failure mode other than cohesion was observed by the authors.

2.3.6. Artificial Intelligence

Even though all aforementioned approaches are capable of effectively modelling the performance of ABJs, they are all based on the One-Factor-at-a-Time (OFAT) analysis philosophy. In other words, most approaches evaluate the effects of only one design parameter on the overall performance as opposed to considering the collective effects of multiple parameters. Indeed, determining the optimal configuration of a bonded joint would be a very complex and laborious task when using traditional methods. The widespread emergence and advancement of artificial intelligence (AI) in recent years have resulted in substantial technological advancements in various fields of science and engineering (Kazi et al., 2020). Machine Learning (ML) is one of the most widely used subfields of AI which is able to understand and simulate human intelligence by implementing procedures based on logical/binary operations that learn from a series of samples (Balcıoğlu & Seçkin, 2021; Paturi et al., 2022).

Gu et al. (2021) developed “black-box” and “grey-box” ML models to determine the failure load of single-lap ABJs. They generated a dataset of 300 numerical single-lap joint

samples with different geometry/material parameters. The obtained dataset was fed into their ML models and consequently, optimal designs of structure and material were established. Silva et al. (2021) also assessed the fatigue response of ABJs by combining FE analysis and ML model. They generated a dataset of 365 samples with the inclusion of four different adhesive materials and four different joint configurations. They developed an extremely randomized tree (ERT) as a supervised ML algorithm that was able to deal with small and noisy datasets. Their developed model was found to be capable of predicting the fatigue responses of bonded joints with a maximum error of 2.13%.

Artificial Neural Network (ANN) is one of the most promising ML algorithms inspired by the performance of the human brain (Maleki et al., 2022). ANN is used to consider nonlinear data and explore complicated relationships between the input and output parameters (Paturi et al., 2022). Tosun and Calık (2016) developed an ANNs model to investigate the strength of bonded lap joints subjected to tensile loading. They collected a set of experimental data from literature related to the performance of single-lap ABJs with various geometries and fed them to their ANNs model. In this work, they utilized a three-layer feedforward ANNs model in which the Levenberg–Marquardt learning algorithm was employed to train their ANNs model. ANNs model was also utilized to predict the response of ABJs constructed by pultruded composite sections with different bonding angles (Balcioğlu et al., 2015). In another study, an ANNs model was used to predict the strength of adhesively bonded single-lap composite joints with varying overlap lengths and adhesive thickness (Rangaswamy et al., 2020). Based on the results produced by the mentioned studies, it is concluded that ANNs-based models are capable of predicting the failure load of single-lap ABJ accurately and optimizing ABJs' configuration.

Another popular ML technique is to employ evolutionary algorithms (i.e., genetic programming (GP) and genetic algorithm (GA)). Li et al. (2021) developed a method by combining FEM, Latin Hypercube Sampling, and GP to assess the impact of the physical configurations on the fracture modes of adhesive single-lap joints. They generated 150 samples by an FE model by which different combinations of adherend and adhesive mechanical properties and thicknesses were considered. As a result, their trained GP models could assess the early-state failure modes of the ABJs quite accurately. Gu et al.

(2023) also proposed a GA model to predict the micro bond properties of composites, evaluate their strength, and simulate crack patterns developed in bolted composite lap joints. The results indicated that the results generated by the GA model were in good agreement with the experimental and numerical results. ML-based models for analyzing ABJs are fairly limited, and the available models have been generally developed based on simple design variables. This indicates the necessity of performing further studies to develop ML capable of analyzing the responses of bonded joints.

Chapter 3: Numerical and Experimental Investigations Into Post-Buckling Responses of Stainless Steel- and Magnesium-Based 3D-Fiber Metal Laminates Reinforced by Basalt and Glass Fabrics

Fatemeh Mottaghian, Hessameddin Yaghoobi, Farid Taheri

Published in the Journal of Composites Part B: Engineering, Volume 200, PP 108300, 2020.

Fatemeh Mottaghian is the principal author of this article. As a part of her Ph.D. program, she performed the fundamental research stated in the article. She conducted the experimental works and produced the article drafts collaboratively with Hessamedin Yaghoobi, who was a postdoctoral fellow within the research group. Moreover, she conducted all numerical simulations and analyzed them against the experimental results. She also applied all the necessary revisions before the publication of the article, all under the supervision and guidance of her supervisor, Dr. Farid Taheri.

Moreover, this paper has been partially modified compared to its original published version to conform to the format of this thesis and to reduce the repetition of topics covered in Chapter 2.

3.1. Abstract

This paper presents the details and results of a series of follow-up experimental and numerical investigations that were conducted to establish the buckling behaviour of special three-dimensional fiber metal laminates (3D-FMLs). This FML is made of a special 3D fiberglass fabric (3DFGF)-epoxy composite, which also hosts a two-part liquid urethane foam within its core cavities and is further reinforced with basalt and E-glass bidirectional fabrics. 3D-FML panels with six different configurations were fabricated and beam-like specimens were extracted from the panels. The specimens were subjected to uniaxial compression loading. This follow-up study focuses on investigating the effects and level of improvement in the performance of the 3D-FMLs by utilizing magnesium and stainless steel as the face-sheet materials and the enhancement gained by the basalt and E-glass fabrics. The responses of the 3D-FMLs are also simulated numerically. By comparing the

numerical and experimental results, it will be explicitly demonstrated that the developed FE framework could serve as an effective and accurate means for establishing the performance of such FMLs, including those with more complex geometries and loading conditions. In addition, the most effective 3D-FMLs are identified and ranked based on their buckling capacity with respect to their cost and weight.

3.2. Introduction

[...] *Some portions of this section have been removed and included in Chapter 2.*

The present study is conducted based on three main objectives. The first objective is to investigate the effect of different metal types on the buckling capacity and post-buckling response of 3D-FMLs formed with SS and Mg face sheets subjected to uniaxial compressive loading. The second objective is to investigate whether the buckling capacities of the SS- and Mg-based 3D-FMLs could be further improved by incorporating additional layers of basalt or glass fabrics. It should be noted that basalt fiber, a natural fiber, offers several advantages, including good resistance to chemical attack, excellent adhesion to resins, remarkable heat and sound insulation properties, low water absorption, and suitability for use in a wide temperature range. Moreover, one of the most advantageous aspects of basalt fibers is their relatively lower cost, due to the abundant availability of the raw material and ease of production compared to the commonly used fibers such as glass and carbon fibers (Monaldo et al., 2019). Finally, the last important objective of the present investigation is to develop an accurate and robust numerical framework for simulating the buckling and post-buckling responses of the 3D-FMLs. Such an effective and robust FE-based framework will enable us to simulate the response of 3D-FML structural components with complex geometries under various and combined loading conditions. In addition, it will capacitate us to conduct a detailed parametric study in the future upon which we could formulate practical semi-empirical design equations for the use of practicing engineers.

3.3. Experimental Procedures

3.3.1. Materials

Two different classes of 3D-FMLs (i.e., SS-based and Mg-based FMLs) are investigated in this research. The 3D-FMLs consist of either SS or Mg alloy sheets, 3DFGF, two types of resins (hot- and cold-cure), basalt or E-glass fabrics, and polyurethane foam.

AZ31B-H24 Mg sheets with 0.5 mm thickness and 304-2B SS sheets with 0.48 mm thickness were purchased from MetalMart (Commerce, CA, US) and locally (Russel Metals Inc.), respectively. It should be noted that in an earlier study, we used a thinner SS sheet with its flexural stiffness being equivalent to that of the Mg sheets (i.e., 0.5 mm thick Mg); however, the low thickness of the SS resulted in a premature wrinkle type failure. The 3DFGF with a thickness of 4 mm, which was used to form the core skeleton of the 3D-FMLs, was supplied by the China Beihai Fiberglass Co. Ltd. (Jiujiang City, Jiangxi, China). West System (Bay City, MI, US) cold-cured structural epoxy system (105 resin and 206 slow hardener) was used to adhere the metallic sheets to the 3DFGF composite core of the 3D-FMLs. A hot-cured structural epoxy system (Araldite LY 1564 epoxy resin along with Aradur 2954 hardener), which was used to impregnate the 3DFGF, was acquired from Huntsman Co. (West Point, GA, US). The bi-axial (0/90) basalt fabric with 450 g/m² and 0.55 mm in thickness, was supplied by GBF basalt fiber Co., Ltd (China). The 0.45 mm thick, 425 g/m² bi-axial (0/90) glass fabric was supplied by Vectorply (Phenix City, AL, US). The two-part liquid, 8-lb density polyurethane foam, which was used to fill the cavities of the 3DFGF, was supplied by US Composites (Palm Beach, FL, US).

3.3.2. Specimen Fabrication

The fabrication process of the 3D-FMLs started with surface treatment of the metallic sheets using sandblasting with 20-30 grit-size crushed glass to roughen their surfaces and promote better adhesion to the FRP materials. Note that both surfaces (i.e., also the surface that would not be adhering to FRP) had to be sandblasted. This is because if only one of the surfaces is sandblasted, the resulting residual stress in such thin sheets would produce

a slight curvature of the sheets, hence causing issues during their bonding and consolidation to FRP. The sandblasted surfaces were cleaned by compressed air and subsequently wiped with acetone and let dry in the air. Next, the metal surfaces were coated by a thin layer of the cold-cure structural epoxy system and fitted inside a vacuum bag for curing at room temperature for 24 h to promote a more effective adhesion of metal sheets to the 3DFGF composite. This process was established after trying various surface preparation procedures and found to be the most effective process for bonding Mg alloy to FRP as documented in (De Cicco & Taheri, 2019b, 2019a). In parallel, fabrication of the 3D-core components of the 3D-FML began by impregnating the 3DFGF with the hot-cured resin by brushing as per the supplier's instructions (see Appendix A for further explanation). The resin-to-hardener ratio was 100:35 by weight, as recommended by the manufacturer. A laboratory mixer was used for stirring epoxy resin and hardener at 100 rpm for 10 min, and then the mixture was degassed in a vacuum chamber at room temperature for 30 min. A 60:40 weight fraction of hot-cure epoxy to 3DFGF was considered and the impregnated fabric was cured based on the temperatures-time curve provided by the manufacturer (i.e., 2 h at 60°C, and then for 8 h at 120°C). In the case of reinforced 3D-FMLs, the basalt or glass fabrics were embedded on the top and bottom surfaces of the 3DFGF at this stage, and then these fabrics were co-cured along with 3DFGF using the same hot-cured resin. In order to enhance the overall performance of the 3D-FML, the hollow cavities of the 3DFGF composite were filled with the polyurethane foam (by mixing part A and part B of the foam with a ratio of 50:50) using the aspiration process (i.e., using a negative pressure provided by an in-house built jig that facilitated a homogeneous distribution of the foam inside the cavities), and were allowed to cure at room temperature for 24 h. In the next step, the pre-treated metal sheets were bonded to the FRP core using the cold-cured epoxy resin and hardener with a weight fraction of 5:1, respectively. The assembly was sealed by the vacuum bagging process (by maintaining the assembly under vacuum for four days at room temperature, as per the manufacturer's recommendation). Finally, the specimens were cut from the fabricated panels into the required dimensions using a computer-controlled abrasive waterjet cutting system. A detailed description of 3D-FML fabrication is presented in Figure 3-1.

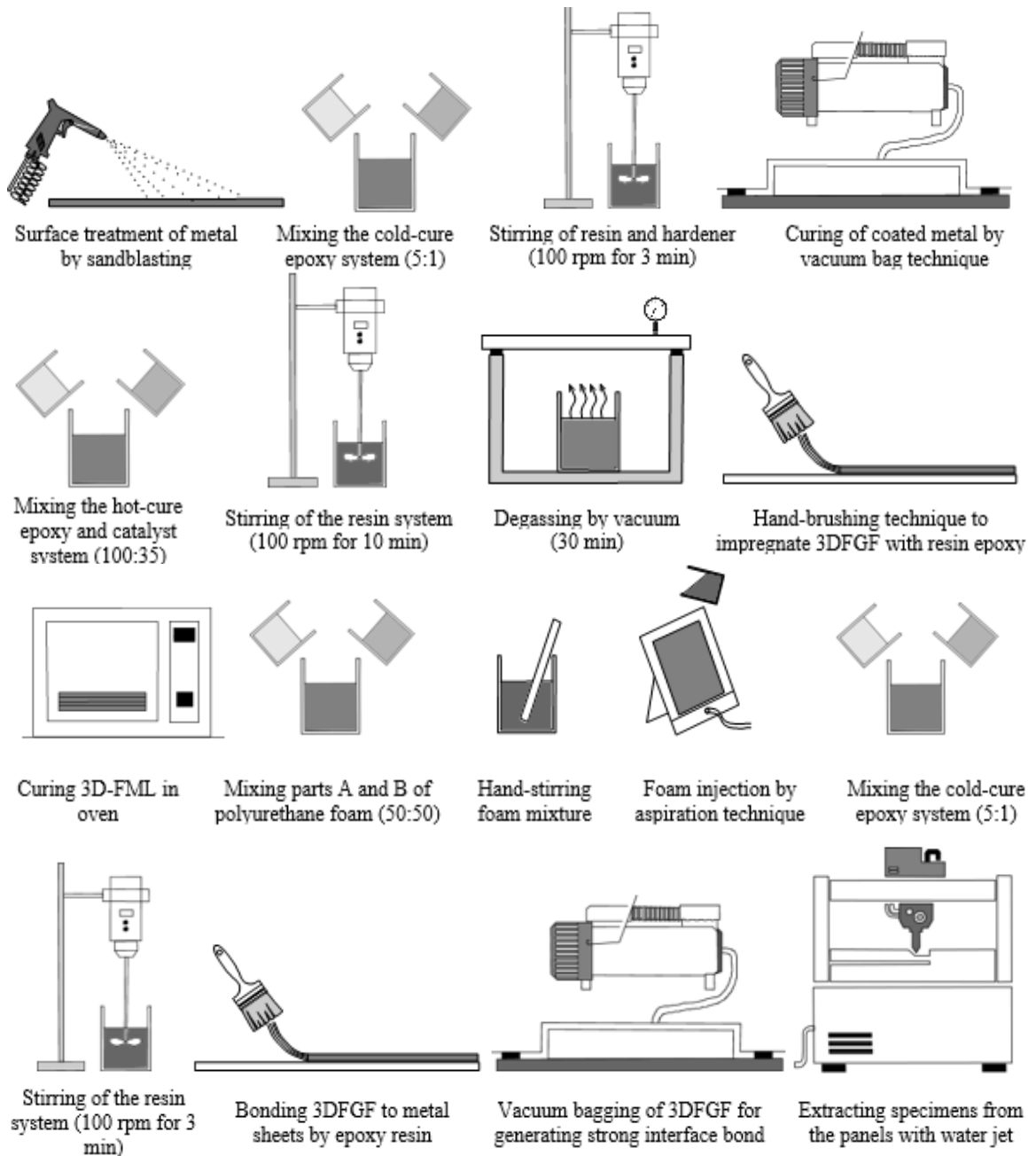


Figure 3-1. Fabrication process sequence of the base 3D-FMLs.

3.3.3. Buckling Experiments

An MTS servo-hydraulic universal testing machine with a 250 kN load cell was used to perform the buckling tests with a constant crosshead displacement rate of 0.5 mm/min. A total of six categories of specimens were fabricated (see Figure 3-2). At least five rectangular specimens with dimensions of $190 \times 20 \text{ mm}^2$ were extracted from the fabricated

3D-FML plates of each category. A gauge length of 150 mm was set for the buckling experiments. The specimens were tested under fixed-fixed boundary conditions facilitated by special support-wedges as illustrated in Figure 3-3.

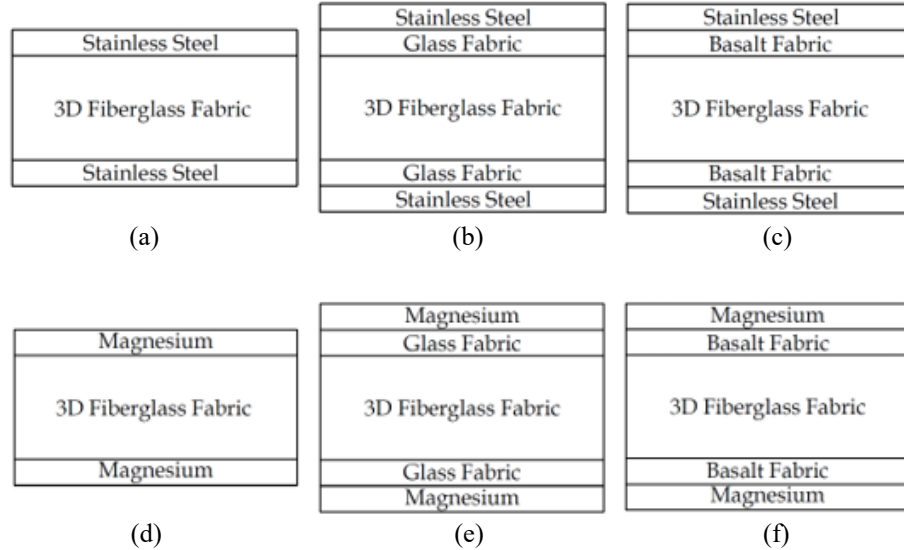


Figure 3-2. Various 3D-FMLs configurations considered in this study: (a) SS-3DFGF-SS, (b) SS-G-3DFGF-G-SS, (c) SS-B-3DFGF-B-SS, (d) Mg-3DFGF-Mg, (e) Mg-G-3DFGF-G-Mg and (f) Mg-B-3DFGF-B-Mg.

3.4. FE simulation Procedure

In this study, LS-DYNA, a commercial FE software, was utilized for two purposes; firstly, to model the 3D-FML specimens with the purpose of gaining a better understanding of the buckling and post-buckling responses of the 3D-FMLs. Secondly, to construct a robust numerical framework by which one could establish the buckling capacity and post-buckling behaviour of these complex hybrid material combinations in a reliable and efficient manner, especially when they are used in complex geometries and subjected to various and combined loading conditions. Therefore, first, a linear buckling (eigenvalue) analysis was conducted to evaluate the buckling capacity and first mode shape of the specimens in order to establish the integrity of the FE results against experimental results. Then, a series of nonlinear post-buckling analyses were carried out to ascertain the stability and post-buckling behaviour of 3D-FML specimens. Some of the earlier investigations employed different approaches using various elements such as solid, shell, T-shell, and combined shell and solid elements to conduct such an analysis. However, in this

investigation, a three-dimensional solid model is generated and used for the analysis. The 3D-FML specimen's model as shown in Figure 3-4, which is subjected to static axial compression load consisted of five main different components: (i) the SS or Mg sheets, (ii) the metal/3DFGF interface adhesive layers, (iii) the 3DFGF's upper and lower biaxial fabrics, (iv) the pillars (the threads connecting the biaxial fabrics of 3DFGF), and (v) the foam. In order to model the reinforced 3D-FML configuration, the basalt or glass fabric layers were added to the aforementioned components by appropriate layers of elements. The mechanical properties of each constituent used in the FE model are presented in Table 3-1.

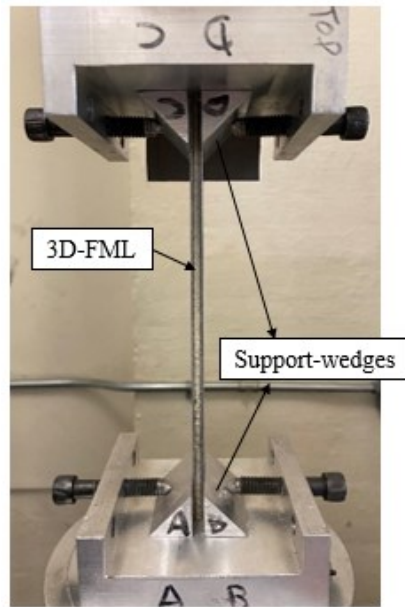


Figure 3-3. Buckling test setup.

The constituent materials forming the 3D-FML were modelled as follows: the Mg and SS layers were modelled with the piecewise linear plasticity material model (MAT_PIECEWISE_LINEAR_PLASTICITY). Both the strain-rate effect and yield stress (σ_{yield}) are considered in this material model. The interface metal/FRP adhesive layers were modelled as an elastic material (*MAT_ELASTIC). It is noted that the metal/FRP adhesive layers should ideally be modelled as a plastic material. The reason for adopting elastic materials instead of plastic ones in this study will be discussed in detail in section 3.5.3.1. The foam was also modelled as an elastic material but in conjunction with the erosion criterion (*MAT_ADD_EROSION), such that, if the foam becomes subjected to

extensive strain, the resulting failure could be captured by this option. In other words, once the defined failure criterion (ϵ_{max}) satisfied, the element would be deleted.

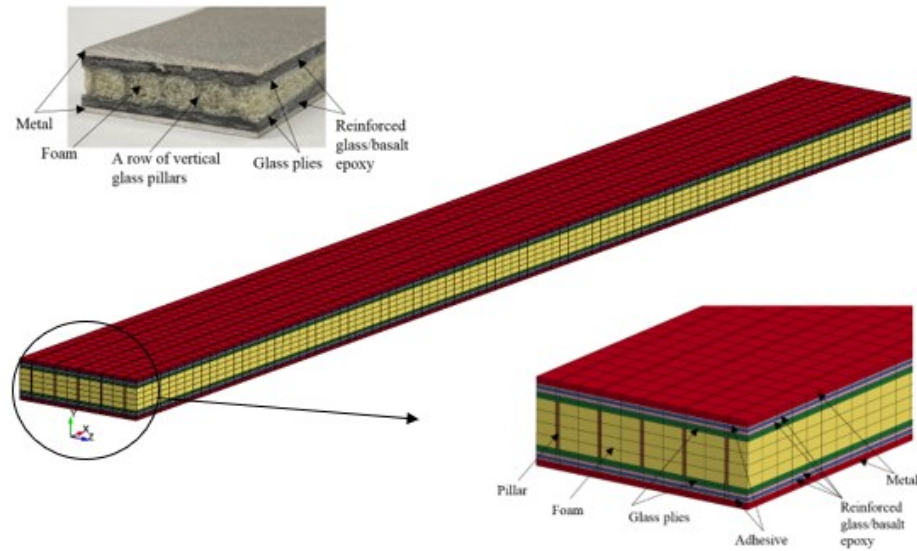


Figure 3-4. Finite element model of the 3D-FML.

The glass plies and pillars were modelled by LS-DYNA's composite damaged material model by incorporating the Chang-Chang failure criterion (*MAT_ENHANCED_COMPOSITE_DAMAGE). This failure criterion is capable of predicting matrix cracking, fiber-matrix cracking, and fiber breakage (Chang & Chang, 1987). Therefore, in this model, the strength properties (i.e., the longitudinal compressive/tensile strengths (X_C/X_T) and transverse compressive/tensile strengths (Y_C/Y_T) and in-plane shear strength (S_C)) are defined. It should be noted that since the glass pillars in the fabric are not oriented vertically, their actual approximately 30° inclination angle with respect to the vertical direction is modelled via the incorporated composite material model (MAT_054/055). Finally, the biaxial glass and basalt-reinforced plies were simulated by using the software's orthotropic composite material model (*MAT_ORTHOTROPIC_ELASTIC). A summary of the material keywords used in LS-DYNA is presented in Table 3-2.

Table 3-1. Material properties used in the finite element simulations.

Property	Mg (De Cicco & Taheri, 2018)	SS (De Cicco & Taheri, 2018)	2D- Glass- epoxy (Gupta et al., 2020)	2D- Basalt- epoxy (Gupta et al., 2020)	West System Epoxy	3DFGF (De Cicco & Taheri, 2018)		
						Glass epoxy-plies	Glass epoxy-pillars	Polyurethane foam
Thickness (mm)	0.50	0.48	0.45	0.55	0.10	0.45	0.35	3.4
ρ (Kg/m^3)	1740	8027	1805	1860	1180	1750	1750	128.1
E_{11} or E (GPa)	36.00	193.74	34.95	37.95	3.17	9.00	3.00	0.05
E_{22} (GPa)			10.93	9.82		9.00	1.00	
ν_{12}, ν_{13} or ν	0.35	0.29	0.27	0.30		0.05	0.05	0
ν_{23}			0.07	0.19				
G_{12}, G_{13} (GPa)			2.5	2.8		1.0	1.0	
G_{23} (GPa)			5.12	4.14		1.00	1.00	
ϵ_{max}								15%
σ_{yield} (GPa)	0.231	0.442						
S_C (GPa)						0.03	0.03	
X_C (GPa)						0.17	0.08	
X_T (GPa)						0.17	0.08	
Y_C (GPa)						0.17	0.08	
Y_T (GPa)						0.17	0.08	

The eight-node hexahedron solid element with reduced integration (ELFORM=1) was implemented for modelling all constituents of 3D-FML specimens. A convergence study was carried out to establish the mesh density that would produce accurate results with a reasonable CPU consumption. Therefore, the models associated with the 3D-FMLs and reinforced-3D-FMLs consisted of 22,800 and 25,650 elements, respectively. An earlier model constructed by the solid element produced the most accurate results; however, it consumed more CPU time compared to other models constructed by the shell and T-shell elements of LS-DYNA (De Cicco & Taheri, 2018).

Table 3-2. LS-DYNA material-related keywords used in the analyses.

Constituents	Material model in LS-DYNA
Magnesium/ Stainless steel	MAT_PIECEWISE_LINEAR_PLASTICITY/ MAT_024
Reinforced glass/ basalt epoxy	MAT_ORTHOTROPIC_ELASTIC/ MAT_002
Glass epoxy plies/ pillars	MAT_ENHANCED_COMPOSITE_DAMAGE/ MAT_054/055
Foam	MAT_ELASTIC/ MAT_001, MAT_ADD_EROSION/ MAT_000
Interface Epoxy resin	MAT_ELASTIC/ MAT_001

To mimic the boundary conditions imposed experimentally, all degrees of freedom (DOF) of the nodes forming one end of the specimens were restrained, while the nodes forming the other end were restrained in all directions but free to move axially. Moreover,

to mimic the applied restrains more accurately, the lateral movement (u_y) of the nodes of the elements falling within the grip regions (i.e., 20 mm from either end) at the grip interface (see Figure 3-3) was also restrained.

A displacement control algorithm with the arc-length method was implemented to run the implicit nonlinear buckling analysis utilizing the following keywords (CONTROL_IMPLICIT_SOLUTION; CONTROL_IMPLICIT_GENERAL; and CONTROL_IMPLICIT_DYNAMICS). To promote buckling, the model also included an initial imperfection in the form of a half-sine wave using the PERTURBATION keyword of LS-DYNA. The magnitude of imperfection amplitude and its wavelength were selected based on a given specimen thickness and feature, respectively, using several trial analyses.

3.5. Results and Discussion

3.5.1. Experimental Results

The evaluated elastic buckling capacities of the various configurations of SS- and Mg-based 3D-FMLs are reported in Figure 3-5. As expected, the 3D-FMLs reinforced by the 2D glass and basalt fabrics produced a higher gain in buckling capacity. Moreover, as also anticipated, the buckling capacity of SS-based 3D-FMLs is higher than that of the corresponding Mg-based 3D-FMLs, as the overall stiffness of the 3D-FMLs is a function of the stiffness values of its constituent, in particular the metallic sheets, which are arranged farthest away from specimens' neutral axis. As an example, the SS-3DFGF-SS configuration produced on average approximately 57% greater buckling capacity than the Mg-3DFGF-Mg configuration. Furthermore, when comparing the buckling capacities of glass-reinforced SS-based to Mg-based 3D-FMLs and also basalt-reinforced SS-based to Mg-based 3D-FMLs, the improvements in the buckling capacity are 26% and 17%, respectively. The results also reveal that the inclusion of a layer of basalt in SS-3DFGF-SS FML improved its capacity by 35% while an average improvement of 80% was exhibited by basalt-reinforced Mg-3DFGF-Mg configuration.

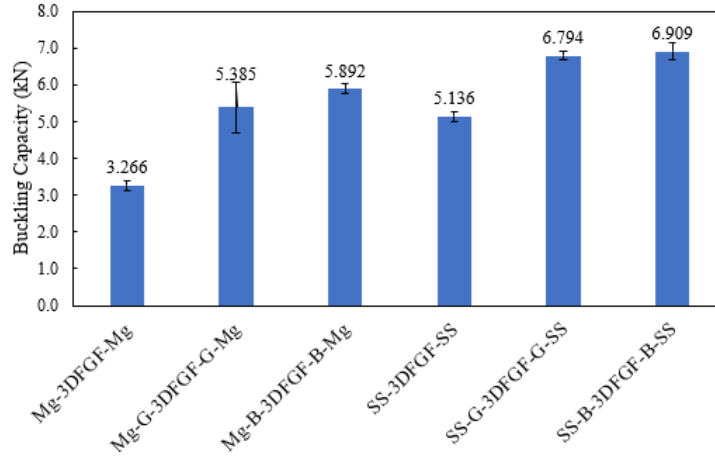


Figure 3-5. Buckling capacities of 3D-FML configurations.

As stated earlier, the choice of a given hybrid material in the industrial applications of interest to us (i.e., aerospace and automotive industries) would be strongly based on two important parameters: weight and cost. Therefore, the buckling capacities were normalized with respect to these two parameters. The buckling capacity results normalized with respect to weight are illustrated in Figure 3-6, revealing that the normalized buckling capacities of the 3D-FMLs reinforced by the biaxial fabrics are higher than that of the corresponding base 3D-FMLs. For instance, the normalized buckling capacity of the Mg-B-3DFGF-B-Mg configuration (see Figure 3-2 for the abbreviated specimen IDs) is 24% higher than the Mg-3DFGF-Mg configuration. In general, Mg-based specimens show greater relative buckling capacities (by at least 31%) compared to SS-based FMLs. It should be noted that the density of SS is approximately five times the density of Mg. It can be seen that among the SS-based 3D-FMLs considered here, the reinforced configurations would render more effective 3D-FMLs in mechanical applications where the weight governs the design selection. Moreover, it can also be observed that the normalized buckling capacities of the SS-based 3D-FMLs reinforced by either glass or basalt fabrics are essentially the same, a fact that also holds in the case of reinforced Mg-based 3D-FMLs.

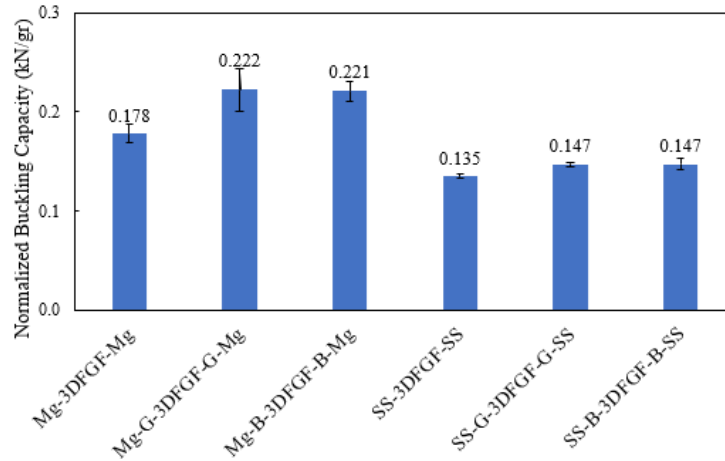


Figure 3-6. Comparison of the normalized buckling capacities (with respect to weight) of 3D-FML configurations.

The effect of cost on the buckling capacity of all six different specimens is demonstrated in Figure 3-7. Note that the normalization has been done purely based on materials costs. As can be seen, the normalized buckling capacities of SS-based 3D-FMLs are significantly higher than Mg-based 3D-FMLs. In fact, the SS-B-3DFGF-B-SS configuration exhibited the highest normalized buckling capacity, with an impressive 193% gain compared to the Mg-3DFGF-Mg configuration. Moreover, the normalized buckling capacity of the SS-3DFGF-SS configuration is almost 166% greater than the Mg-3DFGF-Mg configuration. Therefore, in applications where the cost would be the governing factor, then the SS-based 3D-FMLs would be the more desirable FML.

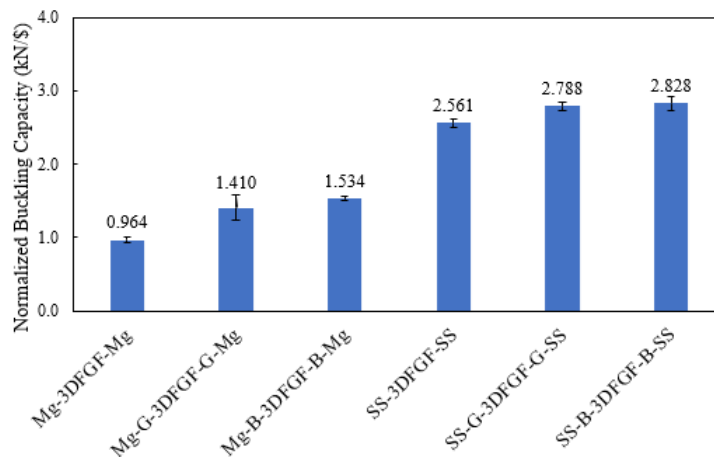


Figure 3-7. Comparison of the normalized buckling capacities (with respect to cost) of 3D-FML configurations.

A comparison of the normalized buckling capacity (with respect to stiffness) of the various configurations of steel- and Mg-based 3D-FMLs is shown in Figure 3-8. As it was stated earlier, one of our objectives was to determine whether by replacing Mg with SS, one could gain more buckling capacity since SS is approximately five times stiffer than Mg. Surprisingly, however, the results indicate that the capacity of the SS configuration would be dramatically reduced if the capacity is normalized with respect to the stiffness. This phenomenon is due to the onset of shear failure in the core (i.e., the thick layer of foam and glass pillars), which interrupted the harnessing of the added stiffness of SS sheets. Moreover, the failure modes of all tested configurations are displayed in Figure 3-9. Two different failure modes could be observed from the results: (i) delamination buckling failure mode, which caused debonding of metal/FRP interface as seen in Figure 3-9(d), and (ii) shear crimping mode, a critical failure mode, which occurred near the restrained regions (grip) as can be observed in Figure 3-9(a-c) and Figure 3-9(e-f). Core shear crimping is classified as an instability buckling mode associated with cores with low shear modulus, which results in the development of excessive shear deformation as opposed to rotation (Coburn & Weaver, 2016).

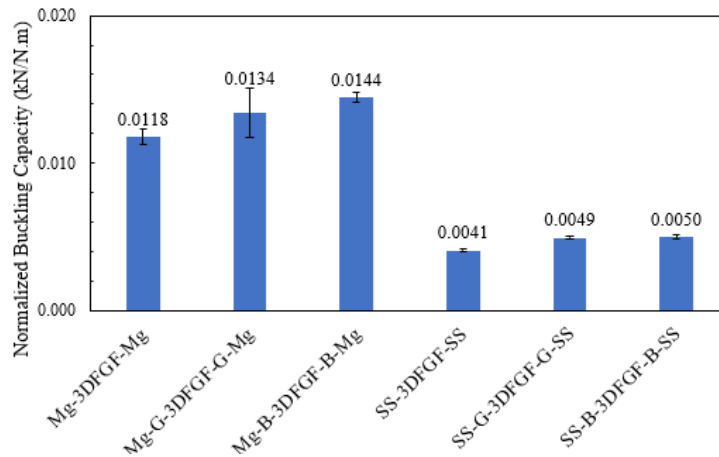


Figure 3-8. Comparison of the normalized buckling capacities (with respect to stiffness) of 3D-FML configurations.

3.5.2. Comparison of the Experimental and Numerical Results

In order to establish the optimal mesh density, a mesh convergence study was performed on the Mg-3DFGF-Mg configuration by changing the mesh density within the plane and through the thickness of the model. The results of the convergence study are

shown in Figure 3-10. The optimal mesh was established by the mesh density that produced a peak load value that did not vary compared to the load produced by a slightly coarser mesh density that was used for the analysis in a previous step of the convergence study. Based on the results presented in this figure, the converged mesh density is a mesh configured with a total of 22800 elements, beyond which no significant variation in the capacity could be observed.

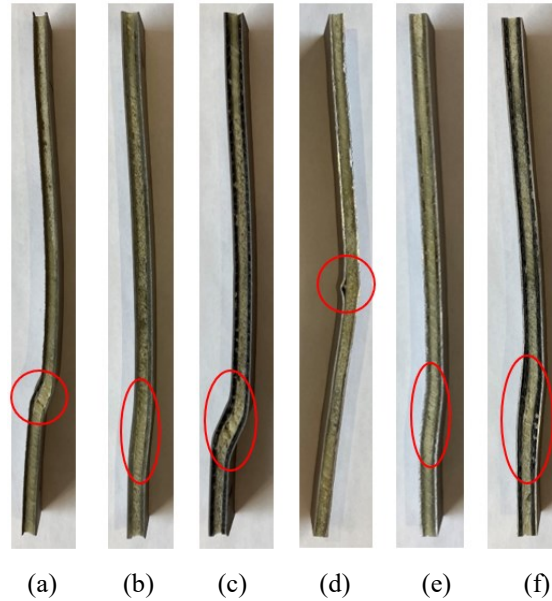


Figure 3-9. Buckling failure modes (a) SS-3DFGF-SS, (b) SS-G-3DFGF-G-SS, (c) SS-B-3DFGF-B-SS, (d) Mg-3DFGF-Mg, (e) Mg-G-3DFGF-G-Mg and (f) Mg-B-3DFGF-B-Mg.

It should be noted that, unlike the conventional metallic test specimens that usually do have some forms of geometric imperfections but are not easily visible by the naked eye, the sandwich hybrid composite specimens considered in this study have invariably relatively large out-of-plane imperfection mode-shape, visually notable. Such an inherent imperfection could stem from a number of factors such as (i) due to the residual stresses-created by the sandblasting process, which in turn creates a slight curvature in the metal sheets (mainly, due to the very thin nature of the sheets); (ii) slight misalignments induced in the fibers of 3DFGF during the hot curing process; and (iii) the potential initial misalignments of the fixing jigs and testing machine grips. Given the fact that there would be some inevitable degree of imperfection in each specimen, to establish the most appropriate amplitude of imperfection that has to be included in any such nonlinear

numerical analysis to promote the instability of the model, analyses with imperfection amplitudes in the range of 0.05 mm to 1.95 mm (0.91 % to 35.45 % of the thickness, respectively) were attempted for the Mg-3DFGF-Mg configuration to establish the influence of the imperfection amplitude on the predicted buckling capacity by the numerical analysis.

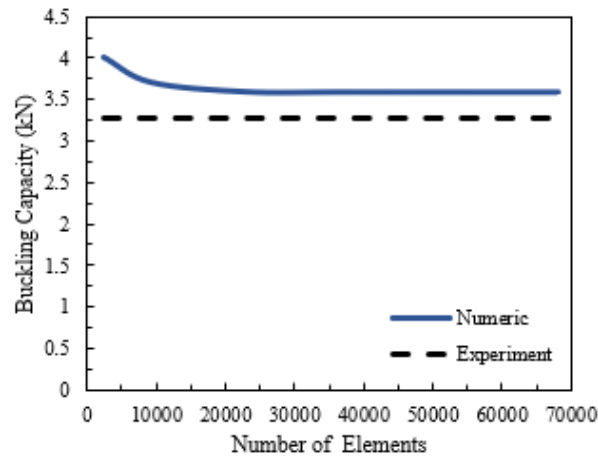


Figure 3-10. Mesh convergence analysis of FE model for Mg-3DFGF-Mg configuration.

Table 3-3. Influence of initial imperfection on the buckling capacity of Mg-3DFGF-Mg calculated numerically and the error margin with respect to the average experimental results.

Imperfection amplitude (mm)	Buckling capacity (kN)	Error (%)
0.05	4.368	33.7
0.15	4.294	31.5
0.25	4.168	27.6
0.35	4.017	23.0
0.55	3.855	18.0
0.95	3.602	10.3
1.45	3.326	1.8
1.95	3.161	-3.2

Table 3-3 illustrates the results of the imperfection amplitude study. Based on the reported results, an imperfection amplitude of 0.95 mm (17.27% of thickness) was selected. This value produced a capacity that corroborated reasonably well with the average experimental capacity. It should be also noted, although the imperfection amplitude of 1.45 mm (26.36% of thickness) produced a lower margin of error compared to the selected imperfection amplitude, nonetheless, that value was not selected. There are two primary reasons for this selection (i) we are interested in predicting the response of the hybrid composites over the entire loading regime (i.e., pre- and more importantly, post-buckling

responses), and (ii) most finite element models are known to exhibit a so-called “stiffer” response than the actual article. Therefore, in order to have consistent results, the selected percent imperfection amplitude was used in all other analyses.

In order to establish the integrity of the FEM simulation framework, the numerical results are compared against typical experimentally obtained curves for both SS-3DFGF-SS and Mg-3DFGF-Mg 3D-FMLs as illustrated in Figure 3-11. As can be seen, all specimens endured the applied load until the load reached a critical limit causing their instability (buckling), leading to delamination failure mode in Mg-3DFGF-Mg configuration and shear crimping in SS-3DFGF-SS configuration. After this stage, the specimens could endure some of the load, though undergoing increasing axial shortening. Once the axial shortening reached a critical value, the capacities decreased drastically due to the total failure and crushing of the specimen.

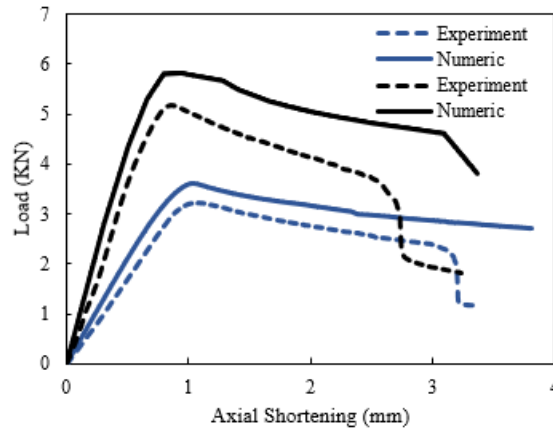


Figure 3-11. Comparison of the numerical and experimental load-axial shortening curves of the SS-3DFGF-SS (black line) and Mg-3DFGF-Mg (blue line) configurations tested under compressive loading.

As can also be seen, the numerical results are in good agreement with the experimental results and could effectively predict the pre- and post-buckling behaviours of the 3D-FMLs; however, as it is typical to most FE predictions, the numerical results are stiffer than the experimental results. Consequently, to account for this discrepancy, the FE model was calibrated in such a way that the numerical simulation-produced results would closely match the experimental results. Based on the results, the buckling capacities in experimental results for Mg-3DFGF-Mg and SS-3DFGF-SS configurations are 10.3 % and

13.4% lower than numerical results. Besides, the experimental results show that the buckling capacity-

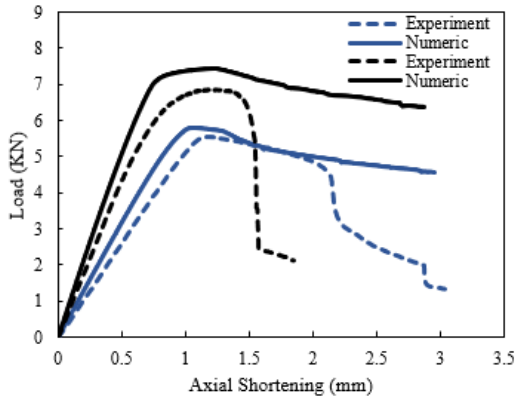


Figure 3-12. Comparison of the numerical and experimental load-axial shortening curves of the SS-G-3DFGF-G-SS (black line) and Mg-G-3DFGF-G-Mg (blue line) configurations tested under compressive loading.

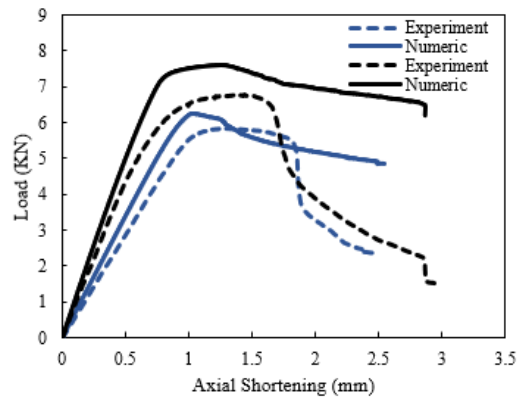


Figure 3-13. Comparison of the numerical and experimental load-axial shortening curves of the SS-B-3DFGF-B-SS (black line) and Mg-B-3DFGF-B-Mg (blue line) configurations tested under compressive loading.

of the SS-3DFGF-SS configuration is higher than the Mg-3DFGF-Mg configuration and this was corroborated with the outcome of the FE simulation as well. The reasons believed to have caused these discrepancies will be discussed in detail in the following section.

The numerical and experimental results for SS-G-3DFGF-G-SS and Mg-G-3DFGF-G-Mg configurations are compared in Figure 3-12. The results reveal that by reinforcing the 3D-FML with 2D glass fabric, which increases the overall stiffness and thickness of the specimen, the specimen endures more load until shear crimping occurs. However, as was seen in the previous figure, the axial shortening curves do not suddenly drop after the occurrence of this failure mode, and the 3D-FML endures the applied load, exhibiting a non-catastrophic failure response. The differences in the buckling capacities predicted numerically and those exhibited experimentally for Mg-G-3DFGF-G-Mg and SS-G-3DFGF-G-SS configurations are 8% and 9.5%, respectively. The axial load versus in-plane displacement relationships are also compared for SS-B-3DFGF-B-SS and Mg-B-3DFGF-B-Mg 3D-FMLs in Figure 3-13. The results indicate that the pre-and post-buckling behaviours of basalt-reinforced specimens are similar to those of glass-reinforced ones and that they also experience shear failure. The buckling capacities of SS-B-3DFGF-B-SS and Mg-B-3DFGF-B-Mg 3D-FMLs obtained numerically are slightly more than the

experimental results (i.e., by 10.3% and 6.2%, respectively). Additionally, the FE results corroborate the experimental findings by revealing that replacing Mg sheets with SS sheets resulted in an increase in buckling capacity. The summary of the numerical and experimental results for the various configurations of 3D-FMLs investigated in this study is tabulated in Table 3-4.

Table 3-4. Comparison of the buckling capacity results (kN) obtained numerically and experimentally.

Samples	Experiment	Numeric	Error (%)
Mg-3DFGF-Mg	3.266	3.602	10.3
Mg-G-3DFGF-G-Mg	5.385	5.815	8.0
Mg-B-3DFGF-B-Mg	5.892	6.259	6.2
SS-3DFGF-SS	5.136	5.826	13.4
SS-G-3DFGF-G-SS	6.794	7.440	9.5
SS-B-3DFGF-B-SS	6.909	7.623	10.3

As briefly mentioned earlier, the slopes of load-axial shortening curves obtained numerically shown in Figure 3-11 to Figure 3-13, which indicate the average extensional stiffness of the specimens, are slightly higher than those produced by the experimental results. The following fabrication-related reasons, which could not be accounted for in the FE models at this time, are believed to have caused the numerical discrepancies: (i) the existence of voids within the composite system; (ii) fiber misalignment; (iii) potentially incomplete matrix cure; (iv) the potential delamination occurring due to the stress concentrations caused by the grips, and finally (v) the fact that the glass pillars have an intricate figure-8 type orientation with a 30° to inclination (with respect to through-thickness direction). It can be appreciated that the simulation of the complex figure-8 type distribution of the pillars would be formidable. Therefore, the through-thickness stiffness produced by the actual pillars would be softer than modelled numerically.

Figure 3-14 exhibits a typical buckling failure mode for SS-B-3DFGF-B-SS configuration as predicted numerically and observed experimentally. As can be seen, the numerical prediction, which corroborates with the experimentally observed result, illustrates a shear crimping failure mode causing the final instability of the specimen. Furthermore, the robust FE model produced in LS-DYNA is capable of deleting the elements in the core region affected by excessive shear-induced stresses. This was achieved by modelling the foam using the combined MAT_ELASTIC and MAT_ADD_EROSION models of the software.

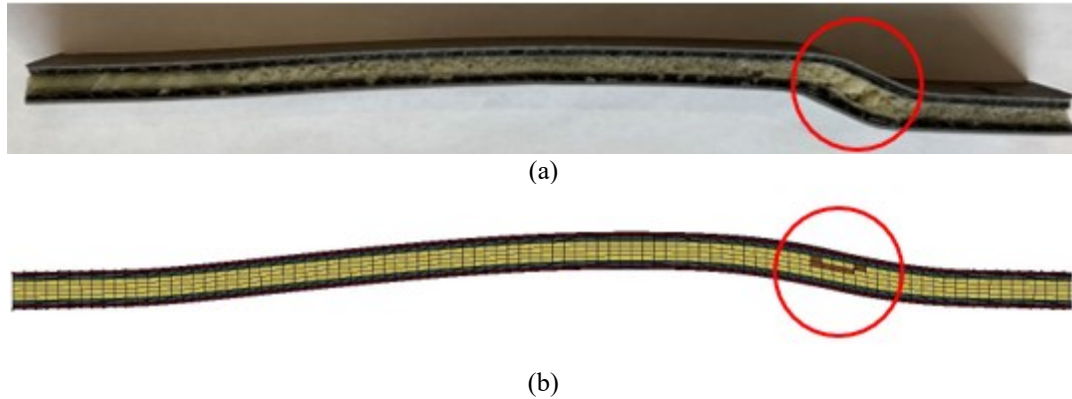


Figure 3-14. Deformed shapes and core failure of SS-B-3DFGF-B-SS (a) Experiment and (b) FE simulation.

Moreover, as stated earlier, it was decided to model the metal/FRP interface epoxy by the elastic material model based on the following findings. Initially, the epoxy adhesive layers were modelled with MAT_PLASTICITY_POLYMER (MAT_089) by considering the actual elastic-plastic stress-strain response of the epoxy. Note that the aforementioned model is suitable for modelling materials that do not exhibit a distinct change from elastic to plastic responses in their stress-strain curve. Figure 3-15 illustrates the responses of Mg-3DFGF-Mg and SS-3DFGF-SS configurations simulated with elastic and plastic material models. As can be seen, there is almost no difference (less than 0.1%) between the results produced by the material models. Therefore, to achieve optimal CPU run time, the elastic material model (MAT_ELASTIC) was adopted in all configurations modelled in this study.

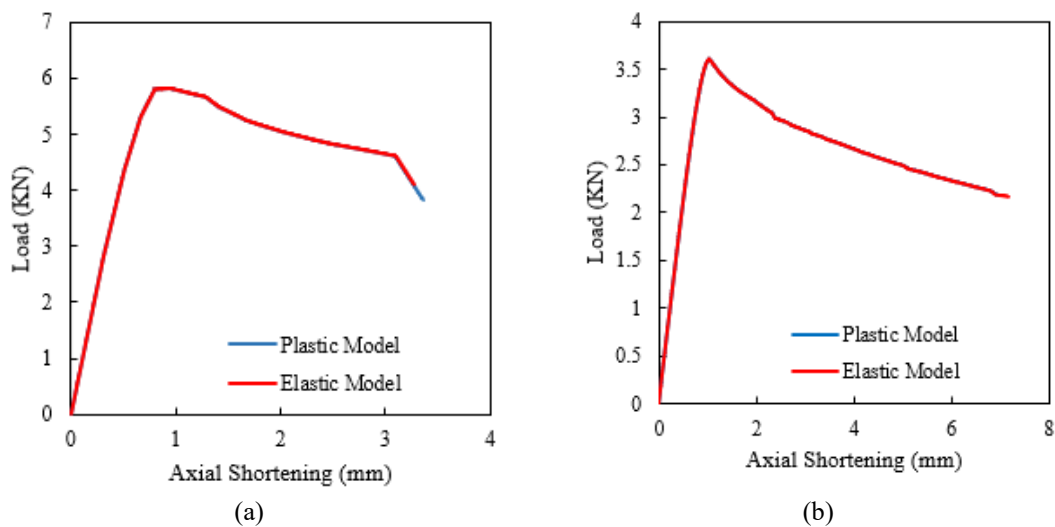


Figure 3-15. Comparison of load-axial shortening curves based on modelling of metal/FRP interface resin with elastic and plastic material models (a) Mg-3DFGF-Mg and (b) SS-3DFGF-SS.

3.5.3. Parametric Studies

After the validation of the FE framework with the experimental results, the influences of fiber orientation and fiber hybridization on the buckling capacity of some 3D-FMLs are examined.

3.5.3.1. Effect of Fiber Orientation

A series of parametric numerical simulations were conducted to investigate the effects of different fiber orientations on the buckling response of 3D-FMLs. The effects of fiber orientation on the pre- and post-buckling behaviours of both SS-G-3DFGF-G-SS and SS-B-3DFGF-B-SS configurations were examined by incorporation of three different ply fiber orientations of (0/90), (± 30) and (± 45) with the outcomes illustrated in Figure 3-17. As can be seen, (± 45) orientation produces the least buckling capacity due to its lowest axial-bending stiffness in comparison to (± 30) and (0/90) fiber orientations. The buckling capacity of SS-G-3DFGF-G-SS configuration increased by 3.8% and 5.6% for 3D-FMLs with (± 30) and (0/90) orientations compared with (± 45) FML, respectively, while the gains were 4.5% and 6.1%, respectively for the SS-B-3DFGF-B-SS configuration.

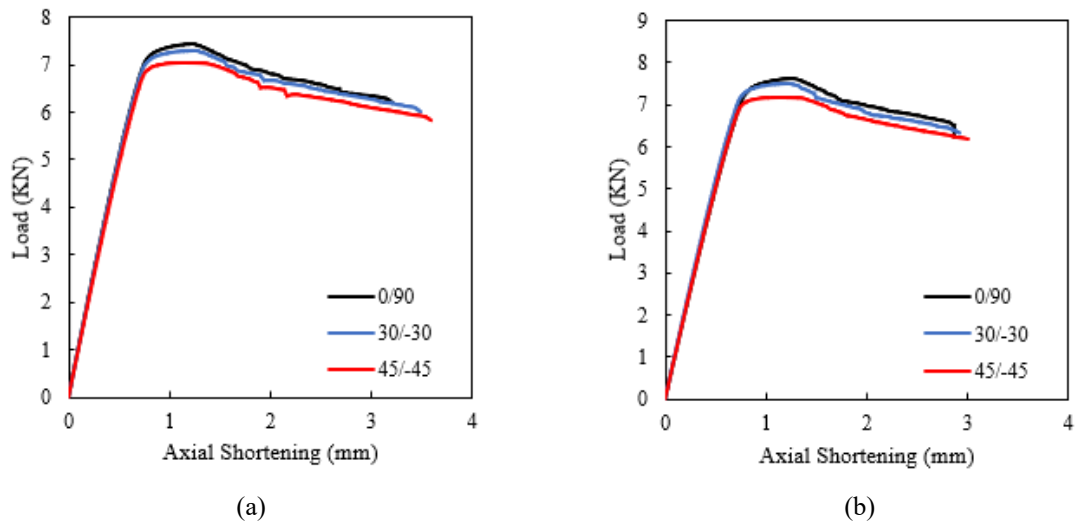


Figure 3-16. Effects of fiber orientation on the buckling behaviour of (a) SS-G-3DFGF-G-SS and (b) SS-B-3DFGF-B-SS.

3.5.3.2. Effect of Glass and Basalt Fiber Hybridization

The effects of fiber hybridization on the load-axial shortening curves of SS- and Mg-based 3D-FMLs are presented in Figure 3-17. It can be observed from the results that fiber hybridization has a significant positive effect on the buckling capacity of Mg-G-3DFGF-G-Mg and SS-G-3DFGF-G-SS configurations. In other words, the buckling capacity of hybridized 3D-FML (i.e., Mg-B-G-3DFGF-G-B-Mg configuration), is approximately 41.1% higher than the unhybridized (Mg-G-3DFGF-G-Mg) configuration, while the gain is 28.7% when comparing SS-B-G-3DFGF-G-B-SS and SS-G-3DFGF-G-SS configurations. Therefore, it can be concluded that the effect of fiber hybridization on the buckling capacity of Mg-based 3D-FML is higher than SS-based 3D-FML, which is attributed to the inherently lower stiffness of Mg alloy. As can be seen in Table 3-1, Young's modulus of SS is much higher than Young's modulus values of basalt-epoxy and glass-epoxy reinforcements; consequently, the hybridization imposes a greater effect on Mg-based FML compared to SS-based FML. Moreover, the gain in the capacity of the SS-B-G-3DFGF-G-B-SS configuration is only 17% higher than the Mg-B-G-3DFGF-G-B-Mg configuration.

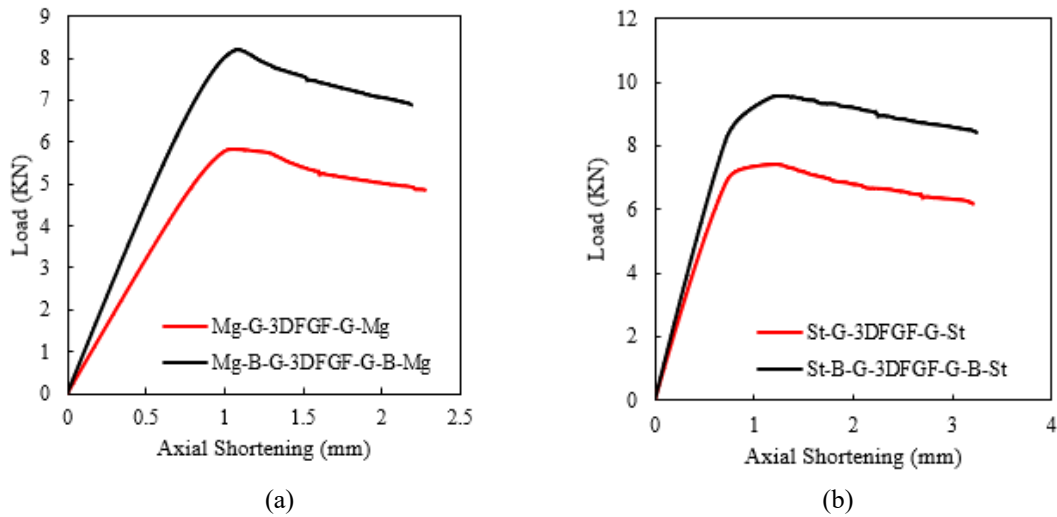


Figure 3-17. Effects of fiber hybridization on the buckling behaviour of (a) Mg-G-3DFGF-G-Mg and (b) SS-G-3DFGF-G-SS.

3.6. Summary and Conclusion

In this study, a comprehensive series of experimental and numerical investigations were conducted to gain a better understanding of the buckling and post-buckling responses of SS- and Mg-based 3D-FMLs possessing different configurations. By analyzing the experimental data, it was found that the SS-B-3DFGF-B-SS configuration exhibited the highest buckling capacity and normalized buckling capacity with respect to materials costs. In terms of weight, the relatively much higher density of SS is considered as a downside of this alloy comparatively, which constraints the utilization of thicker SS in fabricating 3D-FMLs. Interestingly, although the density of SS is almost five times greater than Mg, the SS-B-3DFGF-B-SS configuration just demonstrated 17% less buckling capacity with respect to weight in comparison with the Mg-3DFGF-Mg configuration. Moreover, ironically, despite the relatively much greater stiffness of SS compared to Mg, SS-based 3D-FML exhibited less normalized buckling capacity with respect to stiffness when compared with Mg-based 3D-FML. However, this is postulated to be due to the relatively low stiffness of the foam/pillar core constituents of the FMLs. Therefore, a future study should experimentally clarify the admissibility of this postulation and provide a practical and cost-effective resolution, so that one could take full advantage of the added stiffness of stainless steel.

In general, the comparison of the results produced in this study should encourage designers to select appropriate 3D-FML based on the intended application (i.e., whether the weight or/and material cost are the design constraints). As an important conclusion of this study, it is believed that the SS-B-3DFGF-B-SS configuration could be considered the most optimal 3D-FML among all the configurations examined in this study. This configuration exhibited the highest buckling capacity, and the highest normalized buckling capacity with respect to cost, and the use of basalt fiber as an eco-friendly fiber should also make this configuration more attractive.

The load-axial shortening curves obtained from the numerical simulations showed a good correlation with the experimental results and thus confirming the effectiveness of the present FE modelling framework. The results produced a maximum error of 13.4% which is attributed to fabrication-related anomalies that could not be accounted for in the

simulations at this juncture. Moreover, the results showed that in all 3D-FMLs considered in this study, except, in the case of Mg-3DFGF-Mg configuration, the shear failure mode developed in the foam/pillar core region was the prevailing failure mode instead of the conventional Euler buckling mode.

As briefly stated above, in our future work, we will be attempting to overcome the issue encountered by the SS-based 3D-FMLs. In other words, attempts will be made to improve the strength of the core portion of the FMLs in order to mitigate the premature shear failure observed in this study. A more robust FE simulation framework is currently under development with the aim of generating a more time-efficient model that would produce results with acceptable accuracy.

Chapter 4: Strength and Failure Mechanism of Single-Lap Magnesium-Basalt Fiber Metal Laminate Adhesively Bonded Joints: Experimental and Numerical Assessments

Fatemeh Mottaghian, Farid Taheri

Published in the Journal of Composites Materials, Volume 56(12), PP 1941-1955, 2022.

This paper has been partially modified compared to its original published version to conform to the format of this thesis and to reduce the repetition of topics covered in Chapter 2.

4.1. Abstract

A quick literature search reveals a significant lack of data and information concerning magnesium-to-magnesium bonded joints as well as fiber metal laminates (FMLs) made with magnesium alloys. Therefore, a systematic series of experimental and numerical investigations are carried out to assess the performance of single-lap joints mating FML adherends. The primary goal is to better understand the effects of geometrical and material parameters that influence the performance of magnesium-to-magnesium joints. The FML adherends used in this study consist of basalt natural fiber-epoxy laminate sandwiched in between thin sheets of magnesium alloys, which were subsequently adhesively bonded using a room-cured epoxy resin. The effects of two types of surface treatments, namely “sandblasting” and “sandblasting with resin coating” on the bond strength and failure mechanism of the adhesively bonded joints (ABJs) are investigated. A 3D numerical model was developed to simulate the response of the joints subjected to quasi-static lap shear tests. This model, which accounts for the material and geometrical nonlinearity in the joints, is used to perform a parametric analysis for establishing the optimal overlap bond length. The distributions of the shear and peel stresses in the overlap region and the effects of adhesive thickness on the performance of the joints are systematically examined. The comparison of the experimental data and numerical results confirms the robustness and cost-effectiveness of the numerical model in predicting the response of such single-lap ABJs.

4.2. Introduction

[...] *Some portions of this section have been removed and included in Chapter 2.*

As stated earlier, the lack of research on ABJs joining FMLs in general and joints mating Mg-based FMLs in particular, and the low volume of the currently available relevant database indicate that more investigation is required to better understand the response of FML-ABJs and enhance their performance under different loading conditions. Accordingly, the primary objective of this study is to evaluate the performance of magnesium-basalt (MB)-FML SLJs subjected to quasi-static tensile loading. As stated, this study was motivated due to the lack of research in joining this class of FMLs, especially the fact that Mg requires a completely different surface preparation process compared to other widely used metal counterparts (e.g., Al and steel). As mentioned earlier, surface treatment has a significant influence on the bond strength of ABJs, regardless of the strength of the adhesive selected for a given application. However, one of the issues encountered when using the conventional surface treatments technique on Mg alloys is the requirement for the immediate bonding of the treated surfaces. This may not be deemed practical in most industries. Furthermore, most of the available relevant studies have considered SLJs made of Al, steel, and FRPs adherends; therefore, there is a clear need for characterizing the response of Mg-SLJ under various loading conditions.

It should be noted that compared to other commonly used metallic alloys, Mg alloys are lighter (e.g., 75% lighter than steel, 50% lighter than titanium, and 35% lighter than aluminum), consequently, the weight of Mg alloy structural components is comparable to that of FRPs. High strength-to-weight ratio and improved electromagnetic shielding capability are also among other advantages of Mg alloys. Based on a technical report of automobile mass-reduction technology delivered by Lutsey (2010) the cost of Mg alloys is approximately 20% higher than Al ones. However, despite the higher material costs associated with moving toward more mass-optimized metals and nonmetals, their potential for net component cost improvements leads to considering them as a promising alternative to advance their application in industries.

Cortés & Cantwell (2004) were among the first researchers who studied the fracture properties of Mg-CFRP-FML. They demonstrated that the tensile strengths of Mg-FMLs were higher than that of 2024-T0 Al-FMLs. They also concluded that the comparatively lower elastic modulus and fracture characteristics of Mg-FMLs could be diminished by choosing a suitable volume proportion of the FRPs. In another study, Cortés & Cantwell (2005) also investigated the responses of FMLs made of Mg alloys, glass-FRP, and CFRP subjected to fatigue and LVI loading states and compared their performance against Al-FMLs. The highlight of this research was the indication of the superior corrosion resistance of Mg-FML, which appears to be contradictory compared to other investigators' findings on the performance of Mg alloys in moist environments. Pärnänen et al., (2012) analyzed the LVI performance of Mg-FML in comparison with GLARE. The results indicated that the energy absorption capacity of Mg-FML was approximately equal to GLARE, however, the first-cracking load was considerably lower in the Mg-based FML. Vasumathi & Murali (2013) studied the behaviour of jute/carbon Mg-FML and jute/carbon Al-FML subjected to tensile, flexure, and impact loadings conditions. Interestingly, the bending, tensile strengths, and stiffnesses of both FMLs found to be almost similar to the Al-FML by showing only between 10-15 % superiority.

Moreover, there has been a significant thrust in recent years for the implementation of low-cost, eco-friendly, sustainable, and lightweight natural fibers as an alternative to conventionally used fibers such as glass, carbon, and aramid (Vasumathi & Murali, 2013). The superior performance of basalt fiber-reinforced composites as a relatively low-cost and effective class of composite material has been demonstrated by Mottaghian et al. (2020). Besides their lower cost and superior mechanical properties, basalt fibers also offer several advantages such as being environmentally sustainable, excellent adhesion properties to resins, good resistance against fire and wear, and remarkable heat/sound insulation properties (Mottaghian et al., 2020; Yaghoobi et al., 2021a). The abovementioned facts further justify the necessity for research in joining such robust, effective, and economical hybrid materials. Therefore, this research evaluates the effects of a series of important parameters that affect the performance and strength of single-lap ABJs mating MB-FMLs. The parameters investigated include (i) two types of surface treatments, (ii) overlap length, and (iii) adhesive layer thickness. The failure mechanism of the SLJs is investigated by

utilizing the “sandblasting” and “sandblasting with resin coating” surface treatment methods. Moreover, an FE model is developed in the LS-DYNA environment by which the variations in the stress distributions in the overlap region in SLJs and bond strength of SLJs with different overlap lengths and adhesive thicknesses, are systematically evaluated and compared. The numerical framework accounts for the material and geometrical nonlinearities.

4.3. Experimental Investigation

4.3.1. Materials

The MB-FML consists of Mg alloy sheets, basalt fabrics, and a room-cured epoxy resin. AZ31B–H24 Mg sheets with 0.5 mm thickness were purchased from MetalMart (Commerce, CA, US). The (0/90) bidirectional stitched basalt fabric with a thickness of 0.55 mm and an areal density of 450 g/m² was obtained from the GBF basalt fiber Co., Ltd (China). Moreover, the room-cured structural epoxy system (West System 105 resin and 206 slow hardener) was acquired locally.

4.3.2. Fabrication Procedure and Configuration of the Joints

4.3.2.1. MB-FML Fabrication

MB-FML Specimen preparation began with the fabrication of its FRP core constituent by preparing the basalt-epoxy laminate panels using the vacuum-assisted resin infusion (VARI) technique (Kazemi et al., 2019). The reinforcing basalt fabrics with [0/90]_{2s} layup were covered with peel-ply and resin distribution mesh. The system was sealed in a vacuum bag and monitored for a leakage test for 20 mins. Then, the room-cured epoxy resin and hardener were mixed with a weight ratio of 5:1 and infused into the dry fabrics, and let cured at ambient temperature under vacuum for 48 hrs. In the next step, the cured basalt-epoxy laminate panels (see Appendix B for a detailed fabrication process) were sandwiched in between two pre-treated Mg sheets, which will be thoroughly described in section 4.3.2.3, using the same resin system, which was brushed onto the mating surfaces.

Subsequently, the assembly was sealed by the vacuum bagging process and allowed to cure at ambient temperature for 48 hrs, as per the manufacturer's recommendation.

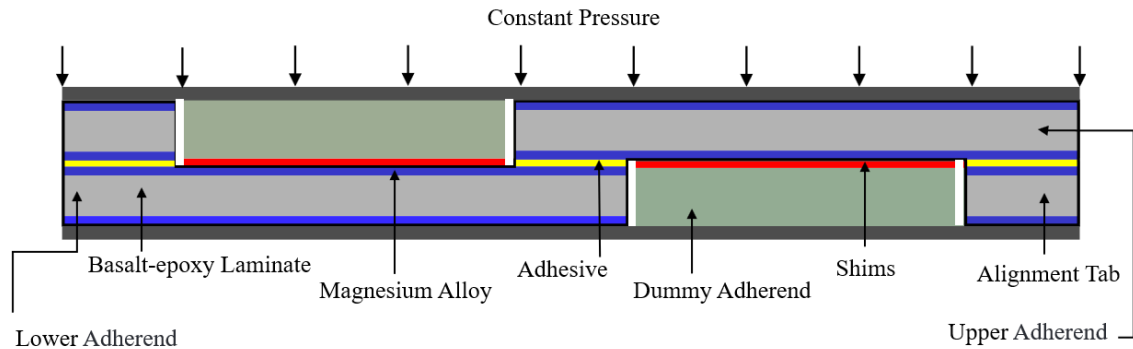


Figure 4-1. Schematic of the fabrication scheme used to produce the single-lap MB-FML ABJs.

4.3.2.2. SLJs Fabrication

Fabrication of SLJs commenced by extracting the appropriate size upper and lower substrate plates from the mother MB-FML panels. Since as stated the thickness of adhesive in the overlap bonded regions plays an important role in the performance of SLJs, special adjustable fabrication jigs, and procedures were adopted to facilitate the fabrication process and to ensure consistency and geometric precision of the fabricated SLJs. The schematic shown in Figure 4-1 provides a visual perspective of the fabrication setup. The area of the overlap was marked, and then the mating regions were wiped clean with acetone and left to fully air dry. To control the desired adhesive thickness, dummy adherends were prepared and placed below the upper adherend as well as on top of the lower adherend in the joint assembly, and then shims were positioned over and under the dummy adherends, respectively. The room-cured adhesive was brushed onto the bonding regions and the upper and lower adherends were bonded together. Subsequently, to eliminate the eccentricity in the loading path, each adherend was bonded to its corresponding alignment tab by the room-cured epoxy resin. In the next step, constant pressure was applied to the upper surface of the assembly area to ensure the appropriate bonding, as per the manufacturer's recommendation. The resulting excess adhesive seepage was cleaned by a slender wooden stick to finalize the joints with 90° fillets. Afterward, the entire system was allowed to cure at ambient temperature for 48 hrs. Next, the SLJ specimens, with appropriate dimensions

as based on ASTM D5868-01(2005) and ASTM D1002-10 (2021), were extracted from the bonded plates using a water-cooled diamond saw (see Figure 4-2).

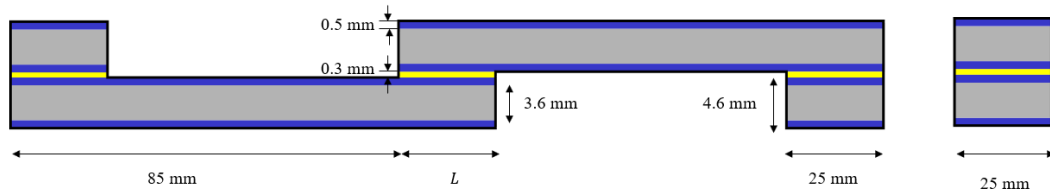


Figure 4-2. Schematic and dimensions of single-lap MB-FML ABJs.

4.3.2.3. Surface Treatment

As mentioned previously, surface preparation plays a significant role in the bond strength of ABJs. Therefore, two surface treatment approaches (namely “sandblasting” and “sandblasting with resin coating” (De Cicco & Taheri, 2019) are explored in this study. The two approaches are referred to as the “S” and hybrid “H” methods, hereafter.

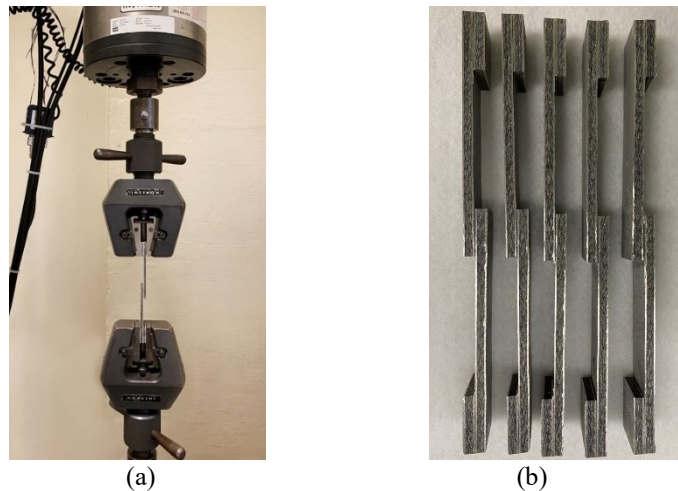


Figure 4-3. (a) lap-shear test setup, (b) MB-FML SLJ specimens.

The “S” approach commenced with cleaning the Mg sheets with acetone to remove any residual protective grease. The Mg sheets were subsequently sandblasted with 20-30 grit crushed glass to roughen the surfaces and promote better adhesion of the adhesive. Incidentally, both surfaces of each Mg sheet had to be sandblasted to avoid any resulting residual stress and slight curvature that would be resulted otherwise if only one of the

surfaces in such thin sheets is sandblasted. Next, the sandblasted sheets were cleaned with compressed air and then wiped with acetone to remove any potential impurities and residues left from sandblasting.

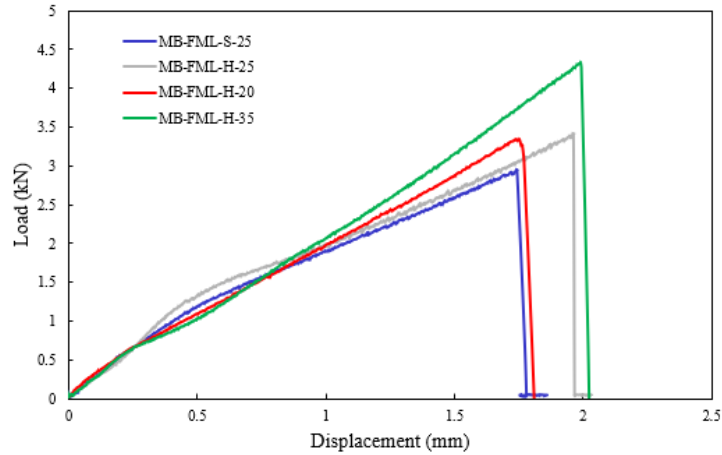


Figure 4-4. Load-displacement responses of the single-lap MB-FML ABJs.

In the “H” surface modification approach, after carrying out the above procedure, a thin layer of room-cured resin was applied on the surfaces of the Mg sheets. Subsequently, the coated surfaces were covered with a layer of porous peel-ply and breather cloth. The thicknesses of the nylon peel-ply and the polyester breather cloth are 0.1016 and 3 mm, respectively. The assembly was then placed inside a vacuum bag and left to cure at the ambient temperature for 48 hrs. It should be noted that in this method, the peel ply leaves a rough resin impression on the coated surface, thereby promoting a more effective adhesion (De Cicco & Taheri, 2019). The other advantages of this approach which is also a very elaborate and complex surface preparation method have been detailed in (De Cicco & Taheri, 2019). It should be noted that as stated, the effectiveness of the hybrid surface treatment in reference to Mg-to-glass epoxy bonding was examined in one of earlier studies (De Cicco & Taheri, 2019); however, the integrity of this technique would have to be examined and verified for Mg-to-Mg bonding, which is one of the objectives of the present work.

4.3.3. Test Setup

In this study, the quasi-static single-lap shear tests were conducted using an MTS servo-hydraulic universal testing machine equipped with a FlexTest-40 controller and a

250 kN Instron load cell. To have accurate experimental results, based on Figure 4-2, at least five specimens were organized in each group, which were tested at a constant crosshead displacement rate of 1.27 mm/min as per ASTM D1002-10 (2005). The quasi-static shear-lap setup and the single-lap Mg-FML specimens are illustrated in Figure 4-3.

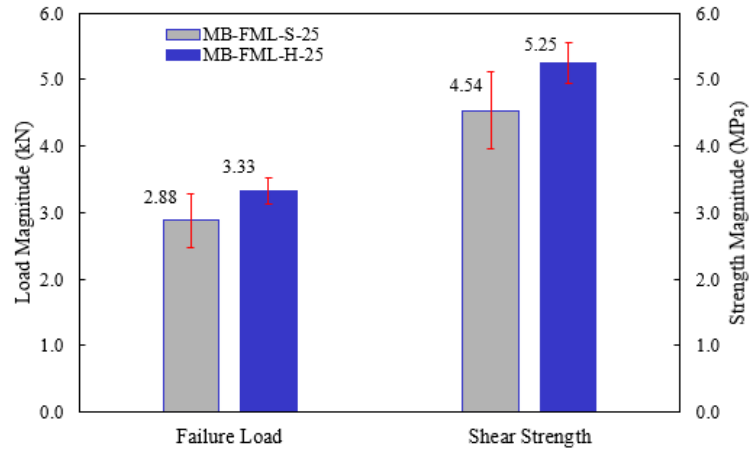


Figure 4-5. Experimentally obtained average failure load and shear strength of MB-FML-S-25 and MB-FML-H-25 group of specimens.

4.4. Results and Discussion

4.4.1. Experimental Results

4.4.1.1. Effects of Surface Treatment on the Bond Strength of SLJs

As mentioned previously, two types of surface treatments were considered to prepare the surfaces of the metal sheets for bonding with the aim of attaining more effective bonding conditions. The specifics of the surface preparation methods were outlined in section 4.3.2.3. Identification and compositions of the groups of single-lap MB-FML ABJs fabricated in this study are reported in Table 4-1. The first two parts of the specimen IDs are self-explanatory; the third part refers to the adopted surface treatment method (i.e., (S) for sandblasting and (H) for hybrid) and the last numerical part denotes the overlap length of the joint in the unit of mm.

The load-displacement responses of the group of specimens subjected to the single-lap shear tests are exhibited in Figure 4-4. The average failure loads of MB-FML-S-25 and MB-FML-H-25 groups were determined to be 2.88 and 3.33 kN, respectively, rendering a

15.6% gain in the ultimate capacity in joints prepared with the hybrid surface treatment. Note that specimens with an overlap of 25 mm in Figure 4-4 were fabricated based on ASTM D5868-01 (2005) and ASTM D1002-10 (2021), and the specimens with overlaps of 20 mm and 35 mm were fabricated based on the numerical results carried out in this study, which will be thoroughly discussed in section 4.4.2.1. The average shear strength of the specimens was obtained using the simple mechanics of materials approach with the following equation:

$$\tau = \frac{F}{L \times w} \quad (4-1)$$

where F , τ , w , L denote failure load, average shear strength, joint width, and overlap length, respectively. Figure 4-5 shows the average failure loads and the maximum shear stresses of the single-lap MB-FML ABJs fabricated with sandblasting and hybrid surface treatments and their standard deviations. As can be seen, the hybrid surface treatment improved the average shear strength of bonded joints by 15.7%. When adhesive is applied on treated surfaces, the adhesive fills the cavities that were created on the surfaces, forming finger-like connections on the irregular topography created on the adherend surfaces once the adhesive is cured (Baldan, 2012). This phenomenon, described as mechanical interlocking, is primarily affected by the roughness and porosity of the treated surfaces. Based on the results illustrated in Figure 4-4 and Figure 4-5, it can be concluded that the generated mechanical interlocking worked more effectively in the SLJs group of specimens fabricated with the hybrid (H) surface preparation technique. This technique is believed to generate greater surface roughness, thus, enhancing the strength of the single-lap MB-FML ABJs. This adopted method is simple and cost-effective, and in contrast to the conventional sandblasting method; it would also inhibit the oxidation and corrosion of Mg sheets. Consequently, there would be no urgency to immediately follow the surface preparation with the bonding process, which would be necessary otherwise. Therefore, this flexible surface preparation method was adopted for fabricating the remaining ABJs used in this study.

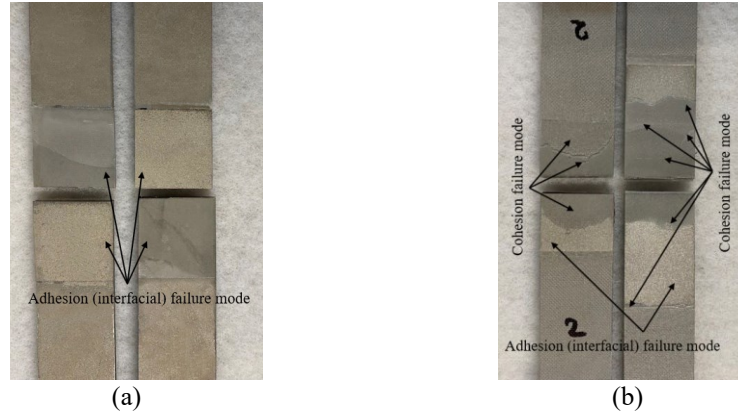


Figure 4-6. The fracture surfaces of the single-lap MB-FML ABJs (a) adhesion, and (b) cohesion failure modes.

4.4.1.2. The Failure Mechanism of SLJs

The failure mode of a given ABJ is considered to be an indicator of adhesion quality and joint strength. In general, failure modes in ABJs are classified into four categories. First is the cohesion mode, which is the most desired failure mode in which the failure occurs in the layer of the adhesive itself. The next mode, or the adhesion (or interfacial) mode, signifies the failure of the adherend/adhesive interface. This type of failure is believed to occur due to inadequate surface treatment and lack of interlocking between the adherend and adhesive. There would also be the mixed cohesion/adhesion mode, which often occurs when the overlap region experiences a relatively large rotation (due to the developed bending moment). Finally, there would be the adherend mode, which is characterized by failure of the adherend(s) instead of the adhesive (Correia et al., 2018). Since the adherends are offset in SLJs and the force path is nonconcentric, a bending moment is developed consequently (Duncan, 2010). This could also occur due to the relative flexibility of the overlap region in such slender systems when tabs are used to minimize the load (Jairaja & Naik, 2019). The resulting overlap rotation due to the developed bending moment is a function of the adherends and adhesive thickness, the distance between the alignment adherends and overlap region, leading to the development of peel and shear stress concentrations near the ends of the overlap region (Guo et al., 2006). Consequently, the damage is usually initiated at the ends of the overlap region, subsequently propagating, and causing the failure of SLJs. As seen in Figure 4-6(a), in MB-FML-S-25, the crack developed at the end of the overlap region and then propagated

toward the mid-span of the region. This crack propagation subsequently resulted in debonding of the adhesive/Mg alloy interface. As seen in the figure, a layer of adhesive remains on one of the bonding surfaces of one of the adherends. Nevertheless, the mixed cohesion/adhesion mode exhibited in Figure 4-6(b) was the predominant failure mode in the overlap region of the remaining ABJs tested in this study. Conforming to the self-explanatory failure mode's name, thin patches of adhesive can be seen on both metal interfaces, indicating the failure plane passed through the adhesive in that region. However, the other portion of the overlap region experienced decohesion of the adhesive from one of the adherends. As can also be discerned, there is no rough resin impression on the failure adhesive regions, indicating the failure did not occur between the coating and adhesive, hence, it is a cohesion failure. The transition from the adhesion (or interfacial) mode of failure to the mixed cohesion/adhesion debonding mode indicates that the hybrid method of surface treatment (e.g., sandblasting with resin coating) was more effective compared to sandblasting in boosting the surface roughness and improving the bond strength. A summary of the surface treatments and failure modes of different groups of specimens is presented in Table 4-1.

Table 4-1. Categories of the fabricated single-lap MB-FML ABJ specimens.

Samples ID	Surface Treatment	Overlap Length (mm)	Failure Mode
MB-FML-S-25	Sandblasting	25	Adhesion
MB-FML-H-25	Sandblasting + Resin Coating	25	Adhesion + Cohesion
MB-FML-H-20	Sandblasting + Resin Coating	20	Adhesion + Cohesion
MB-FML-H-35	Sandblasting + Resin Coating	35	Adhesion + Cohesion

4.4.2. Numerical Investigation and Results

In this study, the commercial FE software LS-DYNA was utilized to model the response of the single-lap MB-FML ABJs subjected to the quasi-static tensile loading state. Constructing a reliable and robust numerical model can assist one to predict the performance of the ABJs subjected to different loading conditions and facilitate the analysis of complex stress distribution within the adhesive layer. An implicit nonlinear FE analysis was conducted to establish the joint's behaviour, accounting for both the geometrical and material nonlinearities of the joints. The model consists of three components (i) the Mg alloy sheets, (ii) the basalt-epoxy laminate layers, and (iii) the

overlap's adhesive layers. Figure 4-7 illustrates the single-lap MB-FML ABJs, in which all the constituents are meshed with the eight-node hexahedron fully integrated solid element with selective reduced integration points (ELFORM = 2) of LS-DYNA. Note that ELFORM= 3 is also a fully integrated formulation; however, the element is more CPU-intensive. ELFORM=2 uses full integration scheme when used with certain material models (including composite material model 54. Therefore, the less CPU-intensive element (i.e., ELFORM=2) was used in this study. Coarser mesh densities were adopted to model the portions of the adherends away from the overlap region, especially near the ends of the region where stress gradients rapidly change. In other words, the mesh density was gradually refined as one nears the edges of the overlap region, which are necessary to capture the rapidly changing stress gradients and produce accurate numerical results. To mimic the boundary conditions in the gripped regions (within 25 mm at either end), all degrees of freedom (DOF) of the nodes located at one gripped end of the specimens were fully restrained. On the other gripped end, all the degrees of freedom of the nodes except those corresponding to the axial movement (u_x) were also restrained. The displacement-controlled algorithm was employed to simulate the experimentally imposed axial quasi-static movement (loading) in this nonlinear implicit analysis.

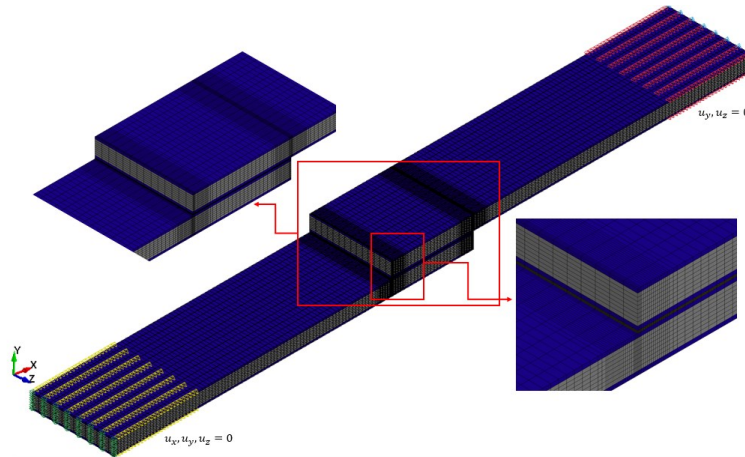


Figure 4-7. Details of the FE model of the single-lap MB-FML ABJ and the boundary conditions.

As for modelling the materials' responses, the Mg alloy sheets were modelled using the piece-wise plastic material model of LS-DYNA, which considers both the strain-rate effect and the actual stress-strain curve of the material up to its ultimate stress (σ_u). In this study, for instance, the stress-strain curve (Figure 4-8(a)) was defined using 101 stress-

strain values taken along the curve. Note that this material model is not able to capture the post-ultimate stress (the declining portion of stress-strain response). The basalt-epoxy laminate was modelled as a linear orthotropic material, and the adhesive layer was modeled also as a plastic material using the polymer plasticity model of the code. The nonlinear responses of both materials were modelled using their actual stress-strain responses. Note that the polymer plasticity model used in LS-DYNA for modelling the adhesive layer is capable of simulating materials that do not exhibit a distinct change from elastic to plastic responses in their stress-strain curve, whereas the piecewise model could contain a linear-elastic region. The mechanical properties, as well as the material keywords utilized in LS-DYNA to simulate the constituents of single-lap MB-FML ABJs are tabulated in Table 4-2 and Table 4-3, respectively. Also, note that the plasticity models use the engineering stress-strain responses of Mg alloy and adhesive utilized in the FE model are illustrated in Figure 4-8.

Table 4-2. Mechanical properties of the materials used in the FE model (Mohamed, 2020; Mottaghian et al., 2020; Yaghoobi et al., 2021a).

property	Thickness (mm)	ρ (Kg/m^3)	E_{11} (GPa)	E_{22} (GPa)	ν_{12}	ν_{13}	ν_{23}	G_{12} (GPa)	G_{13} (GPa)	G_{23} (GPa)	σ_{yield} (GPa)	σ_u (GPa)
Basalt-epoxy	0.45	1860	37.95	9.82	0.3	0.3	0.19	2.80	2.80	4.14		
Mg alloy	0.50	1740	36.00								0.23	0.34
Adhesive	0.30	1180	3.17									0.05

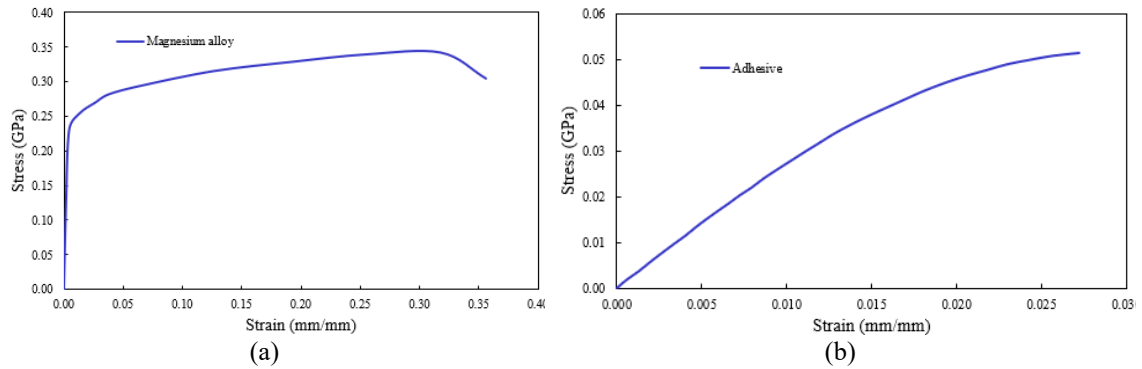


Figure 4-8. Stress-strain responses of (a) Mg alloy, and (b) adhesive utilized in the FE model.

In the first step of the numerical analysis, a mesh convergence study was conducted on the MB-FML-H-25 group of specimens to establish the integrity of the modelling framework. The number of elements in the overlap region, through-the-thickness of FML and adhesive interface layer, and within the plane of the FE model were changed

successively. Moreover, the ultimate capacity of the joint was selected as the convergence criterion by comparing the FE-produced capacity with that evaluated experimentally. Consequently, as exhibited in Figure 4-9, the optimized mesh configuration is achieved by 28,630 solid elements with 35,072 nodes beyond which no significant improvement in accuracy could be obtained. A comparison between the numerical results of SLJs modelled with and without consideration of the tabs was carried out. The difference in the failure load in both linear and nonlinear analyses was found to be 1.04% and 0.75%, respectively. It was also found that the same magnitude of bending moment was generated in the models with and without tabs. Therefore, for the sake of computational efficiency, the model without tabs was considered in this study as opted by other researchers as well (Durmuş & Akpınar, 2020; Jairaja & Naik, 2019). The ultimate strength of joints in this study refers to the resulting strength at the stage when the maximum shear stress in the overlap region exceeds the ultimate shear strength of the adhesive. The numerically obtained failure load for MB-FML-H-25 SLJ is reported as 3.41 kN. The good agreement in the numerical and experimental results and the associated difference of 2.4% confirms the integrity of the FE model.

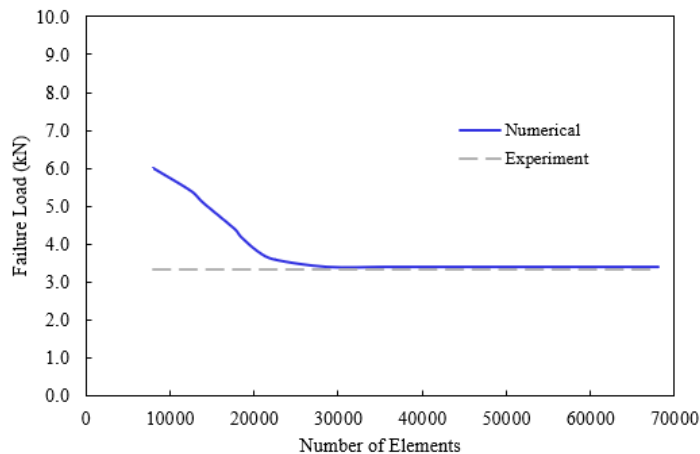


Figure 4-9. Details of the FE model of the single-lap MB-FML ABJ and the boundary conditions.

Table 4-3. LS-DYNA Material models utilized in constructing the FE model.

Constituent	Material Model
Mg alloy	*PIECEWISE_LINEAR_PLASTICITY (MAT_024)
Basalt-epoxy	*MAT_ORTHOTROPIC_ELASTIC (MAT_002)
Adhesive	*MAT_PLASTICITY_POLYMER (MAT_089)

4.4.2.1. Optimized Overlap Length

As stated earlier, an ABJ's performance is affected by parameters such as the thickness and stiffness of its adhesive and adherends, overlap length, as well as spew fillet angle. Among all the aforementioned parameters, the overlap length is believed to have a significant influence on the performance and bond strength (Anyfantis, 2012). However, a longer overlap length does not translate into more capacity. Therefore, a parametric study was conducted to numerically establish the optimal performance of the single-lap MB-FML ABJs based on the resulting joint capacity. For that, 10 different overlap lengths were considered as the initial parameter. The ultimate load capacity produced by the different lengths is illustrated in Figure 4-10. The results indicate that an overlap length of 35 mm would produce the optimal joint capacity beyond which no significant gain in capacity would be obtained. The transition in the overlap length from 35 mm to 5 mm would result in a 74% decrease in the joint capacity.

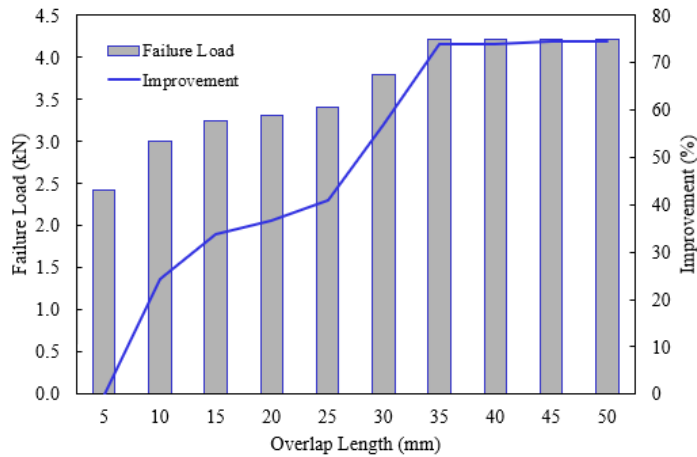


Figure 4-10. Effects of overlap length on the failure load of single-lap MB-FML ABJs.

To further explore the integrity of the developed FE framework, a joint with a mid-range overlap length of 20 mm (i.e., MB-FML-H-20) was fabricated and tested. The joint's performance was compared against the other joints, including the joint with the optimal overlap length of 35 mm (i.e., MB-FML-H-35). The experimentally obtained load-displacement responses of the two joints are shown in Figure 4-4. As can be seen, the capacity of the MB-FML-H-35 is 29.7% and 25.8% higher than the capacities of MB-FML-H-20 and MB-FML-H-25, respectively. Furthermore, the experimental and numerical joint capacities of the referenced ABJs are also tabulated in Table 4-4. One can

see that the results produced by the developed FE model are in excellent agreement with the numerical results with low error margins varying between 1.4% for MB-FML-H-35 to 2.5% for MB-FML-H-20 groups of specimens. Therefore, the FE model is capable of effectively predicting the response of the MB-FML SLJs. Also, the numerical load-displacement response of the joint with the optimal overlap length (i.e., MB-FML-H-35) is compared to the experimental data and shown in Figure 4-11, which further reveals the integrity of the developed FE models.

Table 4-4. Comparison of the experimental and numerical failure loads of single-lap MB-FML ABJs.

Specimens ID	Overlap Length (mm)	Exp. Failure Load (kN)	Num. Failure load (kN)	Failure load ratio (Exp /Num)	Error (%)
MB-FML-H-20	20	3.23	3.31	0.976	2.5
MB-FML-H-25	25	3.33	3.41	0.977	2.4
MB-FML-H-35	35	4.19	4.25	0.986	1.4

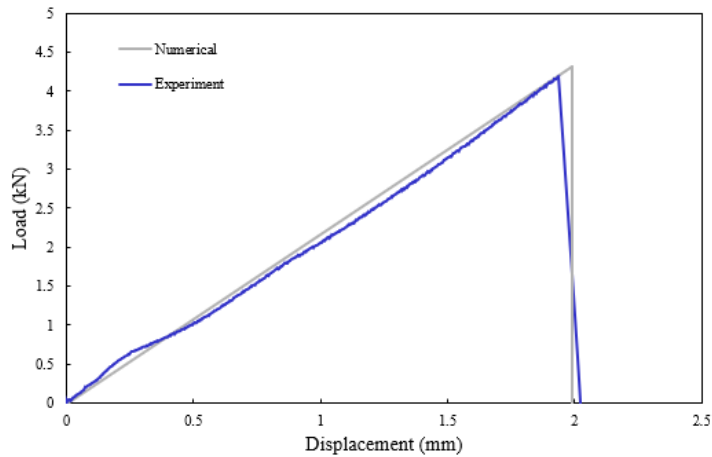


Figure 4-11. Comparison of the numerical and experimental load-displacement responses of MB-FML-H-35 group of specimens.

4.4.2.2. Stress Distribution in the Adhesive

As briefly stated earlier, the resulting nonlinear response of SLJ results in the development of a bending moment in the overlap region and consequently leads to the development of the peel and shear stresses. The stresses in the ABJs are transferred from one adherend to the other one through the adhesive layer. Therefore, to gain a better understanding of the performance of single-lap MB-FML ABJs subjected to a tensile loading state, a more detailed stress analysis of the adhesive layer is carried out in this

section. Figure 4-12 demonstrates the adhesive peel (σ_y) and shear (τ_{xy}) stress distributions along the overlap region in joints with different overlap lengths. Note that the stress distribution is evaluated under an applied tensile load of 2 kN for all joints. As can be seen, both the peel and shear stress distributions are symmetrical about the overlaps' midspan, and their magnitudes are maximized at the free edges of the adhesive layers, particularly where a crack(s) would be initiated and propagated (Anyfantis & Tsouvalis, 2013c). By increasing the overlap length, the peel and shear stresses' peaks decrease and relatively more uniform stress distribution along the overlap is achieved. In joints with longer overlap lengths, the stresses in the middle of the overlap region are relatively small. In other words, in the optimized group of specimens (MB-FML-H-35) a relatively long and stable plateau is obtained which separates the stress distribution at the free edges and middle of the overlap length (Al-Ramahi et al., 2018). Clearly, the elongation of the overlap region beyond a certain length results in the reduction of both shear and peel stresses concentrations at the free edges and consequently leads to the enhancement of the ultimate load-bearing capacity (Wei et al., 2018). However, the rate of reduction in the stresses is not constant and it essentially changes slightly in the joints with longer overlap lengths, indicating that from an economical perspective, the bond length should be elongated to a certain length. This phenomenon is also supported by the results discussed in the previous section. Moreover, overlap length has a more noticeable effect on the shear stress (its concentration near the free edges) in comparison to its effect on the peel stress. The relatively lower and negative values of peel stress, which denotes the existence of normal compressive stress (which is in favourable this case), are observed along a large portion of the overlap region (Anyfantis & Tsouvalis, 2013a).

The distributions of the peel, and shear (τ_{xy} and τ_{zy}) and von Mises (σ_v) stresses along the overlap length and across the width of the adhesive layer in the MB-FML-H-35 specimen are presented in Figure 3-13. Note that the stresses are sampled at the maximum load of the mentioned joint. As can be seen, with the exception of shear stress (τ_{zy}) distribution, which is asymmetrically distributed, and all the other stresses are symmetrically distributed with respect to longitudinal and transverse directions. The asymmetric distribution is due to the asymmetrical nature of SLJs geometry. Furthermore,

the maximum shear stress (τ_{xy}) exhibited in Figure 3-13(a) is equal to the ultimate shear strength of the adhesive (i.e., 25 MPa); however, the peel stress remains significantly lower than the adhesive's ultimate tensile strength of 50 MPa. This implies that the high shear stress developed at the free edges of the overlap region would initiate the failure of the joint; consequently, the SLJ failure mode is shear-governed. The magnitude of shear stress (τ_{zy}) remains at very low levels both along the length and across the width of the overlap and stays just in the elastic region; therefore, it does not contribute to the failure of SLJs significantly. Based on the results presented in Figure 3-13(b), it can be concluded that the peak magnitudes of the peel, shear (τ_{xy}), and von Mises stress, are reached across the width in the region slightly away from the edges, diminishing in regions close to width-free edges. However, in the case of shear stress (τ_{zy}), its maximum and minimum magnitudes occur near the left and the right free edge across the overlap width, respectively, nullifying the mid-width of the region. As can be seen, the differences between the maximum and minimum values of three of the four illustrated stresses are not significant.

4.4.2.3. Effects of Adhesive Thickness on the Bond Strength of SLJs

Adhesive thickness is considered one of the primary parameters governing the response of SLJs. To further understand the response of single-lap MB-FML ABJs subjected to a tensile loading state, an attempt was made to numerically assess the effects of adhesive layer thicknesses on the load-bearing capacity of the SLJ. For this, the maximum load, as well as the ultimate shear strength (based on Eq.(4-1)) of SLJs with an overlap length of 35 mm, are assessed and reported in Table 4-5. As can be seen, by increasing the adhesive thickness from 0.1 mm to 0.4 mm, the ultimate capacity of the joints increases from 2.91 kN to 4.56 kN, respectively. In other words, the failure load of an MB-FML SLJ with a thickness of 0.4 mm would be 56.7% higher than that of the joint with 0.1 mm thick adhesive. The incremental increase in the adhesive thickness in the selected range results in decreasing the shear stress concentration, thereby leading to a stronger joint. However, there is a threshold for the thickness after which no improvement in strength would result by increasing the adhesive's thickness. Indeed, the increase in the thickness beyond the threshold reduced the load-bearing capacity slightly (by 1.1% and

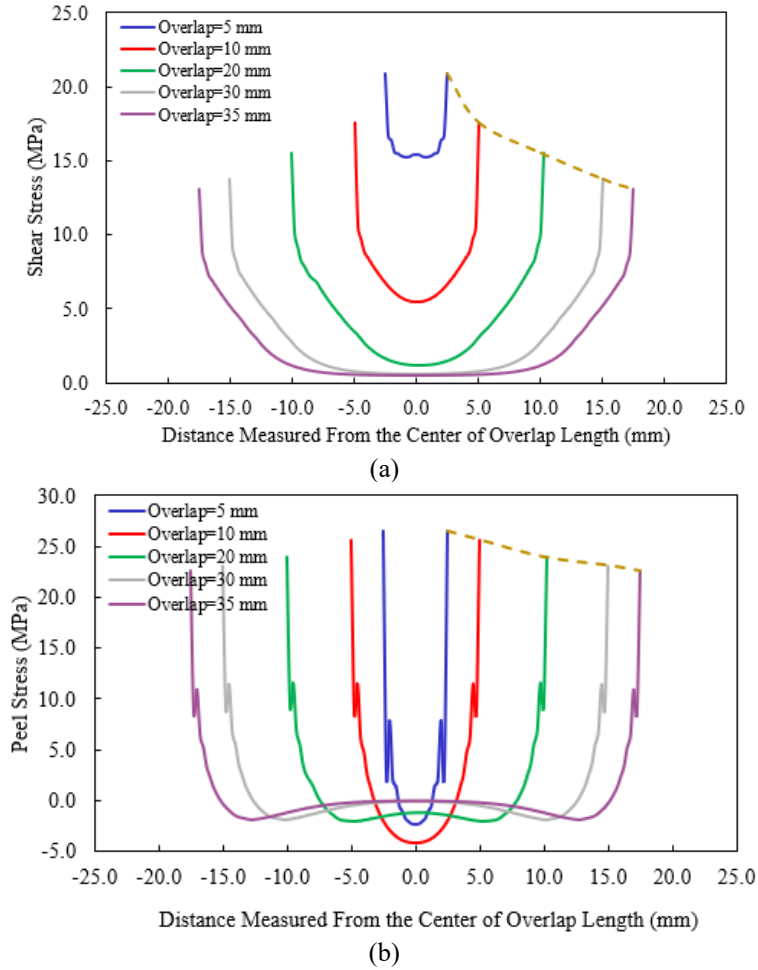
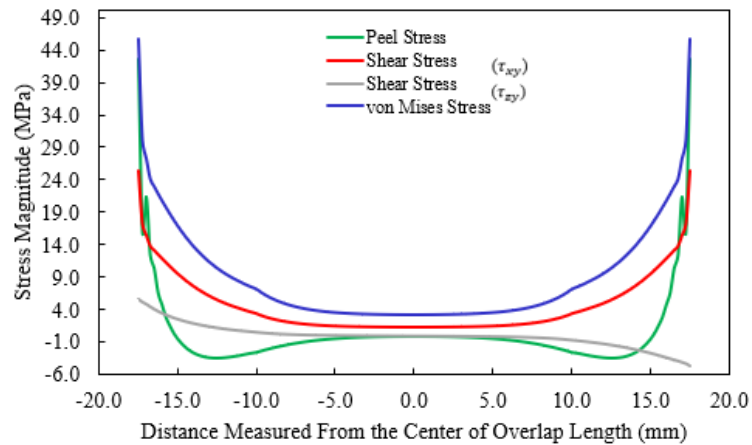


Figure 4-12. Effects of overlap length on the distribution of (a) shear and (b) peel stresses.

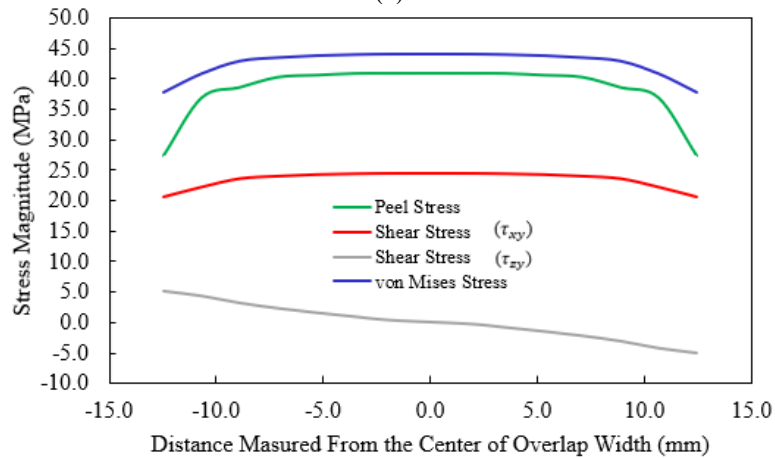
2.2% corresponding to the thicknesses of 0.5 mm and 0.6 mm, respectively, in comparison to the joint with a thickness of 0.4 mm). The phenomenon corroborates with the observation made by other researchers (Huang et al., 2021) who demonstrated an optimal adhesive thickness of 0.5 mm of their investigated SLJ, beyond which the load-bearing capacity of SLJ was decreased. Moreover, the maximum shear strength in the joint with the optimal adhesive thickness is 5.21 MPa, revealing a 56.7% improvement in comparison to the base group of specimens (e.g., the SLJ with 0.1 mm thickness). After this step, further increases in the adhesive thicknesses result in diminishing the shear strength.

Table 4-5. Effects of adhesive thickness on the failure load and shear strength of single-lap MB-FML ABJs with 35 mm overlap.

Adhesive Thickness (mm)	Num. Failure Load (kN)	Num. Shear Strength (MPa)	Improvement (%)
0.1	2.91	3.33	0.0
0.2	3.47	3.97	19.2
0.3	4.21	4.81	44.7
0.4	4.56	5.21	56.7
0.5	4.51	5.15	55.0
0.6	4.46	5.10	53.3



(a)



(b)

Figure 4-13. Stress distributions (a) along the length, (b) across the width of the overlap in the MB-FML-H-35 group of specimens.

4.5. Summary and Conclusion

This study was initiated in response to the clear lack of information on the adhesively bonded joints with an Mg-to-Mg interface. In this study, a series of systematic experimental

and numerical analyses were carried out to investigate the performance of a single-lap adhesively bonded joint made of fiber-metal laminates consisting of basalt-epoxy laminate and Mg alloy (MB-FML ABJs). The combination of the materials results in the formation of significantly lightweight and cost-effective structural components that are highly desirable. The effects of two surface treatment methods (i.e., “sandblasting” and “sandblasting with resin coating” denoted as the hybrid approach) on the ultimate load-bearing capacity as well as the average shear and tensile strengths of single-lap MB-FML ABJs were investigated. Subsequently, the optimal overlap length of the SLJ was numerically established. The distribution of the stresses in the adhesive layers along and across the overlap length and width, respectively, was evaluated for SLJs with different overlap lengths. The important observations made in this study are highlighted as follows:

- The simple and cost-effective hybrid surface treatment method adopted in this study was demonstrated to be more effective in enhancing the response of the single-lap MB-FML ABJs than surface preparation by sandblasting. This method is also more in line with the industry-standard practice of mechanical abrasion and chemical surface treatment. The joint prepared with the hybrid surface preparation technique resulted in a 15.6% and 15.7% improvement in average load capacity and shear strength, respectively, compared to the joints prepared with the conventional sandblasting surface preparation method. Moreover, the failure mechanism of SLJs transitioned from the adhesion (or interfacial) mode to a mixture of adhesion and cohesion mode by using the more effective surface preparation technique.
- The robust nonlinear FE framework constructed in the LS-DYNA environment produced results with excellent correlation with the experimental results with a maximum error margin of 2.5% in predicting the joint capacity. It is believed that the developed model can be confidently used to assess the complex stress distribution along the adhesive layers in SLJs under various loading conditions.
- The ultimate capacity of the single-lap MB-FML ABJs could be enhanced by increasing the overlap length to a certain extent, beyond which no significant changes were observed.
- Increasing the adhesive thickness led to a greater joint capacity and improved the average shear and tensile strengths of the joints. The enhancement continued up to a

certain adhesive thickness, beyond which a slight decrease in the capacity was observed.

Chapter 5: On the Flexural Response of Nanoparticle-Reinforced Adhesively Bonded Joints Mating 3D-Fiber Metal Laminates – A Coupled Numerical and Experimental Investigation

Fatemeh Mottaghian, Farid Taheri

Published in the International Journal of Adhesion and Adhesives, PP 103278, 2023.

This paper has been partially modified compared to its original published version to conform to the format of this thesis and to reduce the repetition of topics covered in Chapter 2.

5.1. Abstract

A coupled experimental/numerical investigation is conducted to characterize the performance of adhesively bonded joints (ABJs) mating three-dimensional fiber-metal laminates (3D-FML) subjected to tensile and flexural loading conditions. The 3D-FML consists of a 3D fiberglass fabric (3DFGF)-epoxy composite sandwiched in between thin layers of Magnesium (Mg) alloys. First, the behaviour of 3D-FML single-lap bonded joints is explored and compared against single-lap joints fabricated with equivalent 2D-FML adherends made of Mg and basalt-epoxy (MB-FML). Subsequently, the effects of different concentrations of graphene nanoplatelets in the adhesive on the joint performance are examined. A 3D-Finite element model (FEM) is developed to investigate the damage initiation and growth in the bond-line and interface layers of the joints. The model accounts for the material and geometrical nonlinearities and incorporates a mixed-mode cohesive zone model (CZM). Finally, the field emission scanning electron microscopy (FESEM) technique is employed to analyze the distribution and agglomeration of GNPs in the adhesive. It is found that the 3D-FML joints provide higher normalized joint and energy absorption capacities compared to their equivalent mated 2D-FML counterparts. Moreover, the 3D-FML joint with 0.5 wt.% GNP-reinforced adhesive performs most optimally, providing 27% and 63% enhancements in its shear and flexural joint capacities, respectively.

5.2. Introduction

[...] *Some portions of this section have been removed and included in Chapter 2.*

As can also be seen, the quasi-static lap-shear test has indeed been the most often used experimental method to analyze the behaviour of ABJs and characterization of their failure mechanism (Adams et al., 1997; Paddy et al., 1987). The involved simplicity, relatively low-cost, and rapid data analysis are some of the reasons that have made the method so popular and widely used. Moreover, almost all the studies utilizing SLJs have examined the response of SLJs by subjecting the joints to a tensile (or shear-lap) loading state. However, in reality, SLJs could also experience other loading states, most notably, a flexural loading state. Nonetheless, comparatively, there is a clear lack of studies that have considered the performance of SLJs under flexural or compressive loading states (Akpınar et al., 2013; Grant et al., 2009; Kadioglu & Demiral, 2020). Indeed, to achieve the most optimum design, one needs to gain a thorough understanding of SLJs' performance under various loading conditions and the associated stress distributions. It could be appreciated that when an SLJ is subjected to an external bending moment, the stress distribution in the joint would be drastically different compared to when the same joint is subjected to a purely axial (shear-lap) loading state. Therefore, it is imperative to characterize SLJs' response subjected to such a potential loading state.

It should also be noted that fiber-reinforced polymer composites (FRP) have been increasingly used to replace metallic materials in different industries in recent years. This evolving development has occurred due to several remarkable inherent attributes of FRP such as high specific strength and stiffness, and superior resistance against fatigue and corrosion, to mention a few. The rapid implementation of composites in various industries in recent decades has also led to a significant reduction in the consumption of fossil fuels and a decrease in greenhouse gas emissions. However, their use in applications that are prone to impact has not been extensive, primarily due to their inherent brittle nature and inability to undergo plasticity (He et al., 2021). To overcome this obstacle, a few researchers in the Netherlands developed Fiber Metal Laminates (FML), by taking advantage of the synergistic combination of FRP's advantages in combination with the plasticity offered by the incorporation of thin metallic sheets. As a result, FMLs provide

all the remarkable advantages of FRP along with ductility, leading to improved load-bearing capacity, all with a significantly lighter weight compared to their metallic counterparts (He et al., 2021; Mottaghian & Taheri, 2022a). More recently, attempts have been made to further enhance the performance of the conventionally used 2D-FMLS by rendering their 3D versions. An example is the 3D-FML developed in our research group, which consists of a special 3D fiberglass fabric (3DFGF) reinforced composite, with its through-thickness cavities infilled with lightweight foam, sandwiched in between two thin sheets of lightweight metal (magnesium (Mg)). Various renditions of this 3D-FML, that is with 3DFGFs having different thicknesses and different metallic sheets with various thicknesses (including stainless steel), have also been tried and tested systematically (Mottaghian et al., 2020; Yaghoobi et al., 2021a). In all, FMLs have gained increased applications in aerospace industries and the number of scholarly articles reporting research on FMLs has also increased exponentially. Nevertheless, to date, and to the best of the authors' knowledge, there exists a very limited number of studies that have investigated the performance of ABJs mating 2D-FMLS (Mottaghian & Taheri, 2022.) and in particular, 3D-FMLS. This becomes more critical in consideration of their performance under bending, compressive, and impact-loading scenarios. This is an important issue because FMLs are susceptible to delamination of their FRP/metal constituents. Therefore, investigating the performances of joints mating such complexly configured hybrid materials is essential in promoting their applications in various industries.

To address this knowledge gap and with the aim of augmenting the few previous studies that have considered the performance of single-lap FML ABJs, the work presented in this paper systematically examines the performances of single-lap 3D-FML ABJs. Accordingly, the main objectives of this study are:

- (i) To evaluate the performance of single-lap 3D-FML bonded joints against equivalent SLJs made of conventional 2D-FML under a quasi-static lap-shear loading state. The single-lap 2D-FML is made of magnesium and basalt fabric, which will be referred to as MB-FML hereafter.
- (ii) To investigate the behaviour of the 3D-FML SLJs under quasi-static three-point flexural loading conditions.

- (iii) To explore the influence of the inclusion of different contents (wt.%) of GNPs in the adhesive and its effect on the response of 3D-FML SLJs, and also to establish the optimal GNP content.
- (iv) To assess the failure mechanisms of the stated SLJs and to perform a morphological study using field emission scanning electron microscopy (FESEM).
- (v) To develop an effective and accurate 3D finite element (FE) framework to simulate the response of the SLJs effectively and accurately.
- (vi) To implement a robust cohesive zone model (CZM) in the FE framework along with the incorporation of a mixed-mode trapezoidal traction-separation cohesive model to enable simulation of crack initiation and propagation.

5.3. Experimental Procedure

5.3.1. Selection of Materials

The MB-FML consists of thin Mg alloy sheets, basalt fabrics, and room-cured resin, whereas the 3D-FML consists of the same Mg alloy sheets, room-cured resin, GNPs, 3DFGF, and a two-part liquid polyurethane foam with a density of 256 kg/m^3 . AZ31B–H24 Mg sheets with 0.5 mm thickness were obtained from MetalMart (Commerce, CA, US). The 3DFGF with a “raised” thickness of 4 mm and biaxial (0/90) stitched basalt fabric with a thickness of 0.55 mm and an areal density of 450 g/m^2 were procured from China Beihai Fiberglass Co. Ltd. (Jiujiang City, Jiangxi, China) and GBF basalt fiber Co., Ltd (China), respectively. The graphene nanoplatelets (xGnP grade M-25) with an average diameter of 25μ , a thickness of 6 nm, and a surface area of $100 \text{ m}^2/\text{g}$ were acquired from XG Science Ltd., Lansing, MI. The liquid polyurethane foam utilized to fill the hollow cavities of the 3DFGF was purchased from US Composites (Palm Beach, FL, US). Moreover, the room-cured structural epoxy system (105 resin and 206 slow hardener) was obtained from West System (Bay City, MI, US).

5.3.2. Fabrication Methodology

5.3.2.1. FML Fabrication

Sample preparation for the FML commenced with surface treatment of the metal sheets. Surface preparation significantly affects the adhesion and long-term performance of a given ABJ. In preparing Mg sheets and generating better bonding/locking surfaces, both surfaces of the sheets were degreased with acetone and sandblasted with 20-30 grit-size crushed glass. Note that due to the thin nature of Mg sheets, both surfaces must be sandblasted to remove (or balance) the basting-induced residual stresses; otherwise, the sheets will warp. In the next step, Mg sheets were cleaned with compressed air and acetone and let dry. Subsequently, the bonding surfaces were covered with a thin layer of room-cured resin and coated with a layer of porous peel-ply and breather. The assembly was fitted inside a vacuum bag under 1 bar vacuum and let cure at ambient temperature for 48 hrs. This surface treatment method, which is simple and cost-effective, prevents the oxidation and corrosion of Mg sheets bonding surfaces. The imprint of peel ply would also create a rough impression on the resin, which in turn will enhance the mechanical interlocking, hence, promoting optimal interface bond strength as demonstrated in (De Cicco & Taheri, 2019a).

In parallel to the surface treatment process, the fabrication process of the core constituents of the FMLs was initiated with the fabrication of the basalt laminate and 3DFGF. The vacuum-assisted resin infusion (VARI) technique was used to fabricate MB-FML panels with a ply sequence of $[0/90]_{2s}$. For this, the room-cured epoxy resin and hardener were mixed with a weight ratio of 5:1 and infused into the dry fabrics under 1 bar vacuum. Subsequently, the assembly was sealed and let cure under the vacuum for 48 hrs at ambient temperature as per the manufacturer's recommendation.

On the other hand, 3DFGF was impregnated by brushing the room-cured epoxy system as per the supplier's instructions and allowed to fully cure at ambient temperature for 48 hrs. To enhance the stiffness of the fabric, its through-thickness cavities were filled with the two-part liquid polyurethane foam (Yaghoobi et al., 2021a). For that, Parts A and B of the foam were mixed with a 1:1 ratio, and the aspiration technique facilitated by a special-

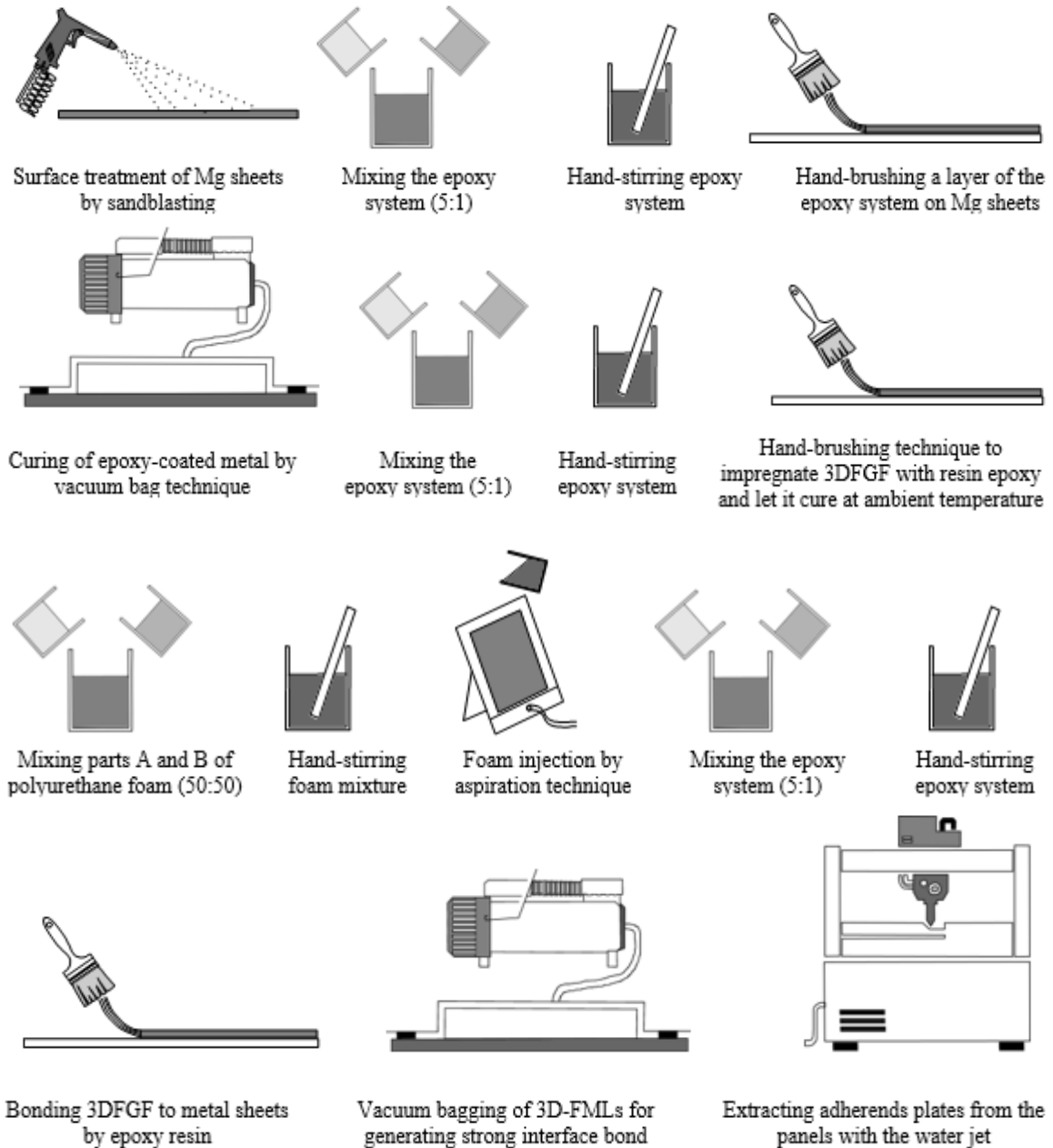


Figure 5-1. The sequence 3D-FML Fabrications.

in-house designed jig (Mottaghian et al., 2020) was implemented to assist the homogeneous distribution of the foam inside the cavities. The foam-reinforced-3DFGF was left to cure at ambient temperature for 24 hrs. Thereafter, the cured core components of the FMLs were sandwiched in between the pre-treated Mg sheets by the room-cured epoxy system and sealed in a vacuum bag under 1 bar, and left to cure at ambient temperature for 48 hrs. It should be noted that in order to compare the response of the MB-

FML and 3D-FML, the number of bidirectional basalt fabrics was selected in a way that its FML had the same bending stiffness as 3D-FML. The sequence of 3D-FML fabrication is depicted in Figure 5-1.

5.3.2.2. SLJs Fabrication

The fabrication of SLJs started by extracting the appropriate size adherends from the FML panels. A special customizable tool was designed to assist the joint assembly with a special emphasis on attaining consistent and uniform adhesive thickness in all SLJ specimens as shown in Figure 5-2(a).

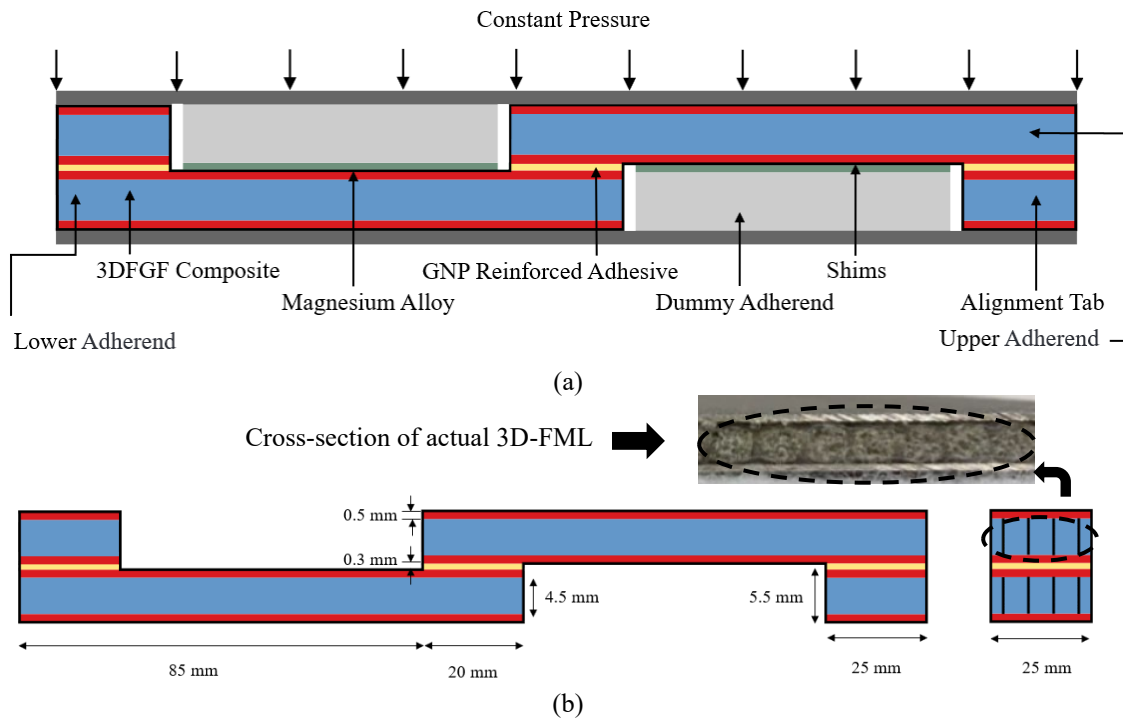


Figure 5-2. Schematic of (a) specially designed fabrication jig, (b) dimension of single-lap 3D-FML ABJs.

After measuring the dimensions precisely, the mating surfaces were wiped with acetone. Then, the dummy adherends, as shown in Figure 5-2(a), were fitted on the top of the lower adherend's surfaces as well as below the upper adherend. Subsequently, the metal shims (spacer) were placed over and under the dummy adherends to control the thickness of the adhesive bond line. Subsequently, GNPs were added to the room-cured epoxy resin at the selected weight contents. First, the epoxy resin and GNPs were mixed by a mechanical stirrer at 2000 rpm for 10 mins. Thereafter, the three-roll mill machine (Torrey

Hills Technologies LLC, San Diego, CA) was utilized to calender the GNPs slurry. The three-roll machine subjects the mixture to large shear forces, thereby breaking down the GNPs agglomeration and leading to better dispersion of GNPs in the resin (Ahmadi Moghadam, 2015). In this research, the roller gaps were optimally set at 30 μm with a constant speed of 174 rpm as established in our previous research (Yaghoobi et al., 2021a). The calendering process was repeated seven times to ensure the perfect dispersion of the materials and minimize the potential agglomeration. Upon completion of this process, the hardener was added to the slurry (with a ratio of 1:5) and mixed by the laboratory stirrer at 400 rpm for 5 min. Next, the GNP-reinforced resin was brushed onto the mating regions of adherend panels, and the panels were then bonded together, as shown in Figure 5-3. Alignment tabs were also utilized to reduce the eccentricity of the load path within the adhesive. In the next step, the upper surfaces of SLJ were covered with a thin layer of the stiff plate and were subjected to constant pressure to facilitate optimal adhesion, as shown in Figure 5-2(a). Afterward, all excess adhesive spews were removed by a slender wooden strip to leave a 90° fillet at each end. The system was left to cure at ambient temperature for 48 hrs. Finally, 25 mm wide specimens were extracted from the SLJ systems based on ASTM D5868-01 (2005) and ASTM D1002-10 (2021), as illustrated in Figure 5-2(b). It should be mentioned that tabs were not required for specimens that underwent flexural testing; therefore, longer dummy adherents and shims were used to guarantee uniform and consistent adhesive thickness in their fabrication process. Identifications of the categories of the fabricated single-lap FML ABJs specimens are reported in Table 5-1.

Table 5-1. Groupings of the fabricated single-lap FML ABJ specimens and their flexural modulus.

Samples ID	MB-FML	3D-FML-1	3D-FML-2	3D-FML-3	3D-FML-4
GNP-Content (wt.%)	0	0	0.25	0.5	0.75
Flexural Modulus	-	17.8±0.5	19.2±0.7	21.1±0.4	18.8±0.5

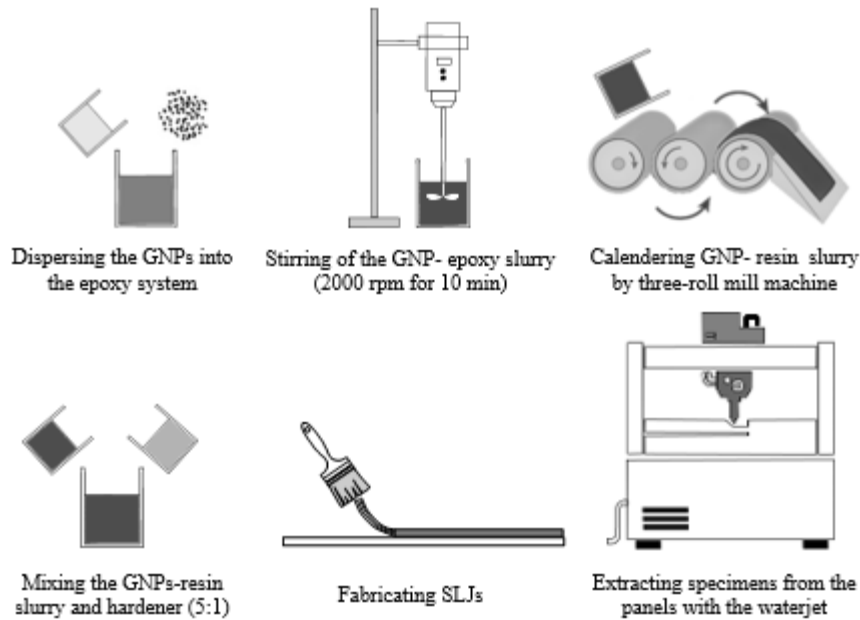


Figure 5-3. Fabrication process sequence of the GNP-reinforced 3D-FML SLJs.

5.3.3. Characterization

In this study, a digitally controlled MTS servo-hydraulic universal testing machine equipped with a 250 kN load cell was used to conduct the quasi-static single-lap shear and three-point flexural tests. To maximize the precision of the experimental results, at least five specimens in each configuration category were tested. The lap-shear tests were conducted at a constant crosshead speed of 1.27 mm/min as per ASTM D1002-10 (2021), whereas the speed of 2 mm/min was used for the three-point flexural tests as per ASTM D790-17 (2017). Note that all the tests were performed at room temperature and mechanical grippers were utilized to secure the specimens in the lap-shear test. The span-to-thickness ratio of 16:1 was set in the flexural test. As the adherends in the SLJ specimens used in the flexural tests were not aligned on the same horizontal plane, one of the supports of the flexural fixture had to be adjusted (or lifted) to compensate for the misalignment. For that, a short beam, having the same thickness as that of the adherends was placed beneath the corresponding fixture, as exhibited in Figure 5-4(a). The values of the shear and flexural strengths and flexural strain were determined using the basic mechanics of materials equations as follows (ASTM D709-17, 2017, ASTM D1002-10, 2021, ASTM D5868-01, 2005):

$$\tau = \frac{F}{L \times w} \quad \sigma_f = \frac{3FL_s}{2wt^2} \quad E_f = \frac{L_s^3 m}{4wt^3} \quad \varepsilon_f = \frac{6\delta_m t}{L_s^2} \quad (5-1)$$

where τ , σ_f , E_f and ε_f are the shear strength, flexural strength, flexural modulus, and flexural strain, respectively. Besides, L , L_s , w , and t are the bond length, specimen's span length, specimen width, and thickness, respectively; and F , m and δ_m refer to the failure load, the slope of the linear region of the load-displacement curve, and mid-span deflection, respectively. The morphology of the GNP-reinforced adhesive in the bonded region of reinforced-single-lap 3D-FML ABJs was examined microscopically through the fracture surfaces of the bonded region using a Hitachi S-4700 cold FESEM (Japan), and all images were taken at an accelerating voltage of 7 kV. It should be noted that, before morphological analysis, the surfaces of samples were sputter-coated by a high vacuum sputter coater LEICA EM ACE 600 (Vienna, Austria) with Gold/Palladium (80/20) to a thickness of 15.14 nm at a current of 30 mA to prevent electrostatic charge build-up during the examinations.

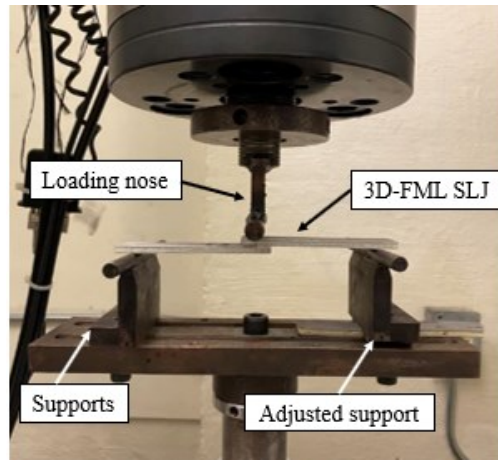
Table 5-2. Material models utilized in LS-DYNA.

Constituent	Material Model
Mg alloy sheets	*MAT_PIECEWISE_LINEAR_PLASTICITY (MAT_024)
Polyurethane foam	*MAT_ELASTIC (MAT_001) + MAT_ADD_EROSION (MAT_000)
Glass pillars and ply	*MAT_ENHANCED_COMPOSITE_DAMAGE (MAT054/055)
Adhesive	*MAT_COHESIVE_MIXED_MODE_ELASTOPLASTIC (MAT_240)
Supports	*MAT_RIGID (MAT_020)

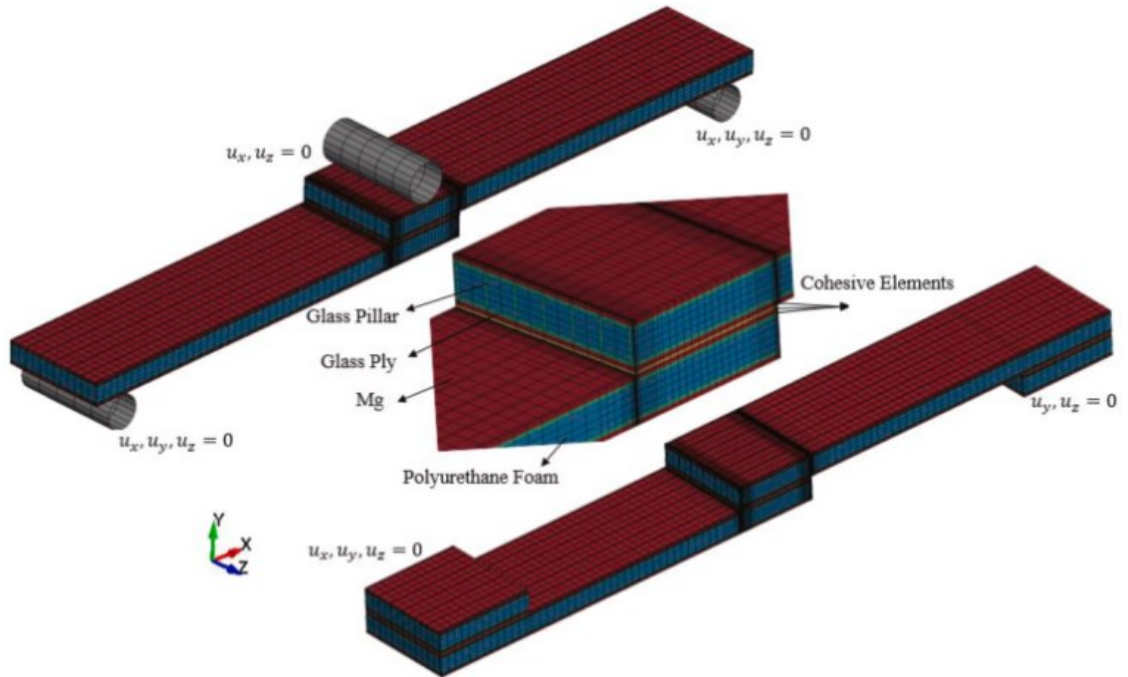
5.4. Numerical Procedure

A FE modelling framework is developed to gain a better understanding of the response of single-lap 3D-FML ABJs subjected to lap-shear and flexural loading conditions as well as simulate damage initiation and progress along the overlap region of the bonded joints. The commercial FE software LS-DYNA V4.8.23, 2021 with R11.2.2 double precision solver is used for this purpose. The developed nonlinear implicit FE model accounts for the geometrical and material nonlinearities. The adhesive layer is modelled by eight-node hexahedron cohesive elements (ELFORM=19), and the remaining parts of the assembly are discretized with the fully integrated solid elements (ELFORM = 2). The FE model of SLJs consists of six components or parts; they are (i) the Mg alloy sheets, (ii) the

Mg/3DFGF interface adhesive layers, (iii) the 3DFGF pillars, (iv) the vertical pillars connecting the upper and lower plies of 3DFGF, (v) the polyurethane foam, and (vi) the overlap adhesive layer. As demonstrated in Figure 5-4(b), coarse meshes are generated on the regions away from the stress-concentration regions and they are gradually refined as they approached the stress-concentration regions (overlap region's ends).



(a)



(b)

Figure 5-4. (a) Single-lap quasi-static flexural test setup, (b) details of the FE models of the single-lap 3D-FML ABJs.

Table 5-3. Mechanical properties of the materials used in the FE model (Mottaghian et al., 2020).

Property	Mg	3D-FGF		
		Glass epoxy-plyies	Glass epoxy-pillars	Polyurethane foam
Thickness (mm)	0.5	0.4	0.35	4.2
ρ (Kg/m ³)	1740	1750	1750	1.28
E_{11}/E (GPa)	36	9	3	0.05
E_{22} (GPa)		9	1	
v_{12}, v_{13} or v	0.35			0
v_{23}				
G_{12}, G_{13} (GPa)		1	1	
G_{23} (GPa)		1	1	
ϵ_{max}				0.15
σ_{yield} (GPa)	0.231			
S_c (GPa)		0.03	0.03	
X_c (GPa)		0.173	0.08	
X_T (GPa)		0.173	0.08	
Y_c (GPa)		0.173	0.08	
Y_T (GPa)		0.173	0.08	

The boundary conditions in the SLJ specimens subjected to the quasi-static lap-shear loading state are imposed as follows. All degrees of freedom (DOF) of the nodes corresponding to the location of the end tabs (i.e., within 25 mm from either end) are fully restrained, except the axial (u_x) DOF of the nodes corresponding to the tab at one of the ends, which are not restrained, thus accommodating the axial movement of the specimen. In the case of the model subjected to the quasi-static flexural loading state, the loading nose and the left and right supports are modelled explicitly using shell element, ELFORM=2. In this modelling framework, the loading nose is allowed to move only perpendicular to the adherend surface, while the supports' movements are restrained in all directions. The CONTACT_AUTOMATIC_SURFACE_TO_SURFACE penalty-based contact algorithm is used to model the contact between the loading nose, supports, and SLJs. Note that SOFT=2 and SOFSCL=0.1 parameters are utilized in the contact keyword. Moreover, the displacement-controlled algorithm is conducted to mimic the flexural and shear loading conditions. As for the material constitutive modelling, the Mg layers are modelled using the piecewise linear plasticity material model of LS-DYNA. The pillars and plies constituents of 3DFGF are modelled using the composite damage material model coupled with the Chang-Chang failure criteria, enabling tracing of damage progress. It should be noted that the glass pillars in 3DFGF are oriented at an approximately 30° angle with respect to the vertical direction; this parameter is also accounted for in the composite model. The foam is modelled by a combination of an elastic material with erosion criteria

in the developed model. The details of the material modelling of the 3D-FML are fully described in our previous studies (Mottaghian et al., 2020; Yaghoobi et al., 2021a). As briefly noted earlier, the adhesive layers, as well as the interface regions of Mg/3DGFG, are modelled using the CZM. In other words, each interface is modelled by a layer of cohesive elements (more details will be provided in section 5.4.1. Besides, all LS-DYNA material keywords utilized in the model are tabulated in Table 5-2 and the pertinent mechanical properties are provided in Table 5-3.

5.4.1. Cohesive Zone Modelling (CZM) Details

CZM, which has been recognized as a progressive damage and failure modelling approach, is capable of simulating the onset and propagation of damage without requiring the existence of an initial flaw but requires the definition of a pre-defined crack path. Using this approach, the complete response of a given structural component up to the final failure stage could be modelled in a single analysis, requiring no post-processing analysis (Bayramoglu et al., 2021; Wciślik & Pała, 2021). In this study, the nonlinear behaviours of the adhesive and interface layers and the associated damage mechanisms are simulated by implementing the mixed-mode (I+II) CZM. The traction-separation law in each mode of failure is employed to reproduce the behaviour of the adhesive layer. It should be noted that as illustrated in Figure 5-5, a separate trapezoidal law is used to account for each pure mode of failure by considering the stresses (σ) and relative displacement (δ) (or traction-separation relationship) in the paired nodes of the cohesive elements used to model the interfaces. In other words, individual trapezoidal traction-separation relationships are used to represent the nonlinear responses of the interfaces if subjected to either pure shear or peel stresses. The combination of the two will closely mimic the nonlinear response of the interfaces which would be subjected to the combined modes. Furthermore, the damage onset is expressed based on a quadratic stress criterion as follows (Campilho et al., 2009):

$$\left(\frac{\sigma_n}{\sigma_{un}}\right)^2 + \left(\frac{\sigma_t}{\sigma_{ut}}\right)^2 = 1 \quad (5-2)$$

where σ_n and σ_t indicate the local stresses in each pure mode I (“n” or peel) and mode II (“t” or shear). Also, σ_{un} and σ_{ut} represent the corresponding strengths. The damage criteria can also be rewritten as a function of the relative displacement (Marzi et al., 2009)

$$\left(\frac{\Delta_n}{\delta_{ni}}\right)^2 + \left(\frac{\Delta_t}{\delta_{ti}}\right)^2 = 1 \quad (5-3)$$

where $i=1,2$ correspond to damage initiation and softening onset, Δ_n , Δ_t correspond to current displacement and δ_{ni} , δ_{ti} represent the relative separation/sliding in pure mode (I) and (II), respectively. δ_{mi} is the equivalent mixed-mode displacement at the onset of damage initiation (softening) onset, which is determined by (Marzi et al., 2009).

$$\delta_{mi} = \delta_{ni}\delta_{ti}\sqrt{\frac{1+\beta^2}{\delta_{ti}^2+(\beta\delta_{ni})^2}} \quad (5-4)$$

where β corresponds to the mixed-mode ratio. The ultimate relative displacement can be determined by (Marzi et al., 2009):

$$\delta_{mf} = \frac{\delta_{m1}(\delta_{m1}-\delta_{m2})E_n G_{IIC} \cos^2 \gamma + G_{IC}(2G_{IIC} + \delta_{m1}(\delta_{m1}-\delta_{m2})E_t G_{IC} \sin^2 \gamma)}{\delta_{m1}(E_n G_{IIC} \cos^2 \gamma + E_t G_{IC} \sin^2 \gamma)} \quad (5-5)$$

The above equation is based on the power-law damage evolution model with an exponent of $\eta = 1$ and by considering the peel and shear stresses across the interface. Here, the initial stiffness in the peel (E_n) and shear (E_t) are calculated based on the Young’s (E) and shear (G) moduli as $E_n = \frac{E}{t_{element}}$ and $E_t = \frac{G}{t_{element}}$, respectively (Marzi et al., 2009).

The mixed-mode traction-separation law will be determined based on δ_{mi} and δ_{mf} , collectively. Subsequently, the separations in peel and shear directions will be evaluated and if the damage criteria are satisfied (i.e., $\Delta_m > \delta_{mf}$), and then complete failure will be deemed accordingly (Marzi et al., 2009).

The cohesive properties of the neat and GNP-reinforced adhesive were experimentally evaluated in one of our previous studies by conducting the double-cantilever beam (DCB) and end-notched flexure (ENF) tests (Mohamed & Taheri, 2017). Note that in the previous study (Mohamed & Taheri, 2017), the bi-linear traction-separation law was used; therefore,

the remaining mechanical parameters required for trapezoidal CZM are obtained by calibrating the model's parameters in reference to the experimental results obtained in the present study. These CZM parameters are reported in Table 5-4.

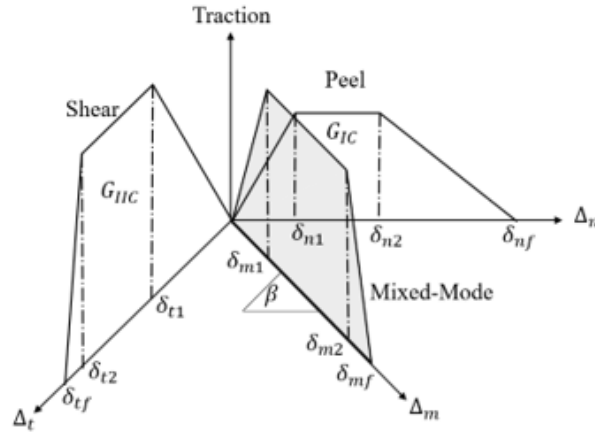


Figure 5-5. The trapezoidal mixed-mode CZM.

5.5. Results and Discussion

5.5.1. Experimental Results

This section presents the results of the experimental investigations on single-lap FML ABJs under quasi-static lap-shear and flexural loading conditions.

Table 5-4. CZM parameter for neat and GNP-reinforced adhesive (Mohamed & Taheri, 2017).

Properties	GNPs (wt.%)	Young's (shear) Modulus (GPa)	Mode I (II) Yield Stress (MPa)	Mode I (II) Energy Release Rate (KJ/m ²)	Initiation Criteria	Propagation Criteria
Neat Adhesive	0	3.50 (1.50)	59 (23)	1.5 (2)	Quadratic Stress Criteria	Power-Law with (η=1)
Reinforced-Adhesive	0.5	3.70 (1.65)	65 (30)	3 (2.5)		

Notes: (i) The adhesive thicknesses in the bond region and the Mg/3DFGF interface are 0.3 mm and 0.1 mm, respectively.
(ii) The numbers in brackets are the values for mode II, while the neighbors on left are for mode I.

5.5.1.1. Lap-shear Performance

As mentioned previously, since the performance of the 3D-FML SLJs has not been investigated in previous studies, in the first step, the performance of 3D-FML SLJs is compared against 2D-FML SLJs (e.g., MB-FML). Note that the two types of FML have an

equivalent bending stiffness. Subsequently, the influence of the different wt.% of GNPs on the performance of 3D-FML SLJs will be presented.

The average values of joint capacity, the normalized joint capacity with respect to weight, and the corresponding standard deviations of the tested FMLs are shown in Figure 5-6. As can be seen, the joint capacities of MB-FML and 3D-FML joints are quite similar due to the equivalency of their stiffness. The results reveal that the joint capacities of the 3D-FML-2 and 3D-FML-3 specimens compared to the based group of specimens (i.e., 3D-FML-1) were improved by the inclusion of 0.25 and 0.5 % wt.% GNPs, respectively. Specifically, the joint capacities of 3D-FML-2 and 3D-FML-3 were determined as 3.40 kN and 4.05 kN, or enhancements of 5% and 25 %, respectively, compared to the based specimen. However, the inclusion of 0.75 wt.% of GNPs in 3D-FML (e.g., 3D-FML-4) led to an 18 % degradation in the joint capacity.

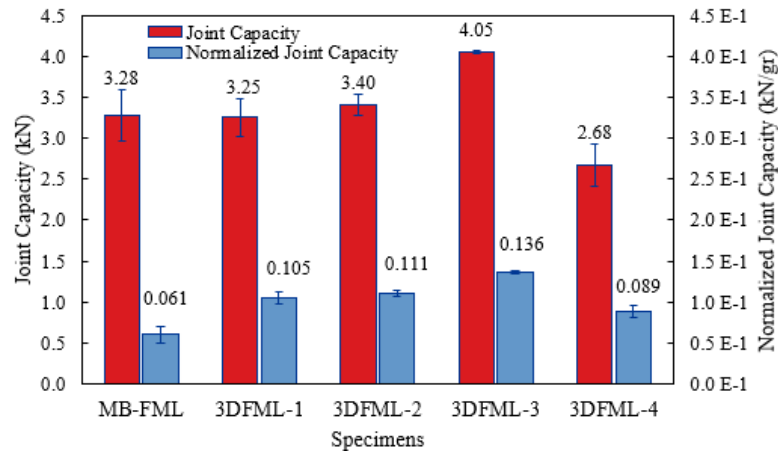


Figure 5-6. Joint capacities of single-lap FML ABJs subjected to quasi-static lap-shear load.

One of the most important criteria in materials selection in different industries, especially in automotive and aeronautic industries, is components' weight as joints' weight affects their dynamic response. Therefore, the results discussed above are normalized with respect to weight, which are also shown in Figure 5-6. As seen, in general, all the 3D-FML configurations produced significantly higher normalized joint capacities compared to their 2D-FML counterparts. Therefore, 3D-FMLs seem to be effective and viable alternatives to 2D-FMLs. As seen, the normalized joint capacity of 3D-FML-1 is 0.105 kN/gr, which is 72 % higher than its equivalent 2D-MB-FML. Moreover, 3D-FML-3, which included only

0.5 wt.% of GNP presented outstanding gains of 123% and 30% compared to the neat 2D-FML and 3D-FML-1 configurations, respectively. An interesting observation is 3D-FML-4 (reinforced with 0.75 wt.%), which exhibited 18% lower joint capacity compared to MB-FML, but when the capacity is normalized, it is 46% superior, comparatively. The overall comparison of the results shown in Figure 5-6 reveals 3D-FML-3 SLJs as the configuration offering the optimal performance.

The graphs of load versus displacement of the FML configurations are exhibited in Figure 5-7. It can be observed that although the joint capacities of MB-FML and 3D-FML-1 are quite similar (3.28 and 3.25 kN, respectively), nevertheless they exhibited considerably different behaviours. Based on the load-displacement curves, MB-FML shows a linear behaviour followed by a catastrophic failure; on the other hand, 3D-FML-1 responded nonlinearly, thereby capable of absorbing a significantly higher amount of energy (by 146%).

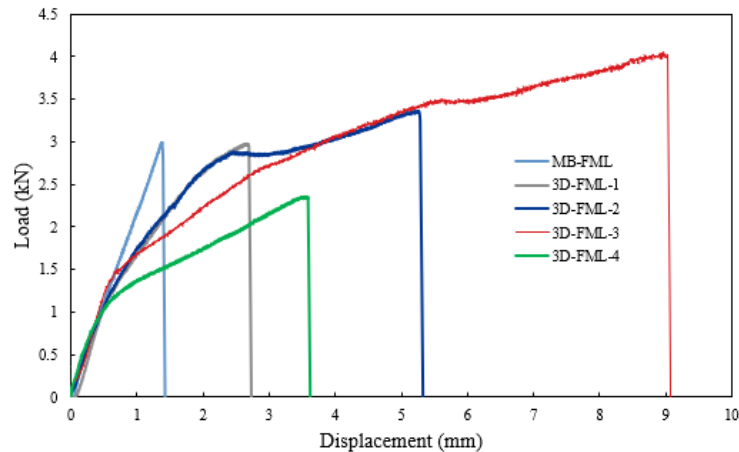


Figure 5-7. Load-displacement responses of single-lap FML ABJs subjected to quasi-static lap-shear load.

The average values of energy absorption capacity of the fabricated single-lap FMLs are depicted in Figure 5-8. The energy absorption capacities were calculated by evaluating the area under the load-displacement curves. One can observe that in general, the inclusion of GNPs led to a considerable improvement in energy absorption. The energy absorption capacities of 3D-FML-3 and 3D-FML2 were substantially enhanced by 609% and 321% compared to MB-FML, whereas the improvements are approximately 188% and 71%, respectively, compared to 3D-FML-1. This is remarkable considering the excellent

mechanical properties of GNPs, especially when such low GNP contents (i.e., 0.25, 0.50, and 0.75 wt.%) could improve the energy absorption capacities of the SLJs by significant margins. It should be noted that while a very small quantity of nanoparticles created significantly stronger interfacial bond strength in the matrix, nonetheless, the increase in the energy absorption is not directly proportional to the GNP wt.% content. That is postulated to be due to the increase in the viscosity of the resin as GNP content increases. As a result, more air bubbles will be entrapped in the matrix, thus, causing less uniform dispersion of the particles in the adhesive, which in turn would impede effective load transfer through the matrix. As can be noted, although the response of 3D-FML-4 reinforced with 0.75 wt.% is nonlinear and its energy absorption is still 115% higher than that of MB-FML, this improvement is 13% inferior to the level of improvement exhibited by 3D-FML-1. Therefore, one may conclude that the optimal GNP content that would produce the SLJ response with the highest energy absorption capacity under a quasi-static lap-shear loading state would be 0.5 wt.% content. The other interesting observation that can be seen through the results presented in Figure 5-7 is that in general, 3D-FML SLJs elongate more compared to MB-FML SLJs. For instance, the optimal 3D-FML SLJs (with 0.5 wt.% GNPs) experienced almost six times more elongation compared to the MB-FML SLJs.

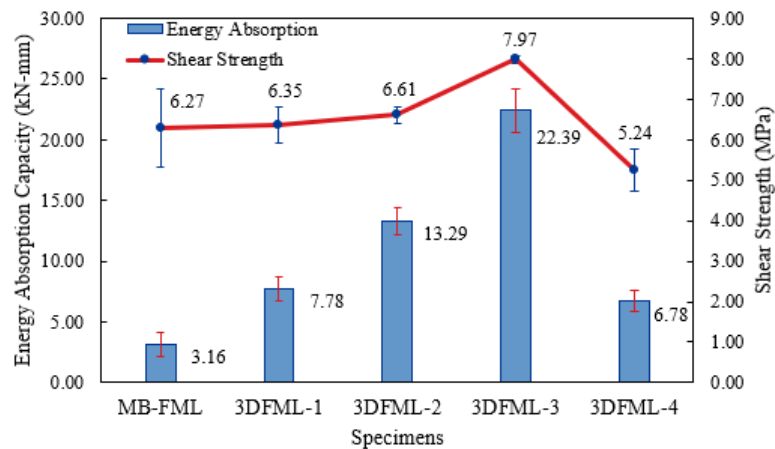


Figure 5-8. Energy absorption capacities and shear strengths of single-lap FML ABJs subjected to quasi-static lap-shear load.

Figure 5-8 also shows the average shear strength of the SLJs which were calculated using Eq. (5-1). The shear strengths of MB- and 3D-FML SLJs are very similar (6.27 MPa

and 6.35 MPa, respectively). Moreover, the shear strengths of single-lap 3D-FML with 0.25 and 0.5 wt.% of GNPs are 6.61 and 7.97 MPa, revealing improvements of 5% and 27%, respectively, compared to MB-FML SLJ. On the other hand, 3D-FML-4 (the SLJ with 0.75 wt.% GNP) showed a 16% degradation in the shear strength compared to MB-FML SLJs, the reasons will be discussed in section 4.4.1.2.

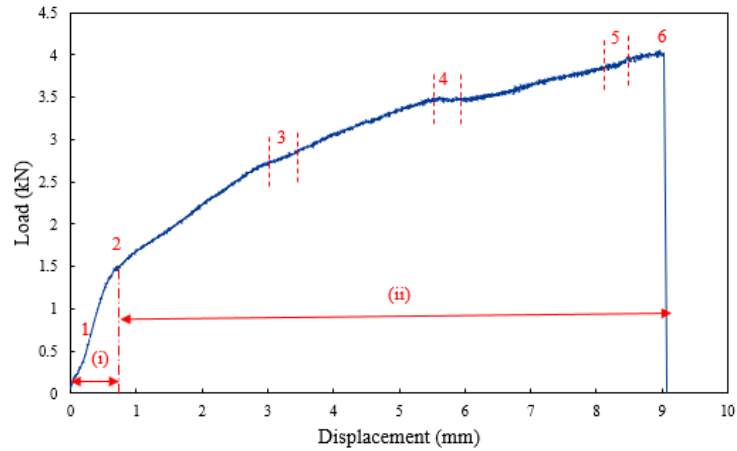


Figure 5-9. Load-displacement response of single-lap 3D-FML-3 ABJ subjected to quasi-static lap-shear load.

Figure 5-9 represents the load-displacement response of 3D-FML-3 SLJ subjected to a lap-shear loading state. The nonlinear load-displacement curve can be divided into two zones, including (i) linear, and (ii) quasi-linear. The first zone reflects the elastic response. The second quasi-linear zone reflects the yielding of the adhesive and potential damage in the adherends. The subregions 3, 4, and 5 in this region reflect the development of sequential damage/crack leading to the catastrophic reduction in the stiffness and rupture of the joint (Duncan, 2010; X. Liu et al., 2019). The strength of the bonded joint will be based on the maximum load carried out by the joint (Duncan, 2010). Note that a detailed comparison of the experimentally observed damage initiation/evolution response was also modelled and predicted numerically as will be seen in Chapter 7.

5.5.1.2. Flexural Performance

SLJs subjected to a flexural loading state experience a remarkable rotation in the configuration. Therefore, under such a loading state, the peel stress concentration is higher than that associated with a lap-shear loading state. The peel stress in an SLJ subjected to

bending varies depending on whether the bonded region is subject to a tensile or compressive loading state. Obviously, crack initiates in a region of the bond-line subject to a tensile stress state, where the peel stress concentration attains a maximum (Çakır et al., 2021). The average joint capacities of 3D-FML SLJ tested under a three-point quasi-static flexural configuration, their standard deviations, and the normalized joint capacities (with respect to weight) are illustrated in Figure 5-10. As can be seen, the inclusion of GNPs resulted in the enhancement of joint capacity as well as normalized joint capacity in all the cases. This is because the inclusion of GNPs improves the toughness and stiffness of the adhesive, thus leading to more resistance against the deflection created by the flexural load in the bond region (Çakır et al., 2021). Indeed, even at such low GNP contents, the particles with their remarkable mechanical properties seemingly enhance the joint capacity of SLJs appreciably. However, as seen earlier, the joint enhancement is not a direct function of the wt.% content. For instance, the joint capacity of 3D-FML-2 and 3D-FML-3 with the inclusion of 0.25 and 0.75 wt.% contents of GNPs are 149.0 N and 136.1 N, respectively, which translate to the gains of 18% and 8%, respectively, when compared to the baseline specimen without GNPs. On the other hand, the average failure load of 3D-FML-3 SLJs is 185.9 N, reflecting a more significant improvement of 48% compared to 3D-FML-1 SLJs. However, this failure load cannot be considered the actual joint capacity for this configuration. That is because of the inclusion of 0.5 wt.% GNP led to significantly enhanced mechanical properties of the adhesive so much that the failure did not occur in the overlap bond region.

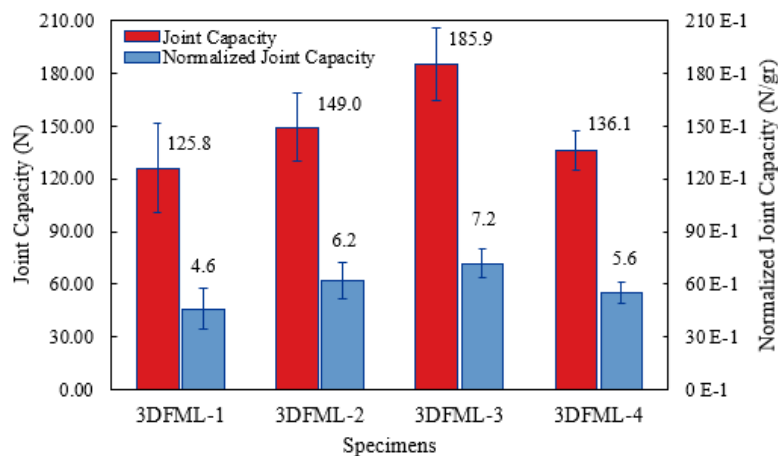


Figure 5-10. Joint capacities of 3D-FML SLJs subjected to quasi-static flexural load.

In fact, the delamination in the interface layer of Mg and 3DFGF caused the catastrophic failure of the joint, as illustrated in Figure 5-11. This interesting observation indicates that the strength of 0.5 wt.% GNP-reinforced adhesive was superior to the interlocking strength of in Mg/3DFGF interface. Consequently, one should not deem the ultimate load as the SLJ's joint capacity. The results in Figure 5-10 also reveal that the normalized joint capacity of 3D-FML-2 and 3D-FML-4 are 6.2 N/gr and 5.6 N/gr, respectively. In other words, the inclusion of 0.25 wt.% GNPs led to an enhancement in the normalized capacity of 35 % compared to the capacity of SLJs without GNPs, whereas this improvement was approximately 22% in SLJs with the highest GNP content (i.e., 0.75 wt.%). The highest normalized failure load was however provided by the 0.5 wt.% of GNP-reinforced SLJs as 7.2 N/gr, translating to a significant gain of 57% compared to the baseline SLJs. Typical load-displacement behaviours of the single-lap 3D-FML ABJs subjected to flexural load are shown in Figure 5-12. As can be seen, the energy absorption capacities of all the GNP-reinforced 3D-FML SLJs are higher than non-reinforced SLJs.

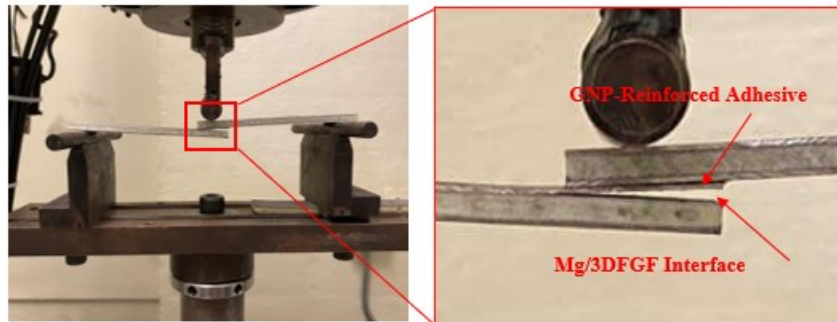


Figure 5-11. Delamination failure of Mg/3D-FGF interface of 3D-FML-3 SLJ with 0.5 wt% GNP reinforced-adhesive subjected to quasi-static flexural load.

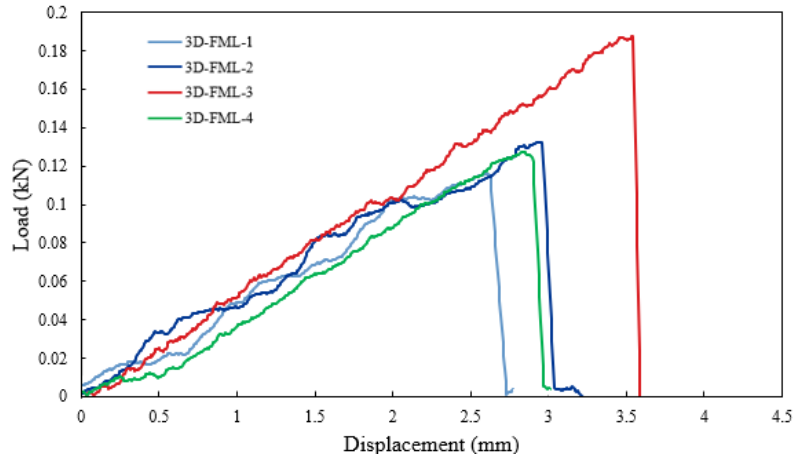


Figure 5-12. Load-displacement curves of 3D-FML SLJs subjected to quasi-static flexural load.

The average flexural strengths and strains of the tested SLJs determined based on Eq. (5-1) are presented in Figure 5-13. The results further confirm that reinforcing the adhesive with GNPs led to the enhancement of the flexural strength and strain of each group of SLJs. It can be observed that in concert with the earlier observations, 3D-FML-3 with a flexural strength of 68.25 MPa delivered the highest improvement (63%), compared to non-reinforced SLJ (3D-FML-1). On the other hand, the inclusion of 0.25 and 0.75 wt.% GNP improved the flexural strength of 3D-FML with gains of 27% and 21%, respectively. Moreover, all the reinforced SLJs demonstrated higher strain capacity compared to the baseline SLJs. For instance, 3D-FML-2 showed 35% more strain capacity than the baseline SLJ and the increase in the GNP content to 0.5 wt.% did not produce further improvement in the strain capacity. Besides, the strain capacity of 3D-FML-4 SLJ reinforced with 0.75 wt.% degraded by 12% compared to 3D-FML-2 and 3D-FML-3 SLJs. Note that, however, this value is still 19% higher than that of 3D-FML-1 SLJs. Agglomeration of the particles is postulated to be responsible for the degradation (this postulation will be discussed further in the following section). Note that the flexural moduli of the SLJ 3D-FMLs are calculated based on Eq. (5-1) and reported in Table 5-1. As seen, the values of the flexural modulus follow the same trend as the rest of the results in this section, indicating that the 3D-FML-3 attained the highest gain (by 18.5%) in the flexural stiffness compared to the 3D-FML-1, while the lowest gain (i.e., 7.8%) was obtained by 3D-FML-4. In summary, based on the

results reported in this section, 3D-FML-3 performed most optimally in terms of flexural strength and strain.

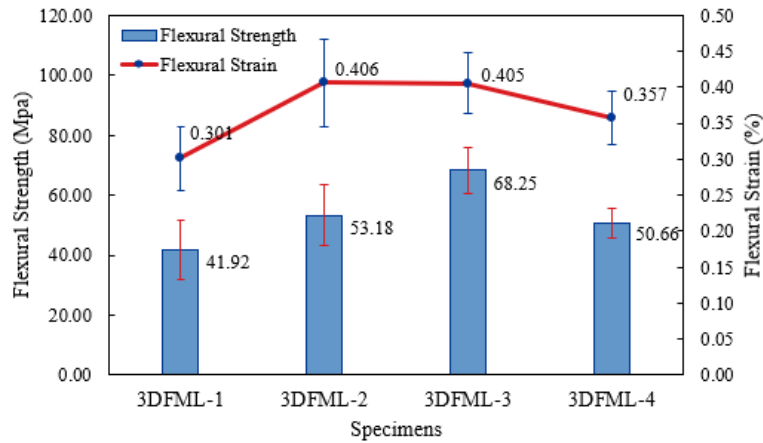


Figure 5-13. The ultimate flexural strengths and strains of 3D-FML SLJs subjected to quasi-static flexural load.

5.5.1.3. Bond Failure Mechanism and Morphological Analysis

The failure mechanisms in ABJs are commonly categorized into four modes:

- (i) interfacial failure mode - in which the failure occurs in the mating surface(s) (or interface(s)) of the adhesive and adherend(s). This mode is precipitated by an inadequate interlocking mechanism on the bonding surfaces, often caused by ineffective surface treatment.
- (ii) cohesion failure mode – the mode in which the failure takes place within the adhesive. In this mode, the adhesive remains on both bonding surfaces and it is the most desirable failure mode, resulting in maximum joint capacity (Ebnesajjad & Landrock, 2015).
- (iii) interfacial-cohesion hybrid mode – a self-explanatory failure mode, which is the mixture of the abovementioned modes.
- (iv) and finally, adherend failure mode, in which the failure occurs in adherend(s) prior to joint adhesion capacity being reached.

It should be noted that the internal and external bending moments developed due to shear and flexural loading states cause the rotation of the bond line. Under a flexural loading condition, the overlap region experiences a significantly larger rotation compared

to the joint being subjected to an axial load. Therefore, the failure will be likely due to the large magnitude of peel stress concentration. In contrast, in the case of an axially loaded SLJ, the joint failure would be shear stress-dominated.

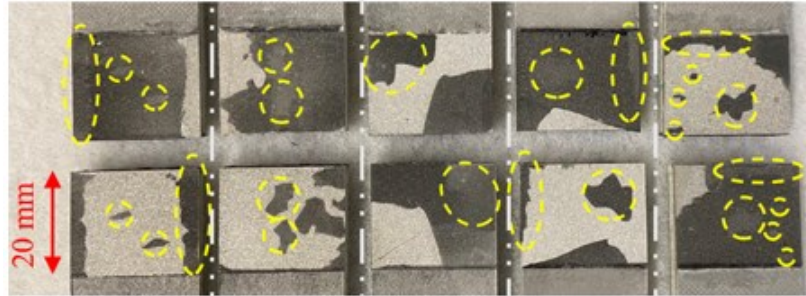


Figure 5-14. Failure surface morphologies of GNP-reinforced 3D-FML SLJs.

The bond failure mechanisms observed in this study are shown in Figure 5-14. In the reinforced joints, the adhesion strength was enhanced as the nanoparticles occupied the micro-voids on the adherends surfaces and created enhanced contact points (Çakır et al., 2021). As can be observed, the hybrid interfacial-cohesion failure mode was observed in the GNP-reinforced SLJs subjected to lap-shear and flexural loading conditions. In this mode, as can be seen, a portion of the failure occurs within the adhesive layers (cohesively), leaving a thin layer of the reinforced adhesive on both adherend bond regions (identified by the yellow dashed lines); while deboning the adhesive from the adherends occurs on the remaining regions of the bond lines.

The micrographs of typical bond fracture surfaces of the GNP-reinforced SLJs are presented in Figure 5-15. As mentioned in previous sections, owing to the superior mechanical property of GNPs, their inclusion enhances the mechanical performance of the SLJs significantly. The strengthening of the reinforced-adhesive is achieved by the GNPs pull-out, bridging, and crack deflection debonding mechanism (Keshavarz et al., 2020). Figure 5-15(a-d) exhibit the pull-out mechanism captured through FESEM analysis. As seen, some of the GNPs which were perpendicularly aligned to the fracture surfaces have been pulled out of the matrix. This mechanism occurs due to the inherent differences in the mechanical properties of GNPs and resin matrix, which also enhances the energy absorption capability, thereby strengthening the reinforced adhesive (Quaresimin et al., 2016). However, in reality, as the examination of the experimental results revealed, the-

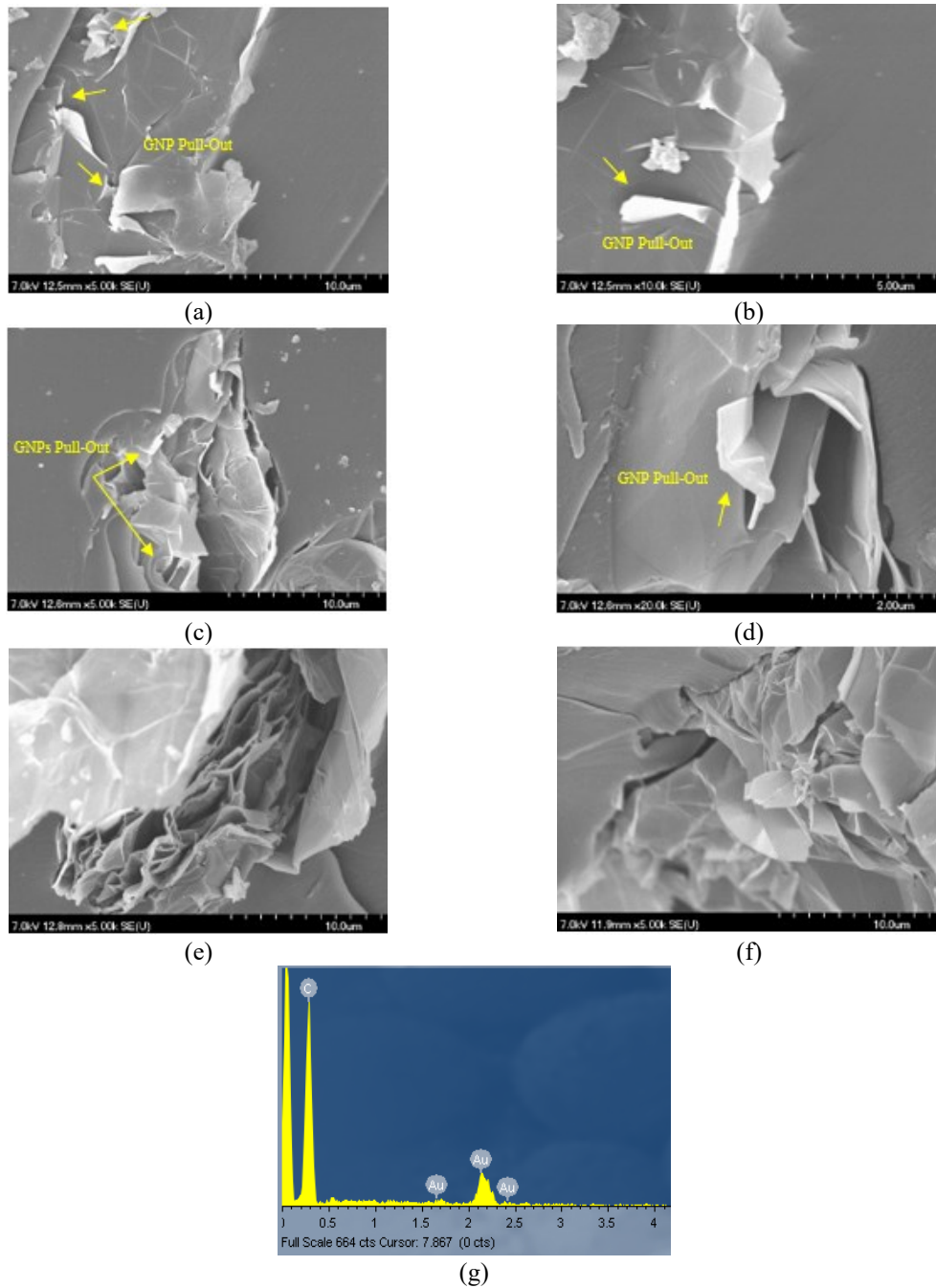


Figure 5-15. FESEM micrographs of the fracture surfaces of 3D-FML SLJs (a–d) GNPs pull-out, (e–f) agglomerated GNPs in adhesive, (g) EDX of a typical GNPs-impregnated adhesive.

inclusion of GNPs in a matrix does not always lead to enhanced mechanical properties. That is because as GNP content is increased, its uniform dispersion within the matrix will be compromised, which would in turn adversely affect the overall fracture toughness of the reinforced matrix. In such a situation, the Van der Waals forces are stimulated leading to the creation of GNP clusters referred to as agglomerations. In turn, stress concentration

would be generated in the agglomerated clusters where the surface areas are relatively small, thus, impeding the strengthening mechanism that could have been attained otherwise (Yaghoobi et al., 2021a). Typically, agglomerated GNP clusters are observed in a relatively heavily loaded GNP matrix as exhibited in Figure 5-15(e-f). It should be noted that the detection of GNP components was achieved through the use of Energy Dispersive X-ray (EDX) microanalysis as shown in Figure 5-15(g).

5.5.2. Numerical Results

The numerically obtained joint capacities are compared against the experimental results for SLJs subjected to the quasi-static lap-shear and flexural loadings in Table 5-5. As seen, a good agreement is observed between the experimental and numerically predicted results. The maximum error in the FE lap-shear test results was determined as 10.8%, while a maximum 5.6% deviation was observed in the bending test results. Figure 5-16 depicts the damage progress of a 3D-FML SLJ modelled by CZM FEM. As stated earlier, when a SLJ is subjected to lap-shear loading, a bending moment will be created due to the relatively flexible and slender nature of the adherends compared to the overlap region. This in turn will develop peel and shear stresses in the overlap region, which would become greatly concentrated near the end regions of the overlap. As a result, the damage would initiate in these regions and propagate towards the mid-span of the overlap, leading to the final failure exhibited in Figure 5-16(a).

Table 5-5. Comparison of the experimental and numerical failure loads of single-lap 3D-FML ABJs.

Samples ID	GNPs (wt.%)	Lap-shear Failure Load			Flexural Failure Load		
		Exp. (kN)	Num. (kN)	% Error	Exp. (kN)	Num. (kN)	% Error
3D-FML-1	0	3.25	3.60	10.8	0.126	0.136	7.9
3D-FML-3	0.5	4.05	4.40	8.6	0.185	0.195	5.4

The damage progress in 3D-FML SLJ bonded with neat epoxy subjected to flexural loading condition is shown in Figure 5-16(b). In this loading configuration, the crack initiates on one of the edges of the bond line. The external and internal bending moments expose one of the free ends to a tensile and the other end to a compressive stress concentration. Consequently, the peel stress would vary from tensile at one end to compressive at the other end. Based on the provided data by the vendor, the adhesive has better performance in compression than tension, the failure initiates in the tension side of

the free edge and then propagates toward the other end. Comparatively, the magnitude of the peel stress generated in the flexure test is larger than that created under lap-shear loading; thus, the peel stress is considered the primary reason for crack initiation and damage propagation in SLJs subject to flexural loadings.

Figure 5-16(c-d) show the development of delamination in the Mg/3DFGF interface of 3D-FML-3 SLJ (with 0.5 wt.% GNP-reinforced-adhesive). As stated earlier, the inclusion of GNPs significantly improved the mechanical interlocking in the bond area of the SLJs, as a result, the crack initiated in the tension zone on Mg/3DFGF interface. As the stress concentration increased, the delamination growth was observed to move toward the other end, leading to the ultimate failure of the joint. Figure 5-16 proves the practicality and effectiveness of the CZM approach for assessing damage mechanisms developed in SLJs. Implementation of an effective CZM within a FE environment would facilitate accurate simulation of the development of crack initiation and its subsequent propagation.

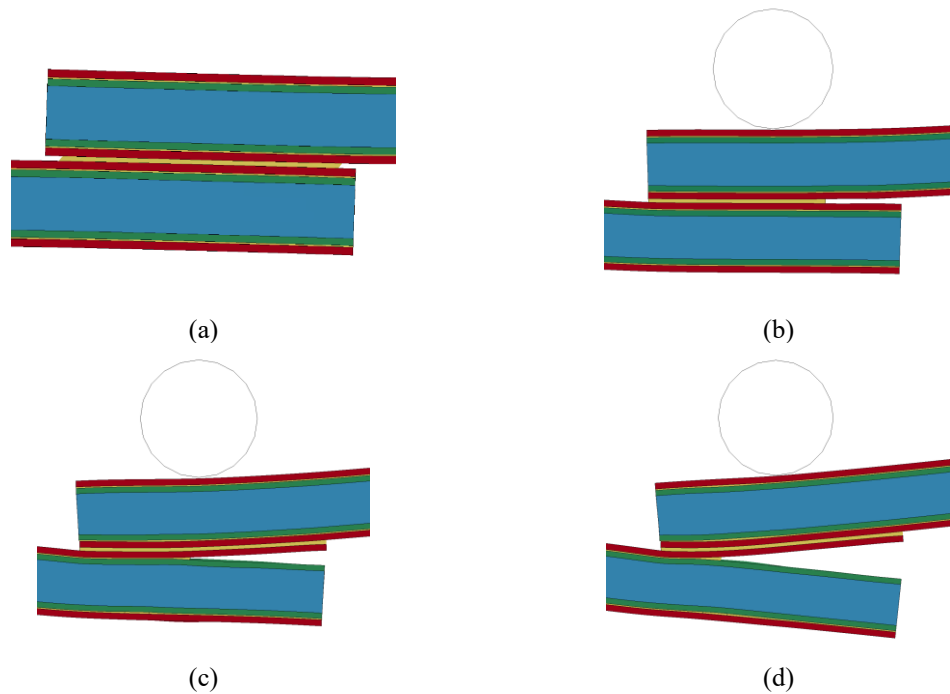


Figure 5-16. Damage propagation in 3D-FML SLJs (a-b) crack growth in bonding area, (c-d) delamination growth in Mg/3DFGF interface.

5.6. Summary and Conclusion

This study presents an investigation into the effects of different GNP concentrations (0, 0.25, 0.5, and 0.75 wt.%) on the flexural and lap-shear performances of single-lap joints mating 3D-FML adherends. The primary aim is to resolve the existing gap in the knowledge and database related to adhesively bonded joints mating 3D-FML under different loading scenarios and compare the performances of 3D-FMLs to their 2D counterparts.

The experimental lap-shear results revealed that SLJs mating 3D-FML adherends produced a similar average joint capacity as SLJs mating MB-2D-FML adherends. However, the normalized joint capacity (with respect to weight) and the energy absorption capacity of 3D-FML SLJs were found to be significantly higher than those offered by their 2D counterparts (by as much as 72% and 146%, respectively). Moreover, the inclusion of GNPs in the adhesive up to a certain extent (0.5 wt.%) resulted in maximum gains of 25%, 30%, 188%, and 26% in the joint capacity, normalized joint capacity (with respect to weight), energy absorption, and shear strength, respectively. However, the inclusion of GNP beyond 0.5 wt.% degraded the joint capacity. All 3D-FML SLJs (i.e., with and without GNPs-reinforced adhesive) exhibited a nonlinear load-deformation response, whereas MB-2D-FML SLJs responded linearly.

By exploring the experimental results obtained from the flexural tests, it was observed the measured mechanical properties were enhanced in all GNP-reinforced 3D-FML SLJs. However, the degree of enhancement was not directly proportional to the wt.% of GNP content. The highest enhancements (in all the aforementioned aspects) were exhibited by 3D-FML SLJs with 0.5 wt.% GNP-reinforced adhesives, while the lowest gain was associated with 3D-FML SLJs with 0.75 wt.% GNP-reinforced adhesive. The maximum gains of 57%, 63%, 35 and 19% in normalized joint capacity (with respect to weight), ultimate strength, strain, and flexural Modulus were observed, respectively.

FESEM micrographs of the fracture surfaces of 3D-FML SLJs evidenced the agglomeration of GNPs in the adhesive containing 0.75 wt.% GNPs, which in turn impede the mechanical effectiveness of GNPs due to high-stress concentration. However, different

strengthening mechanisms, including GNPs pull-out and debonding, were observed in bonded joints with lower GNP contents.

The comparison of the responses of SLJs made with 3D-FML adherends to 2D-FML ones presented in this study should encourage practicing engineers to select 3D-FML in applications where the elongation and weight are the design constraints. The most interesting observation noted in the flexural tests was that the inclusion of 0.5 wt.% GNPs resulted in the generation of such a strong adhesive that it shifted the failure mechanism from the adhesive into the adherend by causing debonding of the Mg/3DFGD interface. The effect of reinforcing this interface region by GNP will be explored in our future studies.

As for the numerical framework developed in this study, the implementation of the mix-mode trapezoidal CZM facilitated the effective and accurate simulation of the response of the SLJs. Moreover, the predicted crack initiation, propagation, and the resulting failure modes, including capturing the delamination that developed in Mg/3DFGF interface, agreed very closely with those observed experimentally. The predicted joint capacities were also simulated with reasonable accuracy, with a maximum error margin of 10.8% and 5.6 in lap-shear and flexural loadings, respectively.

Chapter 6: Performance of a Unique Fiber-Reinforced Foam-Cored Metal Sandwich System Joined with Adhesively Bonded CFRP Straps Under Compressive and Tensile Loadings

Fatemeh Mottaghian, Farid Taheri

Published in the Journal of Applied Composite Materials, PP 339–359, 2023.

This paper has been partially modified compared to its original published version to conform to the format of this thesis and to reduce the repetition of topics covered in Chapter 2.

6.1. Abstract

A new lightweight and resilient sandwich composite panel system, consisting of a unique foam-cored 3D glass fabric sandwiched in between two metal fasciae, was recently introduced. To the best of the authors' knowledge, however, the performance of structural systems configured by the joining of such sandwich systems has not been investigated. This study systematically investigates the performance of double-strap bonded joints designed to mate such sandwich systems. Firstly, the effects of five different combinations of chemical, thermochemical, and mechanical surface modifications on the joint capacity and failure mode are investigated. Subsequently, the effects of CFRP straps' thickness and lengths on the responses of the joined panels subjected to tensile and compressive loadings are investigated. The influence of surface treatments on the failure mode and its transition is also established. Although the joined system shows a similar response in its elastic regime, its post-elastic response varies significantly depending on the joint configuration and surface treatment. It is also observed that there is no direct correlation between the degree of bond regions' surface roughness and joint capacity.

6.2. Introduction

[...] *Some portions of this section have been removed and included in Chapter 2.*

The unique metal sandwich composite used in this paper was developed to further enhance the performance of lightweight fiber-reinforced plastic composites, which was developed by combining the ductility and toughness of thin metal sheets with superior specific stiffness, strength, impact resistance, and fatigue properties of a recently developed 3D-fiber-glass fabric (3DFGF), whose through-thickness core cavities are filled with foam (Asaee et al., 2015). There is, however, a very limited number of studies that have investigated the performances of adhesively bonded joints mating such sandwich composites (Mottaghian & Taheri, 2022). Moreover, most studies have considered the response of adhesively bonded joints subjected to tensile and fatigue loading states and their performance under axial-compressive loading scenarios has not been examined comprehensively. As delamination is the main mode of failure in the metal sandwich system, therefore, the assessment of tensile and compressive performances of adhesively bonded joints mating these materials is of critical importance.

To address the knowledge gap and to contribute to the critically needed database, the performance of double-strap adhesively bonded joints mating the recently developed metal sandwich composite (Mottaghian et al., 2020) subjected to tensile and buckling load is assessed here, to our knowledge, for the first time. The main objectives of this study are (i) to evaluate the effect of five different surface treatment methods on the response of sandwich composite panels joined together with double-strap adhesively bonded joints; (ii) to probe the resulting surface morphologies and surface roughness parameters by confocal laser scanning microscope; (iii) to establish the optimal surface treatment in terms of ease of processing and the resultant joint capacity; (iv) to assess the effects of CFRP straps' length and thickness on the lap-shear and buckling performance of double-strap adhesively bonded joints ; (v) to investigate the differences in the global and local failure mechanisms of the bonded sandwich panels subjected to tensile and compressive loading conditions.

6.3. Material and Methods

6.3.1. Materials

The fabricated double-strap fiber-reinforced foam-cored metal sandwich adhesively bonded joints consist of thin stainless steel sheets, 3D fiberglass fabric, CFRP prepreg, a

cold-cured structural epoxy resin, and a two-part liquid polyurethane foam. Stainless steel 304-2B sheets with 0.48 mm thickness were acquired locally. The 3DFGF with an overall thickness of 4 mm was supplied by China Beihai Fiberglass Co. Ltd. (Jiujiang City, Jiangxi, China). The two-part “16 lb” polyurethane foam was obtained from US Composites (Palm Beach, FL, US). Moreover, the Gurit woven CFRP prepreg with a thickness of 0.25 mm was acquired from Composite Canada (Mississauga, ON, Canada). The West System structural epoxy system (105 resin and 206 slow hardener) was also acquired locally. The mechanical properties of the materials used in this study are tabulated in Table 6-1. Note that the stress-strain curve of the adhesive can be found in (Fatemeh Mottaghian & Taheri, 2022b) and the onset and ultimate glass transition of adhesive based on the supplier’s data sheets are reported as 52.2°C and 59.4°C, respectively.

Table 6-1. Mechanical properties of the materials (Mottaghian & Taheri, 2022b; Mottaghian et al., 2020).

Property	Stainless steel	CFRP	Adhesive	3DFGF		
				Glass plies	Glass pillars	Polyurethane foam
ρ (Kg/m^3)	8027	1870	1180	1750	1750	128.1
E_{11}/E (GPa)	193.74	54	3.17	9	3	0.05
E_{22} (GPa)				9	1	
ν_{12}, ν_{13} or ν	0.29	0.23				0
G_{12}, G_{13} (GPa)				1	1	
G_{23} (GPa)				1	1	
σ_{max}		5.1				
σ_{yield}	0.442					
S_c (GPa)				0.03	0.03	
X_c (GPa)				0.173	0.08	
X_T (GPa)				0.173	0.08	
Y_c (GPa)				0.173	0.08	
Y_T (GPa)				0.173	0.08	

6.3.2. Materials Characterization

In this study, a Keyence profile-analyzing confocal laser scanning microscope model VK-X1000 (Osaka, Japan) was employed to investigate the surface roughness parameters. All measurements were performed at 20X laser magnification. Five different locations on each specimen were tested as per ISO 4287 (ISO, 1997) to maximize the precision of the measurements. In addition, an MTS servo-hydraulic universal testing machine, equipped with a 250 kN load cell, was utilized to conduct the double-strap lap-shear and buckling tests at room temperature. The lap-shear tests were carried out at a constant crosshead speed

of 1.27 mm/min as per ASTM D3528 (2008), while the buckling tests were performed with a constant crosshead speed of 0.5 mm/min as per ASTM E2954 (2020). The values of shear strength were determined using the basic mechanics of material equations ($\tau = F/(2 \times L \times w)$), where, τ , F , L and w , denote the average shear strength, failure load, joint overlap length, and width, respectively. To further maximize the accuracy, at least five specimens were tested in each category. The compressive and tensile tests and confocal laser scanning microscope setups are shown in Figure 6-1.

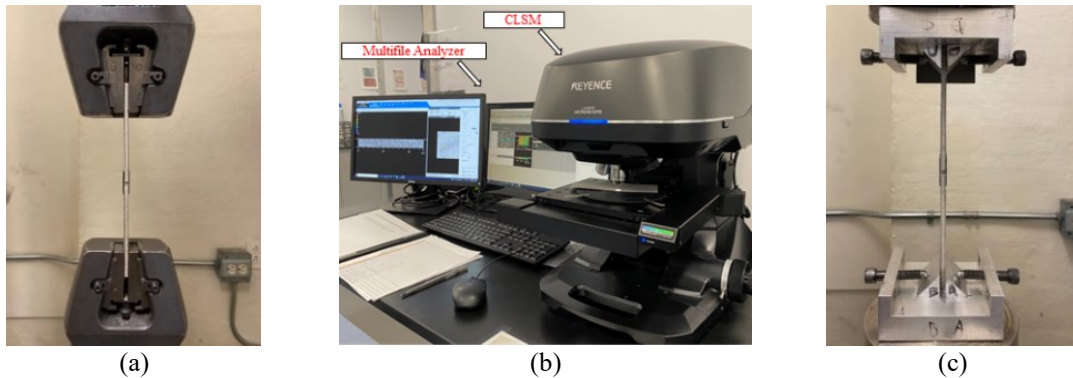


Figure 6-1. (a) Tensile (lap-shear) test setup, (b) confocal laser scanning microscope, (c) compression/buckling test set-up.

6.3.3. Metal Sandwich Panels Fabrication Process

Fabrication of the metal sandwich panels adherends commenced with the fabrication of the core components of the metal sandwich panels. 3DFGF was saturated with structural epoxy with a resin-to-hardener weight ratio of 5:1 and left to cure at ambient temperature for two days. Note that for the sake of consistency in the resin content, after weighing 3D fabrics, the total weight of the resin epoxy system was calculated as $1.3 \times 3\text{D-fabric weight} + 20$. Note that the “20 gr” extra resin in the formula specifically accounts for the wasted resin that remains on the brush and resin container. The amount of resin epoxy system was obtained by many trials in the early stages of our research by subjecting 3DFGF with varying resin weight content to flexural loading tests to assure that (i) consistent mechanical properties would be obtained, (ii) the upper and lower biaxial constituent of 3DFGF would not be “resin-thirsty”, and (iii) the 3DFGF cavities would not be clogged due to excessive amounts of resin. It should be noted that the resin infusion technique would not be suitable for the production of 3DFGF composites as the vacuum would not

allow the 3DFGF, which comes in a 2D configuration in its dry state, to rise and attain its 3D configuration. Consequently, for the sake of consistency, the hand-brushing technique was employed to process the 3DFGF composite constituent of our fiber-reinforced foam-cored metal sandwich system. A 16 lb two-part liquid polyurethane foam with a mixing ratio of 1:1 was utilized to enhance the mechanical response of 3DFGF, which was used to fill the core cavities of 3DFGF. The foam was then left to cure at ambient temperature for one day. Subsequently, the enhanced core components of the metal sandwich panels were sandwiched in between the treated stainless steel sheets, sealed in a vacuum bag under 1 bar vacuum, and left to cure at ambient temperature for two days. Different components of metal sandwich panels are shown in Figure 6-2 and more details of the fabrication procedure can be found in (Yaghoobi et al., 2021a).

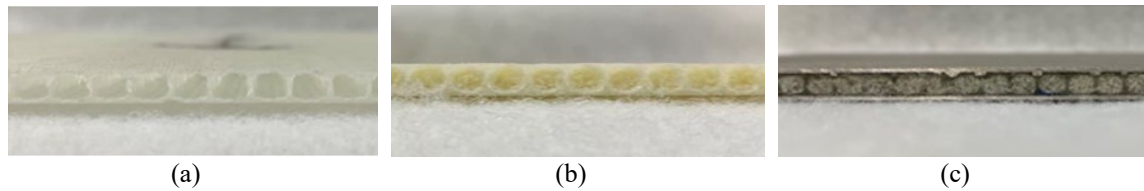


Figure 6-2. Components of the metal sandwich panel (a) 3DFGF-epoxy, (b) 3DFGF cavities infilled with foam, and (c) fiber-reinforced foam-cored metal sandwich system.

6.3.4. Fabrication of Double-Strap Joints

Firstly, appropriate layer numbers of CFRP prepreg were stacked one by one, with each layer having been consolidated by a roller. The CFRP laminate was then sealed within a vacuum bag under a 1 bar vacuum and left to cure in an oven at 120°C for 2hr. Subsequently, the laminate was cut into two equal-size panels and then abraded by 100-grit sandpaper in random directions. The fabricated fiber-reinforced foam-cored metal sandwich system plates were supported against rigid steel plates to ensure they remained aligned during the adhesion processes. The bonding regions were cleaned with isopropyl alcohol, left to dry, and then a thin layer of adhesive was applied to them. Subsequently, one of the CFRP straps was bonded to the 3D-FML under constant pressure and the assembly was cured at the ambient temperature for 6 hrs. Afterward, the second strap was bonded to the fiber-reinforced foam-cored metal sandwich system on the opposite side to the first bonded region, and the double-strap joints assembly was left to cure for 48 hrs at room temperature. Finally, per ASTM D3528 (2008), appropriate-size double-strap

specimens with the dimensions shown in Figure 6-3 were extracted from the bonded assembly. Note that for the sake of accuracy and repeatability of the results, all the specimens were fabricated with an identical procedure, and went under the same processing and rest periods before testing. In other words, all specimens were tested after 48 hrs (\pm 2 hrs), after the bonding of the second CFRP strap to the fiber-reinforced foam-cored metal sandwich system. All fabricated double-strap adhesively bonded joints, their IDs, and their descriptions are summarized in Table 6-2.

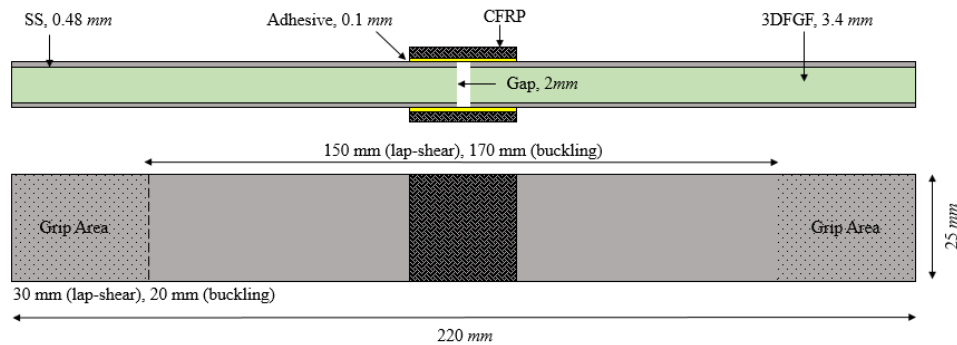


Figure 6-3. Schematics and dimensions of the double-strap bonded metal sandwich panels.

6.3.5. Surface Preparation Techniques

The incorporation of an effective surface treatment procedure has a major role in improving the bond capacity and durability of adhesively bonded joints. The following surface treatment procedures were considered in this study:

Table 6-2. Configurations of the fabricated adhesively bonded joints.

Sample ID	Stacking sequence on Each Side of CFRP Strap	Strap Length (mm)	Strap Thickness (mm)	Performed Test
C3-L25	3 woven plies stacked	25	0.75	Buckling
C5-L25	5 woven plies stacked	25	1.25	Tensile & Buckling
C8-L25	8 woven plies stacked	25	2	Tensile
C5-L35	5 woven plies stacked	35	1.25	Tensile & Buckling
C5-L45	5 woven plies stacked	45	1.25	Tensile

Surface treatment procedure 1, referred to as grit blasting with glass grits (GS, hereafter) entailed degreasing the stainless steel sheets surfaces with acetone, grit blasting them with 30 grit-size crushed glass at 6.9 bars with the gun kept at 60° at a distance of 60 mm to the surface. The surfaces were then whipped with acetone and air-dried. surface

treatment procedure 2, consisted of surface treatment procedure 1 followed by peel-ply coating (referred to as GS+PC, hereafter). In this surface treatment procedure, the GS surface treatment procedure was followed by covering the stainless steel bond regions with a thin layer of resin, which was subsequently covered with a layer of porous woven peel-ply and breather cloth. The assembly was then sealed in a vacuum bag under a 1 bar vacuum and was left to cure for two days at room temperature. The thicknesses of the nylon peel-ply and the polyester breather cloth were 0.1016 and 3 mm, respectively.

Table 6-3. Classifications of the surface treatments.

Codes	Material	Nature of Treatment	Treatment
UT	SS	-	Untreated
GS	SS	Mechanical	Grit blasting with crushed glass grit
GS+PC	SS	Mechanical	Grit blasting + resin coating
GS+AN	SS	Mechanical +Thermochemical	Annealing
AS	SS	Mechanical	Grit blasting with alumina grit
AS+AE	SS	Mechanical + Chemical	Grit blasting with alumina grit + nitric acid etching
UT	CFRP	-	Untreated
AP	CFRP	Mechanical	Abrasive paper

Surface treatment procedure 3 involved surface treatment procedure 1 followed by annealing (referred to as GS+AN, hereafter). After conducting the surface treatment procedure 1, the stainless steel sheets were annealed at atmospheric pressure at 1100°C for 15 mins and then cooled in air. The sheets were then wiped with acetone and then blasted with pressurized air. surface treatment procedure 4 involved grit blasting with alumina grit (referred to as AS, hereafter). In this surface treatment procedure, after degreasing the stainless steel sheets with acetone, they were grit blasted with 30 grit-size alumina grit, and subsequently, the surface was cleaned with acetone and then blasted by air. The grit blasting specifics were the same as that explained in surface treatment procedure 1. Surface treatment procedure 5 is referred to as AS+AE, which entailed surface treatment procedure 4 followed by acid etching. In this procedure, after performing the surface treatment procedure 4, the stainless steel sheets were washed with distilled water, rinsed under deionized water, and then immersed in a solution of 20% volume nitric acid and 80% volume distilled water at the ambient temperature for 30 mins. Subsequently, the sheets were rinsed under cold water followed by deionized water and dried in an oven at 50°C for 45 mins. The above surface treatment procedures are summarized in Table 6-3.

6.4. Results and Discussions

6.4.1. Microscopic Analysis

The surface topography images of the stainless steel sheets treated by the different surface treatment procedures are shown in Figure 6-4(a). The strong orientation resulting from the cold rolling manufacturing process of stainless steel sheets can be observed in the untreated (UT) stainless steel sheets illustrated in Figure 6-4(a). Indeed, the texture of the UT specimen is relatively smooth and uniform with relatively shallow peaks and valleys, which were significantly altered by the GS and GS+PC surface treatment procedures. Based on Figure 6-4(b), the GS surface treatment procedure generated several micron-scale pits; however, rough-oriented patterns were created with the GS+PC surface treatment procedure due to the residual imprint of peel-ply and resin on the surface of stainless steel sheets (see Figure 6-4(c)). As seen in Figure 6-4(d), significantly different surface topography was generated by the GS+AN surface treatment procedure compared to the surfaces generated by the GS and GS+PC procedures. Annealing the stainless steel sheets led to the creation of a rough oxide layer and several randomly distributed micron-scale pits. Moreover, as seen in Figure 6-4(e-f), the AS and AS+AE surface treatment procedures created surfaces with a large number of micron-scale pits that resemble the ones created by the GS surface treatment procedure. The untreated CFRP surfaces had several oriented patterns resembling imprints, similar to that seen on the surfaces treated by the GS+PC surface treatment procedure. However, the AP surface treatment procedure removed the imprint and left a randomly distributed textured surface on the CFRP straps.

To further investigate the surface roughness produced by the different procedures, the surface arithmetical mean height (S_a) is evaluated based on the $S_a = \frac{1}{A} \iint_A |Z(x, y)| dx dy$ equation (ISO, 1997), where A and Z indicate the sampling area and height of the point, respectively, acquired at (x, y) position on the surface. Note that the schematic of this surface parameter is shown in Figure 6-5(a). The average S_a generated by different surface treatments is tabulated in Table 6-4.

As seen, the Sa roughness was significantly improved by the GS surface treatment procedure compared to the untreated surfaces. Also, the Sa roughness values generated by the AS and AS+AE surface treatment procedures were 9.7% and 19.1% higher than that by the GS surface treatment procedure. It can also be concluded that the Sa value produced by the GS+AN and GS+PC surface treatment procedures resulted in 64.5% and 267.7% improved roughness compared to the GS-produced Sa.

The Sa parameter, however, does not account for any differences in the orientation of the surface roughness, therefore, it might not be the most appropriate criterion for assessing the efficacy of a given surface treatment procedure. To further investigate the metal/polymer interlocking, the profile arithmetical mean height (Ra) was calculated for each surface treatment procedure using the $Ra = \frac{1}{lr} \int_0^{lr} |Z(x)| dx$ equation (ISO, 1997), where lr and Z stand for the sampling length and height of the point of interest on the profile at the (x) position, respectively. Figure 6-5(b) represents the schematic of Ra. The average Ra roughness parameters corresponding to each surface treatment procedure, which were determined by incorporating a multiline analyzer, are reported in Table 6-4. As seen, the AS and AS+AE surface treatment procedures generated gains of 26.0% and 33.3% in Ra surface roughness, respectively, compared to the gain produced by the GS surface treatment procedure. The GS+PC and GS+AN surface treatment procedures resulted in 248.5% and 96.3% improvements in the corresponding Ra parameters, respectively, compared to that produced by the GS surface treatment procedure.

The maximum height of the profile (Rz) and the arithmetic mean width of profile elements (Rsm) are the other parameters that could be evaluated by the confocal laser scanning microscope, which are presented in Figure 6-5(c-d). The values of the calculated Rzs and Rsms are reported in Table 6-4. The highest value of the Rz parameter is 53.7 μm , which corresponds to the GS+PC surface treatment procedure. The average values of Rz follow the same trend. On the other hand, the maximum value of Rsm of 400.1 μm , which indicates the average horizontal dimension of the parallel grooves, was produced by the AS+AE surface treatment procedure. In contrast, the GS+PC surface treatment procedure developed the lowest value of Rsm (149.0 μm).

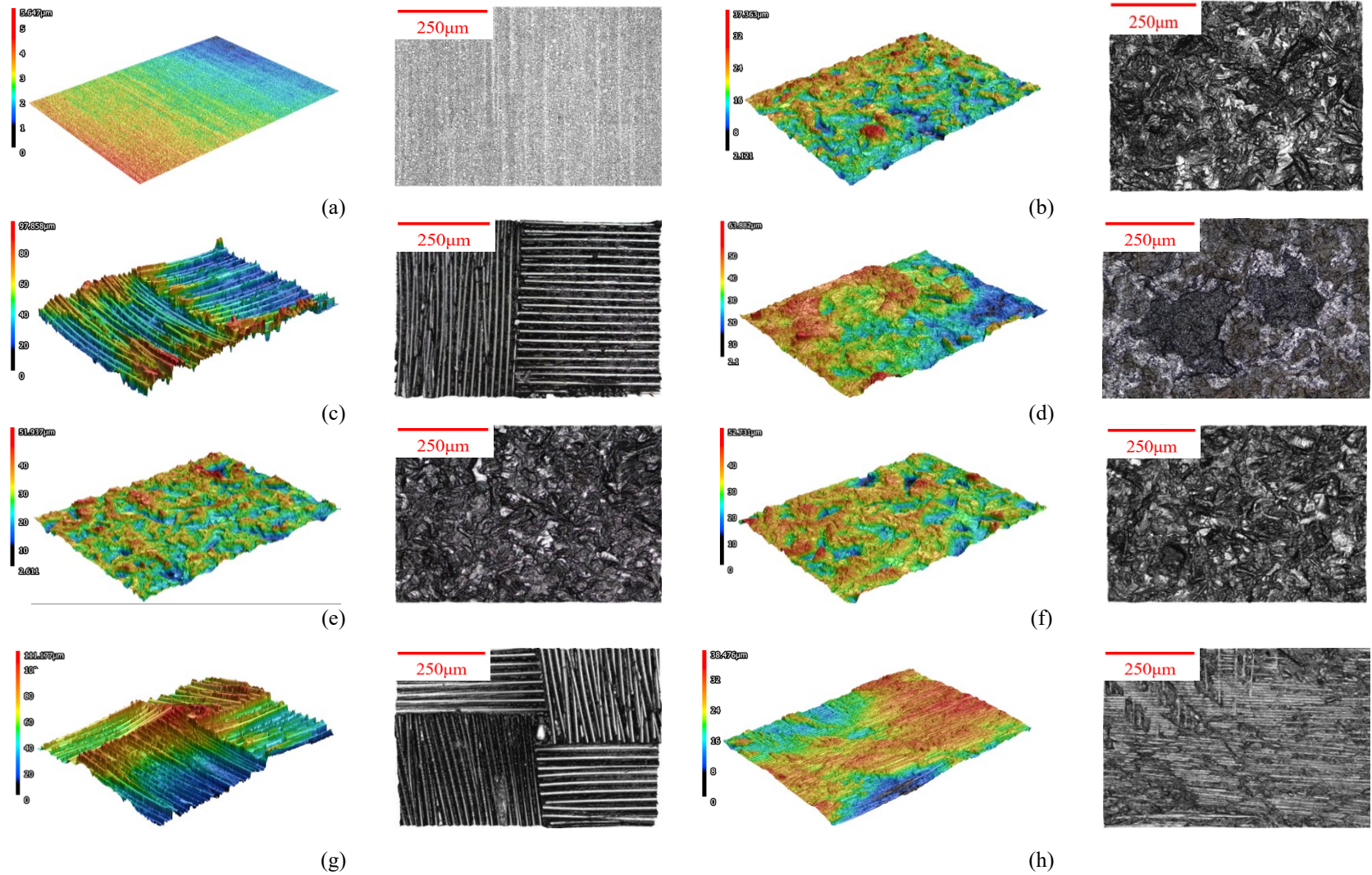


Figure 6-4. The surface topographies of (a) UT, (b) GS, (c) GS+PC, (d) GS+AN, (e) AS, (f) AS+AE, and (g) UT CFRP, and (h) AP surface treatments.

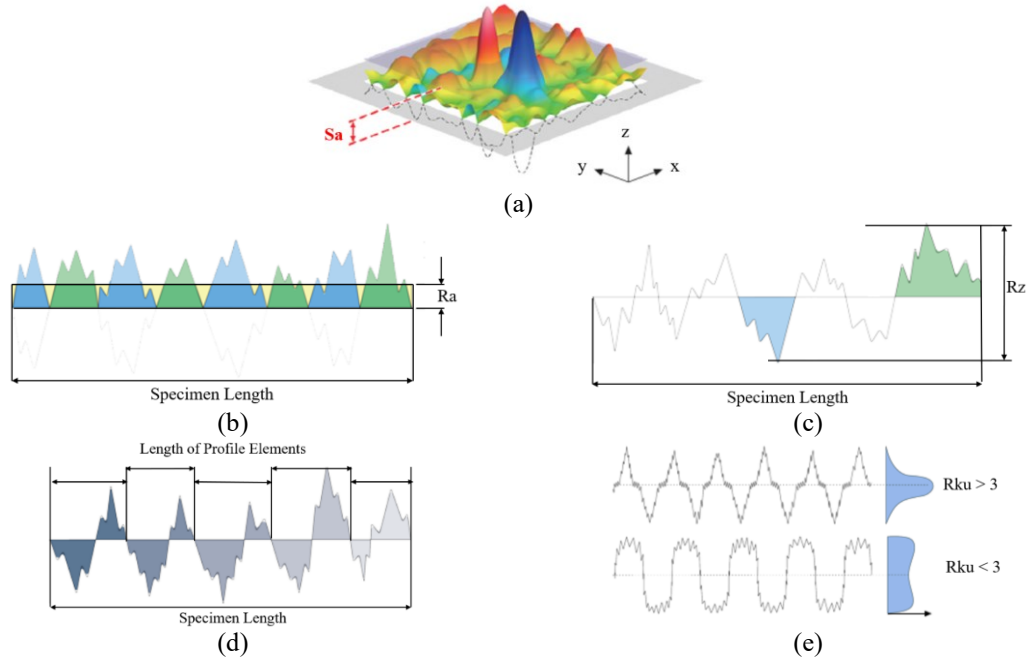


Figure 6-5. Schematic of surface roughness parameters (a) Sa, (b) Ra, (c) Rz, (d) Rsm, and (e) Rku (Mikroskop-Lösungen.)

The maximum Kurtosis (Rku), which represents a measure of the sharpness of a given profile's peaks, is also a valuable parameter to consider. As can be seen in Figure 6-5(e), $Rku > 3$ denotes a sharp profile peak, whereas $Rku < 3$ indicates that blunted shape asperity peaks are generated on the surface. Ironically, according to the values reported in Table 6-4, the GS+PC surface treatment procedure that generated the highest values of Sa, Ra, -

Table 6-4. Joint capacities, shear strength, and average surface roughness parameter values for C5-L25 configuration.

Specimen	Parameter					Joint Capacity (kN)	Shear Strength (Mpa)
	Sa (μm)	Ra (μm)	Rz (μm)	Rsm (μm)	Rku (μm)		
UT	0.2 ± 0.00	0.2 ± 0.0	1.7 ± 0.2	85.0 ± 18	3.2 ± 0.30	-	-
GS	3.1 ± 0.50	2.7 ± 0.3	20.0 ± 6.4	161.1 ± 60	3.2 ± 0.31	7.80 ± 0.67	25.22 ± 2.16
GS+PC	11.4 ± 0.80	9.4 ± 1.5	53.7 ± 7.8	149.0 ± 44	2.9 ± 0.32	8.39 ± 0.42	27.23 ± 4.08
GS+AN	5.1 ± 0.40	5.3 ± 0.4	29.7 ± 4.3	260.8 ± 41	3.3 ± 0.96	7.21 ± 0.59	22.58 ± 2.44
AS	3.4 ± 0.30	3.4 ± 0.2	24.0 ± 2.3	157.9 ± 14	3.4 ± 0.22	9.67 ± 0.36	30.48 ± 1.28
AS+AE	3.7 ± 0.02	3.6 ± 0.1	29.5 ± 4.6	400.1 ± 65	3.7 ± 0.47	9.71 ± 0.35	30.76 ± 1.00
UT	11.4 ± 1.50	7.4 ± 0.5	44.2 ± 2.5	180.1 ± 36	3.1 ± 0.45	-	-
				295.2 ± 62	3.4 ± 0.52		
AP	10.1 ± 1.00	5.5 ± 1.7	32.6 ± 10.4			-	-

and Rz roughness parameters produced the lowest Rku parameters. The maximum peak sharpness was achieved by the AS+AE surface treatment procedure with a magnitude of 3.7 μm . In reference to CFRPs' surfaces, the AP surface treatment procedure essentially removed the imprint traces on the surface, resulting in lower values of Sa, Ra, and Rz surface roughness parameters. In contrast, gains of 64.0% and 6.5%, in the values of RSm and Rku, respectively, were observed.

6.4.2. Effects of Surface Treatments on Joint Capacity

In adhesively bonded joints, the cavities on adherends produced by a surface treatment procedure are filled by the adhesive and subsequently, a mechanical connection is formed upon curing of the adhesive (Yang et al., 2001). Roughness, porosity, and irregularity of the bonding surface are the main factors affecting the quality of the mechanical interlocking mechanism (Yang et al., 2019). Consequently, the greater surface roughness produced by a given surface treatment procedure is expected to improve the interlocking, and in turn, the resulting bond strength. To study the effects of surface roughness on the load-carrying capacity and bond strength of the double-strap bonded metal sandwich composite system, five configurations of specimens were fabricated for each of the surface treatment procedures and were subjected to tensile loading.

Based on the results reported in Table 6-4, the joint capacities in double-strap adhesively bonded joints prepared by the GS+PC surface treatment procedure were on average 7.7% higher than that processed by the GS surface treatment procedure. Ironically, the GS+PC had produced 248.2% and 267.7% higher Ra and Sa roughness parameters, respectively. This indeed indicates that the oriented patterns generated by the GS+PC surface treatment procedure did not result in higher adsorption and fundamental adhesion and were indeed counterproductive. This could also be due to the low peak sharpness (Rku) as well as the arithmetic mean width of the profile elements (Rsm) generated by the GS+PC surface treatment procedure. Another important observation is that although annealing was reported to produce improved bonding between metals and fiber-reinforced plastics (Ghiotti et al., 2021), in our study, however, annealing led to a 7.6% reduction in the joint capacity compared to the capacity of the joints produced by simple grit blasting (GS)

surface treatment procedure. To further investigate the integrity of the results corresponding to annealing, another set of specimens was prepared, fabricated, and tested by incorporating the same surface treatment procedure. The results revealed negligible differences compared to the first set of results. It is believed that the annealing procedure generated a layer of oxidation on the surface of stainless steel sheets, which led to an increase in the overall thickness of the sheets (i.e., stainless steel sheets thickness + oxidation layer thickness), nevertheless, the original thickness of stainless steel sheets was reduced. Note that the reduced stainless steel thickness would adversely affect the overall stiffness of the double-strap joints, thus reducing the joint capacity.

Table 6-5. The average dimension of C5-L25 configuration adhesively bonded joints.

Surface Treatment	Sandwich Thickness (mm)	Double-strap Thickness (μm)	Sandwich Width (mm)	CFRP Strap Length (mm)
GS	4.93 \pm 0.04	7.42 \pm 0.14	24.70 \pm 0.11	25.01 \pm 0.01
GS+PC	5.10 \pm 0.08	7.47 \pm 0.05	24.65 \pm 0.25	25.01 \pm 0.03
GS+AN	5.06 \pm 0.18	7.42 \pm 0.10	25.55 \pm 0.53	24.98 \pm 0.01
AS	5.03 \pm 0.03	7.44 \pm 0.09	25.36 \pm 0.12	25.02 \pm 0.02
AS+AE	5.10 \pm 0.13	7.40 \pm 0.15	25.28 \pm 0.34	24.97 \pm 0.04

The joint capacities of adhesively bonded joints treated by AS and AS+AE surface treatment procedures exhibited gains of 24.1 % and 24.0 %, respectively, compared to that of the base specimen (GS). Interestingly, although the Ra and Sa values in the AS+AE surface treatment procedure were 5.9% and 8.8% higher than those in the AS surface treatment procedure, a negligible improvement in the joint capacities was obtained from the two surface treatment procedures. since the etching procedure is labour-intensive, hazardous, time-consuming, and thus significantly costly compared to the AS surface treatment procedure, the AS is ranked as the optimal surface treatment procedure among the surface treatment procedures considered here. It is also concluded that higher surface roughness would not guarantee a more effective interlocking mechanism. In other words, joint capacity cannot be directly correlated to surface roughness.

The strengths of the double-strap joints mating the metal sandwich panels prepared with the different surface treatment procedures were also evaluated based on the basic mechanics of the material equation noted earlier and are tabulated in Table 6-4. The average dimensions of the fabricated specimens are reported in Table 6-5. As seen, the

joint strengths of the specimens processed using the GS+PC surface treatment procedure were improved by an average of 7.8% by implementing the peel-ply coating method, compared to the specimen treated with the GS surface treatment procedure. Also, the capacities of joints prepared by the GS+PC and GS surface treatment procedures were greater than the capacity of the joints prepared by the GS+AN surface treatment procedure by 17.0% and 10.6%, respectively. On the other hand, the joint strengths of adhesively bonded joints prepared by as and AS+AE surface treatment procedures were improved by 20.7% and 21.8%, respectively, compared to the base specimen. Therefore, based on the results, the optimal surface treatment for fabricating effective Adhesively bonded joints would also be the AS surface treatment procedure

6.4.3. Effects of Surface Treatment on Failure Mode

Failure modes in adhesively bonded joints are generally classified into four modes; that is (i) interfacial mode, (ii) cohesion mode, (iii) mixed-mode, and finally (iv) adherend mode. The effects of different surface treatment procedures on the failure modes in the bonded sandwich system which were subjected to tensile tests are shown in Figure 6-6. Observation of the specimens' surfaces prepared with the GS and GS+PC surface treatment procedures shown in Figure 6-6(a-b) reveals that most of the adhesive remained on the post-failure surface of the CFRP straps, with tiny amounts of adhesive remaining on both adherends. This indicates that the interlocking mechanism within the adhesive and adherend was insufficient. As a result, the crack propagated rapidly in an irregular path through the interface region, thus, generating an interfacial failure mode. Ironically, a negligible difference between the failure modes in the specimens treated with the GS and GS+PC surface treatment procedures could be observed. However, the Ra and Sa surface roughness parameters of the GS+PC surface treatment procedure were significantly higher than that produced by the GS surface treatment procedure. A closer analysis reveals that the GS and GS+PC surface treatment procedures produced similar texture surfaces on the sheets, and the imprint produced by peel-ply coating could not be observed in the post-failure region of the specimens treated with the GS+PC surface treatment procedure. This would indicate that the extra layer of resin coating applied in the GS+PC surface treatment procedure could not generate more effective interlocking between the adhesive and

adherends; however, the extra resin layer developed a significantly stronger adhesion in the adhesive/CFRP interface, and also increased the overall thickness of the adhesive layer in the bond regions. The failure of the joints treated by the GS+PC surface treatment procedure occurred in the interface of the extra layer resin coating and SS sheets. Although the surface imprint produced by the GS+PC surface treatment procedure generated higher roughness, however, the oriented patterns were not effective in strengthening the interlocking mechanism between the adhesive and adherends.

Based on Figure 6-6(c), the failure mode in the joints prepared by the GS+AN surface treatment procedure is a combination of cohesion and interfacial modes. As can be seen, traces of adhesive remained on some of the regions on the CFRP strap and stainless steel adherends surfaces. However, no adhesive is seen on other regions on the CFRP or stainless steel surfaces. Moreover, the lighter colour patches indicate crack initiation and propagation path. Note that the darker colour of the stainless steel sheets in the picture is an outcome of the annealing process. In Figures 6(d-e), one can observe a mixture of cohesion and interfacial modes generated by the AS and AS+AE surface treatment procedures. Ironically, although the surface roughness values generated by the GS+AN surface treatment procedure are higher than those generated by the AS and AS+AE surface treatment procedures, the noted failure-type regions seem to be quite similar in the specimens undergoing the two surface treatment procedures.

One could also see the crack initiation and propagation paths in the adhesive that had remained on the CFRP straps and stainless steel surfaces, which occurred due to the high-stress concentration transferred in the adhesive due to the sufficient interlocking mechanism. Furthermore, the imprints of CFRP on the adhesive remaining on the stainless steel adherends are also visible, which further evidences the strong interlocking mechanism between the stainless steel adherends and adhesive. Note that such imprint traces are not seen on any of the fracture surfaces of the specimens processed by the other surface treatment procedures. This is yet another piece of evidence that a rougher surface would not necessarily lead to a higher joint capacity since it essentially would not guarantee a stronger interlocking mechanism. In addition, the similarity in the combined interfacial and cohesion failure mode generated by the AS and AS+AE surface treatment procedures is

also in concert with the similarity in the resulting joint capacities. Thereafter, as previously, the AS Surface treatment procedure is still ranked as the preferred surface treatment procedure based on the above-noted results and observation. Consequently, the surface treatment procedure was used to process the specimens required for the supplementary investigation outlined below.

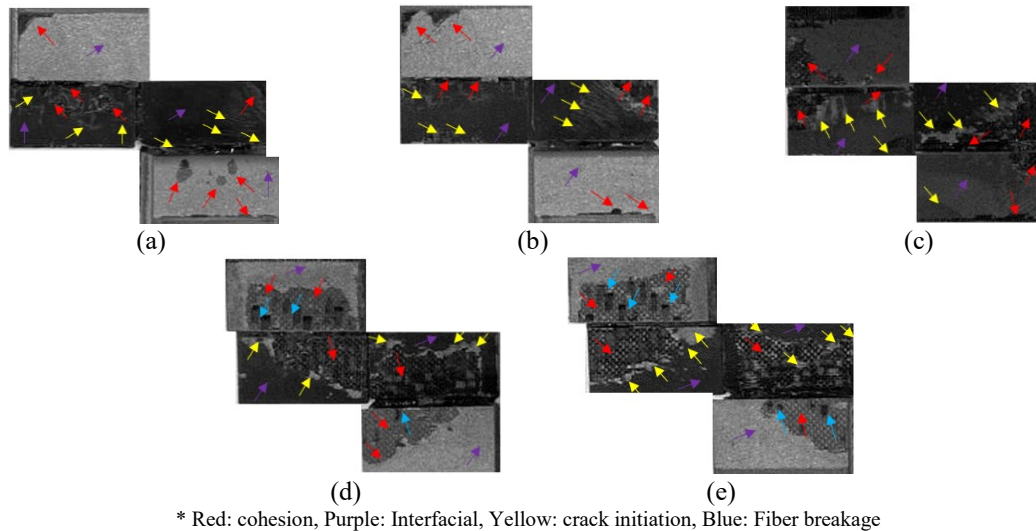


Figure 6-6. The failure modes in the bond regions of adhesively bonded joints prepared by different surface treatment methods: (a) GS, (b) GS+PC, (c) GS+AN, (d) AS, (e) AS+AE.

6.4.4. Effects of CFRP Strap Geometry on Buckling and Tensile Capacities

6.4.4.1. Tensile Loading

To assess the influence of the CFRP straps' thickness and length on the joint capacity, four configurations of double-strap adhesively bonded joints were fabricated and tested under tension. The straps were fabricated with two different thicknesses (i.e., 5 and 8 layers of biaxial woven CFRP on each side of the strap) and three overlap lengths (i.e., 25 mm, 35 mm, and 45 mm), as summarised in Table 6-2. A summary of the capacity and performance of the fabricated joints are reported in Table 6-6 and Figure 6-7, respectively. The results shown in the figure reveal that the joint capacity was improved by 20.8% when the strap length was increased from 25 mm to 35 mm. However, a further increase in the strep length did not improve the capacity markedly, indicating that the effective overlap length of the joint is approximately 35 mm. Moreover, a further increase in the CFRP strap thickness led to a reduction of 24.8 % (see the curves corresponding to C8-L25 and C5-25

configurations). It appears that the increased strap thickness resulted in an over-stiffened strap in comparison to the adherends' stiffness, thereby developing higher stress concentration at the discontinuities in the ends of the straps. Therefore, not only did a thicker CFRP not help to improve the stress distribution, but it also caused higher stress concentrations, thereby causing a reduced joint capacity. Note that the normalized tensile joint capacities are calculated with respect to the joint capacity of the base specimen (i.e., C5-L25); additionally, the normalized tensile joint capacities with respect to the weight of each group of specimens are tabulated in Table 6-6.

Table 6-6. Average values of the capacity, energy absorption, and strength of each group of double-strap ABJ systems.

Sample ID	C3-L25	C5-L25	C8-L25	C5-L35	C5-L45
Tensile (lap-shear) joint capacity (kN)	-	9.67±0.4	7.27±0.9	11.68±0.8	11.71±0.8
Normalized tensile joint capacity w.r.t the base specimen	-	1	0.75	1.21	1.21
Normalized tensile joint capacity w.r.t the specimen weight (kN/g)	-	0.17	0.13	0.20	0.20
Shear strength (MPa)	-	30.50±0.2	23.14 ± 2.6	26.43±1.7	20.71±1.6
Normalized shear strength w.r.t the base specimen	-	1	0.76	0.87	0.67
Energy absorption capacity (kN-mm)	-	26.85 ± 4.8	17.10 ± 5.9	41.73±4.1	45.38±4.7
Normalized energy absorption w.r.t base specimen	-	1	0.64	1.56	1.69
Buckling joint capacity (kN)	5.92±0.1	7.20 ±0.3	-	6.90±0.3	-
Normalized buckling joint capacity w.r.t base specimen	0.82	1	-	0.96	-
Normalized buckling joint capacity w.r.t the specimen weight (kN/g)	0.10	0.13	-	0.12	-

The average shear strengths produced by the different configurations are also summarized in Table 6-6. The results indicate that the average shear strength of the base specimen group (i.e., C5-L25) was greater than the counterpart groups that had longer straps (i.e., C5-L35 and C5-L45) by 13.3% and 32.1%, respectively. Moreover, the configuration with the thicker straps (C8-L25) showed 24.1% lower shear strength than the C5-L25 group that had thinner straps. This is somewhat of an interesting phenomenon in that the joint with the higher local stiffness exhibited a weaker response, which follows the earlier stated reasoning. The normalized shear strength values with respect to the base specimen (e.g., C5-L25) are also reported in Table 6-6.

The effects of CFRP strap length and thickness on the energy absorption capacity of the joints were also established by evaluating the area under the load-displacement curves, as reported in Table 6-6. The average energy absorption capacity of the joints with the thinner straps (C5-L25) was 36.3% higher than their thicker strapped counterparts (C8-L25). In contrast, the increase in the length of the strap from 25 to 35 mm led to a 55.4% enhancement in the energy absorption capacity. However, the joints with 45 mm straps produced only 8.7% additional energy absorption capacity. From the energy absorption perspective, therefore, one may then consider the 35 mm strap length as the optimal strap length for the joints. The energy absorption values are summarized in Table 6-6.

6.4.4.2. Compressive Loading

As mentioned, a great majority of the research conducted on adhesively bonded joints has mainly focused on exploring the performance of joints under an applied tensile load; some works have also considered the fatigue response of adhesively bonded joints. However, in most practical applications, adhesively bonded joints often encounter in-plane compressive loading states, which could potentially result in buckling of the joints. Therefore, investigation of the performance of adhesively bonded joints under a compressive loading state would be important and critical in joint mating fiber-reinforced plastic composites and sandwich composites addends. This is because such adherends are susceptible to buckling delamination, a phenomenon not experienced by their isotropic adherend counterparts. Therefore, the response of the double-strap adhesively bonded joints under a compressive loading state was investigated in this study.

The typical load-axial shortening responses of the adhesively bonded joints subjected to an in-plane compressive loading state are shown in Figure 6-7. The buckling joint capacity, the normalized buckling joint capacity calculated with respect to the capacity of the base specimen (i.e., C5-L25) as well as the normalized buckling joint capacity calculated with respect to the weight of each group of the specimen are also summarized in Table 6-6. As seen, the increase in the thickness of each CFRP strap from three (C3-L25) to five layers (C5-L25) led to a gain of 21.6% in the buckling capacity of the joint. On the other hand, the increase in the length of the straps had a negligible effect, and the

buckling capacity was indeed reduced by only 4.1 %. This is opposite to the expected notion that the increase in the length of the strap would increase the buckling capacity, as the increase in the length would enhance the stiffness of the joint, locally. However, it is believed the resulting decrease in the buckling capacity is due to the observed failure mode, which will be discussed in detail, later. It should also be noted that although all adhesively bonded joint groups responded similarly in the pre-buckling stage of loading, their performances were significantly different in the post-buckling regime.

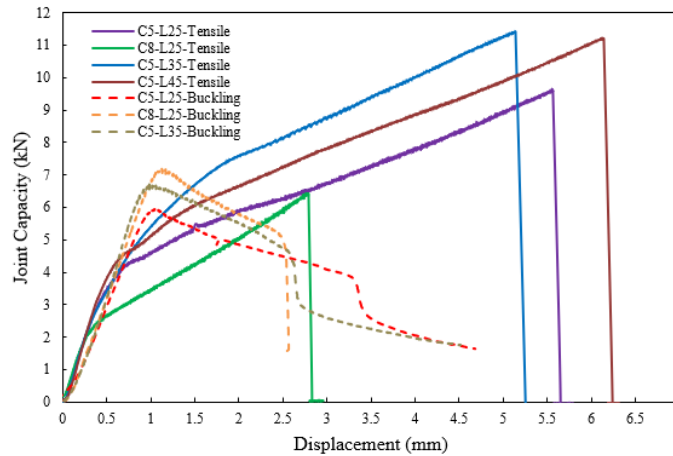


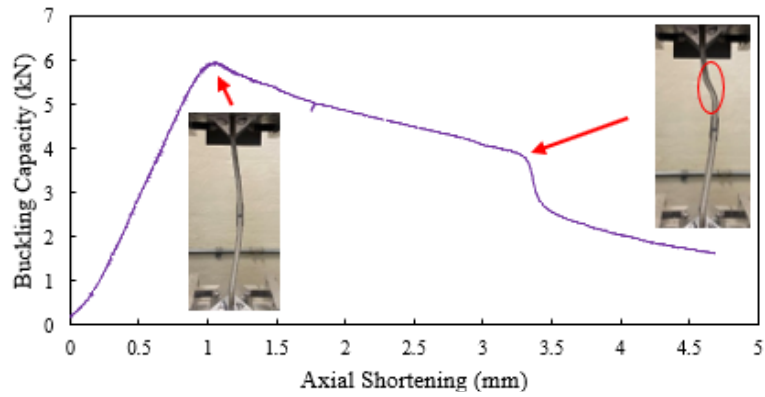
Figure 6-7. The typical load-displacement response of different double-strap ABJ configurations subjected to tensile and compressive loadings.

As can be seen from Figure 6-8(a), the C3-L25 configuration responded in a fundamental Euler buckling mode until it reached its maximum buckling capacity. In other words, the specimen behaved elastically until reaching the 1.2 mm displacement, after which, the specimens underwent significant axial shortening during the post-buckling stage. Subsequently, the specimen experienced a sudden change in the load-bearing capacity (at ~ 3.3 mm deformation), which was accompanied by a shear crimping-like local buckling response of one of its sandwich adherends and asymmetric lateral deformation. The deformation of the specimen continued, and the buckling capacity decreased drastically due to the crushing of the core constituent of the specimen. Core shear crimping is an unstable buckling mode, which often occurs near the restrained (gripped) region and is developed due to insufficient shear stiffness of the core, resulting in excessive shear deformation as opposed to rotation (Coburn & Weaver, 2016). Note that, even after the

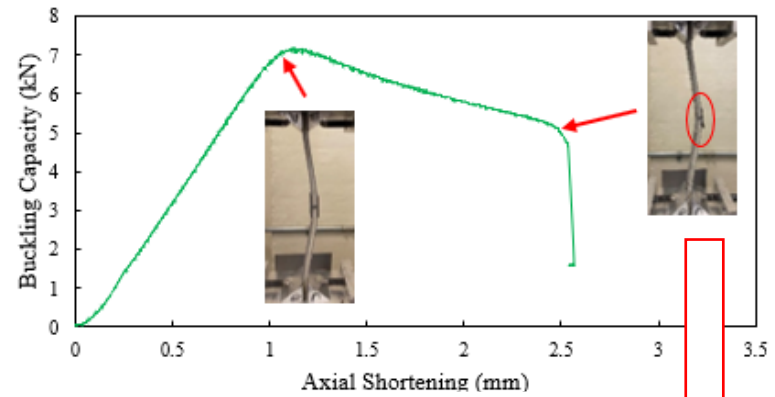
onset of this failure mode, the specimen was able to endure a small amount of load, undergoing a rather non-catastrophic failure mode.

This phenomenon was also observed in another investigation, where the response of intact stainless steel-based sandwich composites to compression loading was assessed (Mottaghian et al., 2020). This proves that the thickness of the CFRP straps in the C3-L25 configuration, which was obtained based on analytical calculations, is the minimum allowable thickness that could be used in joining such sandwich adherends. In other words, in the C3-L25 configuration, the stiffness of the two straps (3-layer CFRP on each side) is equal to the stiffness of the intact sandwich composite.

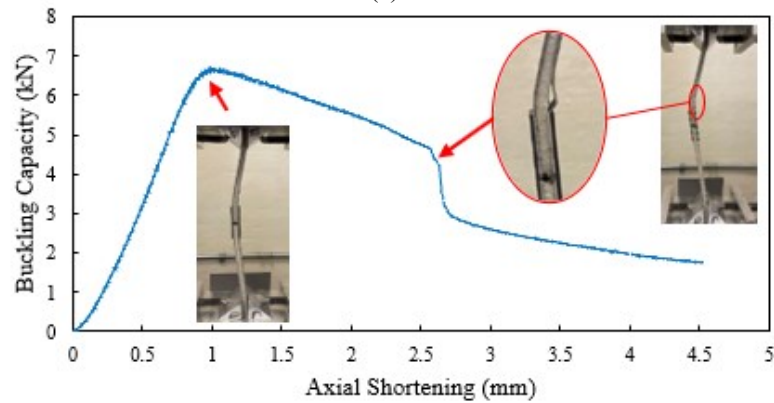
Figure 6-8(b) shows the typical pre- and post-buckling responses of the C5-L25 joint and their typical failure mode. After attaining the maximum buckling capacity, the specimens underwent additional axial shortening, deforming in the fundamental Euler buckling mode while still enduring some load. Once the specimen reached the axial shortening of 2.5 mm, the bonded region failed catastrophically and one of the CFRP straps deboned abruptly from the sandwich adherends (see Figure 6-8(c) for the detail). The other CFRP strap also experienced a sudden crack propagation in the axial direction, which started from the edge of the overlap toward the mid-span. Based on Figure 6-8(c), a combination of cohesion and interfacial failure can be observed in the bond surfaces, where the imprint of CFRP on the adherend is also visible. Further analysis of Figure 6-8(c) reveals that the combination of cohesion and interfacial modes visible on the surface identified by ① is greater than that on the surface ②. As can be seen, the combination of cohesion and interfacial failure mode on the surface ① is shown with the red and purple arrows, respectively. As seen, however, the failure mode is mostly interfacial on the surface ②. Moreover, CFRP imprint can also be seen on the surface ①, indicating that the surface ① had a more effective interlocking mechanism compared to the surface ②. This could be due to the presence of the higher number of voids on the interface adhesive remaining on the surface ② and also the inevitable minute imperfections that could have been developed during the manufacturing of sandwich adherends on the surface ② (i.e., the lower adherend surface in Figure 6-8(c)), which resulted in the development stress concentrations.



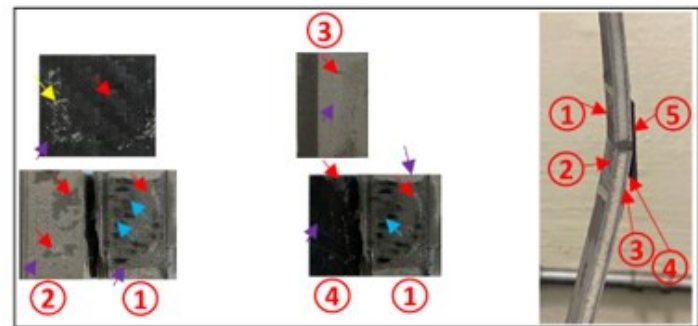
(a)



(b)



(d)



* Red: cohesion, Purple: Interfacial, Yellow: crack initiation, Blue: Fiber breakage

(c)

Figure 6-8. Buckling responses of (a) C3-L25, (b) C5-L25, (c) closer view of C5-L25, (d) C5-L35 configurations.

The comparison indicates that the crack propagation and the consequential failure were first initiated from the surface ②, and then propagated toward the surface ①, which led to the complete separation of the CFRP strap. The same trend was also observed on surfaces ③ and ④, indicating that the interfacial and cohesion strengths generated on the surface ⑤ were greater than those generated on surfaces ③ and ④. Thus, the crack was initiated from this interface. On the other hand, the greater cohesion and interfacial strengths reflect the more effective interlocking mechanism of the surface ⑤, which in turn prevented the crack initiation and propagation on that surface. Consequently, the surface ⑤ did not experience interfacial debonding.

The failure mechanism in the C5-L35 configuration, which was ranked as the most resilient configuration based on the configuration's performance under tensile loading, is shown in Figure 6-8(d). As seen, the load-axial shortening response of this configuration is very similar to the C5-L25 configuration with one difference that shear crimping did not occur in the C5-L35 configuration. However, a local delamination-buckling occurred in this configuration in an earlier stage (at the axial shortening of 2.7 mm compared to 3.3 mm for C5-L25).

The delamination was initiated between the interface of stainless steel and the 3DFGF core, right at the edge end of the strap. It appears that the increase in the combined thickness and length of the strap, which developed more local stiffness in comparison to the straps in the C3-L25 configuration, behaved like somewhat of a gripping boundary condition and combined with the geometric discontinuity, led to the development of a large stress concentration at the edge of the bonded strap (see the region bounded by an ellipse in Figure 6-8(d)). The developed delamination resulted in a sudden decrease in the strain energy and load capacity, causing a significantly large asymmetrical lateral deformation. Nonetheless, the specimen could still carry some load after the local delamination-buckling developed, resulting in further propagation of the delamination in that region. Based on the results obtained by the pre-and post-buckling analyses of double-strap adhesively bonded joints, it can be concluded that in terms of buckling responses, C3-L25 and C5-L35 configurations would be preferred choices for industrial applications, as they would not experience

catastrophic debonding failure even after undergoing two different stages of failure. It should be noted that although the C5-L25 configuration exhibited the maximum buckling capacity, this configuration suffered a sudden and catastrophic failure, which resulted in the debonding of the adherends.

Moreover, the buckling capacity of C5-L35 joints is slightly lower than that of C5-L25. Nonetheless, since this configuration exhibited a non-catastrophic failure mechanism, it is still considered the preferred configuration in terms of buckling response. Interestingly, this configuration was also ranked as the optimal configuration based on the tensile response of the joints in this configuration.

6.5. Conclusion

The performance of foam-cored fiber-reinforced metal sandwich panels joined with double-strap CFRP adhesively bonded configuration was systematically explored. First, the effects of different combinations of mechanical, chemical, and thermochemical surface treatment processes on the joint capacity were systematically investigated. The procedures were ranked based on the resulting surface roughness evaluated by several parameters. However, it was observed that the joint capacities were not directly related to surface roughness.

Investigation of the failure surfaces of the tested adhesively bonded joints revealed the interfacial mode being the dominant failure mode in the bonded joints prepared by the GS and GS+PC surface treatment procedures, whereas the specimens prepared by the other procedures experienced a combination of interfacial and cohesion failure. The strongest interlocking mechanisms were generated by the AS and AS+AE surface treatment procedures. Moreover, since the etching surface treatment is relatively significantly more labour-intensive, hazardous, and more time-consuming, thus, costlier than the simpler AS surface treatment procedure, therefore the AS treatment is rated as the most optimal surface treatment procedure.

The tensile performances of the adhesively bonded joints revealed that the increase in the thickness of the CFRP straps adversely affected the joint capacity. However, the straps'

length significantly affected the joint capacity. It was also observed that there is an optimal length above which the gain in capacity would not be significant. Investigation of the pre- and post-buckling responses of the sandwich systems mated different CFRP strap thicknesses and lengths revealed that all joints exhibited a similar pre-buckling behaviour (i.e., following the fundamental Euler-type buckling response); however, during the post-buckling regimes, each configuration exhibited a unique post-buckling behaviour. It is also concluded that the increase in thickness of CFRP straps could generate a higher buckling capacity when joining such sandwich systems, however, increasing the CFRP strap length would have a negligible effect.

It appeared that the increase in the length of the straps attributes to the development of stress concentrations at the geometric discontinuity regions located at the end of the straps, similar to what would be caused by a restraining (gripping) boundary condition. The stress concentrations invariably caused local delamination-buckling of the facial sheets and the eventual full delamination failure of the system. Moreover, the configuration that performed optimally under tensile loading also performed superiorly under compressive loading.

Chapter 7: Assessment of Failure Mechanism of Double-Strap 3D-FML Adhesively Bonded Joints under Tensile and Compressive Loadings Using Cohesive Zone Modelling Approach

Fatemeh Mottaghian, Farid Taheri

Under review with the Journal of Composite Structures

7.1. Abstract

Despite the widespread applications of Fiber Metal Laminates (FMLs), there is a clear lack of information regarding the performance of bonded joints mating 2D-FMLs and the recently-developed 3D-FMLs, particularly when considering their performances under compressive loading. Therefore, as a follow-up to the authors' recent investigations, an extensive series of numerical analyses are conducted in the present study to simulate the tensile and compressive (i.e., buckling, and post-buckling) responses of double-strap adhesively bonded joints mating 3D-FMLs. The 3D-FMLs are joined using carbon fiber-reinforced plastic (CFRP) straps and structural epoxy resin. The damage initiation and evolution in the bonded regions are modelled by seven different FE models, which incorporated the mixed-mode trapezoidal Cohesive Zone Modelling (CZM) approach in conjunction with continuum elements. Firstly, the effects of different numbers of CZM layers and thicknesses on simulating the damage mechanism are investigated. Subsequently, the influence of CFRP straps' thickness and length on the performance of the adhesive joints is parametrically studied. The distributions of peel and shear stresses along the length of the bonded regions are also systematically explored. Based on the results, the optimal joint configuration is established, and the most effective modelling framework is highlighted by comparing numerically predicted results against experimental results.

7.2. Introduction

[...] *Some portions of this section have been removed and included in Chapter 2.*

The applications of advanced lightweight materials such as fiber-reinforced plastics (FRPs) and fiber metal laminates (FMLs), which consist of layers of FRPs sandwiched in between thin sheets of metals (e.g., stainless steel, magnesium, titanium, and aluminum), have gained significant acceptance across various industries. However, the effective bonding/joining of such hybrid materials is relatively challenging as they require special attention based on their specific characteristics (Banea, 2019). Most of the research works related to adhesive joints have considered the response of joints consisting of metal, FRPs, and dissimilar adherends (e.g., metal to FRP), mainly subjected to tensile loading conditions. However, there is a clear lack of knowledge and engineering database regarding the performance of adhesive joints under bending, compressive, and especially impact loading scenarios. This research paucity becomes even more visible when considering FML bonded joints, particularly in consideration of 3D-FMLs since the Achilles heel of FMLs is the potential delamination or debonding of their FRP and metal constituents.

As briefly stated earlier, CZM has been implemented to model the progressive damage in adhesive joints with a good track record; however, to the best of the authors' knowledge, the progressive through-the-thickness damage mechanism in adhesive joints has not been previously investigated, especially in adhesive joints. Therefore, the investigation of stress distribution along the thickness of the adhesive, and prediction of the consequential sequence of damage and failure modes (i.e., cohesion, interfacial, or their combination), require immediate attention.

To address the aforementioned knowledge gap, for the first time to the best of the authors' knowledge, the performance of double-strap joints mating a new class of recently developed 3D-FML (Mottaghian & Taheri, 2022a) subjected to tensile and compressive loading scenarios is systematically investigated in this study by the CZM-FEM approach. The main objectives of this study are:

- (i) To develop a new and robust mixed-mode trapezoidal CZM-based FEM framework capable of modelling the performances of double-strap adhesive joints subjected to tensile and compressive/buckling loading states with good accuracy.
- (ii) To capture the global failure modes (i.e., FRP/metal delamination, strap debonding, and shear-crimping) in the joints under the stated loadings.
- (iii) To evaluate the effect of CZM element thickness (i.e., zero and non-zero thicknesses) and the number of layers (i.e., one to five) on the progressive damage failure.
- (iv) To assess the sequence of failure along the bond region and the local failure modes (interfacial, cohesion, or combination).
- (v) To accurately simulate the distributions of peel and shear stresses.
- (vi) To investigate the effects of CFRP straps length and thicknesses on the joint performance under tensile and compressive (buckling) loading conditions through a parametric study and establishing the optimal adhesive joint configuration.

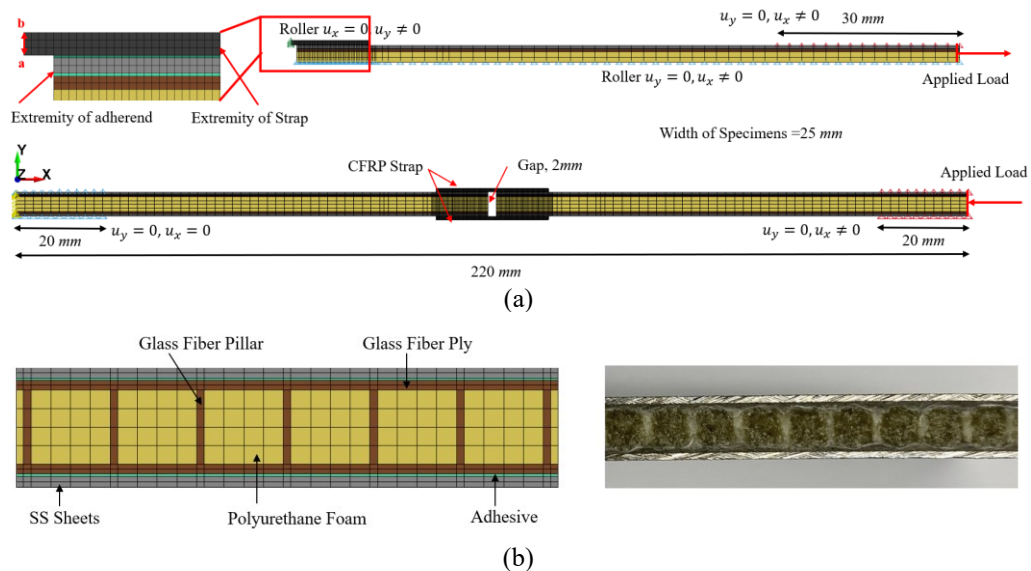


Figure 7-1. A typical double-strap adhesive joint (a) dimensions of the quarter symmetry model (used for tensile loading) and the full model (used for compressive loading) and the associated boundary conditions, (b) FE mesh of the cross-section of the 3D-FML and the actual 3D-FML.

7.3. Summary of the Experimental Study

The 3D-FML is made of 3D fiberglass fabric (3DFGF)-epoxy sandwiched in between thin layers of stainless steel (SS) sheets. The 3DFGF is an integrated fabric consisting of

two bi-directional (0/90) woven fabrics, knitted together by vertical braided E-glass fibers (pillars). From the other perspective (into the depth) in Figure 7-1(b), the pillars have a 30° inclination with respect to the through-thickness direction of the fabric. The fabric is commercially available in various thicknesses, ranging from 2 mm to 30 mm. Two-part liquid polyurethane foam was used to fill the cavities of 3DFGF-epoxy to enhance its performance. The double-strap bonding is formed by carbon fiber reinforced plastic (CFRP) straps and a relatively inexpensive cold-cured structural epoxy resin. The SS sheets were grit-blasted with 30 grit-size alumina media. This specific grit size was selected based on the authors' previous experimental study. Details of the fabrication procedure can be found in (Mottaghian & Taheri, 2023a). The dimensions of the double-strap adhesive joints are shown in Figure 7-1, while the fabricated specimens' IDs and specifications are reported in Table 7-1. The first part of the specimen ID (e.g., "C3", "C5") denotes the number of layers of fabrics in the CFRP strap on each side of the overlap and the second part of the specimen ID (e.g., "L25") refers to the length of CFRP straps. Note that a minimum of five specimens were tested in each category to assure the consistency and accuracy of the results. The tensile and compression tests were carried out using an MTS servo-hydraulic universal testing machine with constant crosshead speeds of 1.27 mm/min as per ASTM D3528 (2008) and 0.5 mm/min as per ASTM E2954 (2020), respectively.

Table 7-1. Configurations of fabricated double-strap adhesive joints.

Joint configuration ID	Configurations of Each CFRP Strap	Straps' Length (mm)	Straps' Thickness (mm)
C3-L25	3 woven plies stacked on each side	25	0.75
C5-L25	5 woven plies stacked on each side	25	1.25
C8-L25	8 woven plies stacked on each side	25	2
C5-L35	5 woven plies stacked on each side	35	1.25
C5-L45	5 woven plies stacked on each side	45	1.25

7.4. Numerical Study

7.4.1. Geometry Modelling

The commercial FE software, LS-DYNA, was utilized to model double-strap 3D-FML bonded joints, as illustrated in Figure 7-1. The model includes five components: (i) the SS sheets, (ii) the 3DFGF including plies and pillars, (iii) the polyurethane foam, (iv) the

adhesive layers (e.g., SS/ 3DFGF and SS/ CFRP strap interfaces), including the cohesive and continuum solid elements, and (v) CFRP layers. The implicit nonlinear analysis with eight-node hexahedron fully integrated solid elements (ELFORM= -1) along with CZM element (ELFORM= 19) was used to simulate the performances of the complex configuration of the hybrid 3D-FML joints. The displacement-controlled algorithm was used to model the quasi-static axial loadings. Due to symmetry in geometry and boundary conditions, only a quarter of the specimen, as shown in Figure 7-1, was modelled in the tensile loading scenario. To mimic the boundary conditions in the grip region, the (u_y) degree of freedom (DOF) of the nodes falling within the 30 mm grip length at the right end of the specimens was restrained and the (u_x) degree of freedom of the nodes was allowed to move freely. As seen, roller boundary conditions were used in the x and y planes of symmetry. In the case of compressive/buckling analysis, the whole model is considered, and to simulate the experimental boundary conditions, u_y and u_x degrees of freedom of the nodes falling within the 20 mm grip lengths at the left end of the specimens were constrained while at the right end transverse DOFs were restrained but longitudinal DOFs were free to move. In LS-DYNA, the “PERTURBATION” keyword is used to impose a small initial imperfection to a given model. The implementation of the imperfection is a necessary and commonly practiced technique to promote buckling in a nonlinear buckling simulation. The imperfection can be imposed in different forms using a mathematical function. In this work, an initial imperfection in the form of a half-sine wave was imposed (Mottaghian et al., 2020). The magnitude of imperfection amplitude and its wavelength were selected based on the thickness and length of the specimen based on a comprehensive comparative study conducted earlier (Mottaghian et al., 2020). As the magnitudes of stresses at the left and right edges of the bonded region are relatively very high due to stress concentration as compared to the remaining regions, those regions were modelled with finer mesh densities. The meshes were gradually transitioned to coarser meshes as the distance from the high-stress regions increased. Note that a very fine uniform element-size mesh was used in the bonded region to reduce the likelihood of instability in the CZM-modelled regions. The finer mesh will also facilitate a more accurate simulation of damage evolution. In addition, a convergence study was performed to establish the optimal mesh

densities to attain results with a reasonable balance of accuracy and CPU time efficiency and to ensure stable crack growth in the cohesive elements.

Table 7-2. LS-DYNA Material models utilized the numerical models.

Constituents	Material Model
SS sheets	*MAT_PIECEWISE_LINEAR_PLASTICITY (MAT_024)
Polyurethane foam CFRP Straps	*MAT_ELASTIC (MAT_001) + MAT_ADD_EROSION (MAT_000)
3DFGF (Pillars and Plies)	*MAT_ENHANCED_COMPOSITE_DAMAGE (MAT054/055)
Adhesive (CZM)	*MAT_COHESIVE_MIXED_MODE_ELASTOPLASTIC (MAT_240)
Adhesive (Continuum)	*MAT_PLASTICITY_POLYMER (MAT_089)

To define the contact after deleting the CZM elements in the bonded regions, the mortar contact was used. Mortar is a robust and accurate contact algorithm for use in an implicit analysis in LS-DYNA (especially, in situations when other contact algorithms fail to converge while using CZM). Note that some difficulties were encountered when using CONTACT_ERODING_SURFACE_TO_SURFACE and CONTACT_AUTOMATIC_SURFACE_TO_SURFACE while implementing CZM in the implicit analysis. However, a sufficient and relatively easier convergence was obtained by using CONTACT_AUTOMATIC_SURFACE_TO_SURFACE_MORTAR. Mortar contacts are segment-to-segment and based on the penalty-based approach. The less stiff constituents were selected as the slave to get the best possible implicit convergence response.

7.4.2. Material Modelling

To simulate the response of the constituent materials of the adhesive joints in LS-DYNA software, the SS sheets were modelled by using the piecewise linear plasticity material in which the material's plasticity and stress rate, and yield strength (σ_{yield}) were accounted for. The constituents of 3DFGF-epoxy (e.g., pillars and plies) were modelled by incorporating the composite damage material model (MAT_054/055) in which the Chang-Chang failure criterion was activated to track the damage evolution. This criterion accounts for both compressive and tensile failure of the bi-directional plies and pillars, as well as inter-ply delamination (Chang & Chang, 1987). Therefore, the transverse compressive/tensile strengths (Y_C/Y_T), longitudinal compressive/tensile strengths (X_C/X_T), and in-plane shear strength (S_C) were defined in this material model. Note that the pillars are oriented at an approximately 30° angle with respect to the through-thickness direction;

this angular orientation was considered in the composite model. The polyurethane foam was modelled by the elastic material model (MAT_001) in conjunction with the erosion material model (MAT_000), which is capable of capturing the potential failure in the foam. It should be noted that some of the material models of LS-DYNA do not include a failure criterion. In such cases, MAT_000 could be effectively used to overcome the shortfall and implement a stress- or strain-based failure criterion, or a combination of these to simulate the eventual material erosion and failure. For instance, if a region of the foam becomes subjected to a strain value greater than the maximum effective strain (ϵ_{max}) of the material, then the elements in that region would be eroded (deleted). Accordingly, the response of CFRP straps consisting of woven carbon fabrics was also simulated with the combined material models (MAT_000 and MAT_001), incorporating the maximum principal stress (σ_{max}) as the failure criterion.

The adhesive layer in the bonded area was modelled by a combination of CZM and continuum elements. The CZM approach will be discussed in detail in section 7.4.2.1. The continuum layers were modelled using the plastic polymer material, which incorporated the actual elastic-plastic stress-strain response of the epoxy, which was also established experimentally (Mohamed & Taheri, 2017). Note that this LS-DYNA material model is capable of modelling materials that do not exhibit a distinct transition in their elastic to plastic responses. The SS/3DFGF interfaces were modelled using one layer of cohesive elements. A summary of the material keywords and properties used in LS-DYNA are reported in Table 7-2 and Table 7-3, respectively.

Table 7-3. Mechanical properties of the materials used in the FE model (Mottaghian et al., 2020).

Property	SS Sheets	CFRP	Adhesive (Continuum)	3DFGF		
				Glass plies	Glass pillars	Polyurethane foam
Thickness (mm)	0.48	0.25	0.10	0.40	0.35	4.20
ρ (Kg/m^3)	8027	1870	1180	1750	1750	1.28
E_{11}, E (GPa)	193.74	54	3.17	9	3	0.05
E_{22} (GPa)				9	1	
ν_{12}, ν_{13} or ν	0.29	0.23				0
G_{12}, G_{13} (GPa)				1	1	
G_{23} (GPa)				1	1	
ϵ_{max} (mm/mm)						0.15
σ_{max} (GPa)		5.1				
σ_{yield} (GPa)	0.442					
S_c (GPa)				0.03	0.03	

$X_c(GPa)$	0.173	0.08
$X_T(GPa)$	0.173	0.08
$Y_c(GPa)$	0.173	0.08
$Y_T(GPa)$	0.173	0.08

7.4.2.1. CZM Formulation

As stated, the CZM technique was used to simulate the behaviour of the adhesive layer in SS/ 3DFGF and SS/CFRP straps' interfaces. Based on the results obtained by Campilho et al., 2013a the choice of the CZM traction-separation curve would depend on the characteristics of the given adhesive and adherends' material interfacial behaviours, the required precision, and the availability and ease of use of the CZM. In order to account for the plasticity and nonlinearity of the adhesive, this study considered a mixed mode (I+II) trapezoidal cohesive model. The stress (σ) and its induced relative displacement (δ), which would vary nonlinearly in each mode are depicted for each pure fracture mode (i.e., modes I and II) as illustrated in Figure 7-2; in other words, the nonlinear responses represent the interfaces' responses when subjected to either pure shear stress or pure peel stress. In essence, the mixed mode depicts the nonlinear response of the interfaces under a combined state of stress. The area under each traction-separation graph, which represents the material's response under tension (mode I) and shear (mode II) states represents the critical energy release rate, G_{IC} and G_{IIC} , of the material, respectively. The magnitudes of G_{IC} and G_{IIC} for the cold-cured epoxy system utilized in this study are reported as $1.5 KJ/m^2$, $2 KJ/m^2$, respectively. Additionally, the damage initiation is assumed to follow a quadratic criterion, mathematically represented by the following equation (Campilho et al., 2009),

$$\left(\frac{\sigma_n}{\sigma_{un}}\right)^2 + \left(\frac{\sigma_t}{\sigma_{ut}}\right)^2 = 1 \quad (7-1)$$

where σ_n and σ_t indicate the local stresses in each pure mode (i.e., "n" refers to peel (or mode I), and "t" refers to shear (or mode II). Also, σ_{un} and σ_{ut} correspond to the ultimate strengths under the two modes, respectively. Eq. (7-1) can also be rewritten as a function of the relative displacement (Campilho et al., 2009),

$$\left(\frac{\Delta_n}{\delta_{ni}}\right)^2 + \left(\frac{\Delta_t}{\delta_{ti}}\right)^2 = 1 \quad (7-2)$$

where $i = 1, 2$ correspond to the material yielding and damage initiations (softening onset), respectively and Δ_n and Δ_t are the current states of separation and sliding displacements, respectively, and δ_{ni} and δ_{ti} represent the relative separation and sliding under pure modes I and II, respectively (Campilho et al., 2013b; LS-DYNA R10.0). Accordingly, the equivalent mixed-mode displacement at the onset of damage (softening), δ_{mi} , can be determined by the following equation (Marzi et al., 2009),

$$\delta_{mi} = \delta_{ni} \delta_{ti} \sqrt{\frac{1+\beta^2}{\delta_{ti}^2 + (\beta \delta_{ni})^2}} \quad (7-3)$$

where $\beta = \frac{\delta_{t1}}{\delta_{n1}}$ stands for the mixed-mode ratio. The ultimate relative displacement in a given interface can be evaluated by (Marzi et al., 2009),

$$\delta_{mf} = \frac{\delta_{m1} (\delta_{m1} - \delta_{m2}) E_n G_{IIC} \cos^2 \gamma + G_{IC} (2G_{IIC} + \delta_{m1} (\delta_{m1} - \delta_{m2}) E_t G_{IC} \sin^2 \gamma)}{\delta_{m1} (E_n G_{IIC} \cos^2 \gamma + E_t G_{IC} \sin^2 \gamma)} \quad (7-4)$$

where $\gamma = \frac{\Delta_n}{\Delta_m}$ and $\Delta_m = \sqrt{\Delta_n^2 + \Delta_t^2}$. Eq.(4) is based on the power-law damage evolution model incorporated here by assuming an exponent of $\eta=1$, thereby rendering the power law as the linear energetic criterion. Here, the initial stiffness of the interface under peel (E_n) and shear (E_t) stresses are determined based on the Young's (E) and shear (G) moduli of the material (i.e., $E_n = \frac{E}{t_{element}}$ and $E_t = \frac{G}{t_{element}}$, respectively) (Marzi et al., 2009).

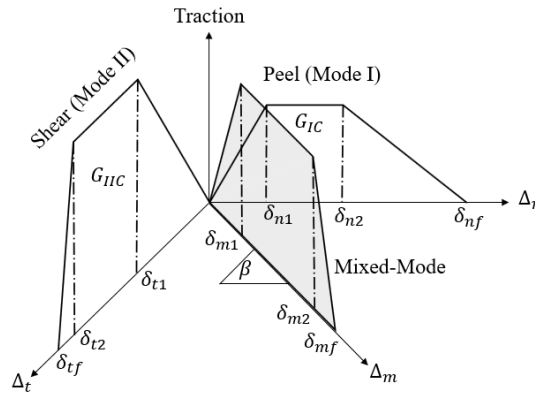


Figure 7-2. The schematics of trapezoidal mixed-mode CZM.

The mixed-mode traction-separation law will be determined based on a combination of δ_{mi} and δ_{mf} . Consequently, the separations in peel and shear directions could be assessed, and if the damage criteria are satisfied (i.e., $\Delta_m > \delta_{mf}$), the complete failure and deletion of the corresponding element will be viewed accordingly (Marzi et al., 2009).

Material models, MAT_185 and MAT_240 of LS-DYNA are commonly used to incorporate the trapezoidal CZM law. However, MAT_185 can only handle one pure fracture mode (mode I or mode II). In contrast, to simulate mixed fracture mode by CZM, which was the focus of this study, MAT_240 had to be used. The mixed-mode trapezoidal behaviour is represented by a quadratic failure initiation criterion for both yield and damage initiations, while the damage evolution follows a power-law criterion with an exponent $\eta = 1.0$. It has been suggested that an energy-based fracture criterion would provide better results than the relative displacement criterion used in this study, as argued by Benzeggagh & Kenane, 1996. However, MAT_240 cannot model energy-based damage. Several studies (Pisavadia et al., 2022; Marzi, 2010; Marzi, 2009; Jayakumar, 2022; Zhou et al., 2020), however, have demonstrated the effectiveness of MAT_240 in predicting the response of adhesive joints compared to experimentally obtained results. Therefore, one of the main objectives of this study is to demonstrate the potential of incorporating MAT_240 for accurately simulating damage evolution in adhesive joints when considering cohesive elements with different thicknesses or numbers of layers.

The double-cantilever beam (DCB) and end-notched flexure (ENF) tests were conducted to characterize mode I and mode II fracture response of the adhesive in the previous works of the authors (Mohamed & Taheri 2017; de Cicco & Taheri 2018; Ahmadi Moghadam, 2015). The trapezoidal model's parameters δ_{n1} and δ_{t1} were obtained by considering the yield strength and stiffness in each mode. Also, δ_{n2} was determined from the stress-strain curve of bulk adhesive as recommended in (Campilho et al., 2008). Subsequently, as recommended in (Carlberger & Stigh, 2007), δ_{t2} was defined by considering the stress softening occurs under a slope similar to that determined in the mode I fracture case. Note that it is known that the length of the constant stress (plateau) region in the trapezoidal law would be larger in mode II compared to that in mode I (Anderson & Biel, 2006), which was also observed in the CZM parameters defined in this study. The

integrity of CZM parameters utilized in the FE model was obtained using the load vs. crack-opening curve and compared with the actual test results obtained by the DCB and ENF tests. These parameters were then used in a mixed-mode case study investigated in one of the authors' previous research (Mottaghian & Taheri, 2023) and the final parameters defining the shape of trapezoidal CZM law in the mixed mode were established by calibrating the trial values in such a way that the numerical simulation-produced results would closely match the experimental results. The parameter $F_{G1} = \frac{(\delta_{n2} - \delta_{n1})}{(\delta_{nf} - \delta_{n1})}$ and $F_{G2} = \frac{(\delta_{t2} - \delta_{t1})}{(\delta_{tf} - \delta_{t1})}$, which are used as input in the MAT_240 model of LS-DYNA, are defined to account for the relative displacement in mode I and mode II, respectively. The cohesive material properties used for modelling the epoxy adhesive are reported in Table 7-4.

Note that according to the literature, two main approaches are commonly used to evaluate the parameters required to define the mixed-mode CZM. In the first approach, the critical energy release rates for modes I and II are determined by performing DCB and ENF tests, respectively. In the second approach, a mixed-mode bending (MMB) test is conducted to directly capture the mixed-mode fracture mechanism and evaluate the energy release rates for modes I and II. However, it may not be possible to directly establish the values of the critical energy release rate from the test results, and one would have to conduct a series of parametric analyses to determine the critical analyses (Gonçalves et al., 2023). Many researchers (e.g., Campilho et al., 2013; Pisavadia et al., 2022; Carvalho & Campilho, 2016; Silva et al., 2018; Campilho et al., 2011; Sugiman et al., 2013; Campilho et al., 2008; Campilho et al., 2010) have validated the effectiveness of the first method, which has also been used in the present study.

Table 7-4. CZM parameter for structural adhesive (Mohamed & Taheri, 2017).

Normal Stiffness (GPa)	Mode I Yield Stress (MPa)	Mode I Energy Release Rate (KJ/m²)	F_{G1}	Initiation Criteria
3.5	59	1.5	0.62	Quadratic Stress Criteria
Shear Stiffness (GPa)	Mode II Yield Stress (MPa)	Mode II Energy Release Rate (KJ/m²)	F_{G2}	Propagation Criteria
1.5	23	2	0.71	Power-Law with ($\eta=1$)

7.4.2.2. FE Modeling of the Bonded Region

The terms adherends and straps in this study refer to the SS sheets and the bonded CFRP straps, respectively, whose strengths are much greater than that of the epoxy adhesive. This means that failure would most probably occur in the adhesive or any other relatively weak regions (e.g., the interface) of the double-strap joints. The failures in the bonded interface regions are generally classified into four modes; (i) interfacial mode, in which the failure occurs in the mating surfaces in between the adhesive and adherends. In this mode, a great majority of the adhesive remains on one of the surfaces; (ii) cohesion mode, in which the failure occurs in the adhesive layer. This failure mode is characterized by some adhesives remaining on both surfaces of adherends; (iii) mixed interfacial-cohesion mode, a self-explanatory failure mode, which corresponds to a combination of the two previously described modes, and finally, (iv) adherends/strap failure mode, in which one of the adherends or straps would experience failure before the adhesive's ultimate capacity is attained.

Simulation of the progressive damage in the adhesive of a bonded joint, which would invariably lead to one or a combination of the first three described failure modes, is essential to accurately establish the performance of bonded joints. Moreover, the accurate depiction of the complex stress distributions and their concentrations along the length and through-the-thickness of the adhesive and strap is essential in understanding the mechanisms of failure in adhesive joints. Most of the research works that have incorporated cohesive models have only assessed the failure load of adhesive joints and have not evaluated the initiation and evolution of damage and the consequential failure modes. To the best of the authors' knowledge, this is the first study to systematically examine the influence of using zero and non-zero-thickness cohesive elements in predicting adhesive joint response. Additionally, the influence of incorporating different numbers of cohesive layers on the initiation and evolution of damage in the bonded region is also systematically investigated in this work. It is important to note that joining 3D-FML is a completely new challenge, thus, requiring attention.

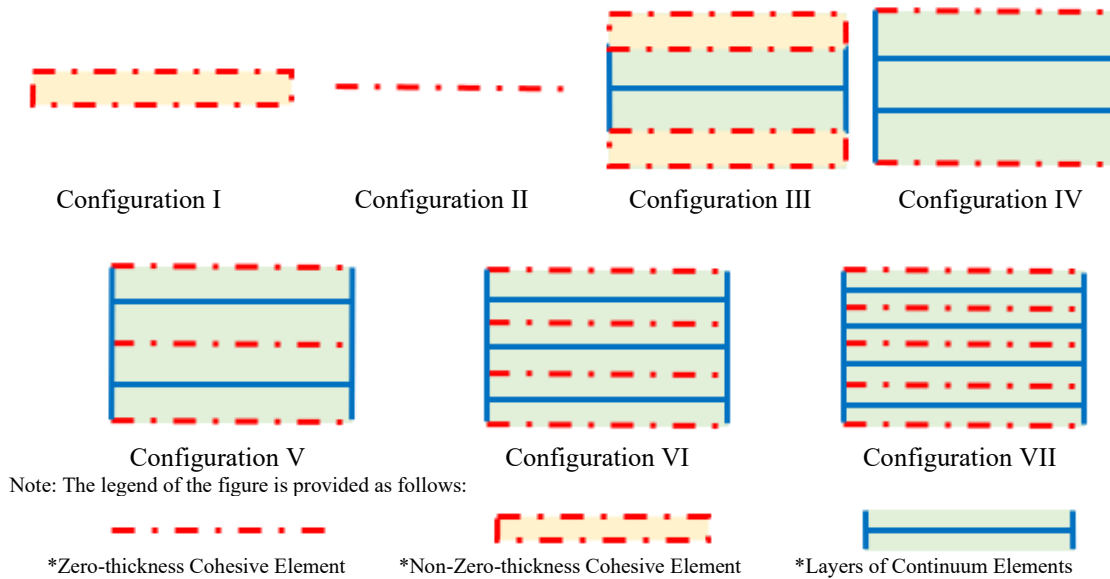


Figure 7-3. Schematics of different FE configurations for the adhesive layers

With the aim of examining the influence of CZM elements on the accuracy of damage prediction, seven different FE configurations were developed to simulate the response of the adhesive joints with 0.1 mm thick adhesive layers, as illustrated in Figure 7-3. where each model's identifier is explained in Table 7-5. For instance, model V refers to the configuration in which each adhesives layer is modelled with three layers of zero-thickness cohesive elements combined with four layers of continuum elements. Besides, the CZM will be activated in LS-DYNA only if a layer of the cohesive element is present in a given model whose nodes are shared with the neighbouring continuum elements. As the cohesive element in LS-DYNA is just a physical model (i.e., no stress distribution could be depicted by the element), the implementation of continuum elements facilitates the evaluation and distribution of a complex stress state within a given adhesive/interface layer.

Table 7-5. Specifications of the developed FE configurations.

Configuration ID	Specifications
I	1 non-zero-thickness cohesive element
II	1 zero-thickness cohesive element
III	2 non-zero-thickness cohesive elements combined with continuum elements
IV	2 zero-thickness cohesive elements combined with continuum elements
V	3 zero-thickness cohesive elements combined with continuum elements
VI	4 zero-thickness cohesive elements combined with continuum elements
VII	5 zero-thickness cohesive elements combined with continuum elements

7.5. Results and Discussions

7.5.1. Refinement of the Interface Model

The effects of modelling the interface regions with zero and non-zero thickness cohesive elements and the influence of incorporation of different numbers of layers on the predicted failure load and damage evolution of the double-strap adhesive joints are comprehensively investigated in this section. Figure 7-4 presents the load-displacement responses of the C5-L25 group of the specimen subjected to tensile (or lap-shear) loading predicted by the seven FE models. To assess the integrity of the predicted results by the FE models, the results are compared with data obtained experimentally. As seen, the most accurate predictions were produced by the VII, VI, and V models, yielding only 3.1%, 4.3 %, and 6.8 %, error margins compared to the experimental values, respectively. In other words, the models which incorporated the mixed cohesive-continuum models and the use of more than two layers of cohesive elements produced the closest results to the experimental values. In contrast, the largest error margin of 31.3% was associated with models I and II. The reason for the discrepancies will be discussed in section 7.5.1.1.

7.5.1.1. Damage Evolution in the Adhesive

In this section, the damage initiation and evolution within the thickness of the adhesive layer modelled by various layers of cohesive elements are investigated by the seven developed FE models. As mentioned previously, the mixed-mode CZM utilized in this study accounts for the combination of peel and shear failure mechanisms. By investigating the damage mechanism in configurations I and II, it was found that they are generally similar with a slight difference in the size of damage evolution. Damage was initiated at the extremity of the strap (i.e., at the farthest distance from the joint midspan). As the load is increased, the stress concentration is also increased, which caused the onset damage at the extremity of the adherend, at the edges closer to the mid-span of the joint. The evolution of the damage is traced by the entire cohesive layer of elements that were deleted, which essentially signifies the catastrophic failure of the joint. Despite the success of these two models in capturing the damage evolution, nevertheless, the local failure type in the

adhesive (i.e., whether interfacial or cohesion) could not be determined by these models (i.e., by modelling the adhesive layer with a single layer of cohesive elements).

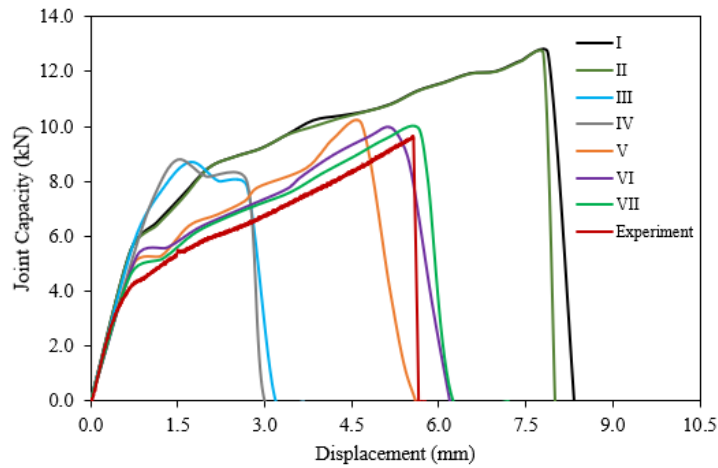


Figure 7-4. Comparison of the numerically predicted load-displacement responses of the FE models of the C5-L25 configuration subjected to tensile loading and the experimental results.

On the other hand, no crack propagation was observed in either cohesive element layer in the III FE configuration. Interestingly, in this model, the entire two layers of elements that were used to model the adhesive layer were simultaneously deleted, thus, rendering the failure of the joint. This abrupt event could be the reason for the relatively lower overall deformation of the joint which is illustrated in Figure 7-4. On the other hand, the damage in the IV model was initiated by the deletion of a few of the zero-thickness cohesive elements, which then propagated at a significant speed, causing the eventual catastrophic failure of the first layer of cohesive elements (i.e., the layer closest to the SS adherends). However, comparatively, the damage evolved slower in the second layer of cohesive elements (in the layer closest to the CFRP straps). It can therefore be concluded that according to this model's predictions, interfacial failure would be the predominant mode of failure, expected to occur along the SS/adhesive interface.

Based on the aforementioned analyses, it is believed that the zero-thickness cohesive elements are more capable of predicting the progressive damage evolution. Therefore, hereafter, the predictive capability of the CZM approach will be examined by models which will include various layers of zero-thickness cohesive elements.

The V model progressive damage predictions indicate that the damage is initiated in all three layers at the same stage (i.e., at three different elevations though-thickness of the adhesive). In other words, the adhesive will experience cohesion and interfacial failure modes simultaneously, though judging by the sequence of element deletion, the interfacial mode would be more prevalent. The damage evolution predicted by the VI model indicates that although cracks were initiated simultaneously at all four layers (elevations) at the same time; however, the greatest number of deleted cohesive elements occurred at the first layer (in the layer closest to the adherend). Based on the results, many elements in the second cohesive layer also experienced a high magnitude of stress and thus were eliminated. The extent of the damage is smaller on the third and fourth layers compared to the first two layers, indicating the predominant failure occurred at the SS/adhesive interface, which gradually moved toward the strap/adhesive interface.

Four layers of cohesive elements were used to discretize the adhesive layer in this model, however, it could not be discerned whether the cohesion failure occurred in the mid-plane of the adhesive thickness; therefore, another layer of cohesive elements was incorporated into this model to investigate the location of cohesion failure more precisely, (see Figure 7-3 and Table 7-5). The damage evolution in configuration VII is demonstrated by the deletion of the cohesive element (red colour) in the x-z plane in Figure 7-5. As seen, the damage essentially initiated the SS adherend/adhesive interface (in the first cohesive element layer, Figure 7-5(a)), and then the second layer is affected. Besides, the adhesive/strap adherend interface experienced a relatively large stress concentration, which led to the removal of many cohesive elements. Interestingly, the cohesive layer running along the mid-elevation of the adhesive layer experienced the lowest stress concentration. However, comparatively, the element layers two and four were subjected to higher stress concentration and experienced cohesion failure. This occurred as a result of the stress transfer from the critically stressed interface layers toward the mid-plane of the adhesive.

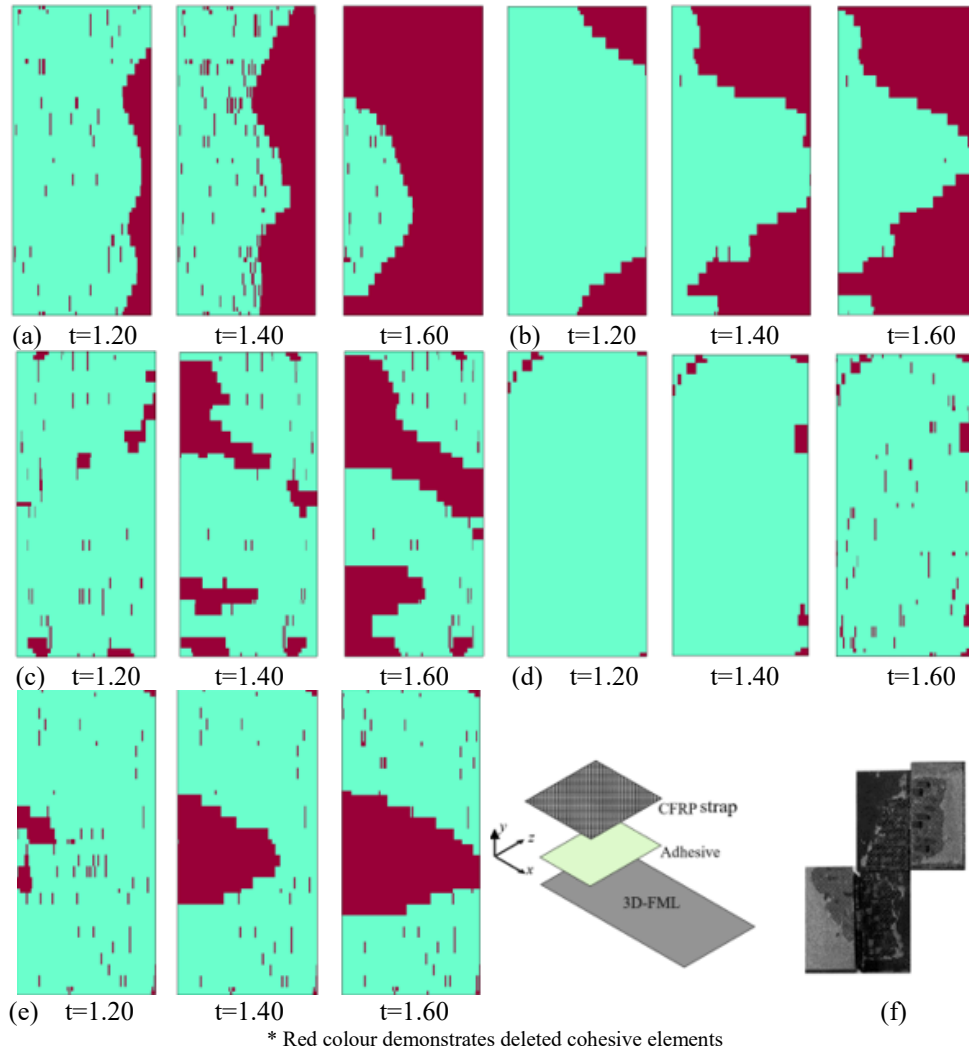


Figure 7-5. Top view (x-z plane) showing the sequence of cohesive crack growth in the bonded region of configuration VII (a) first layer, (b) second layer, (c) third layer, (d) fourth layer, and (e) fifth layer at different time steps, (f) mixed interfacial-cohesion failure mode in the actual C5-L25 configuration.

To further explore the predictions of the VII model, the through-thickness distributions of the shear and peel stresses in the adhesive layer predicted by this model for the joint with C5-L25 configuration are plotted in Figure 7-6. Cross-referencing Figure 7-3 would indicate each layer of zero-thickness cohesive is bonded by two layers of continuum elements. Therefore, to determine the stress in each zero or any-thickness cohesive element, one would take the average of stresses in the neighbouring continuum elements as illustrated in Figure 7-6. As seen, the highest magnitudes of shear and peel stresses occur near both interfaces. Based on the mixed-mode CZM technique, the zone(s) that experience the higher combination of shear and peel stresses would meet the defined criterion, thus,

would be deemed failed (deleted). Therefore, the results illustrated in Figure 7-6 corroborate with the results presented in Figure 7-5.

Based on the comparison of the experimental and numerical results shown in Figure 7-4, Figure 7-5, and Figure 7-6 it was found that the predictions of model VII were closest to the experimentally observed results; therefore, this model is used to carry out the remaining investigations in this study.

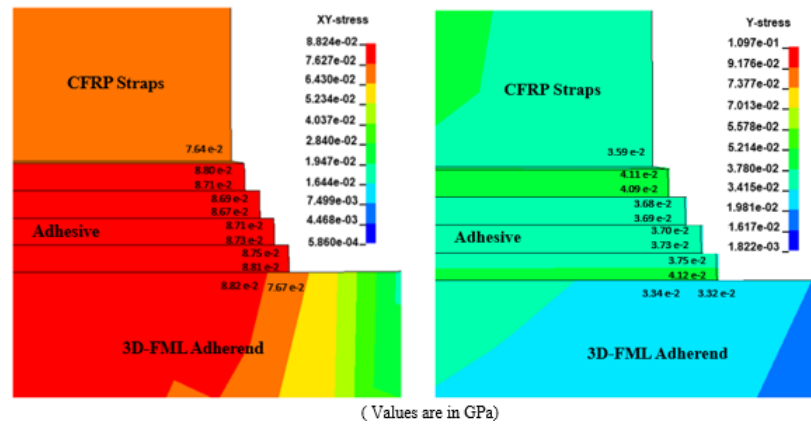


Figure 7-6. Magnitudes of the shear and peel stress at a different layer of the model for C5-L25 configuration under a tensile load.

7.5.2. CFRP Straps Length and Thickness Optimization

In this section, a series of parametric studies are performed to evaluate the effects of CFRP straps' thickness and length on joints' performances and capacities and subsequently, the most optimal adhesive joints configuration is established. To this end, 10 different overlap lengths (i.e., 5 mm, 10 mm, ... up to 50 mm) and 8 different layers (i.e., one, two, ..., up to eight) of CFRP straps that are subjected to tensile loading are numerically analyzed and their ultimate joint capacities are depicted in Figure 7-7. Using the mechanics of materials, it was concluded that straps should be constructed with at least three layers of CFRP to prevent premature rupture of the straps. Nevertheless, the reasons for considering joints with straps made with less than three CFRP layers are twofold: (i) to check the integrity of the material failure model defined for the CFRP straps, and (ii) to gain insight into the resulting stress distribution and the influence of strap thickness on the failure modes. Failures in joint configurations with short and thin CFRP straps (i.e., straps shorter than 15 mm with less than 3 layers of CFRP) occurred in both interfacial and strap

rupture modes. In joints with thicker and longer CFRPs, the failure occurred cohesively. Increasing the strap thickness (up to 5 layers of CFRP) resulted in progressively improved joint capacity. However, the results indicate that increasing the strap thickness beyond five CFRP layers would not improve the joint capacity noticeably. In fact, the use of thicker straps (with more than 5 layers of CFRP) could be counterproductive, as they would adversely affect the capacity, particularly in joints with longer CFRP straps. This is attributed to the development of excessive stress concentration at the edges of the thicker straps, an effect that will be further examined in the next section. Therefore, based on the results, a strap thickness consisting of 5 layers of CFRP is deemed optimal for constructing joints with optimum capacity.

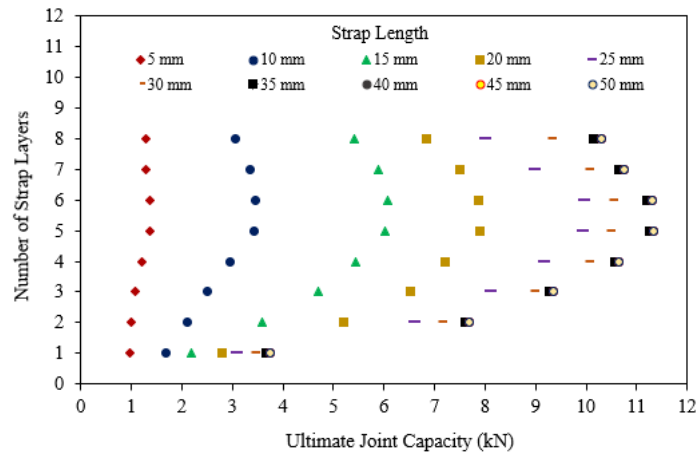


Figure 7-7. Effects of strap length and thickness (number of CFRP layers) on joint capacity.

The influence of strap length on joint capacity was also investigated numerically, and the results are also reported in Figure 7-7. The results show that increasing the CFRP strap length up to a certain value (i.e., up to 35 mm) would improve the joint capacity, and joints with straps longer than 35 mm would offer negligible improvement in capacity. Moreover, in configurations with straps made of more than three layers of CFRP, the strap length would have a greater influence on the joint capacity than strap thickness. As mentioned, strap rupture was the predominant failure mode observed in joint configurations with strap thicknesses of less than three layers of CFRP. When the strap length of joints with 5 layers of CFRP straps was changed from 5 mm to 35 mm, the resulting improvement in capacity was found to be eleven-fold. Therefore, based on the results, the optimal joint configuration

would be the joint constructed with 35 mm long and 5-layer CFRP thick straps (designated as "C5-L35" hereafter).

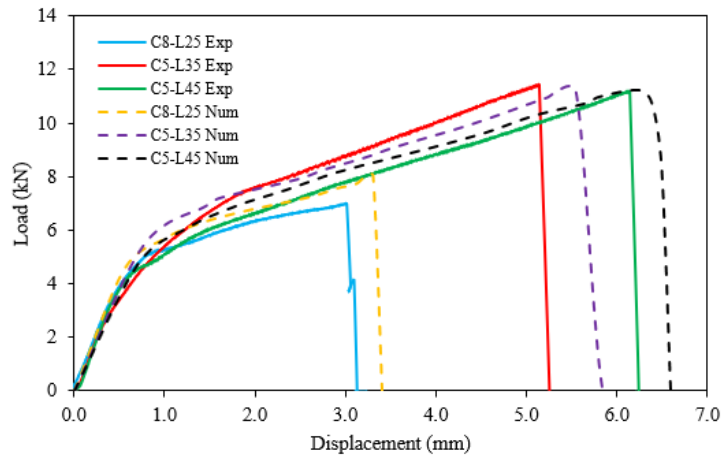


Figure 7-8. Comparison of the experimental and numerical responses of various configurations of the double-strap adhesive joints under tensile loading.

To further illustrate the validity of the developed FE model, the response and capacity of the joints configured with different parameters were analyzed and compared against the corresponding experimental results, as illustrated in Figure 7-8 and tabulated in Table 7-6. Note that the experimental values reported in Table 7-6 are the average values of five tested specimens in each specimen category, while the responses shown in Figure 7-8 are typical experimentally obtained results. As can be seen, the numerically predicted results closely match the experimental results. In terms of the predicted joint capacities, the minimum and maximum error margins were 3% and 10%, respectively.

Table 7-6. Comparison of numerical and experimental results.

Sample ID	Lap-shear Capacity (kN)-Exp	Lap-shear Capacity (kN)-Num	Numeric to Experiment Ratio	Buckling Capacity (kN)-Exp	Buckling Capacity (kN)-Num	Numeric to Experiment Ratio
C3-L25	-	-	-	5.92±0.1	6.21	1.05
C5-L25	9.67±0.4	9.97	1.03	7.20±0.3	7.43	1.03
C8-L25	7.27±0.9	8.04	1.10	-	-	-
C5-L35	11.68±0.8	11.20	0.97	6.90±0.3	7.32	1.06
C5-L45	11.71±0.8	11.21	0.95	-	-	-

7.5.3. Stress Distribution in the Bond Regions

Understanding the local deformation of the bonded region(s) in adhesive joints and the resulting stress distributions is essential in characterizing the failure mechanisms of adhesive joints. Therefore, the numerically depicted deformation and mechanism of the bonded region of double-strap adhesive joints (modelled by taking advantage of the quarter symmetry) is shown in Figure 7-9. Subjecting the joint to a tensile load, T , and a bending moment of M at the center line of strap will cause generation of the transverse stress, σ_n , as well as a longitudinal force, $\frac{T}{2}$ in the mid-plane of the adherend (note the figure shows a quarter symmetry of the joint). The prescribed moment and force will cause compressive and tensile deformation modes, at the adherends' extremities (i.e., near the midspan) and straps' extremities (i.e., the furthest distance from the joint's midspan), respectively (Tsai & Morton, 2010).

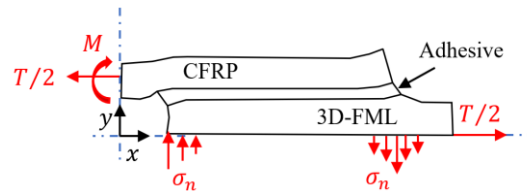


Figure 7-9. Deformation of the quarter symmetry model of the double-strap adhesive joints subjected to tensile loading.

To further investigate and appreciate the influence of the bending moment developed in the overlap region, the variation in the distributions of the longitudinal stress (σ_x) within the thickness of the strap at its midspan (identified by line a-b in Figure 7-1) is illustrated in Figure 7-10 for some configurations. The configurations selected to produce the results shown in the figure include a variety of strap thicknesses and lengths, facilitating a more in-depth comparison of the stress distribution. As can be seen, the effect of the bending moment is quite ubiquitous since the magnitude of the stress varies significantly as a function of strap thickness and length. In other words, the joints with very thin, very thick or short straps show a larger difference in the magnitude of the longitudinal stress along the thickness of the strap. On the other hand, the nonuniformity in the stress (or the bending moment) is less significant in the C5-L35 joint, which was established as the optimal joint configuration. All the joint configurations used to produce the stress distributions discussed

in this section were subjected to a tensile load of 1.3 kN. Note that the applied load magnitude was selected such that it would not cause the yielding of the materials or inflict damage.

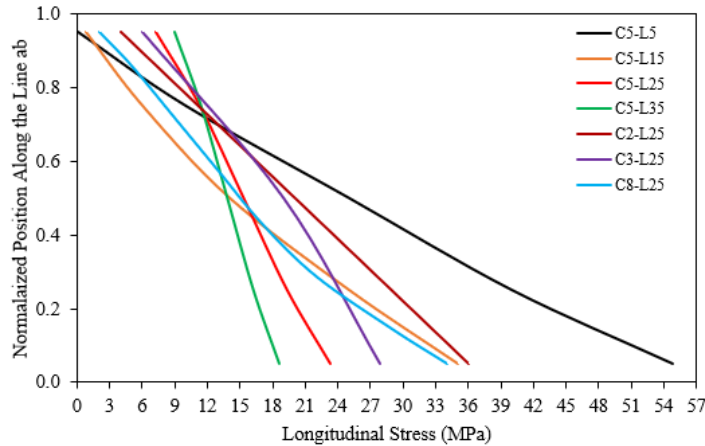


Figure 7-10. Variation in the distributions of the longitudinal stress (σ_x) within the thickness of the strap (path ab is identified in Figure 7-1), at its midspan.

To further investigate the change in the distribution of the stresses in CFRP straps, the distributions of the peel and shear stresses along the length and thicknesses (layer numbers) of the CFRP straps in the C5-L35 configuration are illustrated in Figure 7-11. Note that the stress distributions are captured by the quarter-symmetry model, the results are shown along one-half length of the 35 mm straps (i.e., the x-axis represents half of the 35 mm strap length). The relative deformation between the straps and adherends generated the shear stress, which has the highest magnitude in the first layer of the CFRP straps. The shear stress decreases as the thickness of the straps increases. The peak shear stress in the left part of the figures occurs in the extremity of the adherends due to the developed bending moment.

To further assess the influence of the gap on the stress distribution and the abrupt stress variation in the area closer to midspan, a numerical investigation is performed on the C5-L35 joints but this time with no gap in between the adherends. The resulting shear stress distributions are shown in Figure 7-12. As seen, the shear stress concentration at the left edge of the configuration observed in the previous joints with a gap vanishes in the one with no gap. Moreover, the peaks in peel stress seen near the midspan of the straps (on the

left side of the figure) in Figure 7-11(b) are developed due to the bending moments that are generated in the vicinity of the region near the adherends ends (near the midspan gap).

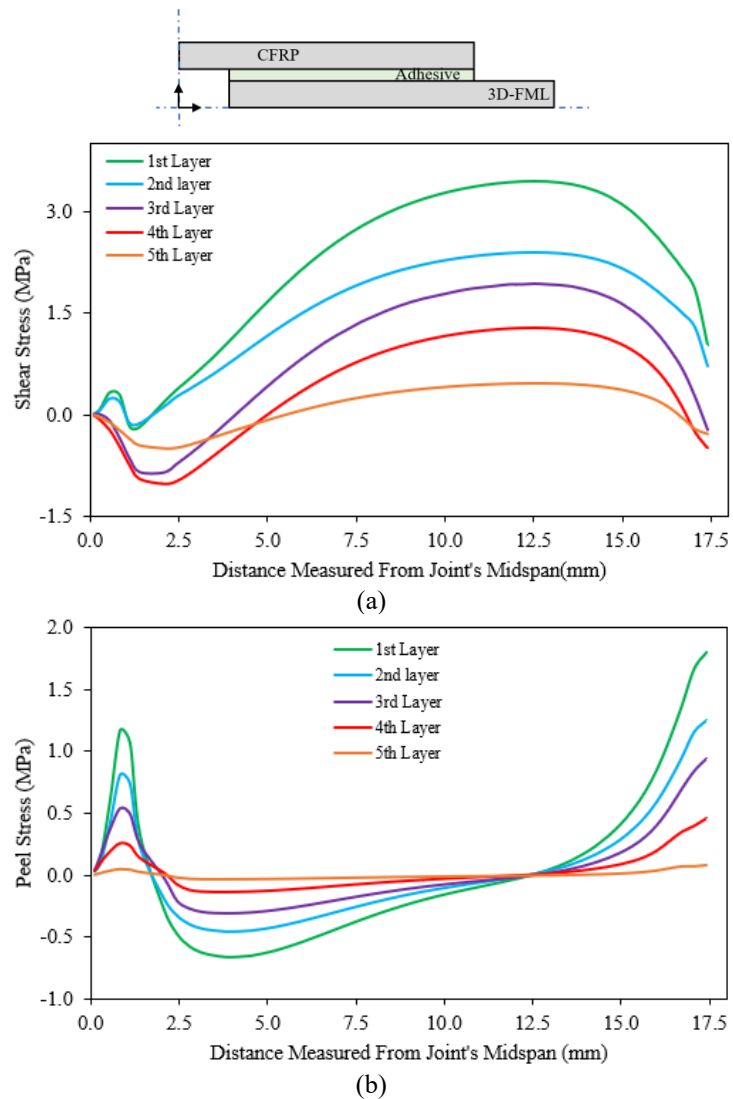


Figure 7-11. Distribution of the shear (a) and peel (b) stresses on each CFRP layer of the straps in C5-L35 configuration.

The presence of the gap in double-strap joints has been recommended in ASTM 3528, though the gap size has not been specified. According to the literature, the gap size considered by researchers varies between 0.1 mm to 2 mm. In this study, as shown in Figure 1, a gap size of 2 mm is used in both experimental and numerical investigations (Perera et al., 2022). The small gap in the double-strap allows the inner adherend to deform in the out-of-plane direction, thereby reducing the maximum bending moment developed at the midspan (Shahin & Taheri, 2006; Shahin & Taheri, 2007). As seen in Figure 7-11(b), the

peel stress decreases as the distance from this region increases until near the end of the bonded region which shows the highest peel stress concentrations. Moreover, the peel stress in the first layer of the CFRP strap, which is adjacent to the adhesive, experiences the highest magnitude, while the layer farthest away from the adhesive experiences the lowest magnitude of the stress.

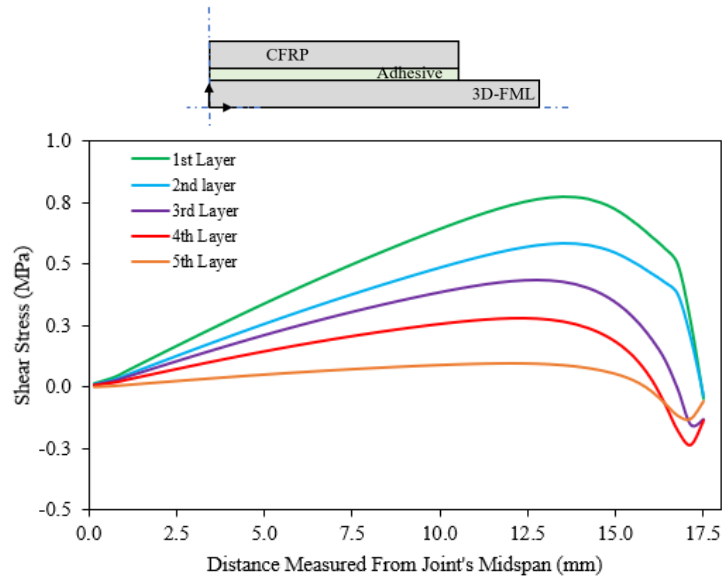


Figure 7-12. Shear stress distribution on each CFRP layer of the straps in the C5-L35 configuration without any midspan gap.

Evaluation of the stress distributions along the length of the adhesive layers is essential for assessing the performance and failure mechanism of adhesive joints. Therefore, distributions of the peel and shear stress in the adhesive elements immediately adjacent to the strap(s) for the eight differently configured adhesive joints (having different thickness straps) are compared in Figure 7-13. Note that the length of CFRP straps was kept constant at the optimal length of 35 mm. Based on the results shown in Figure 7-13(a), the increase in the thickness of the straps (from one to five layers), reduced the stress concentration near the edge of the bonded region close to the midspan, thus resulting in higher ultimate joint capacity. Indeed, the significantly high-stress concentration developed in the C1-L35 group of specimens caused the rupture of the CFRP straps, as discussed earlier. Interestingly, as seen, the adhesive joints with straps having more than six layers of CFRP exhibited higher stress concentration than those with five layers, which resulted in lower ultimate joint capacities as explained in the previous sections. The general trend attests to the non-

uniformity in load transfer along the bond length, which peaks up at both extremities of the bond regions.

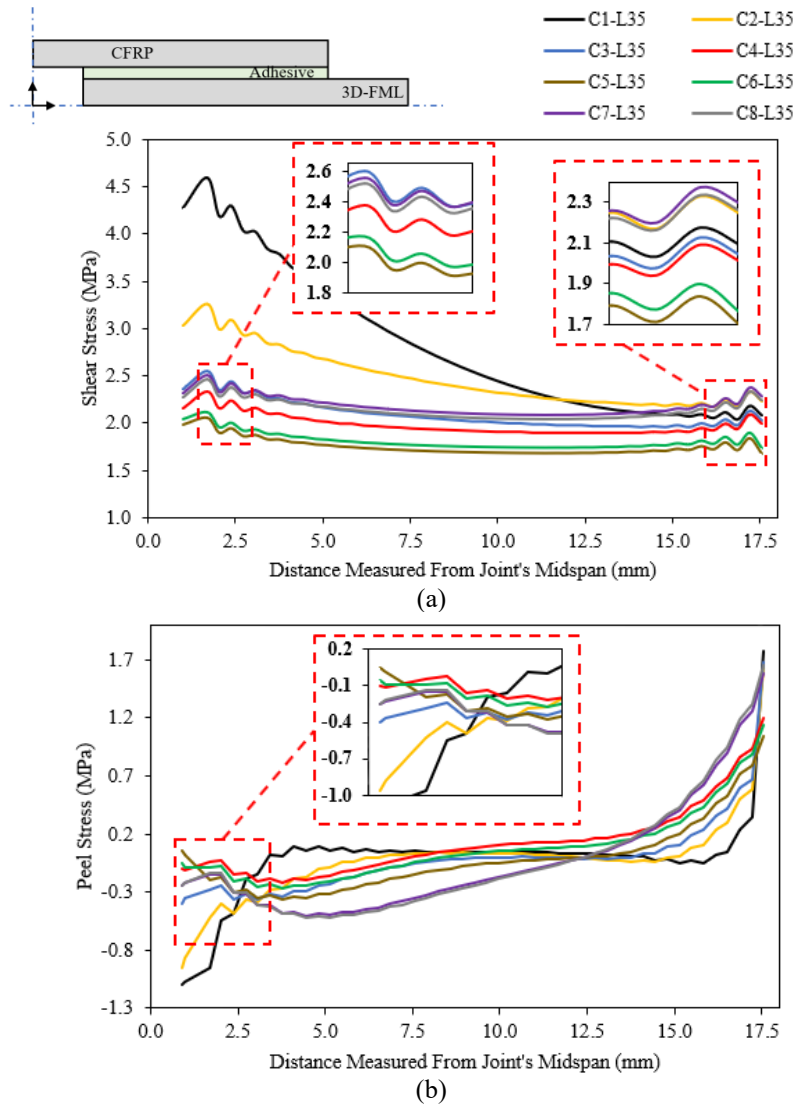


Figure 7-13. Influence of strap thickness on the distribution of (a) shear and (b) peel stresses on the adhesive layer.

The peel stress developed in the adhesive is also a critical parameter that could initiate joint failure. The distribution of the peel stresses in the considered adhesive joints is presented in Figure 7-13(b). As discussed earlier, the compressive and tensile variations in the distribution of the peel stresses are generated due to the bending moments developed within the straps of such joints. As seen, the maximum absolute peel stress develops at the edges of the bond regions of the specimens with one and two layers of CFRP straps. The magnitude of the stress is reduced as the straps are thickened up to six layers of CFRP.

Further thickening of the straps causes an increase in the peel stress, especially at the edges of the straps. This phenomenon is another reason for the decrease in the overall joint capacities of configurations with thick CFRP straps (i.e., more than 6 layers) observed in the earlier results.

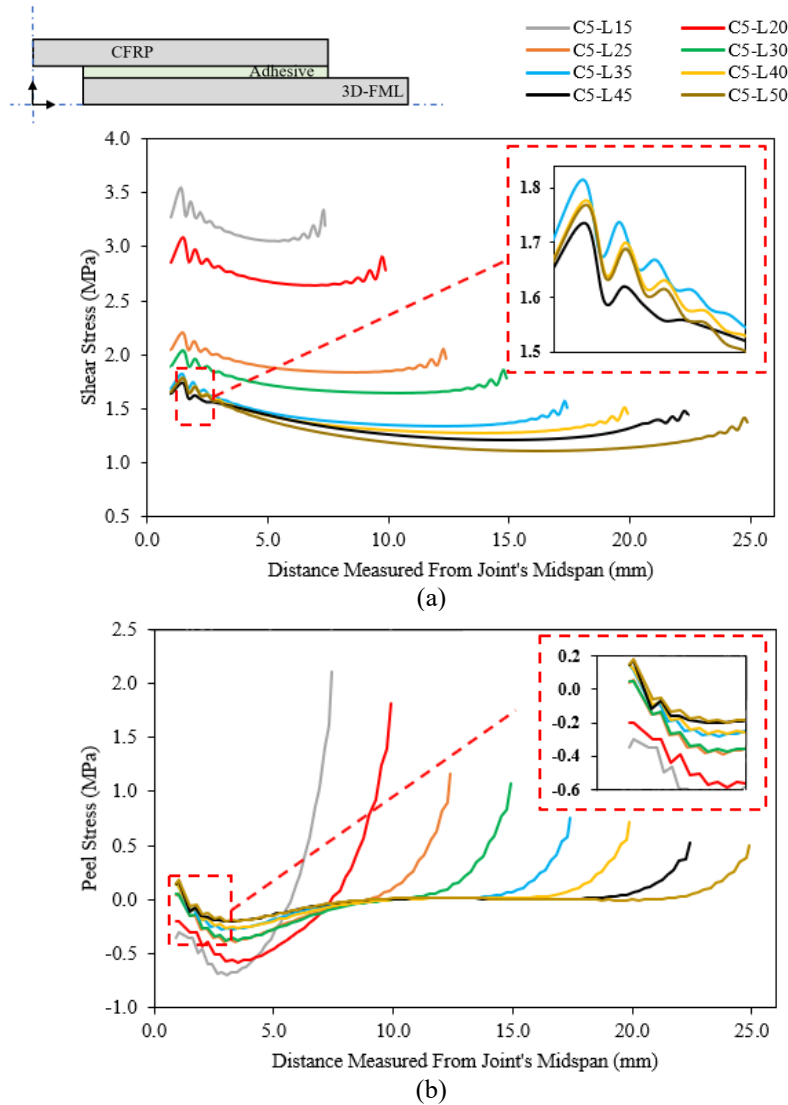


Figure 7-14. Influence of strap length on the distribution of (a) shear and (b) peel stresses on the adhesive layer.

The performance of the joints configured with the optimal thickness straps (i.e., with 5 layers of CFRP) is further scrutinized by examining the shear and peel stress distribution within the adhesive layer, in the vicinity of straps interfaces, by varying the length of the strap. The resulting shear and peel stress distributions are illustrated in Figure 7-14. As seen therein, the peak shear stresses are significantly reduced as the overlap length is

increased to 35 mm beyond which no appreciable decrease in the stress can be observed. As seen previously, the highest stress concentration occurred at the extremities of the bond regions. Moreover, the same trend in the distribution of the peel stress as observed previously is also seen in these joints (see Figure 7-14(b)). The stress distributions seen in Figure 7-13 and Figure 7-14 further attest to the integrity of the C5-L35 joint as being the optimal configuration.

The peel stress developed in the adhesive is also a critical parameter that could initiate joint failure. The distribution of the peel stresses in the considered ABJs is presented in Figure 7-13(b). As discussed earlier, the compressive and tensile variations in the distribution of the peel stresses are generated due to the bending moments developed within the straps of such joints. As seen, the maximum absolute peel stress developed at the edges of the bond regions of the specimens with one and two layers of CFRP straps. The magnitude of the stress is reduced as the straps are thickened up to six layers of CFRP. Further thickening of the straps caused an increase in the peel stress, especially at the outer edges, which indicates another reason for the decrease in the capacities observed in the earlier results.

7.5.4. Failure Simulation in Buckling Analysis

As mentioned previously, understanding the behaviour of adhesive joints under compressive loading is essential in order to accommodate their applications in various industries. To this end, the buckling and post-buckling responses of three different configurations of specimens, namely, C3-L25, C5-L25, and C5-L35, were numerically explored. The results of these analyses are compared against the results obtained experimentally as illustrated in Figure 7-15. Based on this figure, all specimens, in the linear regime could endure the applied load until the critical limit is reached. The critical limit is identified by the instability or buckling response of the joint followed by a nonlinear post-buckling response. As can also be seen, the predicted load-axial shortening results are in close agreement with the experimental results, thus, rendering the modelling framework capable of effectively predicting the pre- and post-buckling responses of double-strap adhesive joints. The numerically predicted buckling capacities are also reported in Table

7-6. The results indicate that the increase in the straps' thickness from three layers of CFRP to five layers (i.e., C3-L25 and C5-L25), results in a gain of 19.7% in the ultimate buckling capacity. However, the increase in the length of the CFRP straps does not produce any tangible improvement in ultimate capacity and would be in fact counter-productive, in that the buckling capacities would be slightly reduced. The reason for this phenomenon will be discussed later. Moreover, the developed FE model could predict the adhesive joints' ultimate buckling capacity fairly accurately with a minimum and maximum error margin of 3% and 6%, respectively. Note that the experimentally observed capacities reported in Table 7-6 are the average capacities of five tested specimens in each specimen category.

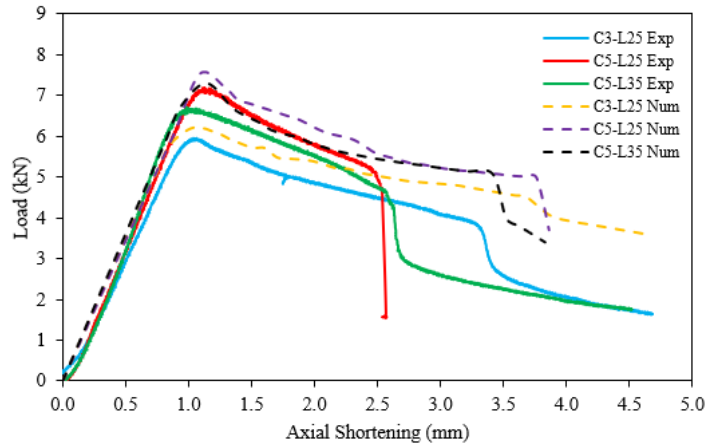


Figure 7-15. Comparison of the experimental and numerical responses of various configurations of the double-strap adhesive joints under compressive loading.

To further assess the pre- and post-buckling responses of the adhesive joints, their predicted global failure modes are compared with the experimentally observed modes as shown in Figure 7-16. As seen, the predominant failure mode in the C3-L25 joint was “shear crimping”. This failure mode is often attributed to the excessive shear deformation that is developed in cores with a low shear modulus (Coburn & Weaver, 2016). As seen in Figure 7-16(a), the FE model was able to capture the failure mode. Note that no local failure mode (i.e., in the bonded regions) is observed in this group of specimens. However, the primary failure mode of the specimen with the thicker straps (see failure mode of C5-L25) is observed to be the debonding of one of its straps from its adherends, resulting in a catastrophic failure, as illustrated in Figure 7-16(b). This mode occurred due to the development of a large magnitude of peel stress in the bonded region, which was

successfully captured by the automatically deleted cohesive elements in the appropriate region in the adhesive in the numerical simulation. Please note that to better visualize the numerical prediction, only the cohesive layers are illustrated in Figure 7-16(b); in other words, the continuum elements are not shown in the figure. After the development of extensive damage in the adhesive layer and debonding of the lower strap, the LS-DYNA solver was halted. Consequently, although damage growth and cohesive element deletion were seen in the edges of the upper straps, the FE model was not able to fully capture the full debonding of the upper strap developed in experiments. Interestingly, by increasing the CFRP strap length from 25 mm to 35 mm, as can be seen in Figure 7-16(c), the local delamination was initiated between the interface of SS sheets and 3DFGF core, in a location corresponding to one of the strap's ends. This response is attributed to the increased length and thickness of the straps, which in turn created additional local stiffness, thereby increasing the stress concentration in that location. In other words, the additional stiffness of the straps behaved somewhat like a gripping boundary condition and in combination with the geometric discontinuity, led to the development of a large stress concentration at the location.

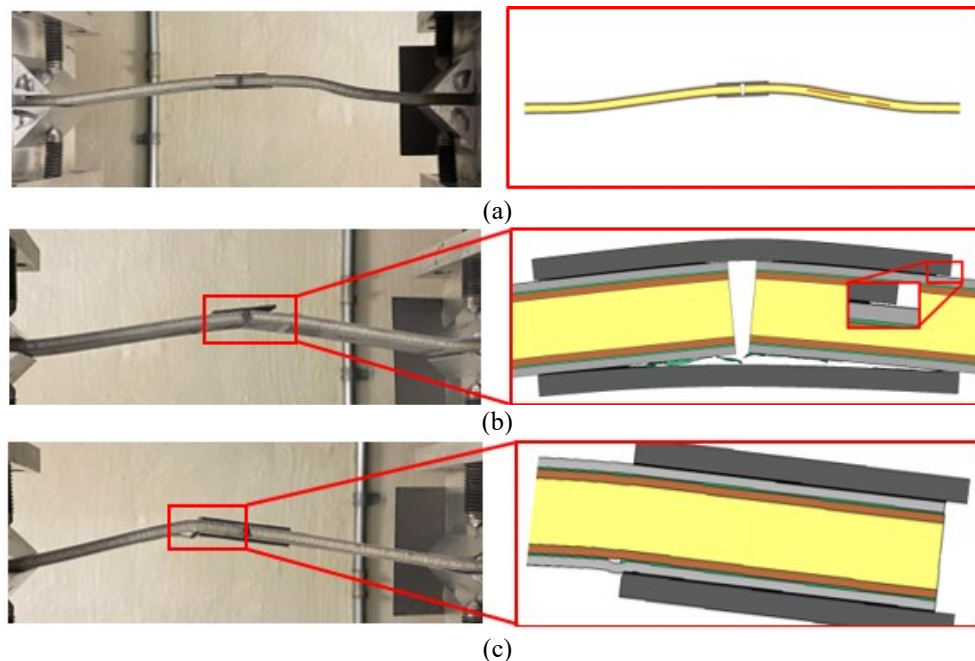


Figure 7-16. Comparison of the experimental and numerically predicted global failure modes in (a) C3-L25, (b) C5-L25, and (c) C5-L35 joint configurations subjected to compressive loading.

As seen, the FE model could capture the global failure mechanisms of the adhesive joints fairly accurately. It is also concluded that the C5-L35 configuration, which was established as the optimal configuration under tensile loading, also responded most effectively under a compressive loading state. Although this configuration sustained a slightly lower buckling capacity compared to the C5-L25 configuration, its resulting failure mode was non-catastrophic and could endure more load after undergoing its initial failure stage.

7.6. Conclusion

In this study, seven different FE models were developed to simulate the responses of double-strap adhesive joints mating 3D-FML adherends subjected to tension and compression loading states and prediction of the damage initiation and evolution in their bonded regions. A mixed mode (I+II) trapezoidal approach combined with continuum elements was employed to simulate the response of the adhesive. The influences of multilayered CZM, having different cohesive element thicknesses (i.e., zero- and non-zero thicknesses) on the cohesion and interfacial failure modes, and numbers of CFRP layers forming the straps (i.e., one to eight layers) and their length (i.e., 5mm to 50 mm) on the ultimate joint capacities were systematically explored.

It was found that the use of zero-thickness cohesive layers led to a more accurate prediction of the resulting damage evolution. Moreover, the utilization of more than two cohesive layers resulted in a more precise prediction of adhesive joint capacities and their load-displacement responses. The results also revealed that the model constructed with five layers of zero-thickness cohesive elements was the most effective model in accurately predicting the ultimate load-bearing capacity, the resulting stress distributions in the adhesive, and simulating the damage initiation and evolution in the joint. The models with three layers of zero-thickness cohesive elements, however, could be considered as an alternative where the accurate prediction of joint capacity with optimal CPU run takes priority. Note that one could not expect an accurate simulation of the damage evolution with such a model.

Subsequently, a set of parametric studies was performed to assess the effects of CFRP strap thickness and length on the joint capacity. The results indicated that the joint capacity of the adhesive joints could be enhanced by increasing the strap's length and thickness to a certain extent, beyond which no additional improvement could be attained. Based on the results, the adhesive joint configuration with straps consisting of five layers of CFRP and a length of 35 mm (identified as C5-L35 configuration) was established as the optimal configuration. The detailed analysis of the complex shear and peel stress distributions developed in the joints revealed the existence of a critical bending moment developed at the joints' midspan. This bending moment in turn led to the development of large magnitudes of shear and compressive stresses at the adherends end near the joints' midspan, while large tension peel and shear stresses were developed at the straps' extremities.

Simulation of the response of the joints under compressive loading revealed a similar pre-buckling response for all adhesive joint configurations but different post-buckling responses. While shear crimping was the predominant failure mode in the C3-L25 configuration, the debonding of CFRP straps and delamination in SS/3DFGF-epoxy interfaces were the main failure modes in C5-L25 and C5-L35 configurations, respectively. The comparison of the numerical and experimental results showed that the developed numerical modelling framework could accurately capture the local failure modes (i.e., cohesive and interfacial) and global failure modes (i.e., shear crimping, delamination) in adhesive joints under tensile or compressive loads.

Chapter 8: Machine Learning/Finite Element Analysis - A Collaborative Approach for Predicting the Axial Impact Response of Adhesively Bonded Joints with Unique Sandwich Composite Adherends

Fatemeh Mottaghian, Farid Taheri

Under review with the Journal of Composites Science and Technology

8.1. Abstract

Despite the increasing usage of adhesively bonded joints (ABJs) in various industries, optimization of their bond strength in a cost-effective manner remains a challenging task, particularly when complex loading scenarios such as static and dynamic compressive loadings are considered. The task becomes even more challenging in bonded joints with sandwich composite adherends. This study focuses on the performances of double-strap ABJs configured by unique sandwich composite adherends, carbon fiber-reinforced plastic straps, and a room-cured structural epoxy resin under axial impact loading. A Finite Element-Cohesive Zone (FE-CZ) model is developed to simulate the response of the joints, and its integrity is validated against the experimental tests at three impact energy levels. The model is used to simulate the response of various ABJ configurations under axial impact loading, taking into account 13 material, geometrical, and testing-related parameters that influence joint strength, thereby generating 410 data sets. Subsequently, three Machine Learning (ML) models, including deep neural networks and genetic evolution (i.e., genetic programming and genetic algorithms) are developed and trained by the data sets to predict the ABJs load-bearing capacity. The ML models explore the relationship between the design parameters and the joint's ultimate load-bearing capacities, leading to the development of cost-effective and accurate empirical equations, and optimized joint configurations.

8.2. Introduction

[...] *Some portions of this section have been removed and included in Chapter 2.*

The number of ML-based models developed for analyzing ABJs is fairly limited, and the available models have been generally developed based on simple design variables. There are only a few ML-based studies that have systematically investigated ABJ's capacities.

From the perspective of loading scenario consideration, while extensive research has been conducted to assess the performances of ABJs subjected to fatigue and tensile loading scenarios, there is a clear lack of knowledge regarding the performance of ABJs subjected to static and particularly dynamic (impact) axial compressive loading. The axial impact causes the evaluation of the response of ABJs with sandwich composite adherends to become more complex, as the loading can cause the system to buckle. As a result, this phenomenon is referred to as impact-buckling, hereafter. To the best of the authors' knowledge, there has only been a few studies that have assessed the response of ABJs joining sandwich composites. Moreover, no design equations exist for establishing the impact-buckling capacity of these joints.

Therefore, to bridge the knowledge gap, this study explores the impact-buckling responses of double-strap ABJs constructed with unique sandwich composite adherends, CFRP straps, and a commonly used room-cured structural epoxy. Firstly, a set of experimental tests are performed to capture the axial impact behaviours of the bonded joints subjected to different energy levels (i.e., 5J, 10J, and 20J). Subsequently, an FE model is developed in which zero-thickness cohesive elements combined with continuum elements are implemented to capture the failure mechanism in the bonded area. The numerical results are validated against experimental results. Thereafter, ML models (Deep Neural networks (DNNs), GP, and GA) are developed to account for 13 design parameters that affect the dynamic responses of the ABJs. The design variables are categorized into three groups: (i) mechanical properties (i.e., adherends, straps, and adhesive) (ii) geometrical configurations (i.e., adherends and straps thickness and length and perturbations characteristics), (iii) experimental variables (i.e., impact energy and

boundary conditions). The dataset generated by the FE model is utilized to train the developed ML models. Subsequently, an empirical equation based on the developed ML models is established by which the ultimate joint capacity of bonded joint panels subjected to an in-plane low-velocity impact is predicted. The proposed simple yet accurate equation enables practicing engineers to conduct preliminary designs of ABJs that consist of such robust and intricate 3D composites, thereby facilitating and encouraging their applications in various industries. Finally, the optimal combination of the design parameters that led to the highest ultimate buckling capacity was also explored by the proposed GA model. The schematic of the overall research presented in this study is depicted in Figure 8-1.

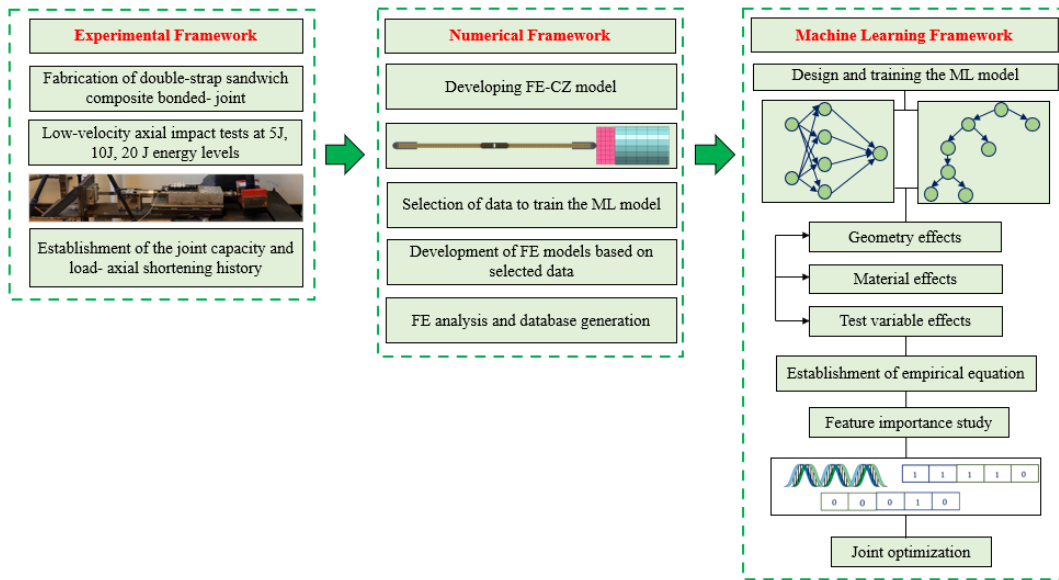


Figure 8-1. Schematic of the research conducted in this study.

8.3. Experimental Framework

8.3.1. Materials

The fabricated double-strap sandwich composite components include thin stainless steel (SS) sheets, 3D fiberglass fabric (3DFGF), CFRP prepreg, a cold-cured structural epoxy resin, and a two-part liquid polyurethane foam. SS 304-2B sheets with 0.48 mm thickness and the West System structural epoxy system (105 resin and 206 slow hardener) were purchased locally. The 3DFGF with a nominal thickness of 4 mm was obtained from China Beihai Fiberglass Co. Ltd. (Jiujiang City, Jiangxi, China). The two-part “16 lb”

polyurethane foam was supplied by US Composites (Palm Beach, FL, US). Moreover, the Gurit woven CFRP prepreg with a thickness of 0.25 mm was obtained from Composite Canada (Mississauga, ON, Canada).

8.3.2. Specimen Fabrication

Fabrication of the unique sandwich composite adherends began with the fabrication of the core components of these hybrid materials. The 3D fabric (3DFGF) used in this work is an integrated fabric consisting of two bi-directional woven fabric surfaces, knitted together by vertical glass fiber pillars. The pillars have an intricate figure-8 type orientation, with a 30° inclination with respect to the through-thickness direction. Due to their unique structure, the delamination between the core and fabrics is completely suppressed in this material (Mottaghian & Taheri, 2023). The 3DFGF was then impregnated with structural epoxy (resin-to-hardener weight ratio of 5:1) and left to cure for 48 hrs; the 3DFGF-epoxy resin system is referred to as 3DFRP, hereafter. To reinforce the 3DFRP, a “16 lb” two-part liquid polyurethane foam (with a mixing ratio of 1:1) was utilized to fill the core cavities of 3DFRP; the foam was left to cure for 24 hr. Subsequently, the reinforced core was sandwiched in between the grit-blasted SS sheets, sealed in a vacuum bag under 1 bar vacuum, and left to cure for 48 hrs. The sandwich system takes advantage of the positive attributes of the FRP core and the metal sheets.

To fabricate the double-strap joints, the layer of CFRP prepreg were stacked one by one, and CFRP laminate was subsequently sealed within a vacuum bag and let cure in an oven at 120°C for 2hr. The laminate was then cut into two appropriate equal-size panels and its bonding surface regions were abraded by 100-grit sandpaper in random directions. The sanded regions were air blasted and wiped clean with acetone. Once dried, a thin layer of resin was applied to the regions. CFRP straps were then bonded to the sandwich composite under constant pressure, and the assembly was left to cure for 48 hrs and subsequently was divided into the desired dimensions using a water jet. More detail on the fabrication process is provided in (Mottaghian & Taheri, 2022). The dimensions of the fabricated double-strap ABJs are shown in Figure 8-2(a).

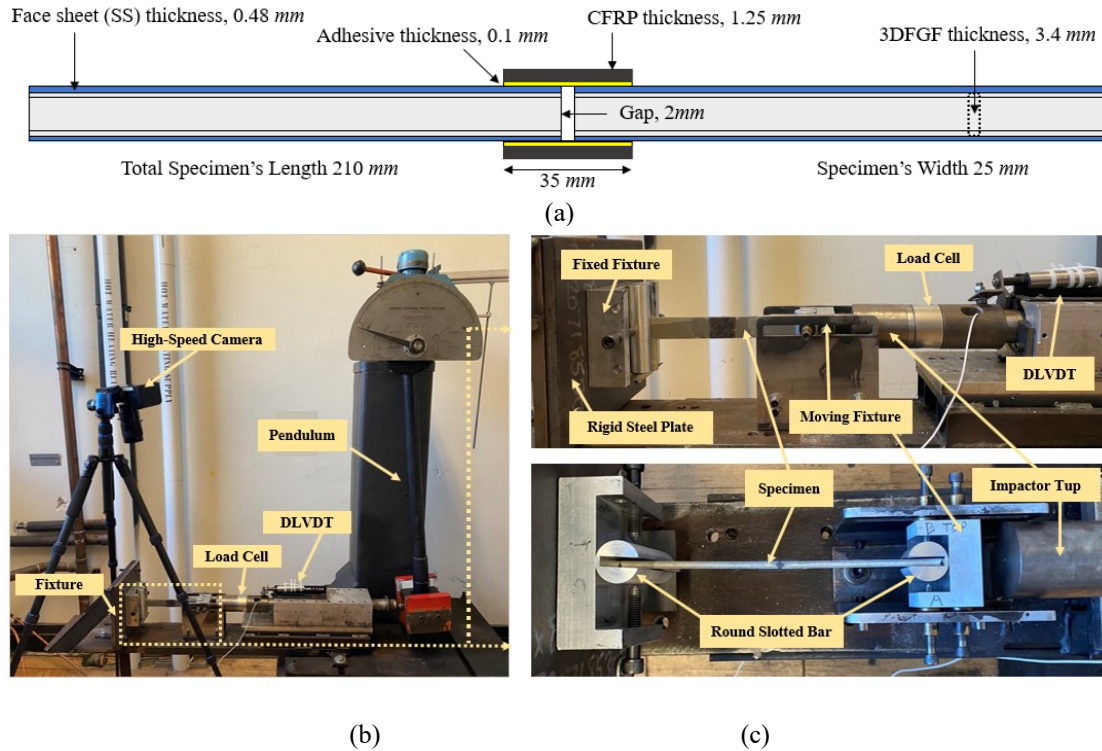


Figure 8-2. (a) Dimensions of the double strap bonded sandwich joints, impact-buckling set up (b) overall view of the test setup, (c) close-up side- and top view of the specimen holding fixture.

8.3.3. Impact Testing Procedure

The compressive axial low-velocity impact (LVI) tests were performed by a modified Charpy impact test equipment, consisting of a pendulum, an impactor, a bearing-assisted guiding box, and a fixture that holds the specimens in place (see Figure 8-2(b)). The fixture was designed to hold each end of the specimens in a simply-supported state; the detail of the fixture is shown in Figure 8-2(c). As shown, the specimens are allowed to displace longitudinally (axially) on the impacted side (at the right end portion of the specimen), while it was restrained to move longitudinally at the left end of the specimen. Note that the aluminum round slotted bars shown in the figure allow free rotation on both ends of the specimens. The impactor tup was made of a 52 mm-diameter steel cylinder. The impact load and axial-shortening history data were recorded by using a dynamic load cell and a dynamic linear variable displacement transducer (DLVDT) at a sampling rate of 50 kHz. The captured signals were transferred to a PC using a National Instruments data acquisition system synchronized using the Signal Express software. To calibrate the load cell, six

impact tests with pendulum angles ranging from 30° to 76° were performed, generating impact energies ranging from 5 J to 35 J. Consequently, a curve was fitted to the data points, and the angle for generating a desired impact energy was established. The ABJs were subjected to LVI of 5J, 10 J, and 20 J energies, which corresponds to velocities of 1.34 m/s, 1.9 m/s, and 2.7 m/s, respectively

Note that in each test, the impactor tip impacts the aluminum fixture holding the specimen, which is free to translate axially and in turn subject the specimen to a compressive impact load; in other words, as seen in Figure 8-2(c), the specimen's end is not impacted directly. The correct alignment of the specimen before each test was verified by a digital level indicator and a square ruler. A minimum of three specimens was tested to guarantee accurate and consistent results. The root mean square (RMS) of the collected signals of each specimen was determined to avoid the unwanted and inevitable signal noise recorded by the sensors and obtain so-called "refined" curves. A Kronotek Chronos high-speed camera was used to record the impact events at a rate of 4498 fps. The recorded images were later employed to verify the axial impact response of the specimen simulated numerically.

8.4. Numerical Framework

The commercially available FE software LS-DYNA was utilized to simulate the response of double-strap sandwich composite bonded joints subjected to the exact boundary condition and loading as in the experiments, as shown in Figure 8-3. The model was constructed using explicit nonlinear analysis using the 8-node fully integrated solid elements (ELFORM= -1) along with the CZM element (ELFORM= 19). The metal sheets components of the sandwich composite were modelled by piecewise linear plasticity (MAT_024) by considering yield strength (σ_{yield}). The plies and pillars constituents of the 3DFRP were modelled by using the composite damage material model (MAT_054/055) with the Chang-Chang failure criteria capable of assessing the damage evolution. The polyurethane foam was modelled by the elastic material model (MAT_001) in conjunction with the erosion material model (MAT_000), which deletes the specimen once the effective strain in the element exceeds the set strain limit. Note that many of LS-DYNA's material

models have no provision for modelling the failure of the material. In such cases, MAT_000 provides the option to include failure reassessment. Stress- or stain-based failures or combinations of them could be defined by the user in MAT_000 to account for failure and erosion of the material. MAT_001 model was used to model the straps in conjunction with the use of principal stress (σ_{max}) criterion in MAT_000 to declare the failure of the material.

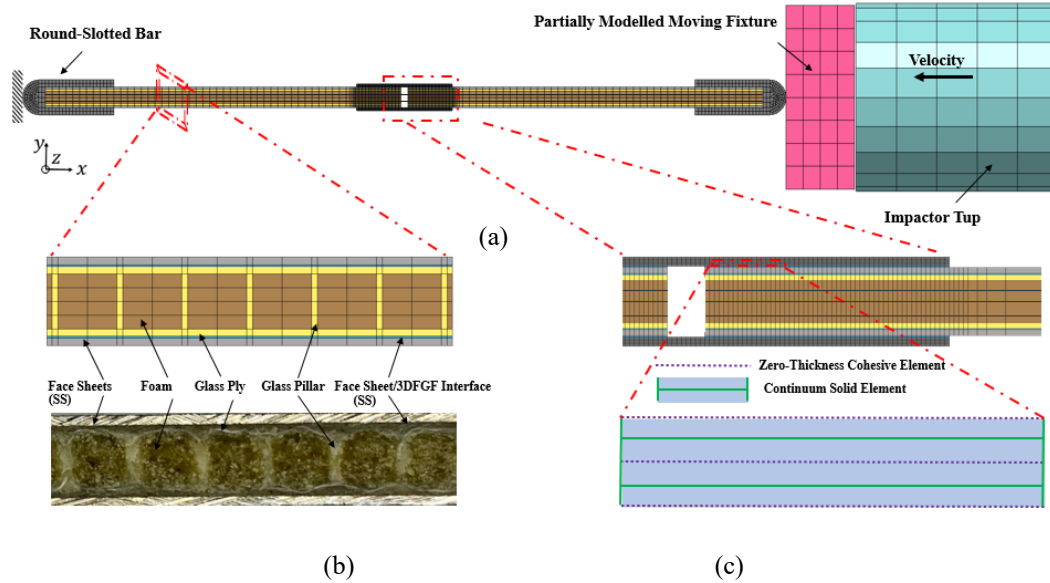


Figure 8-3. The FE model (a) overall model, (b) FE mesh of the cross-section of the adherends and actual sandwich composite, and (c) FE mesh of the bonded area including three layers of zero-thickness cohesive elements combined with continuum solid elements.

The adhesive in the bonded area was modelled by three layers of zero-thickness cohesive elements combined with continuum solid elements as shown in Figure 8-3(c). The plastic polymer material mode (MAT_089), and mixed-mode cohesive zone model (MAT_240), were used in conjunction with the continuum solid and cohesive elements, respectively. Each metal/3DFRP interface was modelled by one layer of cohesive elements. Figure 8-3(b) shows various constituents of the sandwich composite.

Table 8-1. Mechanical properties of 3DFRP (Yaghoobi et al., 2021b).

Properties	E_{11}, E (GPa)	E_{22} (GPa)	G_{12}, G_{13} (GPa)	G_{23} (GPa)	S_c (GPa)	X_c (GPa)	X_T (GPa)	Y_c (GPa)	Y_T (GPa)	ϵ_{max}
Glass plies	9	9	1	1	0.03	0.173	0.173	0.173	0.173	
Glass pillars	3	1	1	1	0.03	0.08	0.08	0.08	0.08	
Foam	0.05									0.15

As mentioned earlier, the mixed mode (I+II) trapezoidal cohesive model was used in this study to simulate the potential debonding, decohesion, and delamination. The model accounts for the peel and shear failure modes (mode I and II, respectively) and their combination. This model considers the elastic-plastic softening damage response (Biel & Stigh, 2010) that could develop during unloading/reloading. In this model, the residual displacement and damage from the previous time step are accounted for when the system is fully unloaded (Watson, 2021). Note that the results obtained in the author's previous study indicated that accurate failure prediction could be attained so long as the adhesive layer is modelled by using at least three layers of cohesive elements interleaved by layers of solid elements (see the configuration shown in Figure 8-3(c)). It was also shown that the implementation of five layers of cohesive elements resulted in the most accurate damage growth simulation in the bonded area. Modelling the adhesive layer with a higher number of cohesive element layers will improve the prediction further. However, since the main objective of this study is the optimization of the double-strap sandwich composite bonded joint, hence, for the sake of CPU time efficiency, three layers of the cohesive element were selected for the modelling. Moreover, since CZM is a mesh-sensitive approach, a fine and uniform mesh was used to model the bonded region, and the mesh was gradually transitioned to coarser meshes away from the region. A detailed explanation of modelling sandwich composite and CZM was discussed in Chapter 7. The mechanical properties of sandwich composites used in the FE models are tabulated in Table 8-1-Table 8-3.

Table 8-2. CZM parameter of adhesive in the bonded area.

Properties	Poisson's ratio	Normal (shear) Stiffness (GPa)	Mode I (II) Yield Stress (MPa)	Mode I (II) Energy Release Rate (KJ/m²)
Epoxy (Mottaghian & Taheri, 2022)	0.32	3.50 (1.50)	59.00 (23.00)	1.50 (2.00)
Loctite EA 9494 (Kanani et al., 2020)	0.29	7.71 (3.34)	25.35 (16.00)	0.26 (0.90)
Araldite 2015 (Campilho et al., 2013b)	0.33	1.85 (0.92)	21.63 (17.90)	0.43 (4.70)
FM94 (Liu et al., 2018, 2019)	0.35	3.00 (1.20)	30.00 (20.00)	1.50 (2.70)
AV138 (Campilho et al., 2013b)	0.35	4.89 (2.41)	39.45 (30.20)	2.00 (3.80)

Notes: (i) The numbers in brackets are the values for mode II, while the neighbours on left are for mode I.

(ii) The quadratic stress and power-law with ($\eta=1$) were considered as initiation and propagation criteria, respectively.

When modelling a compressive axial impact event, special attention should be given to explicitly modelling the geometric imperfection, which is required to numerically trigger the instability of the specimen. Additionally, the boundary conditions should also be modelled as closely as possible to the actual restraining mechanism. Therefore, the steel impactor tup, the aluminum moving fixture, and the round-slotted bar fixtures were all modelled with solid elements in the FE model (see Figure 8-3(a)). Note that the appropriate mechanical properties were assigned to each part. To mimic the boundary conditions, all degrees of freedom (DOFs) of a row of the nodes at the left end of the round-slotted bar were restrained. Also, all DOFs but the longitudinal DOFs (u_x) of a row of the nodes of the moving fixture on the impacted side (the right end in Figure 8-3(a)), was restrained. The automatic surface-to-surface contact algorithm was incorporated to simulate the interaction between the impactor tup and the moving aluminum fixture. This contact algorithm allows the impactor to bounce back from the fixture if necessary. The interfaces between the moving fixture and slotted bar fixtures, and the slotted-bar fixture and the specimen, were modelled by employing the tied-surface-to-surface contact algorithm. An initial velocity was applied to the impactor tup to simulate the loading scenarios and the quasi-frequency-independent damping coefficients were incorporated to account for the effects of material damping on the vibration response of the specimens subjected to axial impact.

Table 8-3. Mechanical properties of the strap and face sheets.

Properties	Young's modulus (GPa)	Poisson's ratio	Yield Strength (GPa)	Tensile Strength (GPa)
Stainless Steel	193.74	0.29	0.442	
Aluminum	68.95	0.33	0.207	
Titanium	82.74	0.32	0.774	
Magnesium	36.12	0.35	0.231	
Cartridge	110.32	0.33	0.230	
Glass fiber-reinforced composite (Ekşi & Genel, 2017)	14.40	0.24		0.22
Carbon fiber-reinforced composites (Mottaghian & Taheri, 2022)	54.00	0.23		0.510
Aramid fiber-reinforced composites (Ekşi & Genel, 2017)	19.09	0.38		0.357
Polyphtalamide (50% glass fibre) (Kanani et al., 2020)	17.62	0.32		0.241

8.5. Machine Learning Framework

8.5.1. Data Collection

In this study, a systematic parametric study was performed by incorporating the FE-CZ model to generate a robust database of the ultimate impact-buckling capacities of the double-strap sandwich composite subjected to LVI as a function of 13 design variables. The considered parameters are tabulated in Table 8-4. The parameters are categorized into three groups as previously stated in the Introduction section. The Latin hypercube sampling. The Latin hypercube sampling (Trinh & Jun, 2021) technique was adopted for the design of the experiments to certify that the selected points represent the full range of each variable, devoid of unnecessary samples. In other words, this technique guarantees that smaller yet necessary samples with uniform distributions would be considered in the design space. Based on this technique, different combinations of variables were generated by assuring a high-quality variable space, which was then implemented in the FE models. The Latin hypercube sampling code was generated using the "lhsmdu" library in Python. Once the integrity of the numerical model was validated against the experimental results, further numerical analyses were performed, resulting in the collection of 410 samples; this will be discussed in detail in section 8.6. The detailed reason for implementing 3-fold cross-validation will be further discussed in section 8.6.2.

Table 8-4. Defined design parameters in double-strap sandwich structure bonded joints.

Design variable	Input ID	Lower Bound	Upper Bound
Strap Material Type	x_1	9 Materials Provided in Table 8-3	
Metal Material Type	x_2	for Each Variable	
Adhesive Material Type	x_3	5 Materials Provided in Table 8-2	
3DFRP Thickness (mm)	x_4	1	15
Strap Thickness (mm)	x_5	0.5	1.5
Metal Thickness (mm)	x_6	0.4	1.5
Specimen Length (mm)	x_7	200	750
Strap Length (mm)	x_8	5	60
Gap Length (mm)	x_9	0	2
Location of Straps w.r.t Specimen Length	x_{10}	0.2	0.8
Impact Energy (kJ)	x_{11}	5	60
Perturbation	x_{12}	0.1	1.7
Boundary Conditions	x_{13}	Simply-Supported and Clamped-Clamped	

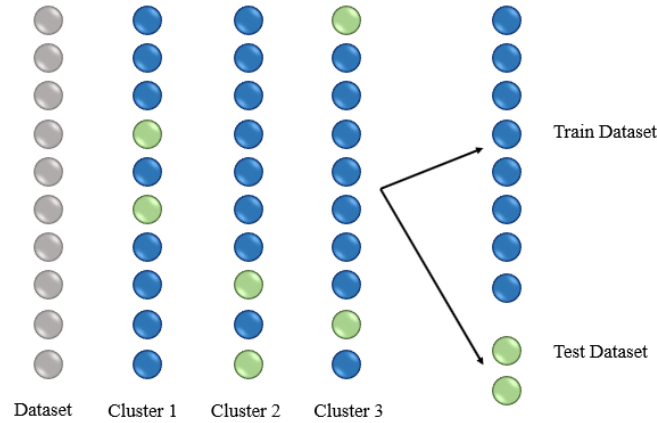


Figure 8-4. Schematic of 3-fold cross-validation technique.

8.5.2. Data Pre-processing

The data pre-processing technique, which includes cleaning and organizing the data, is a crucial step in ML as it improves the quality of the data, facilitating the extraction of useful insights. Raw data is often full of issues such as missing values, noise, inconsistencies, and redundancies, which can adversely impact the performance of later steps. In this study, the data (i.e., design parameters) were normalized between 0 and 1 by the implementation of the following equation to minimize the effect of such issues on the quality and reliability of the subsequent step.

$$x_{Normalized} = \frac{x - x_{Minimum}}{x_{Maximum} - x_{Minimum}} \quad (8-1)$$

The normalization transforms parameters so they are on a similar scale, thus, improving the stability and performance of the model. The “train-test split methodology” is implemented to evaluate the performance of the ML algorithm developed in this study. The data set is divided into two subsets, called train and test datasets. In this study, 80% of the whole data (328 sets) is dedicated to the train dataset, which was used to train and fit the ML models, while the rest (82 sets) were implemented as the test datasets, to evaluate the accuracy of the ML model. The train-test split technique enables the estimation of a model's performance on new data that were not used during training. Cross-validation is a technique used to mitigate overfitting in predictive models, especially when data is limited. It involves dividing the data into a fixed number of folds, running the analysis on each fold

as a validation set while using the rest for training, and then evaluating the accuracy and generalization performance of the model. In this study, a 3-fold cross-validation was used to evaluate the general performance of developed ML models as shown in section 8.6.2.

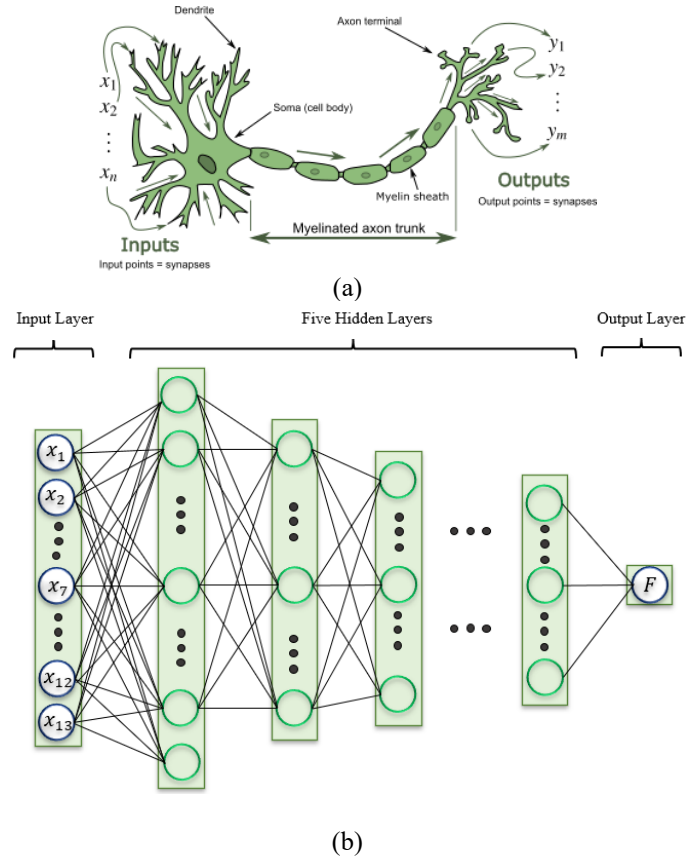


Figure 8-5. Schematic of (a) biological and mimicked artificial neural network (Gerstner et al., 2014), (b) architecture of the deep neural network designed to predict the impact-buckling ultimate capacity of the bonded joints.

8.5.3. Deep Neural Networks

ANNs is a neuroscience-inspired computing system that mimics a biological neural network. It consists of simple processing units, known as neurons, which interact with the external environment or other neurons, similar to their biological counterparts. A biological neuron takes in signals from its dendrites and adjusts them to different levels. The adjusted information will only be transmitted through the synapses if the strength of the signals reaches a particular threshold. The concept of an ANNs is illustrated in Figure 8-5(a). Similarly, artificial neurons are linked by synapses and replicate the actions of biological neurons. In ANNs, neurons receive inputs that are the sum of the weighted outputs of

neurons from the previous layer. They use activation functions to process the sum of the inputs and pass the resulting information to other neurons or produce results. ANNs are robust algorithms capable of adaptive learning and can solve intricate regression and classification problems (McCulloch & Pitts, 1943).

A neural network typically consists of an input layer, one or more hidden layers, and an output layer. The input layer is the initial layer of the neural networks that receive input values and forwards them to the following layer. In this layer, no operations would be performed since no bias and weight are defined. The hidden layers contain neurons that perform various operations on the input data. Every neuron in a hidden layer is linked to every neuron in the previous and next layers, making the hidden layers fully connected. The output layer is the final layer of the network, which provides the predicted values of the model. An ANNs algorithm is referred to as deep neural networks (DNNs) model when it has more than two hidden layers (DNNs) model when it has more than two hidden layers (Montesinos López et al., 2022; Raissi et al., 2019). The fundamental mathematical equations of ANNs can be found in (Tao et al., 2021).

Table 8-5. Configurations of the designed DNNs model.

Type of Layer	Output Shape	Parameters	Activation Function
Visible Input layer	13	13	-
Hidden Layer 01	130	1820	Leaky Relu
Hidden Layer 02	70	9170	Leaky Relu
Hidden Layer 03	50	3550	Leaky Relu
Hidden Layer 04	30	1530	Leaky Relu
Hidden Layer 05	15	465	Leaky Relu
Visible Output Layer	1	16	Linear
Other Features :			
Total Parameters: 16733	Trainable Parameters: 16733	Batch size: 32	
Learning Rate: 0.001	Optimizer: Adam	Number of Epoch: 3000	
Kernal Regularizer : 0.001,L2	Bias Regularizer: 0.001,L2		

The schematic of the structure of the DNNs model developed in this study is depicted in Figure 8-5(b). The “Keras” and “TensorFlow” libraries in Python are implemented to code the designed DNNs model in this study. Table 8-5 presents the features used to design the model. As seen, the model consists of five hidden layers, and the Leaky-ReLU activation function is implemented for each layer. Bias and a learning rate of 0.001 are set for the algorithm. To train the model a total of 16733 parameters are employed. The number of parameters in each layer is calculated by multiplying the number of neurons in the

current layer by the number of neurons in the previous layer and summing them to the number of neurons in the current layer. Note that Gaussian noise, as well as Keras weight regularization, were used to mitigate the overfitting problem. Regularization is a technique utilized to calibrate the ML models and minimize the loss function, thus preventing underfitting or overfitting. It should be noted that the sequence of steps typically taken to arrive at the optimal architecture of ML models includes (i) defining the problem and gathering data, (ii) determining the input and output, (iii) selecting a basic architecture, (iv) training and evaluating the initial model, (v) adjusting the architecture, (vi) training and evaluating the updated model, (vii) repeating steps v and vi, and (viii) testing the final model. In this study, the developed DNNs model was employed to establish the mathematical relationship between the 13 defined design parameters and the ultimate impact-buckling capacities, with the aim of predicting the performances of double-strap sandwich composite bonded joints subjected to axial impact loadings.

8.5.4. Evolutionary Models

8.5.4.1. Genetic Programming

Evolutionary algorithms are problem-solving techniques that are inspired by the Darwinian principle of natural selection and survival of fittest. Based on this theory, the organisms capable of adapting best to their surroundings are the ones that have the highest chances of survival. They would reproduce along with a genetic recombination (crossover and mutation) operation appropriate for mating. The schematic of individual mutated DNA generated with a predetermined tendency toward a development inherited from the previous generation is shown in Figure 8-6(a). GP is a well-known evolutionary algorithm that utilizes computer programs to construct its population. These programs are represented as binary trees, which are composed of branches and leaves that are characterized by functions and terminals, respectively. The functions can be arithmetic operations, standard programming operations, logic functions, or custom-defined functions. The terminals in a computational model can be variables, constants, or specific quantities that the designer needs to define (Koza & Poli, 2005). The structural tree and cross-over genetic evolutionary combinations in a simple GP model are presented in Figure 8-6(b). The

evolutionary offspring shown in the figure can be used to deduce simple mathematical equations such as $\frac{2-4(3-z)}{8+y}$ and $6 + 5x$.

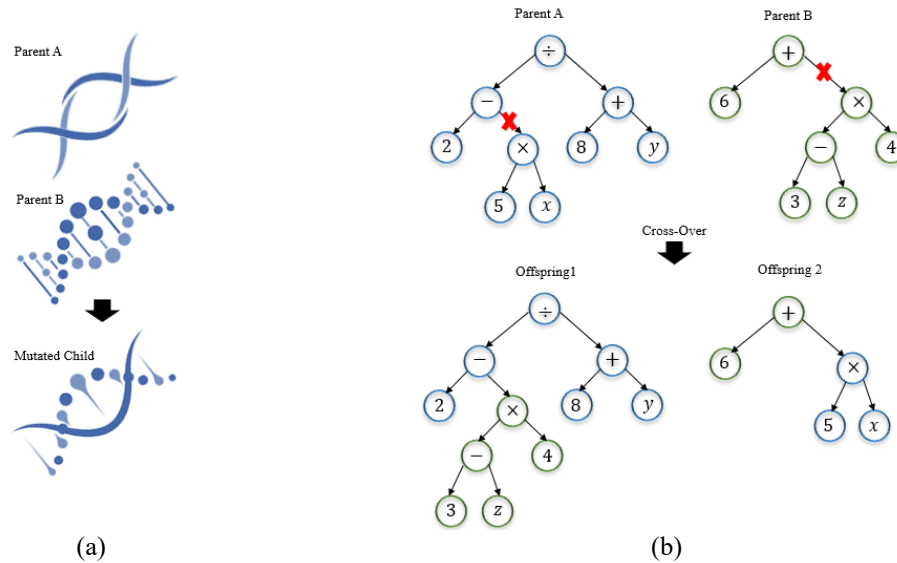


Figure 8-6. Evolutionary schematic of (a) biological DNA mutation, (b) tree structure of GP cross-over representing $\frac{2-4(3-z)}{8+y}$ and $6 + 5x$ equations.

GP has distinct characteristics that set it apart from other evolutionary algorithms. This method utilizes trees as a representation of its population, which allows for variable-length computer programming. This feature allows GP to effectively identify redundant elements in complex problems. In contrast, other evolutionary algorithms use fixed-length representations. GP also employs a unique crossover operator that swaps fragments of two trees to create new offspring, reducing the likelihood of producing repetitive trees during the evolution process. To begin, GP generates an initial set of trees through a random selection process, using a set of functions and terminals. The functions are used to represent the root or internal connections of the tree, while terminals represent the end nodes. This random search method allows GP to explore the solution space and identify potential solutions. Each tree in the population is assessed using a fitness measure to determine its effectiveness in solving the problem. This evaluation process is applied to all individuals in the population. Consequently, the population experiences crossover and mutation operations to generate new offspring (Ale Ali et al., 2022).

Table 8-6. Specific parameters used in the designed GP model.

Parameters	Magnitude
Function Set	$+, -, \div, \times, \sqrt{\quad}, \quad , x^n, e^n (n \in Z \& D)$
Population Size	12000
Generations	300
Crossover	0.8
Subtree Mutation	0.1
Hoist Mutation	0.01
Point Mutation	0.01
Point Replace	0.05
Constant Range	(-5,5)
Initial Depth	(2,15)
Maximum Sample	0.9
Stopping Criteria	0.001
Initialization Method	Full

After applying these operations, GP collects all the new offspring and adds them to a pool. The next generation population is then selected from this pool using a probabilistic fitness proportionate method, and the initial population is replaced by the newly generated one. This process is repeated for multiple generations, with the goal of increasing the average fitness of each generation until a stopping criterion is met. The best individual from this evolution process is considered the solution to the optimization problem. The GP model developed in this study is coded by the “Gplearn” library of Python. The specific parameters of the developed model are provided in Table 8-6. The initial population of 12,000 with a maximum number of evolution generations of 300 is selected for the model. And the chances of crossover and mutation are defined as 0.8 and 0.1 respectively. This model is used to map the defined 13 design parameters and the ultimate impact-buckling capacities, as well as the establish the equation governing the performances of double-strap sandwich composite bonded joints subjected to lateral impact loadings.

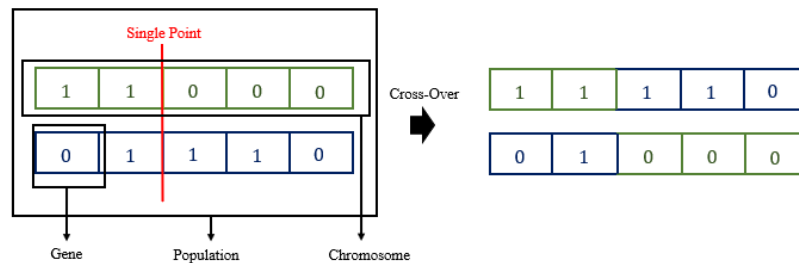


Figure 8-7. Representation of single point cross-over evolution in a GA population.

8.5.4.2. Genetic Algorithm

The genetic algorithm is another subset of the ML evolutionary model which generally follows the same principles as described in section 8.5.3.1. The main difference is that GAs are typically implemented using arrays of bits or characters to represent the chromosomes, whereas GP utilizes computer programs represented as binary trees that are composed of branches and leaves characterized by functions and terminals, respectively. In GA, the individuals in the population undergo a simulated evolution process. Basic bit manipulation techniques are used to carry out operations such as crossover and mutation (see Figure 8-7). Typically, the number of bits and decimal ranges used to represent each gene (parameter) is the same. One of the most prominent features of genetic algorithms (GAs), compared to other evolutionary algorithms, is their emphasis on using fixed-length character strings as the genetic representation. The main difference between GA and genetic programming (GP) is that GA focuses on optimizing a fixed number of variables, while GP aims to optimize entire structures of variable sizes and any parameters within those structures. The “genetic algorithm” library in Python was used to code the GA model in this study.

Table 8-7. Specific parameters used in the designed GA model.

Parameters	Magnitude
Maximum Number of Iteration	1000
Population Size	800
Mutation Probability	0.3
Cross-over Probability	0.7
Parents Portion	0.3

The Specific parameters of the developed GA model are reported in Table 8-7. The population size of 800 with mutation and cross-over probability of 0.3 and 0.7, respectively we considered. This model is used to establish the optimal configuration of the defined 13 design parameters in the performances of double-strap sandwich composite bonded joints subjected to lateral impact loadings. The working flowcharts of the GP and GA models are depicted in Figure 8-8.

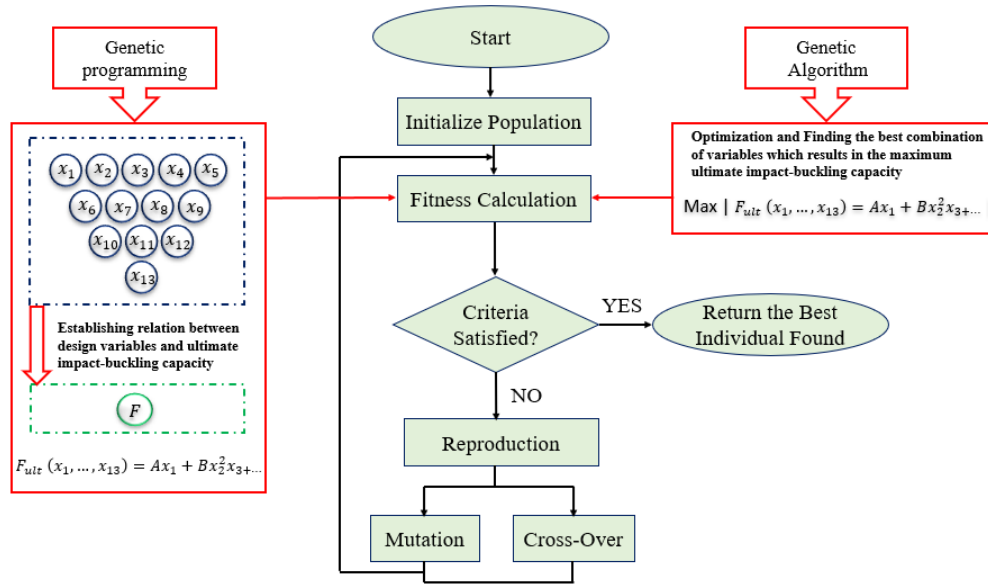


Figure 8-8. Flowcharts of GP and GA processes.

8.6. Results and Discussions

8.6.1. Experimental and Numerical Validation

To investigate the performance of double-strap sandwich structure bonded joints, the fabricated specimens with the dimensions shown in Figure 8-2(a) were subjected to three different levels of impact energies (i.e., 5J, 10J, and 20J). An FE-CZ model was developed to perform a parametric study to assess the effects of design parameters on the performances of bonded joints, and the integrity of the numerical model was validated against the experimental results. The plots of load and axial shortening history obtained experimentally and numerically are shown in Figure 8-9. As seen, higher ultimate impact-buckling capacities are attained when the impact energy is increased. Compared to the ultimate impact-buckling capacity of the specimens impacted by 5J, 5.28% and 27.47 % enhancement in ultimate impact-buckling capacity were attained in specimens that were subjected to impact energies of 20J and 30J, respectively. The graphs shown in Figure 8-9 depict typical responses for the specimens attested in each category. Moreover, a good correlation between the experimental and numerical results is observed. The predicted numerical ultimate impact-buckling capacities, the stiffness characteristics, and the decline in load-bearing capacity after the onset of buckling are all in good agreement with the

experimental results. The minimum and maximum values of error margins between the average experimental and numerical results are 6.36% and 6.92%, respectively. Similarly, good agreement is observed between the experimental and numerically predicted axial shortening history, which validates the accuracy and robustness of the developed model. The increase in the impact energy resulted in a larger magnitude of lateral deformation, thus higher axial shortening.

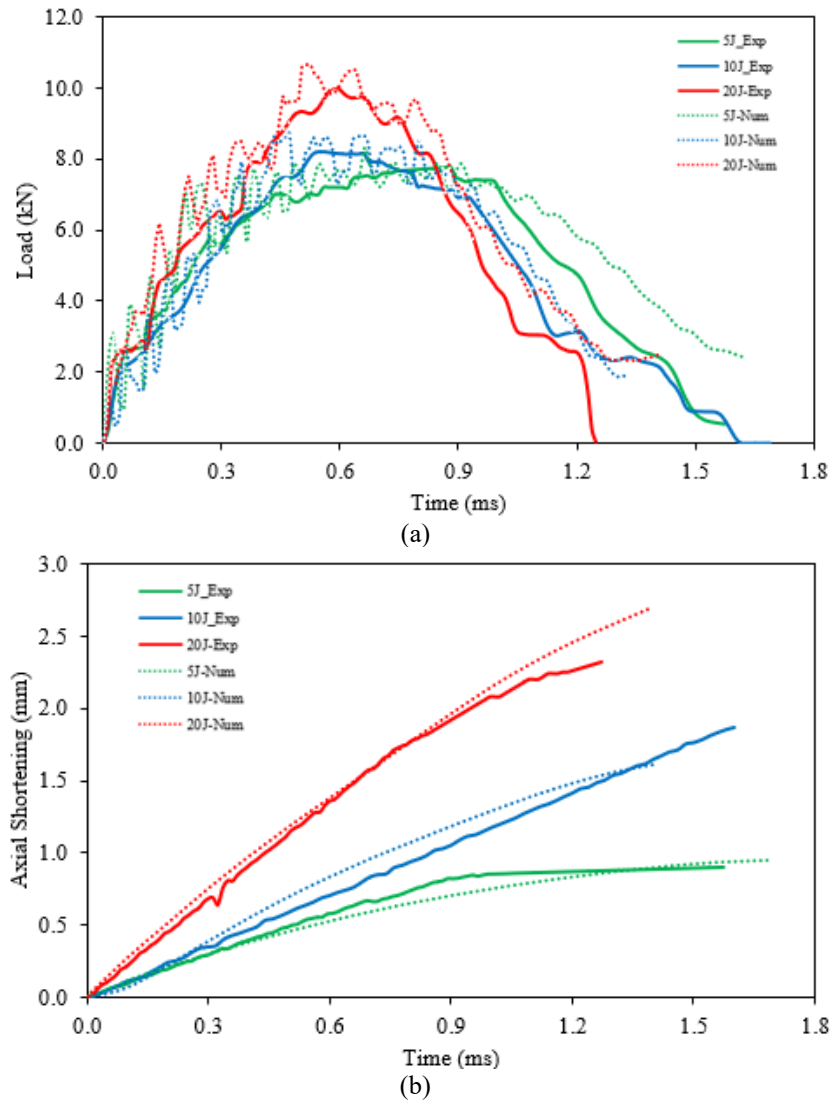


Figure 8-9. Comparison of experimental and numerical load and axial shortening history of double-strap sandwich composite bonded joints subjected to different impact energies.

The deformations of the specimens followed the typical second Euler buckling mode. Note that increasing the impact energy from 5J to 20J resulted in a larger deformation in the second mode, which is believed to have been triggered by the shear crimping of the

core. This failure mode, which is the result of excessive shear deformation, occurs typically in hybrid material systems with a low shear modulus core. The experimentally observed buckling and shear crimping modes were also captured by the numerical models as seen in Figure 8-10.

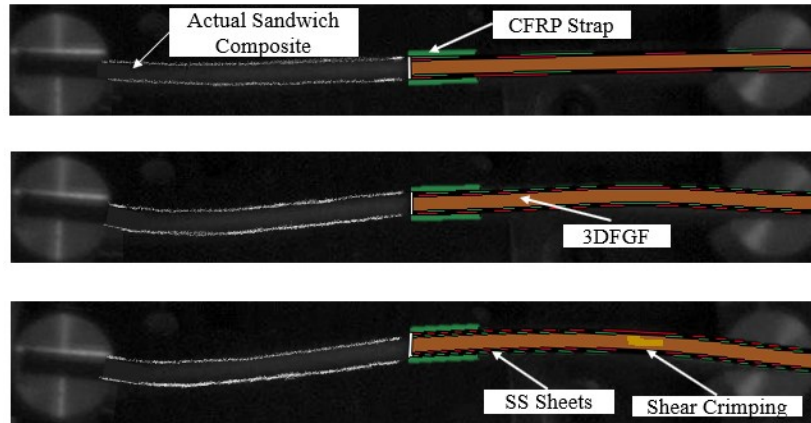


Figure 8-10. Qualitative comparison between the experimental and numerically predicted deformed shapes at different time instances during the impact event, indicating the second mode of buckling followed by shear crimping.

As mentioned previously, the FE investigation examined the influence of 13 different design parameters on the impact-buckling response of the joints, generating 410 datasets. The 13 parameters used in this study are tabulated in Table 8-4. Note that both metal and fiber-reinforced polymer (FRP) composite facias were used to augment the performance of the 3DFRP core of the sandwich. Also, both metal and FRP straps were considered. The second buckling mode was the predominant deformation observed in the experimental tests and the numerical predictions. It should also be stated that other failure modes including shear crimping, debonding in the strap/adherend region as well as delamination in the face sheet/core interface(s) were also observed sparsely in some of the configurations analyzed numerically. Note that the debonding in the strap/adherend region, which resulted in a catastrophic failure mode, was mostly seen in specimens with short straps with insufficient stiffness compared to the sandwich composite adherends. Also, the delamination in the face sheet/3DFRP interface was observed right at the edge end of the strap when a local stiffness and large stress concentration were generated due to the excessive combined thickness and length of the straps. This type of failure was also observed in another study (Mottaghian & Taheri, 2022), where double strap sandwich composite bonded joints were

subjected to quasi-static compressive loadings. The distribution of the 410 data points generated by the FE model is depicted in Figure 8-11.

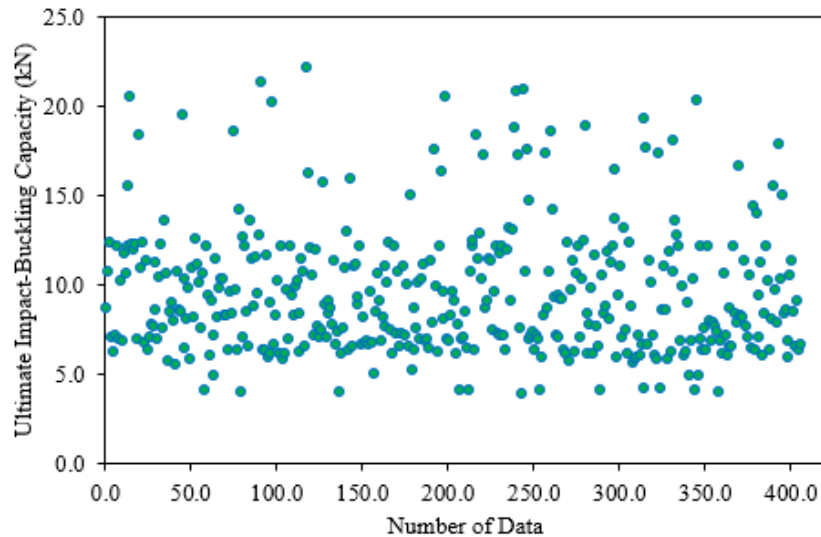


Figure 8-11. Ultimate impact-buckling capacities calculated through 410 FE-CZ analyses by considering 13 different design parameters.

8.6.2. Machine Learning Results

The dataset generated numerically was fed into the developed DNNs and GP models. As mentioned previously, 20% of the data was allocated as the test dataset and the rest was used as the train dataset. It should be noted that during the initial stages of designing ML models, it was observed that the model tended to exhibit strong performance on the training data, but poor performance on the test data, indicating the occurrence of overfitting in the model. As previously explained in section 8.5.2, a 3-fold cross-validation method was performed on the dataset to avoid the overfitting phenomenon, which refers to the process of creating an analysis that fits too closely to a certain collection of data. This phenomenon makes it difficult for the models to fit additional data or make accurate predictions. Therefore, the results are presented in three different clusters. The analysis of the clusters would lead to a more effective evaluation of the model's performance.

The coefficient of multiple determination (R^2) of each predicted set of results was calculated to establish the predictive accuracy of each model. The R^2 value reflects the proportion of the variation in the dependent variables that is predictable from the

independent variables. In other words, R^2 indicates the goodness of fit of a regression model. Figure 8-13 depicts the performance of the DNNs model in predicting the ultimate impact-buckling capacities for the train and test datasets in the different clusters against the

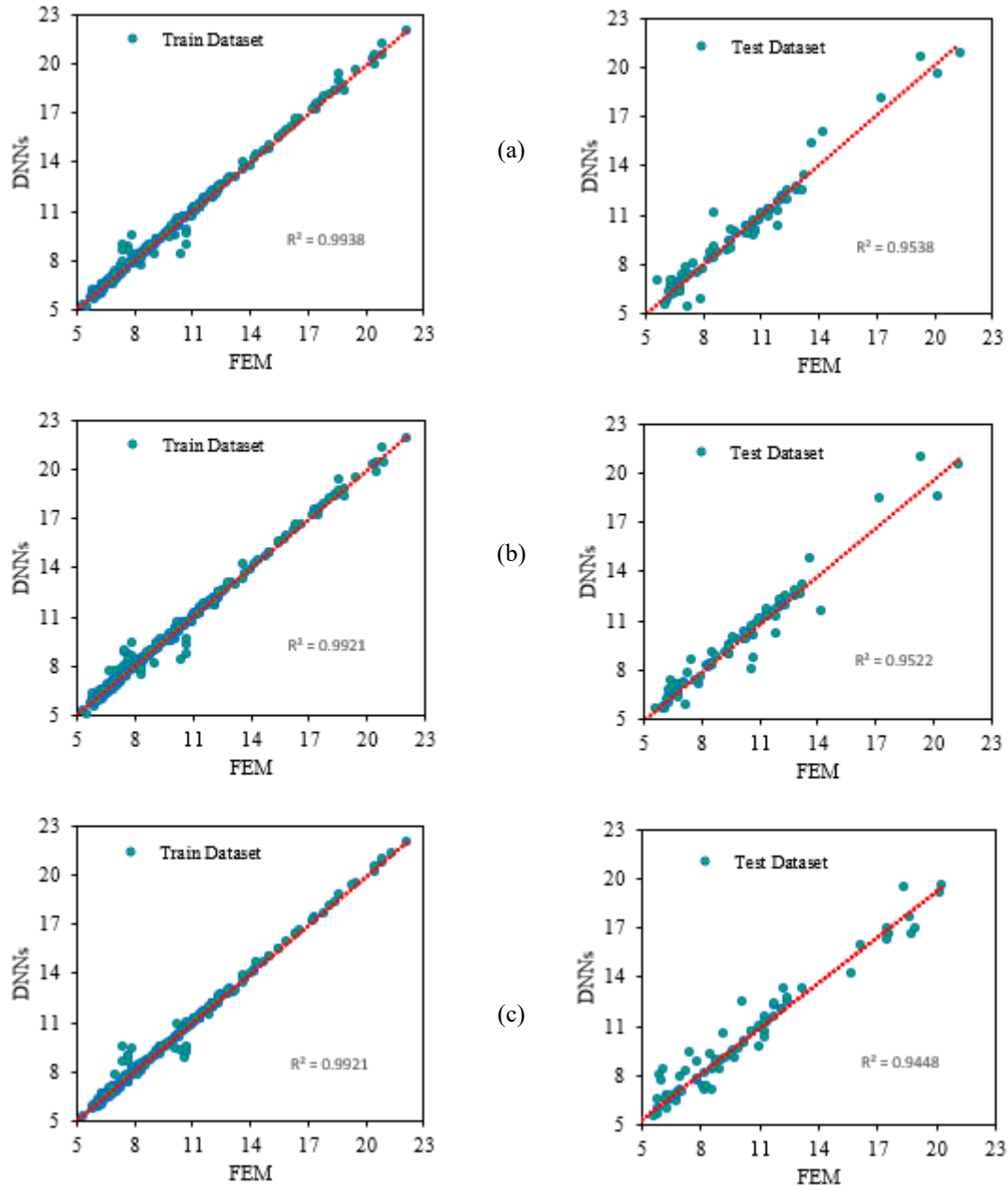


Figure 8-12. The correlation between FEM and DNNs for the train and test datasets in (a) cluster 1, (b) cluster 2, and (c) cluster 3.

numerically predicted results. As seen, very good agreements are observed in all three clusters with R^2 values of 0.9938, 0.9921, and 0.9921 associated with the train datasets. The designed DNNs model was also able to precisely predict the ultimate impact-buckling

capacities of the specimen in the test dataset. The R^2 values associated with the test data sets are reported as 0.9538, 0.9522, and 0.9448 in three clusters. Although there are some slight discrepancies in the results for the test dataset, the 3-fold cross-validation and the high R^2 guarantees that the DNNs model was trained well and did not face over-fitting issues, and therefore was capable of predicting the ultimate capacities of the joint. Note that the R^2 values for the whole dataset (i.e., summation of train and test dataset) were calculated as 0.9862, 0.9921, and 0.9802.

To evaluate the performances of the developed GP model, the results generated by the GP model were validated against the numerical results as shown in Figure 8-13. As seen, all the R^2 values in each cross-validation cluster are greater than 0.93, which indicates that the GP was able to accurately predict the joints' ultimate impact-buckling capacities. As for the DNNs model, a very good correlation was also observed between the numerical results and those generated by the GP model for the test dataset. The R^2 values the whole dataset in the three clusters were determined as 0.9535, 0.9614, and 0.9567.

Based on the results shown in Figure 8-12 and Figure 8-13, it is concluded that both ML models performed successfully and effectively. The results obtained by the DNNs models were slightly more accurate than those generated by the GP models. Also, shorter CPU times were consumed for running and training the DNN model. The mathematical equation representing the nonlinear relation between the input and output by DNNs model is indeed very intricate and not easily visible. The DNNs models generally consist of many sophisticated layers that link the defined design parameters and the output (here, the ultimate impact-buckling capacity), which makes the establishment of any mathematical equation very difficult. These types of models are referred to as black-box models in ML (i.e., models in which the measurement data could be easily obtained but not the mathematical equation); nevertheless, the black-box models are usually the most accurate ones. In contrast, the mathematical nonlinear relation between inputs and output would be visible in the GP models. The GP is considered a gray-box ML model, which combines the benefits of both black-box and white-box. The gray-box ML models usually generate results with good accuracy. In these models, the equation and some parameters are known, and the measurement data can be obtained. In contrast with white-box models, gray-box

models tend to fit nonlinear and more complicated type equations between the inputs and outputs. It should be noted that both DNNs and GP models designed in this study are found to be effective and efficient tools for designing bonded joints subjected to axial impact scenarios and predicting their ultimate capabilities.

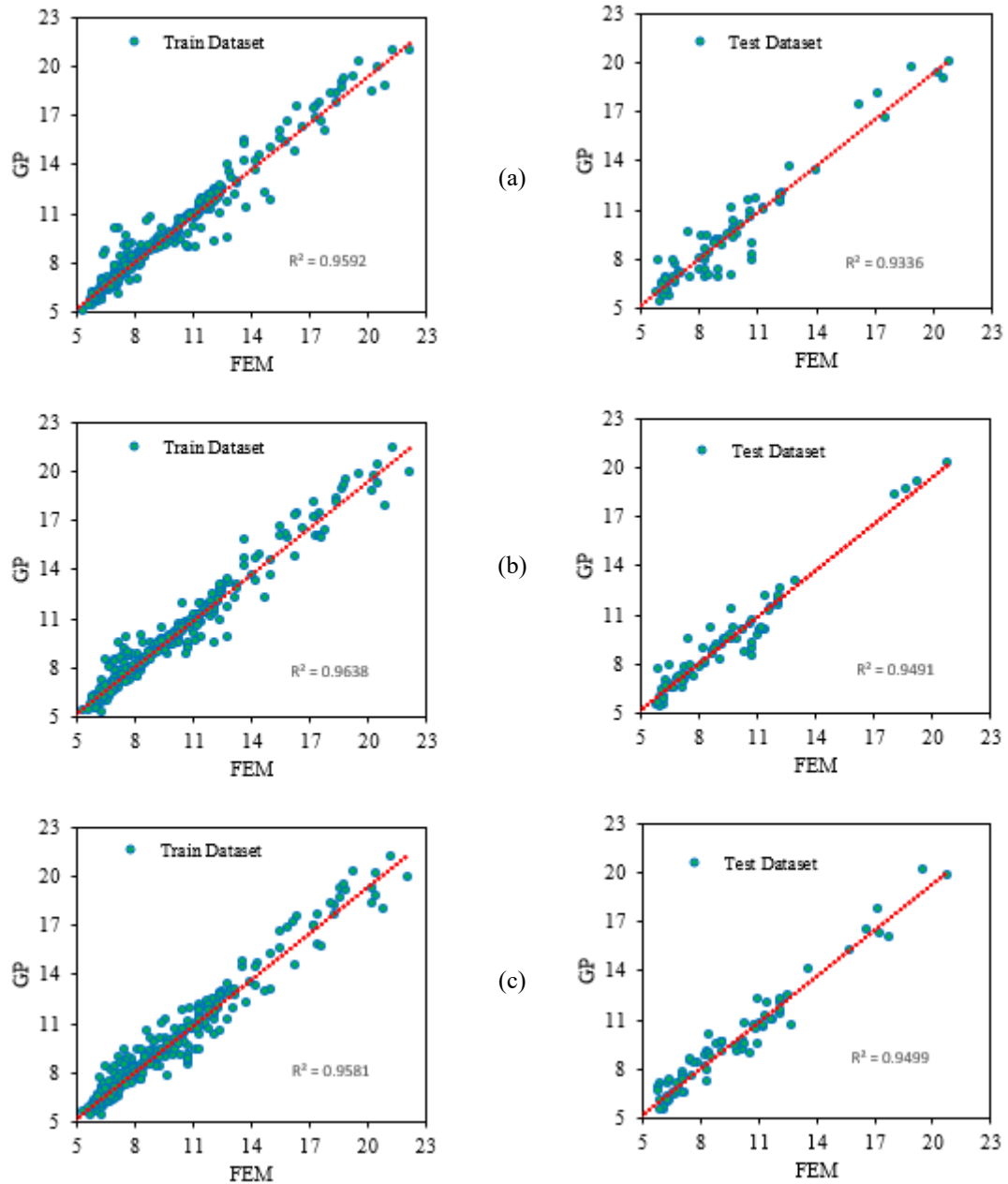


Figure 8-13. The correlation between FEM and GP for the train and test datasets in (a) cluster 1, (b) cluster 2, and (c) cluster 3.

The following equation is generated based on cluster 2 in the designed GP model. Note that this equation is one of the possible solutions searched by the GP algorithm that essentially maps the nonlinear relationship between the design parameters (i.e., the 13 geometric-, material-, and test-related parameters (x_1, x_2, \dots, x_{13})) and ultimate impact-buckling capacity of the sandwich composite bonded joints subjected to axial LVI.

$$f(x_1, x_2, x_3, x_4, x_5, x_6, x_7, x_8, x_9, x_{10}, x_{11}, x_{12}, x_{13}) = \frac{x_1^{0.125}}{x_9} + x_{11} - x_{12} + A + B + C \quad (8-2)$$

where,

$$A = (x_8 + x_9)(x_2 + x_4)^{0.25} e^{x_{10} + x_9} e^{x_6^{0.5} - x_7} \quad (8-3)$$

$$B = \left| -x_6^{0.5} + \left(-x_8 + \frac{x_8}{x_{11}} \right)^2 + \left(-x_8 + \frac{1}{x_8} + \frac{x_8}{x_{11}} \right)^{0.5} - x_7 \right|^{-0.25} \quad (8-4)$$

$$C = -\frac{x_3}{x_{11}} + \frac{0.32(x_2 + x_4) - (x_{13}^4)}{x_5} \quad (8-5)$$

It should be noted that both models designed in this study are valid for the range of data considered in Table 8-4.

8.6.3. Design Variable Importance and Selection

In this section, a sensitivity assessment is conducted to evaluate the importance of each design variable considered on the ultimate impact-buckling capacity of the joints. The sensitivity analysis is coded in Python, and the results are depicted in Figure 8-14. Note that 1,200 values within the upper and lower bound of each design parameter were randomly selected to perform the sensitivity analysis. As can be seen, face sheets' thickness, impact energy, face sheets' material type, and strap length have the largest influence on the ultimate impact-buckling capacity of the double-strap joints. In contrast, the gap length, location of the straps with respect to specimen length, boundary conditions, and adhesive material type have the least influence on the ultimate bonded joint's capacity. Note that the second buckling mode and the resulting shear crimping in some models were

the main failure modes observed in the analysis, which led to high-stress concentration regions primarily in the areas closer to the ends of the specimens. Consequently, the failure in the bonded region was observed only in a few specimens. Accordingly, the adhesive type did not significantly affect the performance of the joints subjected to axial impact loading.

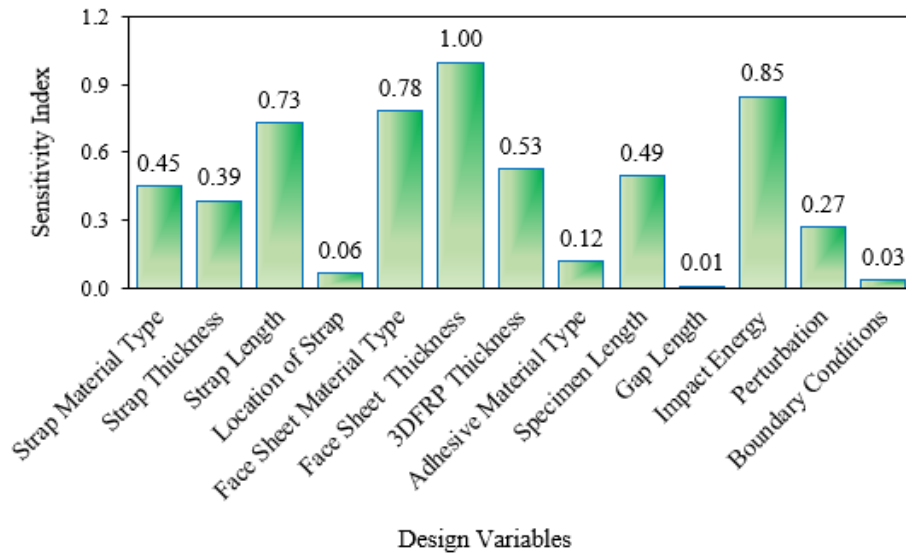


Figure 8-14. Sensitivity analysis on the design variables defined for double-strap sandwich structure bonded joints subjected to impact-buckling loading.

The next investigation was conducted to evaluate the simultaneous effects of multiple design variables on the ultimate impact-buckling capacity of the bonded joints by DNNs and GP models. The results of this investigation are presented in Figure 8-15 and Figure 8-16, respectively. Four different configurations were considered to further investigate the capability of the developed ML models in terms of covering the defined upper and lower bounds of each variable. As identified in Table 8-8, the effects of only two of the 13 design parameters on the buckling capacity were assessed in each configuration, and the remaining design parameters were kept stationary. Note that the range of each selected design variable is reported in Table 8-4. The design parameters were selected based on the feature importance obtained by sensitivity analysis.

As seen in Figure 8-15 and Figure 8-16, the DNNs and GP models generated quite similar results. Note that all values shown in each axis of the figures (i.e., the defined design variables and the corresponding ultimate capacities) have been normalized using Eq. (8.1).

Figure 8-15(a) and Figure 8-16(a) present the effects of face sheet and strap material type on the ultimate impact-buckling capacity predicted by DNNs and GP, respectively.

Table 8-8. Specifications of the configurations selected for parametric study and optimization.

Design variable	Group 1	Group 2	Group 3	Group 4	Optimal Configuration by GA
Strap Material Type	--V--	CFRP	Aramid	Aluminum	Cartridge
Metal Material Type	--V--	Titanium	Aluminum	Cartridge	Stainless Steel
Adhesive Material	Epoxy	Araldite	FM94	Loctite EA	AV138
3DFRP Thickness (mm)	5	3.4	3.4	--V--	13
Strap Thickness (mm)	1	1.2	1.5	1.12	0.7
Metal Thickness (mm)	0.5	0.5	--V--	0.48	1.5
Specimen Length (mm)	220	--V--	220	220	300
Strap Length (mm)	30	35	--V--	30	59.5
Gap Length (mm)	2	2	2	2	2
Location of Straps w.r.t Specimen Length	0.1	0.5	0.5	1	0.75
Impact Energy (kJ)	30	--V--	20	10	51.7
Perturbation	0.5	0.5	0.5	--V--	0.55
Boundary Conditions	SS	CC	CC	CC	SS

Notes: The "--V--" refers to as varying design parameters.

The results indicate that sandwich composite joints consisting of face sheets with relatively low stiffness, and straps with high stiffness would offer comparatively high ultimate impact-buckling capacity. It should be noted that a high ultimate impact-buckling capacity could also be generated when face sheets with a relatively high stiffness are incorporated; however, the improvement in the ultimate capacity will reach a maximum value beyond which no additional improvement could be gained regardless of the further increase in the stiffness of the face sheets. The reason for the phenomenon is postulated to be due to the insufficient strap length which limits the advantage of stiffer face sheets; in other words, the inadequate strap length may cause debonding of the straps and the consequent catastrophic failure. As can be seen from the sensitivity analysis results, the strap length has a more significant effect on the performances of bonded joints compared to the strap material. Nonetheless, since the strap length was kept stationary among the design variables that generated the results used in plotting these figures, the joints with stiffer face sheets exhibited lower ultimate buckling capacities. Similarly, the GP models could also accurately predict the maximum and minimum joint capacities, with maximum error margins of 6.8% and 7.5% compared to the results generated by DNNs models, respectively.

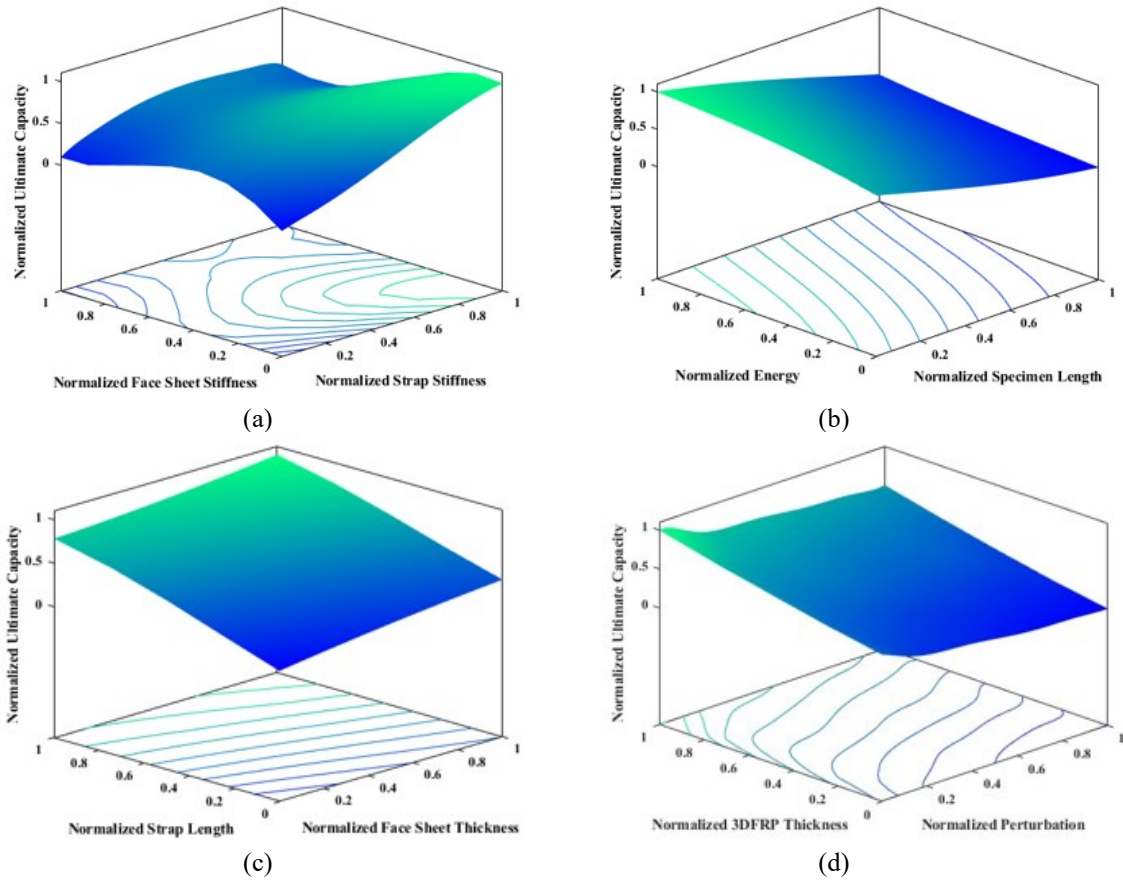


Figure 8-15. 3D surface plot indicating the effects of (a) straps and metal stiffness, (b) specimen length, and impact energy, (c) strap length and face sheet thickness, and (d) 3DFRP thickness and perturbation on the ultimate impact-buckling capacity of bonded joints based on DNNs model.

Based on Figure 8-15(b) and Figure 8-16(b), it is seen that as the specimen length increases, the buckling capacity decreases. Also, the increase in the impact energy results in higher buckling capacities, a phenomenon reported by several researchers (de Cicco et al., 2019; Yaghoobi et al., 2021). Note that an error margin of 5.5% and 3.2% corresponding to the minimum and maximum ultimate capacities, respectively, was obtained by the results generated by the GP model compared with the results obtained by the DNNs model. The results reported in Figure 8-15(c) and Figure 8-16(c) also indicate that the incorporation of thicker face sheets in the sandwich composites would result in improved buckling capacity. The same trend is also observed in joints having longer strap lengths. The maximum and minimum ultimate joint capacities predicated by the DNNs model were 3.7% and 8.6% higher than those obtained by the GP model, respectively.

Assessment of the results presented in Figure 8-15(d) and Figure 8-16(d) also reveals a direct correlation between the thickness of the 3DFRP and ultimate buckling capacities, while an inverse relation is observed between the magnitude of perturbation and ultimate buckling capacities. In other words, an increase in the thickness of the 3DFRP would result in an improvement in the buckling capacity, while a slight decline in capacity would emerge when the magnitude of the perturbation is increased. The maximum ultimate joint capacity predicated by the DNNs model is 3.8% lower than those obtained by the GP model, while a 7.5% higher minimum ultimate joint capacity was predicted by DNNs as opposed to the GP model.

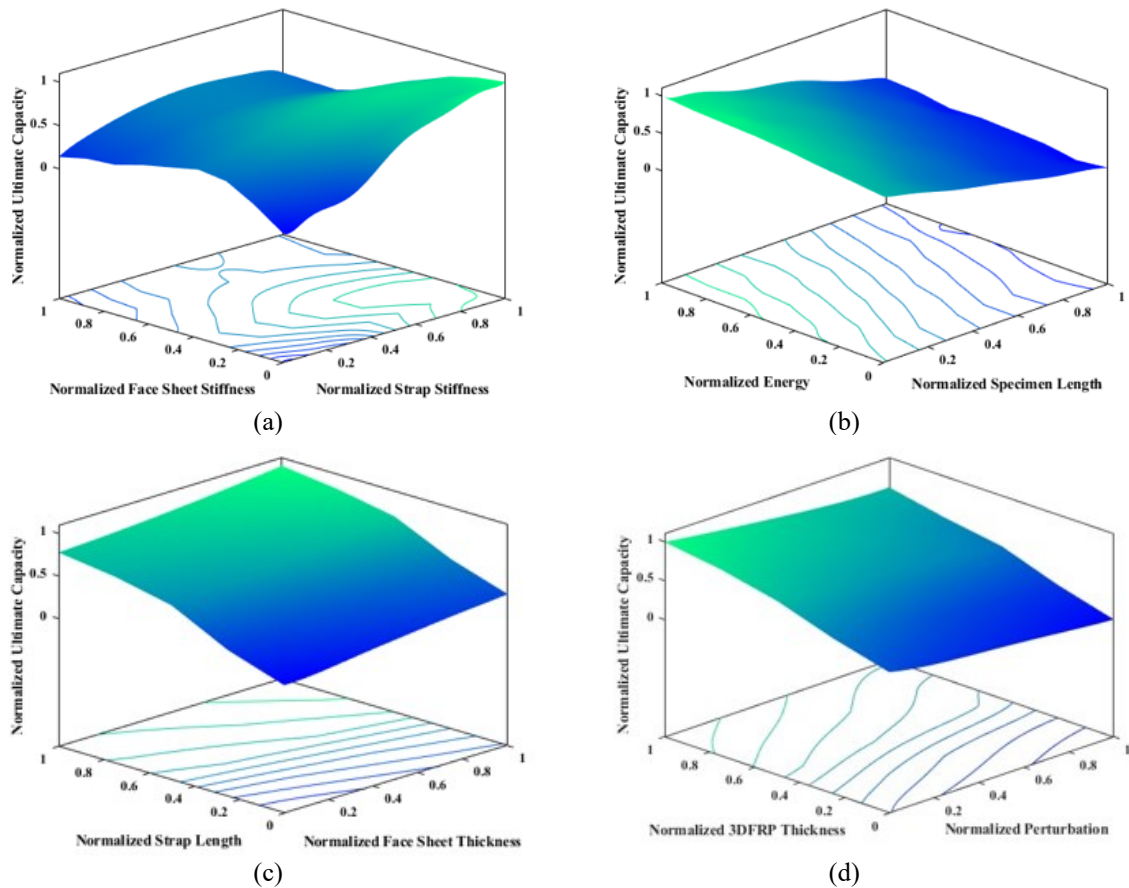


Figure 8-16. 3D surface plot indicating the effects of (a) straps and metal stiffness, (b) specimen length, and impact energy, (c) strap length and face sheet thickness, and (d) 3DFRP thickness and perturbation on the ultimate impact-buckling capacity of bonded joints based on GP model.

Generally, there are some differences between the GP- and DNN-generated results, which are postulated to be due to the difference in the inherent accuracy of the GP models (see the R^2 values in Figure 8-12 and Figure 8-13). Moreover, GP models explore the linear

and nonlinear relationships between the input and output; this in turn results in less smooth predictions compared to the predictions generated by DNNs-based models. In all, both ML models predicted the maximum/minimum joint capacities with a maximum error margin of 8.6%; this confirms the capability and robustness of the developed models. Note that more than 160 sample points were considered when assessing each of the four configuration groups. The processing time by the ML models was less than a few seconds, however, the processing time required to analyze one sample problem by FEM code ran on the same PC took more than a few hrs. Thus, the significantly lower CPU demand of machine learning models for analyzing such complex multivariable problems compared to that required by the FEM is expected to pave the way for AI to be the favourite analysis tool in a near future.

8.6.4. Optimization

The influence of different design parameters on the performance of sandwich composite bonded joints subjected to axial impact was carefully investigated in the previous sections. The final aim of the study is to establish the joint configurations (fabricated with different material combinations), that offer optimal impact-buckling capacity. For that, an appropriate combination of design variables would have to be identified. Using the lower and upper bounds for each variable, the GA was used to explore the minima of Eq.(8-1) over 1,000 iterations. The minima of a function is sought since the objective was to establish the joint with the highest impact-buckling capacity; therefore, Eq.(8.2) was multiplied by a negative in the Python code. The resulting sets of design variables for each joint configuration that yielded the highest ultimate buckling capacity are listed in the last column of Table 8-8.

8.7. Conclusions

The response of double-strap adhesively bonded joints (ABJs) under low-velocity axial impact loading was systematically investigated. The adherends of the ABJs were fabricated using a unique sandwich composite. Carbon fiber reinforced plastic (CFRP) straps and a room-cured structural epoxy were used to assemble the joints. The fabricated specimens were subjected to three different axially applied impact energies. The load and

axial shortening histories were recorded. A cohesive-zone-based finite element (CZ-FE) model was developed to predict the performance of the ABJs. The model was used to investigate the influence of 13 different geometric-, material- and test-related parameters on the ultimate impact-buckling capacity of the joints. The model incorporated zero-thickness cohesive and solid elements to model the bond region. The integrity of the model was validated against the experimental results. A maximum error margin of 6.92% confirmed the integrity of the modelling framework. The numerical model was successful in simulating the experimentally observed behaviour and failure modes of the joints.

Subsequently, three different machine learning models were developed. The models were constructed based on Deep Neural Networks (DNNs), Genetic Programming (GP), and Genetic Algorithm (GA). A dataset of 410 samples was generated by the numerical model by considering the effects of 13 combined design variables on the performances of the ABJs. The dataset was then fed to the DNNs and GP models. The models were capable of accurately predicting the performance and ultimate capacity of the bonded joints, with the results matching closely to the numerical results.

The DNNs and GP model were then utilized to assess the simultaneous combined effects of design parameters on four different joint configurations, by employing over 160 sample points for each configuration group. The ultimate impact-buckling capacities predicted by the ML models were in very good agreement with each other, with a maximum difference of 8.6%. To process these complex multivariable problems, the DNNs and GP models required substantially less CPU time to reach solutions than FE models, indicating their excellent potential to be used as the preferred computational tool.

Comparatively, the DNNs model consumed a lower CPU than the GP model and provided slightly higher accuracy. However, the GP model could generate a visible mathematical equation representing the intricate nonlinear relationship between a large number of design variables and ultimate impact-buckling capacity. The developed equation enables engineers to conduct preliminary designs of ABJs made of such intricate hybrid sandwich composites, thus facilitating their application in various industries. The designed GA model was also used to establish the optimized configuration by selecting the most

suitable combinations of design parameters, thereby generating a double-strap joint with the greatest ultimate impact-buckling capacity.

Chapter 9: Conclusion

9.1. Summary and Conclusion

The research presented in this dissertation systematically investigated the responses of adhesively bonded joints (ABJs) joining magnesium- and stainless-steel-based three-dimensional fiber metal laminates (3DFML) adherends. The 3D-FML ABJs were subjected to static and dynamic in-plane and out-of-plane (i.e., tensile, compressive, and flexural) loading scenarios. The effects of the bond (overlap) length and thickness, various surface modification procedures, as well as adhesive thickness on the joint capacity of different configurations were also examined. In addition, an attempt was made to improve the mechanical properties of a room-cured adhesive by the incorporation of graphene nanoplatelets (GNPs). The investigation was conducted qualitatively and quantitatively; that is (i) by examination of the experimentally acquired load, displacement data, and global responses of the ABJs ; (ii) by conducting a systematic and extensive series of finite element (FE) analyses, and (iii) by applying machine learning techniques to establish the complex relationship between geometrical and material parameters and joint capacities. The specific outcomes made through the conducted studies will be summarized in this chapter.

The first phase of this dissertation was aimed at developing six different renditions of 3D-FMLs constructed with stainless steel (SS) and magnesium (Mg) face sheets and by integrating additional layers of basalt or glass fabrics.

- A layer of basalt included in SS- and Mg-based 3DFMLs improved their buckling capacities by 80.4% and 65.8%, respectively. The improvements in capacities were 24.2% and 8.9% when normalized by weight, 59.1% and 10.4% when normalized by cost, and 22.0% and 22.0% when normalized by stiffness, respectively.
- The buckling and normalized buckling capacities of the 3D-FMLs reinforced with basalt or glass fabrics were comparable; however, the use of basalt, which is less expensive and more environmentally friendly, makes these configurations more appealing.

- The SS-based 3DFML reinforced with basalt exhibited the highest buckling capacity and normalized buckling capacity with respect to material cost. However, the relatively higher density of SS compared to Mg is a disadvantage.
- The shear failure mode that developed in the foam/pillar core region was the dominant failure mode in all configurations, except for Mg-based 3D-FMLs, whose failure load was observed to correspond to its conventional Euler buckling mode capacity. The shear failure is believed to have occurred due to the relatively low stiffness of the FML core.
- The developed FE model simulated the pre-and post-buckling responses of all six different configurations fairly accurately with a maximum error of 13.4% in predicting the buckling capacity. All failure modes observed in the experimental tests could also be simulated accurately by the FE models.
- Based on the numerical results, the considered basalt and glass fiber orientations (i.e., (0/90), (± 30), (± 45)) demonstrated negligible effects on the buckling capacities. However, an extra layer of glass and basalt fiber hybridization was found to enhance the performance of 3D-FMLs by a maximum gain of 41.1%.

The next phase of the study concentrated on an in-depth understanding of the performances of single-lap 2D-FML bonded joints constructed with Mg and basalt fabrics. The surface modifications were found to be an important factor governing the performance and enhancement of the bonded joints. Therefore, the effect of two types of surface treatments, namely "sandblasting" and "sandblasting with resin coating," on the joint strength subjected to tensile loading was investigated. The findings of the conducted study are provided as follows:

- The new hybrid (i.e., sandblasting with the resin coating) surface modification procedure improved the interlocking mechanism and resulted in a 15.7% advancement in the average shear strength of the single-lap FMLs bonded joints. This method is relatively simple and cost-effective compared to conventional methods; it also completely inhibits the oxidation and corrosion of Mg sheets. As a result, there is no

need to immediately proceed with the bonding process after the sandblasting process, which is the case in conventional bonding methods.

- The hybrid surface treatment procedure transferred the undesirable interfacial failure mode in the bonded region to a mixture of cohesion and interfacial, thereby evidencing the enhancement of the interlocking mechanism.
- The numerical simulation results showed good agreement with the experimental results, with a maximum error of 2.5%. This demonstrates the robustness and accuracy of the FE model in simulating the response of the bonded joints.
- The results of the parametric analyses showed that an overlap length of 35 mm provided the optimal joint capacity, with a negligible increase beyond that point. The joint capacity increased by 74% when the overlap length changed from 5 mm to 35 mm. Additionally, the optimal adhesive thickness was found to have a significant impact on the joint capacity.
- The adhesive thickness had a strong influence on the joint capacity. The optimum adhesive thickness was established as 0.4 mm, beyond which a slight decline in the joint capacity was noticed.
- The stress analysis indicated that the increase in the overlap length up to a certain value (i.e., 35 mm) resulted in a reduction of the maximum peel and shear stresses. In addition, a stress plateau was observed in the mid-region of the overlap in the joints with a longer overlap.

Another attempt was made in conjunction with the proposed surface modification procedure to further improve the adhesive's mechanical response. For that, different weight contents of graphene nanoplatelets (GNPs) were included in the epoxy-resin utilized to adhesively bond the Mg-based 2D- and 3D-FMLs. In this phase of the study, the single-lap joints mating FMLs were subjected to quasi-static tensile and flexural loading conditions. The following findings were observed:

- The tensile joint capacities of single-lap 2D-FML formed by Mg and basalt and Mg-based 3D-FML (with equivalent stiffness) were similar. However, the normalized joint capacity of 3D-FMLs (with respect to the weight) was 72.1% higher than that of the 2D counterpart. Based on the load-displacement responses, 3D-FML SLJs showed nonlinear responses and presented 146% greater energy absorption capacity compared to their 2DFML counterparts.
- The joint capacity of 3D-FML joints fabricated with 0.5 wt.% GNP-reinforced adhesive improved by 25% compared to the joints fabricated with unreinforced adhesive. Conversely, the inclusion of 0.75 wt.% of GNPs in the adhesive resulted in an 18% reduction in the joint capacity. Similarly, the energy absorption capacity of the joints constructed with 0.5 wt.% improved by 187.8%.
- The micromechanical analysis indicated that the strengthening mechanism in GNP-reinforced adhesive was due to GNP pull-out and debonding. GNP agglomeration was observed in specimens reinforced with 0.75 wt.% GNPs.
- The numerical results were in good agreement with the experimental results, with a maximum error margin of 10.8 % and 5.6 % in calculating the lap-shear and flexural capacities, respectively. The developed FE model could also simulate the local and global crack initiation, and propagation, as well as simulate the resulting failure modes quite accurately.
- In conclusion, 3D-FMLs performed better than their 2D counterparts, which should encourage engineers to select 3D-FML in applications, particularly where weight is the essential design variable.

In the next two phases of the research, extensive experimental and numerical analyses were performed to study the behaviour of double-strap bonded joints under tensile and compressive loadings. Stainless steel-based 3D-FML adherends were adhesively bonded using CFRP straps. The effects of five different surface modification procedures on joint behaviour were assessed. Additionally, seven different mixed-mode trapezoidal CZM-

based finite element models were developed to examine various combinations of continuum and cohesive element layers. The study's outcomes are summarized as follows:

- The effectiveness of surface preparation procedures was ranked based on microstructural analysis, as follows: grit blasting + resin coating (GS+PC) > grit blasting + annealing (GS+AN) > grit blasting with alumina grit + nitric acid etching (AS+AE) > grit blasting with alumina grit (AS) > grit blasting with crushed glass grit (GS).
- Higher interface surface roughness would not necessarily result in a higher joint capacity. The annealing procedure led to the degradation of the joint capacity.
- AS+AE and AS procedures produced the highest joint capacities with gains of 24.0 % and 24.5 % compared to the base specimens, respectively. The two procedures also generated a stronger interlocking mechanism between the stainless steel adherends and adhesive.
- Comparatively, the acid etching procedure was found to be relatively more labour-intensive, costly, and hazardous, thus not a preferred surface preparation procedure.
- The numerical analysis results led to the conclusion that to obtain accurate results, at least three layers of cohesive elements should be incorporated in modelling such ABJs. However, incorporating five layers of the zero-thickness cohesive element used in modelling the adhesive yielded the lowest error margins (i.e., 3.1%) compared to the models produced by one layer of the cohesive element, which had an error of 31.3%.
- All models that used more than two layers of zero-thickness cohesive elements to model the adhesive were able to capture damage initiation and growth. However, the model with 5 layers of cohesive elements captured the experimentally observed failure mode most accurately.
- The FE parametric study revealed that increasing the thickness of CFRP straps would enhance the failure capacity up to a certain point, after which the capacity was degraded

due to the high-stress concentration generated by thick CFRP straps. Increasing the number of layers of the straps from 3 to 5 increased the joint capacity by 42%.

- The optimal overlap length of 35 mm resulted in the highest joint capacity.
- The numerical results indicated that the CFRP strap layer closest to the adherends experienced the highest magnitude of peel and shear stresses, with their concentration observed near the midspan gap due to the generated bending moments. This stress concentration vanished in the double-strap configurations with no mid-span gaps.
- The numerically predicted pre- and post-buckling responses of the bonded joints were in good agreement with the experimental tests with a maximum error margin of 6%.
- Increasing the thickness of the CFRP straps caused a 19.7% improvement in the buckling capacity, while a slight degradation in capacity was observed when a longer strap length was used.
- The numerical model could simulate the shear crimping that was seen in some of the specimens (with 3-layer straps) during the experiments. However, the primary failure mode in the specimens with longer CFRP strap lengths was delamination in their metal/3DFGF interfacial region, which was also successfully simulated numerically.

In the last phases of the research, the performance of double-strap sandwich composite bonded joints under axial low-velocity impact loading was studied using a combination of experimental, numerical, and analytical analyses. The bonded joints were subjected to three different impact energy levels (5J, 10J, 20J) in experimental tests. An accurate FE model was developed to conduct a parametric study investigating the influence of 13 different parameters, generating a dataset of 410 samples, which were subsequently used to develop three different machine learning models to explore the nonlinear relationship between the design parameters and impact-buckling capacity of the sandwich composite bonded joints. The findings of the study are summarized as follows:

- The impact resistance of the joints impacted by 20J was 29% more than the resistance of the joint impacted by 5 J.

- The numerical results were in good agreement with the experimental results with a maximum error margin of 6.36%. The FE model also accurately simulated the load and axial shortening histories as well as the failure modes of the joints.
- The results generated by the two ML models were in good agreement with the numerical results with a minimum statistical R^2 value of 0.93.
- An empirical equation was generated by the GP model which established the complex relations between 13 design parameters and impact-buckling capacities.
- The sensitivity analysis highlighted the strong dependency of the impact-buckling capacity on 4 out of 13 variables (i.e., metal type and thickness, impact energy, and strap length).
- The developed genetic algorithm model was used to establish the optimal joint by combining the design parameters.
- The designed ML models were found to be accurate and reliable, computationally fast, and cost-effective alternative tools for investigating the effects of different parameters on the performances of bonded joints and optimizing their design

9.2. Recommendations for Future Works

As mentioned previously, 3D-FMLs are a recently-developed class of hybrid materials. Consequently, their current database is limited, and further studies should be conducted to expand it. These studies should focus on different types of loading and environmental conditions, to achieve a comprehensive understanding of the material's performance. Therefore, a series of recommendations are offered in this section, which aims to further enhance the overall performances of this effective class of FMLs, with the end goal of facilitating commercialization.

- The main targets for the applications of 3D-FMLs are expected to be in the automotive, aerospace, and renewable energy industries. Long-term exposure of components to harsh environments, including extreme cold or heat, is an inevitable loading scenario in real-life applications. Therefore, the response of ABJs mating 3D-FMLs panels subjected to such conditions needs to be explored. The importance of investigating this issue becomes even more crucial when considering the significantly different coefficients of thermal expansion and Poisson's ratio of metals and FRPs, which are the main constituents of FMLs.
- Moisture and salinity are known to degrade the integrity of ABJs. Parameters such as plasticization in the bulk adhesive, reduction of the interlocking mechanism in the adhesive/adherends/straps interfaces, and swelling leading to developed internal residual stresses affect the durability of bonded joints under such environments. The existence of metallic layers in 3D-FMLs exacerbates their performance under such conditions. Therefore, investigating the long-term and aging performances of ABJs mating 3D-FML in humid and salty environments is crucial.
- Fatigue fracture is one of the most common causes of failure in engineering components that contain ABJs. Crack initiation and propagation due to repeated loading cycles, and the inherent complex configurations of ABJs make precise fatigue prediction a very challenging task. Therefore, the fatigue performances of ABJs made of 3D-FMLs should be assessed.
- Survivability of aircraft and automotive structures under low- and high-velocity impact loadings is of critical importance for engineers to increase design safety and prevent

catastrophic failure. The crashworthiness of bonded 3D-FMLs under higher velocities should also be considered in the future.

- Joining structural components with adhesives is a straightforward procedure; nonetheless, the uniformity of bond quality requires attention and is considered a limiting factor for their application. The use of film adhesive could significantly reduce void creation in bonded joints. Appropriate adhesive films could not be used due to the low glass transition temperature of the commonly used room-cured thermoset resins (as the one used in this study). In such circumstances, ultrasonic and sonic vibration techniques can be effectively used to detect dis-bond and voids in the bonded joints.
- The use of rivet joints is widespread in the aerospace and automotive industries. For example, a typical aircraft uses 1.5 million rivets to assemble its components. Therefore, it is natural to consider investigating the possibility of using rivet joints to join 3D-FMLs and comparing their capabilities with adhesively bonded joints. However, it is postulated that using a series of rivets to join 3D-FMLs may lead to unwanted fatigue issues in the adherends. On the other hand, it has been demonstrated that the strength of bonded joints could be significantly improved by adding one or more mechanical fasteners, such as bolts or rivets. Therefore, it is anticipated that this approach would be a more effective solution compared to fully riveted 3D-FML joints, and it should be investigated in the future.
- Exploration of the capabilities of alternative modern numerical techniques, such as the incorporation of the discrete element method, eXtended FEM, as well as meshfree methods, is also highly recommended for a more comprehensive assessment of damage initiation and evolution in ABJs.
- Finally, investigation of the simultaneous effects of different parameters on the response of ABJs is complicated, time-consuming, and costly, which makes bonded joint optimization a very challenging task. To overcome this issue, a theory-guided machine learning (TGML) model could be designed and developed. In contrast to conventional ML models, the TGMLs are proven to be fairly accurate in prediction, particularly outside the training zone. They are also capable of being trained with modest datasets. As well, special attention should be paid to optimizing the bonded configuration with respect to cost, weight, and stiffness to make them more attractive

for use by practicing engineers. TGML is one of the best candidates in terms of time, cost, and accuracy for establishing the performances and optimization of the configuration of 3D-FML ABJs subjected to different loading scenarios.

References

- Abdelfattah, I., Ferreira, F., Saleh, M. N., Reis, P. N. B., & Freitas, S. T. De. (2022). Flexural performance of squared one-sided CFRP patches: modelling and experimental study. *The Journal of Adhesion*, 99(3), 1–19.
- AC-107B, FAA, (2009). Advisory Circular - Composite Aircraft Structure, *U.S. Department of Transportation - Federal Aviation Administration (FAA)*.
- Adams, R. D., Adams, R. D., Comyn, J., Wake, W. C., & Wake, W. C. (1997). *Structural adhesive joints in engineering*. Springer Science & Business Media.
- Adams, R. D., Atkins, R. W., Harris, J. A., & Kinloch, A. J. (1986). Stress analysis and failure properties of carbon-fibre-reinforced-plastic/steel double-lap joints. *The Journal of Adhesion*, 20(1), 29–53.
- Adams, R. D., & Harris, J. A. (1987). The influence of local geometry on the strength of adhesive joints. *International Journal of Adhesion and Adhesives*, 7(2), 69–80.
- Ahmad, Z., Abdullah, M. R., & Tamin, M. N. (2015). Experimental and Numerical Studies of Fiber Metal Laminate (FML) Thin-Walled Tubes Under Impact Loading. *Mechanical and Materials Engineering of Modern Structure and Component Design*, 433–443.
- Ahmadi Moghadam, B. (2015). Development of a Highly Resilient Graphene Nanoplatelet Resin/Adhesive. *Doctoral thesis, Department of Civil Engineering, Dalhousie University, Halifax, NS, Canada*
- Ahmadi-Moghadam, B., Sharafimasooleh, M., Shadlou, S., & Taheri, F. (2015). Effect of functionalization of graphene nanoplatelets on the mechanical response of graphene/epoxy composites. *Materials & Design (1980-2015)*, 66, 142–149.
- Akpınar, S., Doru, M. O., Özel, A., Aydın, M. D., & Jahanpasand, H. G. (2013). The effect of the spew fillet on an adhesively bonded single-lap joint subjected to bending moment. *Composites Part B: Engineering*, 55, 55–64.
- Ale Ali, M. M. A., Jamali, A., Asgharnia, A., Ansari, R., & Mallipeddi, R. (2022). Multi-objective Lyapunov-based controller design for nonlinear systems via genetic programming. *Neural Computing and Applications*, 34(2), 1345–1357.
- Alderliesten, R., Rans, C., & Benedictus, R. (2008). The applicability of magnesium based Fibre Metal Laminates in aerospace structures. *Composites Science and Technology*, 68(14), 2983–2993.
- Alfano, G. (2006). On the influence of the shape of the interface law on the application of cohesive-zone models. *Composites Science and Technology*, 66(6), 723–730.

- Ali, A., Pan, L., Duan, L., Zheng, Z., & Sapkota, B. (2016). Characterization of seawater hygrothermal conditioning effects on the properties of titanium-based fiber-metal laminates for marine applications. *Composite Structures*, 158, 199–207.
- Al-Ramahi, N. J., Joffe, R., & Varna, J. (2018). Investigation of end and edge effects on results of numerical simulation of single lap adhesive joint with non-linear materials. *International Journal of Adhesion and Adhesives*, 87, 191–204.
- Ameh, E. S. (2020). Consolidated derivation of fracture mechanics parameters and fatigue theoretical evolution models: basic review. *SN Applied Sciences*, 2(11), 1800.
- Andersson, T. and Biel, A., (2006). On the effective constitutive properties of a thin adhesive layer loaded in peel. *International Journal of Fracture*, 141.227-246.
- Anyfantis, K. N. (2012). Finite element predictions of composite-to-metal bonded joints with ductile adhesive materials. *Composite Structures*, 94(8), 2632–2639.
- Anyfantis, K. N., & Tsouvalis, N. G. (2013a). Analysis of an adhesively bonded single lap joint subjected to eccentric loading. *International Journal of Adhesion and Adhesives*, 41, 41–49.
- Anyfantis, K. N., & Tsouvalis, N. G. (2013b). Loading and fracture response of CFRP-to-steel adhesively bonded joints with thick adherents – Part I: Experiments. *Composite Structures*, 96, 850–857.
- Anyfantis, K. N., & Tsouvalis, N. G. (2013c). Loading and fracture response of CFRP-to-steel adhesively bonded joints with thick adherents – Part II: Numerical simulation. *Composite Structures*, 96, 858–868.
- Anyfantis, K.-I. N. (2012). Analysis and design of composite-to-metal adhesively bonded joints. Doctoral thesis, *School of Naval Architecture and Marine Engineering National Technical University of Athens, Athens, Greece*.
- Arachchi, K.K. and Gamage, J.C.P.H., (2022). An analytical approach to predict cohesion and interfacial failures of CFRP/steel composites under prolonged exposure to aqueous solutions. *Case Studies in Construction Materials*, 16.e00949.
- Asaee, Z. (2017). Low Velocity Impact Response of a Novel Class of Fiber Metal Laminates Consisting of a 3D Fiberglass Fabrics. *Doctoral Thesis, Department of Mechanical Engineering, Dalhousie University, Halifax, NS, Canada*.
- Asaee, Z., Mohamed, M., Soumik, S., & Taheri, F. (2017). Experimental and numerical characterization of delamination buckling behavior of a new class of GNP-reinforced 3D fiber-metal laminates. *Thin-Walled Structures*, 112, 208–216.
- Asaee, Z., Shadlou, S., & Taheri, F. (2015). Low-velocity impact response of fiberglass/magnesium FMLs with a new 3D fiberglass fabric. *Composite Structures*, 122, 155–165.

- ASTM D709-17, Standard Test Methods for Flexural Properties of Unreinforced and Reinforced Plastics and Electrical Insulating Materials. (2017). *ASTM International, West Conshohocken, PA.*
- ASTM D1002-10, Standard Test Method for Apparent Shear Strength of Single-Lap-Joint Adhesively Bonded Metal Specimens by Tension Loading (Metal-to-Metal). (2021). *ASTM International, West Conshohocken, PA.*
- ASTM D3528, Standard test method for strength properties of double lap shear adhesive joints by tension loading. (2008). *ASTM International, West Conshohocken, PA.*
- ASTM D5868-01, Standard Test Method for Lap Shear Adhesion for Fiber Reinforced Plastic (FRP) Bonding. (2005). *ASTM International, West Conshohocken, PA.*
- ASTM International. (2020). ASTM E2954 Standard Test Method for Axial Compression Test of Reinforced Plastic and Polymer Matrix Composite Vertical Members. *ASTM International, West Conshohocken, PA.*
- Balcıoğlu, H. E., & Seçkin, A. Ç. (2021). Comparison of machine learning methods and finite element analysis on the fracture behavior of polymer composites. *Archive of Applied Mechanics, 91*(1), 223–239.
- Balcıoğlu, H. E., Seçkin, A. Ç., & Aktaş, M. (2015). Failure load prediction of adhesively bonded pultruded composites using artificial neural network. *Journal of Composite Materials, 50*(23), 3267–3281.
- Baldan, A. (2012). Adhesion phenomena in bonded joints. *International Journal of Adhesion and Adhesives, 38*, 95–116.
- Banat, D., & Mania, R. J. (2017). Failure assessment of thin-walled FML profiles during buckling and postbuckling response. *Composites Part B: Engineering, 112*, 278–289.
- Banat, D., & Mania, R. J. (2018). Progressive failure analysis of thin-walled Fibre Metal Laminate columns subjected to axial compression. *Thin-Walled Structures, 122*, 52–63.
- Banea, M. D. (2019). Influence of adherend properties on the strength of adhesively bonded joints. *MRS Bulletin, 44*(8), 625–629.
- Banea, M. D., & da Silva, L. F. M. (2009). Adhesively bonded joints in composite materials: An overview. *Proceedings of the Institution of Mechanical Engineers, Part L: Journal of Materials: Design and Applications, 223*(1), 1–18.
- Barbosa, N. G. C., Campilho, R. D. S. G., Silva, F. J. G., & Moreira, R. D. F. (2018). Comparison of different adhesively-bonded joint types for mechanical structures. *Applied Adhesion Science, 6*(1), 15.

- Bayramoglu, S., Akpinar, S., & Çalık, A. (2021). Numerical analysis of elasto-plastic adhesively single step lap joints with cohesive zone models and its experimental verification. *Journal of Mechanical Science and Technology*, 35(2), 641–649.
- Benzeggagh, M. L., & Kenane, M. (1996). Measurement of mixed-mode delamination fracture toughness of unidirectional glass/epoxy composites with mixed-mode bending apparatus. *Composites Science and Technology*, 56(4), 439–449.
- Benzeggagh, M.L. and Kenane, M.J.C.S., (1996). Measurement of mixed-mode delamination fracture toughness of unidirectional glass/epoxy composites with mixed-mode bending apparatus. *Composites science and technology*, 56(4), pp.439-449.
- Biel, A., & Stigh, U. (2010). Damage and plasticity in adhesive layer: an experimental study. *International Journal of Fracture*, 165, 93–103.
- Birman, V., & Kardomateas, G. A. (2018). Review of current trends in research and applications of sandwich structures. *Composites Part B: Engineering*, 142, 221–240.
- Bogy, D. B. (1968). Edge-Bonded Dissimilar Orthogonal Elastic Wedges Under Normal and Shear Loading. *Journal of Applied Mechanics*, 35(3), 460–466.
- Bowditch, M. R. & Adams RD (2006). *Adhesive Bonding: Science, Technology and Applications*, CRC Press, USA and Woodhead Publishing Ltd., Cambridge, England.
- Budhe, S., Banea, M. D., de Barros, S., & da Silva, L. F. M. (2017). An updated review of adhesively bonded joints in composite materials. *International Journal of Adhesion and Adhesives*, 72, 30–42.
- Burlayenko, V. N., & Sadowski, T. (2008). FE modeling of delamination growth in interlaminar fracture specimens. *Budownictwo i Architektura*, 2, 95–109.
- Çakır, M. V., Erkliğ, A., & Ahmed, B. F. (2021). Graphene nanoparticle effect on flexural and shear behaviors of adhesively bonded single lap joints of GFRP composites. *Journal of the Brazilian Society of Mechanical Sciences and Engineering*, 43(4), 211.
- Campilho, R. D. S. G., Banea, M. D., Neto, J. A. B. P., & da Silva, L. F. M. (2013a). Modelling adhesive joints with cohesive zone models: effect of the cohesive law shape of the adhesive layer. *International Journal of Adhesion and Adhesives*, 44, 48–56.
- Campilho, R. D. S. G., Banea, M. D., Neto, J. A. B. P., & da Silva, L. F. M. (2013b). Modelling adhesive joints with cohesive zone models: effect of the cohesive law shape of the adhesive layer. *International Journal of Adhesion and Adhesives*, 44, 48–56.
- Campilho, R. D. S. G., Banea, M. D., Pinto, A. M. G., da Silva, L. F. M., & de Jesus, A. M. P. (2011). Strength prediction of single- and double-lap joints by standard and

- extended finite element modelling. *International Journal of Adhesion and Adhesives*, 31(5), 363–372.
- Campilho, R. D. S. G., de Moura, M. F. S. F., Ramantani, D. A., Morais, J. J. L., & Domingues, J. J. M. S. (2009). Tensile behaviour of three-dimensional carbon-epoxy adhesively bonded single- and double-strap repairs. *International Journal of Adhesion and Adhesives*, 29(6), 678–686.
- Campilho, R. D. S. G., de Moura, M. F. S. F., Ramantani, D. A., Morais, J. J. L., & Domingues, J. J. M. S. (2010). Buckling strength of adhesively-bonded single and double-strap repairs on carbon-epoxy structures. *Composites Science and Technology*, 70(2), 371–379.
- Campilho, R.D., De Moura, M.F.S.F. and Domingues, J.J.M.S., (2008). Using a cohesive damage model to predict the tensile behaviour of CFRP single-strap repairs. *International Journal of Solids and Structures*, 45(5).1497-1512.
- Carlberger, T. and Stigh, U., (2007.) An explicit FE-model of impact fracture in an adhesive joint. *Engineering fracture mechanics*, 74(14).2247-2262.
- Carrillo, J. G., Gonzalez-Canche, N. G., Flores-Johnson, E. A., & Cortes, P. (2019). Low velocity impact response of fibre metal laminates based on aramid fibre reinforced polypropylene. *Composite Structures*, 220, 708–716.
- Carvalho, U.T.F. and Campilho, R.D.S.G., (2016). Application of the direct method for cohesive law estimation applied to the strength prediction of double-lap joints. *Theoretical and Applied Fracture Mechanics*, 85.140-148.
- Cavezza, F., Boehm, M., Terryn, H., & Hauffman, T. (2020). A Review on Adhesively Bonded Aluminium Joints in the Automotive Industry. *Metals*, 10(6).
- Chai, G. B., & Manikandan, P. (2014). Low velocity impact response of fibre-metal laminates - A review. *Composite Structures*, 107, 363–381.
- Chang, F.-K., & Chang, K.-Y. (1987). *a progressive damage model for laminated composites containing stress concentrations*. 21, 834–855.
- Coburn, B. H., & Weaver, P. M. (2016). Buckling analysis, design and optimisation of variable-stiffness sandwich panels. *International Journal of Solids and Structures*, 96, 217–228.
- Correia, S., Anes, V., & Reis, L. (2018). Effect of surface treatment on adhesively bonded aluminium-aluminium joints regarding aeronautical structures. *Engineering Failure Analysis*, 84, 34–45.
- Cortés, P., & Cantwell, W. J. (2004). Fracture properties of a fiber-metal laminates based on magnesium alloy. *Journal of Materials Science*, 39(3), 1081–1083.

- Cortés, P., & Cantwell, W. J. (2005). The fracture properties of a fibre-metal laminate based on magnesium alloy. *Composites Part B: Engineering*, 37(2–3), 163–170.
- Cortés, P., & Cantwell, W. J. (2006). The prediction of tensile failure in titanium-based thermoplastic fibre-metal laminates. *Composites Science and Technology*, 66(13), 2306–2316.
- da Silva, L. F. M., & Campilho, R. D. S. G. (2012). Advances in Numerical Modelling of Adhesive Joints. In *Advances in Numerical Modeling of Adhesive Joints* (pp. 1–93). Springer Berlin Heidelberg.
- da Silva, L. F. M., das Neves, P. J. C., Adams, R. D., & Spelt, J. K. (2009). Analytical models of adhesively bonded joints—Part I: Literature survey. *International Journal of Adhesion and Adhesives*, 29(3), 319–330.
- De Cicco, D. (2019). In-depth Understanding of the Stability Response of a Novel 3D Fiber-Metal Laminate under Axial Impact Loading. *Doctoral Thesis, Department of Mechanical Engineering, Dalhousie University, Halifax, NS, Canada*.
- De Cicco, D., & Taheri, F. (2018). Robust numerical approaches for simulating the buckling response of 3D fiber-metal laminates under axial impact – Validation with experimental results. *Journal of Sandwich Structures & Materials*, 1099636218789614.
- De Cicco, D., & Taheri, F. (2019a). Enhancement of magnesium-composite bond-interface by a simple combined abrasion and coating method. *Journal of Magnesium and Alloys*, 7(2), 227–239.
- De Cicco, D., & Taheri, F. (2019b). Performances of magnesium- and steel-based 3D fiber-metal laminates under various loading conditions. *Composite Structures*, 111390.
- De Cicco, D. and Taheri, F., (2018). Delamination buckling and crack propagation simulations in fiber-metal laminates using xFEM and cohesive elements. *Applied Sciences*, 8(12), p.2440.
- de Freitas. (2015). Holding Aircraft Together. *TEDxDelftSalon*. <https://www.youtube.com/watch?v=kuBrcoQ07g4>
- de Morais, A. B., Pereira, A. B., Teixeira, J. P., & Cavaleiro, N. C. (2007). Strength of epoxy adhesive-bonded stainless-steel joints. *International Journal of Adhesion and Adhesives*, 27(8), 679–686.
- Delzendehrooy, F., Akhavan-Safar, A., Barbosa, A. Q., Beygi, R., Cardoso, D., Carbas, R. J. C., Marques, E. A. S., & da Silva, L. F. M. (2022). A comprehensive review on structural joining techniques in the marine industry. *Composite Structures*, 289, 115490.

- Dirschmid, F. (2014). Die CFK-Karosserie des BMW i8 und deren Auslegung. In G. Tecklenburg (Ed.), *Karosseriebautage Hamburg*, 217–231.
- Dobrzański, P., & Oleksiak, W. (2021). Design and analysis methods for composite bonded joints. *Transactions on Aerospace Research*.
- Duncan, B. (2010). 14 - Developments in testing adhesive joints. In D. A. Dillard (Ed.), *Advances in Structural Adhesive Bonding*, Woodhead Publishing, 389–436.
- Durmuş, M., & Akpınar, S. (2020). The experimental and numerical analysis of the adhesively bonded three-step-lap joints with different step lengths. *Theoretical and Applied Fracture Mechanics*, 105, 102427.
- Ebnesajjad, S., & Landrock, A. H. (2015). Chapter 1 - Introduction and Adhesion Theories. *Adhesives Technology Handbook*, William Andrew Publishing, 1–18.
- Ekşi, S., & Genel, K. (2017). Comparison of mechanical properties of unidirectional and woven carbon, glass and aramid fiber reinforced epoxy composites. *Acta Physica Polonica A*, 132(3), 879–882.
- Galliot, C., Rousseau, J., & Verchery, G. (2012). Drop weight tensile impact testing of adhesively bonded carbon/epoxy laminate joints. *International Journal of Adhesion and Adhesives*, 35, 68–75.
- Gastens, M., Sadeghi, M. Z., Weiland, J., Reisgen, U., & Schröder, K.-U. (2022). A methodology for detection of crack initiation in adhesively bonded joints under constant and variable amplitude fatigue loading. *The Journal of Adhesion*, 98(6), 758–779.
- Gerstner, W., Kistler, W. M., Naud, R., & Paninski, L. (2014). *Neuronal dynamics: From single neurons to networks and models of cognition*. Cambridge University Press.
- Ghiotti, A., Bruschi, S., Kain, M., Lizzul, L., Simonetto, E., & Tosello, G. (2021). Simultaneous bonding and forming of Mg fibre metal laminates at high temperature. *Journal of Manufacturing Processes*, 72, 105–114.
- Gonçalves, D.C., Sánchez-Arce, I.J., Ramalho, L.D.C., Campilho, R.D.S.G. and Belinha, J., (2023). A meshless crack propagation algorithm extended to mixed-mode loading of adhesive joints. *Composite Structures*, 305.116502.
- Grant, L. D. R., Adams, R. D., & da Silva, L. F. M. (2009). Experimental and numerical analysis of single-lap joints for the automotive industry. *International Journal of Adhesion and Adhesives*, 29(4), 405–413.
- Gu, Z., Ding, X., Hou, X., & Ye, J. (2023). A genetic evolved machine learning approach for 3D DEM modelling of anisotropic materials with full consideration of particulate interactions. *Composites Part B: Engineering*, 250, 110432.

- Gu, Z., Liu, Y., Hughes, D. J., Ye, J., & Hou, X. (2021). A parametric study of adhesive bonded joints with composite material using black-box and grey-box machine learning methods: Deep neuron networks and genetic programming. *Composites Part B: Engineering*, 217, 108894.
- Gültekin, K., Akpınar, S., Gürses, A., Eroglu, Z., Cam, S., Akbulut, H., Keskin, Z., & Ozel, A. (2016). The effects of graphene nanostructure reinforcement on the adhesive method and the graphene reinforcement ratio on the failure load in adhesively bonded joints. *Composites Part B: Engineering*, 98, 362–369.
- Guo, L., Liu, J., Xia, H., Li, X., Zhang, X., & Yang, H. (2021). Effects of surface treatment and adhesive thickness on the shear strength of precision bonded joints. *Polymer Testing*, 94, 107063.
- Guo, S., Dillard, D. A., & Plaut, R. H. (2006). Effect of boundary conditions and spacers on single-lap joints loaded in tension or compression. *International Journal of Adhesion and Adhesives*, 26(8), 629–638.
- Gupta, M., Prabhakaran, R. T. D., & Mahajan, P. (2020). Non-linear material characterization and numerical modeling of cross-ply basalt/epoxy laminate under low velocity impact. *Polymer Testing*, 84, 106349.
- Hadei, M. R., Akbarlou, N., & Nejati, H. R. (2020). A new development cracked chevron notched direct tension method for determining the mode I fracture toughness of rocks. *Theoretical and Applied Fracture Mechanics*, 110, 102811.
- Han, S., Meng, Q., Araby, S., Liu, T., & Demiral, M. (2019). Mechanical and electrical properties of graphene and carbon nanotube reinforced epoxy adhesives: Experimental and numerical analysis. *Composites Part A: Applied Science and Manufacturing*, 120, 116–126.
- Hanumantharaya, R., Sogalad, I., & Basavarajappa, S. (2020). Investigations on the influence of nano reinforcement on strength of adhesively bonded joints. *Manufacturing Engineering*, 2214, 7853.
- Harris, A. F., & Beevers, A. (1999). The effects of grit-blasting on surface properties for adhesion. *International Journal of Adhesion and Adhesives*, 19(6), 445–452.
- Harris, J. A., & Adams, R. A. (1984). Strength prediction of bonded single lap joints by non-linear finite element methods. *International Journal of Adhesion and Adhesives*, 4(2), 65–78.
- He, W., Wang, L., Liu, H., Wang, C., Yao, L., Li, Q., & Sun, G. (2021). On impact behavior of fiber metal laminate (FML) structures: A state-of-the-art review. *Thin-Walled Structures*, 167, 108026.

- Heshmati, M., Haghani, R., Al-Emrani, M., & André, A. (2018). On the strength prediction of adhesively bonded FRP-steel joints using cohesive zone modelling. *Theoretical and Applied Fracture Mechanics*, 93, 64–78.
- Hill, J. (2003). Adhesively bonded structural composites for Aston Martin vehicles. *Ford Motor Company Research and Advanced Engineering*.
- Hirsch, J. (2014). Recent development in aluminium for automotive applications. *Transactions of Nonferrous Metals Society of China*, 24(7), 1995–2002.
- Huang, J., Zeng, J., Bai, Y., Cheng, Z., Wang, Y., Zhao, Q., & Liang, D. (2021). Effect of adhesive layer properties on the shear strength of single-lap structures of dissimilar materials based on the cohesive zone model. *Journal of Mechanical Science and Technology*, 35(1), 133–143.
- ISO, E. N. 4287. (1997). *Geometrical Product Specifications (GPS). Surface Texture. Profile Method. Terms, Definitions and Surface Texture Parameters*. International Organization for Standardization, Geneva.
- Jayakumar, S., Stolz, L., Anand, S., Hajdarevic, A. and Fang, X.F., (2022). FE Crash Modeling of Aluminum-FRP Hybrid Components Manufactured by a Hybrid Forming Process. In *Key Engineering Materials*, Trans Tech Publications Ltd. (926), 2050-2059.
- Jiang, L., Xiao, S., Yang, B., Yang, G., Zhu, T., Dong, D., & Zhang, J. (2019). Finite Element Analysis of Tensile Properties for the Single-Strap Butt Joint of a Carbon Fiber Reinforced Composite. *Computing in Science & Engineering*, 21(3), 42–50.
- Kadioglu, F. (2021). Mechanical behaviour of adhesively single lap joint under buckling conditions. *Chinese Journal of Aeronautics*, 34(2), 154–164.
- Kadioglu, F., & Demiral, M. (2020). Failure behaviour of the single lap joints of angle-ply composites under three point bending tests. *Journal of Adhesion Science and Technology*, 34(5), 531–548.
- Kanani, A. Y., Liu, Y., Hughes, D. J., Ye, J., & Hou, X. (2020). Fracture mechanisms of hybrid adhesive bonded joints: Effects of the stiffness of constituents. *International Journal of Adhesion and Adhesives*, 102, 102649.
- Kazemi, M. E., Shanmugam, L., Lu, D., Wang, X., Wang, B., & Yang, J. (2019). Mechanical properties and failure modes of hybrid fiber reinforced polymer composites with a novel liquid thermoplastic resin, Elium®. *Composites Part A: Applied Science and Manufacturing*, 125, 105523.
- Kazemi, M. E., Shanmugam, L., Yang, L., & Yang, J. (2020). A review on the hybrid titanium composite laminates (HTCLs) with focuses on surface treatments,

- fabrications, and mechanical properties. *Composites Part A: Applied Science and Manufacturing*, 128, 105679.
- Kazi, M. K., Eljack, F., & Mahdi, E. (2020). Predictive ANN models for varying filler content for cotton fiber/PVC composites based on experimental load displacement curves. *Composite Structures*, 254, 112885.
- Kemiklioğlu, U., & Baba, B. O. (2019). Mechanical response of adhesively bonded composite joints subjected to vibration load and axial impact. *Composites Part B: Engineering*, 176, 107317.
- Keshavarz, R., Aghamohammadi, H., & Eslami-Farsani, R. (2020). The effect of graphene nanoplatelets on the flexural properties of fiber metal laminates under marine environmental conditions. *International Journal of Adhesion and Adhesives*, 103, 102709.
- Khoshmanesh, S., Watson, S. J., & Zarouchas, D. (2022). The effect of the fatigue damage accumulation process on the damping and stiffness properties of adhesively bonded composite structures. *Composite Structures*, 287, 115328.
- Kim, H., & Kedward, K. (2001). Stress analysis of in-plane, shear-loaded, adhesively bonded composite joints and assemblies. *Department of Mechanical and Environmental Engineering California University, Santa Barbara, CA, United States of America*.
- Koza, J. R., & Poli, R. (2005). Genetic programming. In *Search methodologies* (pp. 127–164). Springer.
- Kumar, A., Kumar, K., Ghosh, P. K., Rathi, A., Yadav, K. L., & Raman. (2018). MWCNTs toward superior strength of epoxy adhesive joint on mild steel adherent. *Composites Part B: Engineering*, 143, 207–216.
- Lawcock, G., Ye, L., Mai, Y. W., & Sun, C. T. (1997). The effect of adhesive bonding between aluminum and composite prepreg on the mechanical properties of carbon-fiber-reinforced metal laminates. *Composites Science and Technology*, 57(1), 35–45.
- Lee, D. W., Park, B. J., Park, S. Y., Choi, C. H., & Song, J. Il. (2018). Fabrication of high-stiffness fiber-metal laminates and study of their behavior under low-velocity impact loadings. *Composite Structures*, 189, 61–69.
- Li, Y., Yang, Y., Li, J., Wang, B., & Liao, Y. (2020). Experimental-numerical analysis of failure of adhesively bonded lap joints under transverse impact and different temperatures. *International Journal of Impact Engineering*, 140, 103541.
- Liu, X., Shao, X., Li, Q., & Sun, G. (2019). Experimental study on residual properties of carbon fibre reinforced plastic (CFRP) and aluminum single-lap adhesive joints at different strain rates after transverse pre-impact. *Composites Part A: Applied Science and Manufacturing*, 124, 105372.

- Liu, Y., Gu, Z., Hughes, D. J., Ye, J., & Hou, X. (2021). Understanding mixed mode ratio of adhesively bonded joints using genetic programming (GP). *Composite Structures*, 258, 113389.
- Liu, Y., Lemanski, S., Zhang, X., Ayre, D., & Nezhad, H. Y. (2018). A finite element study of fatigue crack propagation in single lap bonded joint with process-induced disbond. *International Journal of Adhesion and Adhesives*, 87, 164–172.
- Liu, Y., Zhang, X., Lemanski, S., Nezhad, H. Y., & Ayre, D. (2019). Experimental and numerical study of process-induced defects and their effect on fatigue debonding in composite joints. *International Journal of Fatigue*, 125, 47–57.
- Lucintel. (2021). Composites Market: Trends, Opportunities and Competitive Analysis. <https://www.lucintel.com/composites-market.aspx>
- Lutsey, N. (2010). Review of technical literature and trends related to automobile mass-reduction technology. *Institute of Transportation Studies, University of California, Davis, CA, United States of America*.
- Majerski, K., Surowska, B., & Bienias, J. (2018). The comparison of effects of hygrothermal conditioning on mechanical properties of fibre metal laminates and fibre reinforced polymers. *Composites Part B: Engineering*, 142, 108–116.
- Maleki, E., Unal, O., Guagliano, M., & Bagherifard, S. (2022). Analysing the Fatigue Behaviour and Residual Stress Relaxation of Gradient Nano-Structured 316L Steel Subjected to the Shot Peening via Deep Learning Approach. *Metals and Materials International*, 28(1), 112–131.
- Malingam, S. D., Feng, N. L., Khoon, L. C., Fadzullah, S. H. S. M., Mustafa, Z., & Subramonian, S. (2020). The Influences of Fibre Parameters on the Tensile and Flexural Response of Lightweight Thermoplastic Kenaf Fibre Reinforced Metal Composites. *Journal of Natural Fibers*, 17(7), 966–978.
- Marami, G., Nazari, S. A., Faghidian, S. A., Vakili-Tahami, F., & Etemadi, S. (2016). Improving the mechanical behavior of the adhesively bonded joints using RGO additive. *International Journal of Adhesion and Adhesives*, 70, 277–286.
- Mariano, M., El Kissi, N., & Dufresne, A. (2014). Cellulose nanocrystals and related nanocomposites: review of some properties and challenges. *Journal of Polymer Science Part B: Polymer Physics*, 52(12), 791–806.
- Marques, A.C., Mocanu, A., Tomić, N.Z., Balos, S., Stammen, E., Lundevall, A., Abrahami, S.T., Günther, R., de Kok, J.M. & Teixeira de Freitas, S., (2020). Review on adhesives and surface treatments for structural applications: Recent developments on sustainability and implementation for metal and composite substrates. *Materials*, 13(24), p.5590.

- Marzi, S., Hesebeck, O., Brede, M., & Kleiner, F. (2009). A Rate-Dependent, Elasto-Plastic Cohesive Zone Mixed-Mode Model for Crash Analysis of Adhesively Bonded Joints. *9th European LS-Dyna Conference*, 1–11.
- Marzi, S., (2010). An Extension of MAT 240 to Consider the Failure of Structural Adhesive Joints in Crash Simulations. *In German LS-Dyna Forum, conference proceedings*, Bamberg.
- Masoudi Nejad, R., Ghahremani Moghadam, D., Hadi, M., Zamani, P., & Berto, F. (2022). An investigation on static and fatigue life evaluation of grooved adhesively bonded T-joints. *Structures*, 35, 340–349.
- Mata, R. (2013). Impact of adhesive joints for the automotive industry at low and high temperatures. *Bachelor's thesis, Universitat Politècnica de Catalunya, Barcelona, Spain*.
- McCulloch, W. S., & Pitts, W. (1943). A logical calculus of the ideas immanent in nervous activity. *The Bulletin of Mathematical Biophysics*, 5(4), 115–133.
- Medjahed, A., Derradji, M., Zegaoui, A., Wu, R., & Li, B. (2019). Mechanical and gamma rays shielding properties of a novel fiber-metal laminate based on a basalt/phthalonitrile composite and an Al-Li alloy. *Composite Structures*, 210, 421–429.
- Mikroskop-Lösungen. Surface Roughness Measurement—Parameters. *OLYMPUS*. <https://www.olympus-ims.com/>
- Mohamed, M. (2020). Characterization and Optimization of Composite/Metallic Adhesively Bonded Joints Subjected to Thermal Fatigue. *Doctoral Thesis, Department of Civil Engineering, Dalhousie University, Halifax, NS, Canada*.
- Mohamed, M., & Taheri, F. (2017). Influence of graphene nanoplatelets (GNPs) on mode I fracture toughness of an epoxy adhesive under thermal fatigue. *Journal of Adhesion Science and Technology*, 31(19–20), 2105–2123.
- Monaldo, E., E., Nerilli, F., & Vairo, G. (2019). Basalt-based fiber-reinforced materials and structural applications in civil engineering. *Composite Structures*, 214, 246–263.
- Montesinos López, O. A., Montesinos López, A., & Crossa, J. (2022). Fundamentals of Artificial Neural Networks and Deep Learning. *In Multivariate Statistical Machine Learning Methods for Genomic Prediction*. 379–425. Springer.
- Moreira, R. D. F., de Moura, M. F. S. F., Silva, F. G. A., & Reis, J. P. (2020). High-cycle fatigue analysis of adhesively bonded composite scarf repairs. *Composites Part B: Engineering*, 190, 107900.

- Mottaghian, F., Darvizeh, A., & Alijani, A. (2018). Extended finite element method for statics and vibration analyses on cracked bars and beams. *Journal of Solid Mechanics*, *10*(4), 902–928.
- Mottaghian, F., & Taheri, F. (2022). Strength and failure mechanism of single-lap magnesium-basalt fiber metal laminate adhesively bonded joints: Experimental and numerical assessments. *Journal of Composite Materials*, *56*(12), 1941-1955.
- Mottaghian, F., & Taheri, F. (2022). Effects of surface treatment on the strength of double-strap adhesively bonded joints mating 3D-fiber metal laminates. *Materials Letters*, *324*, 132698.
- Mottaghian, F., & Taheri, F. (2022). Performance of a Unique Fiber-Reinforced Foam-Cored Metal Sandwich System Joined with Adhesively Bonded CFRP Straps Under Compressive and Tensile Loadings. *Applied Composite Materials*. *30*, 339–359.
- Mottaghian, F., Yaghoobi, H., & Taheri, F. (2020). Numerical and experimental investigations into post-buckling responses of stainless steel- and magnesium-based 3D-fiber metal laminates reinforced by basalt and glass fabrics. *Composites Part B: Engineering*, *200*, 108300.
- Mottaghian, F. and Taheri, F., (2023). On the flexural response of nanoparticle-reinforced adhesively bonded joints mating 3D-Fiber Metal Laminates—A coupled numerical and experimental investigation. *International Journal of Adhesion and Adhesives*, *120*, 103278.
- Murray, R. E., Roadman, J., & Beach, R. (2019). Fusion joining of thermoplastic composite wind turbine blades: Lap-shear bond characterization. *Renewable Energy*, *140*, 501–512.
- Nassir, N. A., Birch, R. S., Cantwell, W. J., Sierra, D. R., Edwardson, S. P., Dearden, G., & Guan, Z. W. (2020). Experimental and numerical characterization of titanium-based fibre metal laminates. *Composite Structures*, *245*, 112398.
- Omar, M. A. (2011). The automotive body manufacturing systems and processes. *John Wiley & Sons*.
- Paddy, J. F., Johnson, R. E., & Kinloch, A. J. (1987). Adhesion and adhesives: science and technology. *Chapman and Hall, London*.
- Parabeam. (2022). *3D Fiber Glass*. Composites and Advanced Materials Exhibition in Anaheim, CA. <https://parabeam.com>
- Park, H., & Kim, H. (2010). Damage resistance of single lap adhesive composite joints by transverse ice impact. *International Journal of Impact Engineering*, *37*(2), 177–184.
- Park, S.-M., Roy, R., Kweon, J.-H., & Nam, Y. (2020). Strength and failure modes of surface treated CFRP secondary bonded single-lap joints in static and fatigue tensile

- loading regimes. *Composites Part A: Applied Science and Manufacturing*, 134, 105897.
- Pärnänen, T., Alderliesten, R., Rans, C., Brander, T., & Saarela, O. (2012). Applicability of AZ31B-H24 magnesium in Fibre Metal Laminates – An experimental impact research. *Composites Part A: Applied Science and Manufacturing*, 43(9), 1578–1586.
- Pärnänen, T., Kanerva, M., Sarlin, E., & Saarela, O. (2015). Debonding and impact damage in stainless steel fibre metal laminates prior to metal fracture. *Composite Structures*, 119, 777–786.
- Paturi, U. M. R., Cheruku, S., & Reddy, N. S. (2022). The Role of Artificial Neural Networks in Prediction of Mechanical and Tribological Properties of Composites— A Comprehensive Review. *Archives of Computational Methods in Engineering*, 29(5), 3109–3149.
- Pisavadia, H., Toussaint, G., Dolez, P. and Hogan, J.D., (2022). Cohesive zone failure modeling of polymeric adhesives used in ceramic/metal armor. *International Journal of Impact Engineering*, 170, 104364.
- Quaresimin, M., Schulte, K., Zappalorto, M., & Chandrasekaran, S. (2016). Toughening mechanisms in polymer nanocomposites: From experiments to modelling. *Composites Science and Technology*, 123, 187–204.
- R, J., & Naik, G. N. (2019). Single and dual adhesive bond strength analysis of single lap joint between dissimilar adherends. *International Journal of Adhesion and Adhesives*, 92, 142–153.
- Raissi, M., Perdikaris, P., & Karniadakis, G. E. (2019). Physics-informed neural networks: A deep learning framework for solving forward and inverse problems involving nonlinear partial differential equations. *Journal of Computational Physics*, 378, 686–707.
- Rangaswamy, H., Sogalad, I., Basavarajappa, S., Acharya, S., & Manjunath Patel, G. C. (2020). Experimental analysis and prediction of strength of adhesive-bonded single-lap composite joints: Taguchi and artificial neural network approaches. *SN Applied Sciences*, 2(6), 1055.
- Rao, Q., Huang, H., Ouyang, Z., & Peng, X. (2020). Synergy effects of multi-walled carbon nanotube and graphene nanoplate filled epoxy adhesive on the shear properties of unidirectional composite bonded joints. *Polymer Testing*, 82, 106299.
- Razavi, S. M. J., Ayatollahi, M. R., Majidi, H. R., & Berto, F. (2018). A strain-based criterion for failure load prediction of steel/CFRP double strap joints. *Composite Structures*, 206, 116–123.
- Redmann, A., Damodaran, V., Tischer, F., Prabhakar, P., & Osswald, T. A. (2021). Evaluation of Single-Lap and Block Shear Test Methods in Adhesively Bonded

- René C. Alderliesten. (2017). *Fatigue and Fracture of Fibre Metal Laminates*. Springer, New York, United States of America.
- Russian, O., Belarbi, A., & Dawood, M. (2022). Effect of surface preparation technique on fatigue performance of steel structures repaired with self-stressing SMA/CFRP patch. *Composite Structures*, 280, 114968.
- Saleh, M. N., Saeedifar, M., Zarouchas, D., & De Freitas, S. T. (2020). Stress analysis of double-lap bi-material joints bonded with thick adhesive. *International Journal of Adhesion and Adhesives*, 97, 102480.
- Sauer, R. A. (2016). A Survey of Computational Models for Adhesion. *The Journal of Adhesion*, 92(2), 81–120.
- Shahin, K. and Taheri, F., (2006), January. Optimization of Single-Strap Composite Joints. In *ASME International Mechanical Engineering Congress and Exposition*, (47675). 879-883.
- Shahin, K. and Taheri, F., (2007). Analysis of deformations and stresses in balanced and unbalanced adhesively bonded single-strap joints. *Composite structures*, 81(4).511-524.
- Silva, G. C., Beber, V. C., & Pitz, D. B. (2021). Machine learning and finite element analysis: An integrated approach for fatigue lifetime prediction of adhesively bonded joints. *Fatigue and Fracture of Engineering Materials and Structures*, 44(12), 3334–3348.
- Silva, N. D. D. (2019). Experimental and numerical study of the impact behaviour of an adhesively bonded automotive structure, *Master's Thesis, Faculty of Mechanical Engineering, University of Porto, Portugal*.
- Silva, D.F.O., Campilho, R.D.S.G., Silva, F.J.G. and Carvalho, U.T.F., (2018). Application a direct/cohesive zone method for the evaluation of scarf adhesive joints. *Applied Adhesion Science*, 6.1-20
- Singh, S., & Angra, S. (2018). Experimental evaluation of hygrothermal degradation of stainless steel fibre metal laminate. *Engineering Science and Technology, an International Journal*, 21(1), 170–179.
- Soltannia, B., Mertiny, P., & Taheri, F. (2020). Static and dynamic characteristics of nano-reinforced 3D-fiber metal laminates using non-destructive techniques. *Journal of Sandwich Structures & Materials*, 23(7), 3081–3112.
- Soltannia, B., & Taheri, F. (2015). Influence of nano-reinforcement on the mechanical behavior of adhesively bonded single-lap joints subjected to static, quasi-static, and impact loading. *Journal of Adhesion Science and Technology*, 29(5), 424–442.

- Sonat, E., & Özerinç, S. (2021). Failure behavior of scarf-bonded woven fabric CFRP laminates. *Composite Structures*, 258, 113205.
- Srinivasan, V. D., Ravisankar Padma, S., & Idapalapati, S. (2022). Comparative study of composite scarf and strap joints for equivalent repair signature under uniaxial tension. *Composites Part A: Applied Science and Manufacturing*, 158, 106950.
- Sugiman, S., Crocombe, A.D. and Aschroft, I.A., (2013). Modelling the static response of unaged adhesively bonded structures. *Engineering Fracture Mechanics*, 98.296-314.
- Swati, R. F., Wen, L. H., Elahi, H., Khan, A. A., & Shad, S. (2019). Extended finite element method (XFEM) analysis of fiber reinforced composites for prediction of micro-crack propagation and delaminations in progressive damage: a review. *Microsystem Technologies*, 25(3), 747–763.
- Taheri, F. (2020). Improvement of the Performance of Structural Adhesive Joints with Nanoparticles and Numerical Prediction of Their Response. *Structural Adhesive Joints: Design, Analysis and Testing*, 35–78.
- Taheri, F., & Zou, G. P. (2004). Treatment of Unsymmetric Adhesively Bonded Composite Sandwich Panels-To-Flange Joints. *Mechanics of Advanced Materials and Structures*, Ed.,: K.L. Mittal, S. K. Panigrahi, Willey Online Books, 11(2), 175–196.
- Tao, F., Liu, X., Du, H., & Yu, W. (2021). Learning composite constitutive laws via coupling Abaqus and deep neural network. *Composite Structures*, 272, 114137.
- Tosun, E., & Çalik, A. (2016). Failure load prediction of single lap adhesive joints using artificial neural networks. *Alexandria Engineering Journal*, 55(2), 1341–1346.
- Trinh, M.-C., & Jun, H. (2021). Stochastic bending and buckling analysis of laminated composite plates using Latin hypercube sampling. *Engineering with Computers*.
- Tsai, M. Y., & Morton, J. (2010). An investigation into the stresses in double-lap adhesive joints with laminated composite adherends. *International Journal of Solids and Structures*, 47(24), 3317–3325.
- Ucan, H., Scheller, J., Nguyen, C., Nieberl, D., Beumler, T., Haschenburger, A., Meister, S., Kappel, E., Prussak, R., Deden, D., Mayer, M., Zapp, P., Pantelelis, N., Hauschild, B., & Menke, N. (2019). Automated, Quality Assured and High Volume Oriented Production of Fiber Metal Laminates (FML) for the Next Generation of Passenger Aircraft Fuselage Shells. *Science and Engineering of Composite Materials*, 26(1), 502–508.
- Vaidya, U. K., Hosur, M. V, Earl, D., & Jeelani, S. (2000). Impact response of integrated hollow core sandwich composite panels. *Composites Part A: Applied Science and Manufacturing*, 31(8), 761–772.

- Vasumathi, M., & Murali, V. (2013). Effect of Alternate Metals for use in Natural Fibre Reinforced Fibre Metal Laminates under Bending, Impact and Axial Loadings. *Procedia Engineering*, 64, 562–570.
- Vlot, A., (2007). Glare: history of the development of a new aircraft material. *Springer Science & Business Media*. Delft, Netherlands.
- Vlot, A. and Gunnink, J.W. eds., (2011). Fibre metal laminates: an introduction. *Springer Science & Business Media*. Delft, Netherlands.
- Vinson, J. R. (2001). Sandwich structures. *Mechanical Engineering, University of Delaware, Newark, Delaware, United States of America*.
- Völkerink, O., Kosmann, J., Schollerer, M. J., Holzhüter, D., & Hühne, C. (2019). Strength prediction of adhesively bonded single lap joints with the eXtended Finite Element Method. *The Journal of Adhesion*, 95(5–7), 474–494.
- Volkersen, O. (1938). Die Nietkraftverteilung in zugbeanspruchten Nietverbindungen mit konstanten Laschenquerschnitten. *Luftfahrtforschung*, 15, 41–47.
- Watson, B. (2021). Characterizing and Modeling the Effects of Mode Mixity and Bond Line Thickness on the Traction-Separation Response of Structural Adhesive Joints. *Department of Mechanical and Mechatronic Engineering, Waterloo University, Waterloo, ON, Canada*
- Wciślik, W., & Pała, T. (2021). Selected Aspects of Cohesive Zone Modeling in Fracture Mechanics. *Metals*, 11(2).
- Wei, K., Chen, Y., Li, M., & Yang, X. (2018). Strength and failure mechanism of composite-steel adhesive bond single lap joints. *Advances in Materials Science and Engineering*, 2018.
- Xará, J. T. S., & Campilho, R. D. S. G. (2018). Strength estimation of hybrid single-L bonded joints by the eXtended Finite Element Method. *Composite Structures*, 183, 397–406.
- Xi, J., Xia, R., He, Y., & Yu, Z. (2020). The fatigue repairing evaluation of hybrid woven composite patch with 2D&3D styles bonded Al-alloy plates under UV and thermal curing. *Composites Part B: Engineering*, 185, 107743.
- Xie, Y., Yang, B., Lu, L., Wan, Z., & Liu, X. (2020). Shear strength of bonded joints of carbon fiber reinforced plastic (CFRP) laminates enhanced by a two-step laser surface treatment. *Composite Structures*, 232, 111559.
- Xu, J.-Q., Liu, Y.-H., & Wang, X.-G. (1999). Numerical methods for the determination of multiple stress singularities and related stress intensity coefficients. *Engineering Fracture Mechanics*, 63(6), 775–790.

- Xu, Y., Zhu, J., Wu, Z., Cao, Y., Zhao, Y., & Zhang, W. (2018). A review on the design of laminated composite structures: constant and variable stiffness design and topology optimization. *Advanced Composites and Hybrid Materials*, 1(3), 460–477.
- Yaghoobi, H., Mottaghian, F., & Taheri, F. (2021a). Enhancement of buckling response of stainless steel-based 3D-fiber metal laminates reinforced with graphene nanoplatelets: Experimental and numerical assessments. *Thin-Walled Structures*, 165, 107977.
- Yaghoobi, H., Mottaghian, F., & Taheri, F. (2021b). Enhancement of buckling response of stainless steel-based 3D-fiber metal laminates reinforced with graphene nanoplatelets: Experimental and numerical assessments. *Thin-Walled Structures*, 165, 107977.
- Yaghoubi, A. S., & Liaw, B. 2014. Influences of thickness and stacking sequence on ballistic impact behaviors of GLARE 5 FML plates: Part II–Numerical studies. *Journal of Composite Materials*, 48(19), pp.2363-2374.
- Yang, G., Yang, T., Yuan, W., & Du, Y. (2019). The influence of surface treatment on the tensile properties of carbon fiber-reinforced epoxy composites-bonded joints. *Composites Part B: Engineering*, 160, 446–456.
- Yang, J.-M. (2008). Damage Tolerance and Durability of Fiber-Metal Laminates for Aircraft Structures. *The Joint Advanced Materials and Structures Center of Excellence, University of California, Los Angeles, Unites States of America*.
- Yang, S., Gu, L., & Gibson, R. F. (2001). Nondestructive detection of weak joints in adhesively bonded composite structures. *Composite Structures*, 51(1), 63–71.
- Ye, J., Yan, Y., Li, J., Hong, Y., & Tian, Z. (2018). 3D explicit finite element analysis of tensile failure behavior in adhesive-bonded composite single-lap joints. *Composite Structures*, 201, 261–275.
- Zamani, P., Jaamialahmadi, A., & Da Silva, L. F. M. (2021). The influence of GNP and nano-silica additives on fatigue life and crack initiation phase of Al-GFRP bonded lap joints subjected to four-point bending. *Composites Part B: Engineering*, 207, 108589.
- Zan, D. Q., Sun, Q., Pan, H. L., Chen, J. J., & Wang, Z. D. (2017). Application of the cohesive zone model for analysing the edge crack propagation of steel sheet in the cold rolling process. *Fatigue & Fracture of Engineering Materials & Structures*, 40(6), 869–881.
- Zenkert, D. (1997). (1997). An introduction to sandwich construction. *Engineering Materials Advisory Services. United Kingdom*.
- Zheng, Z., Chen, X. and Zheng, H., (2022). Compression Performance of Composite Honeycomb Sandwich Structures with Prefabricated Defects. *In Proceedings of the International Conference on Aerospace System Science and Engineering 2021*. 449-464

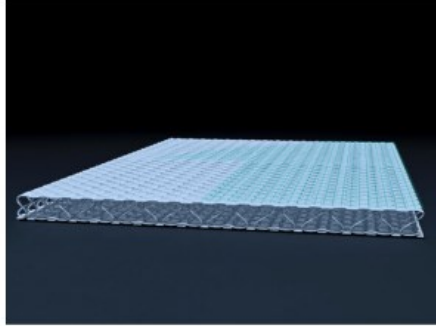
Zhou, G., Sun, Q., Fenner, J., Li, D., Zeng, D., Su, X. and Peng, Y., (2020). Crushing behaviors of unidirectional carbon fiber reinforced plastic composites under dynamic bending and axial crushing loading. *International Journal of Impact Engineering*, (140),103539.

Zou, G. P., Shahin, K., & Taheri, F. (2004). An analytical solution for the analysis of symmetric composite adhesively bonded joints. *Composite Structures*, 65(3–4).

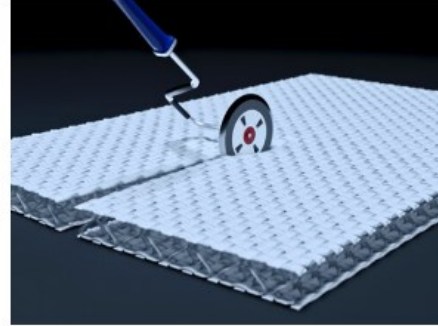
Appendix A: Fabrication Manual of 3DFGF (Parabeam, 2022)



Hand Lay-Up Process



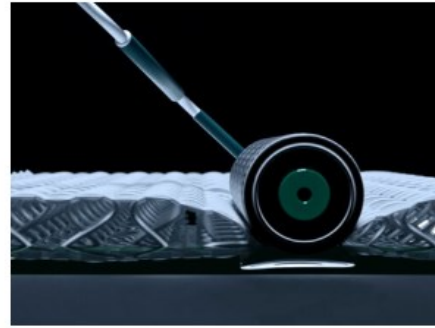
STEP 1 | MEASURE FABRIC
Measure the surface of the fabric and calculate fabric weight to determine the amount of resin needed.



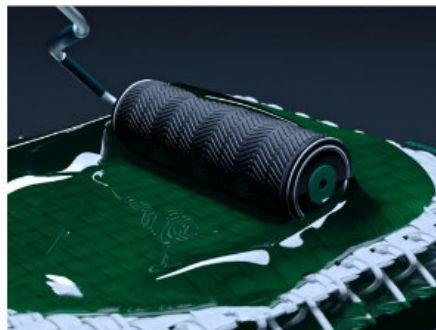
STEP 2 | CUT FABRIC
Cut the fabric to the needed size with a tool such as a rotary cutter or scissors.



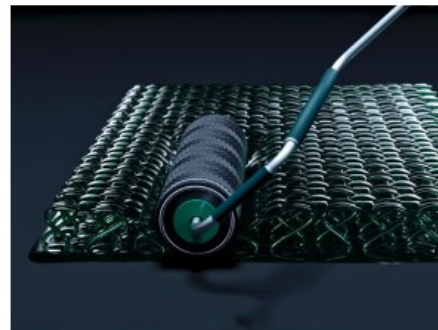
STEP 3 | APPLY RESIN
Apply 40% of the calculated resin to the mould and spread it evenly.



STEP 4 | ROLL FABRIC
Roll the fabric to ensure that the resin is



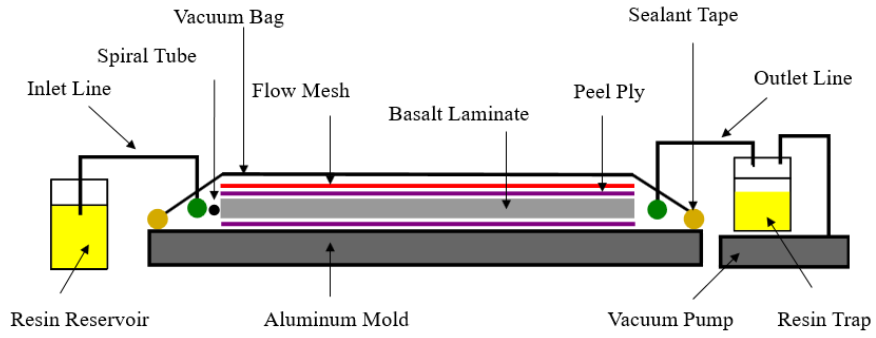
STEP 5 | APPLY REMAINING RESIN
Apply the remaining resin and spread it evenly. It will automatically start absorbing into the fabric.



STEP 6 | ROLL FABRIC
Lightly roll the fabric against the pile direction to ensure an optimal rise.

Appendix B: Basalt-Epoxy Fabrication with Vacuum-Assisted Resin Infusion Procedure

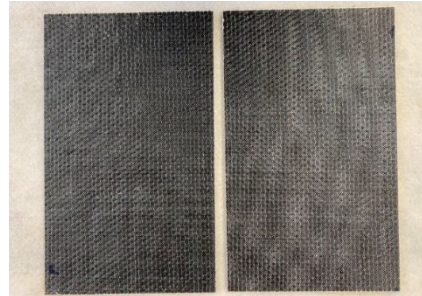
Fabrication of the core components of the MB-FML started by preparing the basalt-epoxy laminate using the vacuum-assisted resin infusion (VARI) technique. The $[0/90]_{2s}$ layup sequences of the bidirectional reinforcing basalt fabrics were placed over a thick aluminum plate that was covered with a thin layer of peel-ply. The assembly was then interleaved with another layer of peel-ply and a resin distribution mesh was placed on top of the upper layer of peel-ply. Note that the resin distribution mesh and the peel-ply facilitate the resin flow into the dry basalt fabrics during the vacuum infusion process as well as releasing the composite laminate after polymerization of its resin, respectively. Next, the assembled system was enclosed by vacuum bagging sheets, and the resin reservoir was connected to the vacuum bag by an input hose. A vacuum pump connected to the bag by a hose was placed on the opposite side of the bag, which facilitates the resin to be infused into the laminate system. Before allowing the resin to infuse into the laminate/bag, the inlet line was clamped, and the system was placed under 1 bar vacuum to remove the entrapped air in the system. At that stage, the outlet hose was clamped, and the system was monitored for any air leakage for 20 mins. After passing the leakage test, the room-cured epoxy resin and hardener were mixed with a weight ratio of 5:1 and poured into the resin reservoir. The vacuum pump was then turned on, the hose clamps were released, and the resin system was infused into the dry fabrics until the fabrics were fully saturated. Then, the inlet and outlet lines were clamped, and the fully infused basalt-epoxy laminate was left to cure at ambient temperature under the vacuum for 48 hrs. In the next step, the cured basalt-epoxy laminate panels were sandwiched in between two pre-treated Mg sheets using the same resin system, which was brushed onto the mating surfaces. Subsequently, the assembly was sealed by the vacuum bagging process under 1 bar vacuum and allowed to cure at ambient temperature for 48 hrs, as per the manufacturer's recommendation. The schematic of the VARI setup and the basalt-epoxy laminates are illustrated in Figure D-1.



(a)



(b)



(c)

Figure D-1. VARI setup (a) front-view schematic, (b) top-view, and (c) the fabricated basalt-epoxy laminates.

Appendix C: Copyright Permissions

Copyright Permission for Chapter 3



Thank you for your order!

Dear Ms. Fatemeh Mottaghian,

Thank you for placing your order through Copyright Clearance Center's RightsLink® service.

Order Summary

Licensee:	Dalhousie University
Order Date:	Dec 7, 2022
Order Number:	5443640431915
Publication:	Composites Part B: Engineering
Title:	Numerical and experimental investigations into post-buckling responses of stainless steel- and magnesium-based 3D-fiber metal laminates reinforced by basalt and glass fabrics
Type of Use:	post on a website
Order Total:	0.00 CAD

(Original Order Number: 501778217)

View or print complete [details](#) of your order and the publisher's terms and conditions.

Sincerely,

Copyright Clearance Center

Tel: +1-855-239-3415 / +1-978-646-2777
customercare@copyright.com
<https://myaccount.copyright.com>



Copyright Permission for Chapter 4

Dear Farid Taheri,

Congratulations on the acceptance of your paper *Strength and Failure Mechanism of Single-Lap Magnesium-Basalt Fiber Metal Laminate Adhesively Bonded Joints: Experimental and Numerical Assessments* (DOI: 10.1177/00219983221088095/ ID: JCM-21-1356.R1).

Open access publication for your paper in **Journal of Composite Materials** has been requested by Canadian Research Knowledge Network (CRKN). Thanks to your institution's participation in the CRKN-SAGE Publishing agreement, your article is eligible to be published open access via SAGE Choice without additional cost. [Please click here for more information on CRKN's arrangement with SAGE.](#)

Best wishes,
SAGE Publishing Open Access Team
openaccess@sagepub.com

SAGE Creative Commons License

Contributor's Publishing Agreement

Article	Strength and Failure Mechanism of Single-Lap Magnesium-Basalt Fiber Metal Laminate Adhesively Bonded Joints: Experimental and Numerical Assessments
DOI	10.1177/00219983221088095
Journal	Journal of Composite Materials
Author(s)	Fatemeh Mottaghian, Farid Taheri

This Agreement will grant to the owner(s) SAGE Ltd. (the "Proprietor") of the Journal, Journal of Composite Materials (the Journal title subject to verification by SAGE Publishing ("SAGE")) a commercial license to produce, publish, sell and sub-license your article ("Article") and any accompanying abstract or Supplemental Material (all materials collectively referenced as the "Contribution"), in all languages and all formats through any medium of communication for the full legal term of copyright (and any renewals) throughout the universe.

The Proprietor will publish the Contribution under this Creative Commons license:
[Creative Commons Attribution license \(CC BY 4.0\)](#)
This license allows others to [re-use](#) the Contribution without permission as long as the Contribution is properly referenced.

The copyright to the Contribution is owned by you
You represent and warrant that the copyright to the Contribution is owned by you.


Terms & Signature

I have read and accept the Terms of the Agreement (copied below)

I warrant that I am one of the named authors of the Contribution and that I am authorized to sign this Agreement; in the case of a multi-authored Contribution, I am authorized to sign on behalf of all other authors of the Contribution

Signing Author:	Fatemeh Mottaghian (electronic signature)
Date:	02 March 2022

Published In



[Journal of Composite Materials](#)
Volume 56, Issue 12
Pages: 1941 - 1955


Open access | | | First published online March 30, 2022

Strength and failure mechanism of single-lap magnesium-basalt fiber metal laminate adhesively bonded joints: Experimental and numerical assessments

[Fatemeh Mottaghian](#) and [Farid Taheri](#) [View all authors and affiliations](#)

Rights and permissions

© The Author(s) 2022.



This article is distributed under the terms of the Creative Commons Attribution 4.0 License (<https://creativecommons.org/licenses/by/4.0/>) which permits any use, reproduction and distribution of the work without further permission provided the original work is attributed as specified on the SAGE and Open Access page (<https://us.sagepub.com/en-us/nam/open-access-at-sage>).

History

Published online: March 30, 2022
Issue published: May 2022

Copyright Permission for Chapter 5



Thank you for your order!

Dear Ms. Fatemeh Mottaghian,

Thank you for placing your order through Copyright Clearance Center's RightsLink® service.

Order Summary

Licensee: Dalhousie University
Order Date: Dec 7, 2022
Order Number: 5443640405011
Publication: International Journal of Adhesion and Adhesives
On the flexural response of nanoparticle-reinforced
adhesively bonded joints mating 3D-Fiber Metal Laminates –
Title: A coupled numerical and experimental investigation
Type of Use: post on a website
Order Total: 0.00 CAD

(Original Order Number: 501778219)

View or print complete [details](#) of your order and the publisher's terms and conditions.

Sincerely,

Copyright Clearance Center

Tel: +1-855-239-3415 / +1-978-648-2777
customercare@copyright.com
<https://myaccount.copyright.com>



RightsLink

Copyright Permission for Chapter 6

SPRINGER NATURE

Thank you for your order!

Dear Ms. Fatemeh Mottaghian,

Thank you for placing your order through Copyright Clearance Center's RightsLink® service.

Order Summary

Licensee: Dalhousie University
Order Date: Dec 5, 2022
Order Number: 5442541288706
Publication: Applied Composite Materials
Performance of a Unique Fiber-Reinforced Foam-Cored Metal
Sandwich System Joined with Adhesively Bonded CFRP
Title: Straps Under Compressive and Tensile Loadings
Type of Use: Thesis/Dissertation
Order Total: 0.00 CAD

View or print complete [details](#) of your order and the publisher's terms and conditions.

Sincerely,

Copyright Clearance Center

Tel: +1-855-239-3415 / +1-978-646-2777
customercare@copyright.com
<https://myaccount.copyright.com>



RightsLink